



<https://theses.gla.ac.uk/>

Theses Digitisation:

<https://www.gla.ac.uk/myglasgow/research/enlighten/theses/digitisation/>

This is a digitised version of the original print thesis.

Copyright and moral rights for this work are retained by the author

A copy can be downloaded for personal non-commercial research or study,
without prior permission or charge

This work cannot be reproduced or quoted extensively from without first
obtaining permission in writing from the author

The content must not be changed in any way or sold commercially in any
format or medium without the formal permission of the author

When referring to this work, full bibliographic details including the author,
title, awarding institution and date of the thesis must be given

Enlighten: Theses

<https://theses.gla.ac.uk/>
research-enlighten@glasgow.ac.uk

Planar Silica Optical Device Technology

Giovanni Barbarossa
Ingegnere Elettronico

**A thesis submitted for the degree of Doctor of Philosophy
in the Faculty of Engineering in the University of Glasgow**

December MCMXCII

© Giovanni Barbarossa MCMXCII

ProQuest Number: 10992100

All rights reserved

INFORMATION TO ALL USERS

The quality of this reproduction is dependent upon the quality of the copy submitted.

In the unlikely event that the author did not send a complete manuscript and there are missing pages, these will be noted. Also, if material had to be removed, a note will indicate the deletion.



ProQuest 10992100

Published by ProQuest LLC (2018). Copyright of the Dissertation is held by the Author.

All rights reserved.

This work is protected against unauthorized copying under Title 17, United States Code
Microform Edition © ProQuest LLC.

ProQuest LLC.
789 East Eisenhower Parkway
P.O. Box 1346
Ann Arbor, MI 48106 – 1346

Thesis
9413
copy 1

GLASGOW
UNIVERSITY
LIBRARY

to Bartolomeo, Pupa and Federico

*Pertinacia impedimentum omne trascendit
ostenditque nihil esse difficile,
cuius sibi ipsa mens patientiam indiceret.*

Lucius Anneus Seneca (4 B.C., 65 A.D.)

De ira, 2, 12, 5

(The pertinacity overcomes any obstacle, and it demonstrates that nothing is difficult for the man that has voluntarily imposed to himself to use patience).

Acknowledgements

The completion of this project would not have been possible without the help of many people of whom I can only thank a few here.

First I would like to take this opportunity to thank Professor John Lamb for providing the facilities in the Department of Electronics and Electrical Engineering for this research. Particularly my thanks go to my supervisor Professor Peter J.R. Laybourn for his interest and support, both in this work and with regard to the author's welfare. I would also warmly like to thank Professor Richard M. De La Rue for taking an active interest in the work and for many useful discussions; thanks also to Professor Chris D. Wilkinson for the etching facilities and to Dr. John Arnold and Dr. Stewart Aitchison for their helpful suggestions.

I would also like to thank the whole of the technical staff of the Department and particularly: Mr. Roy Turnbull for his help in the assembling and maintenance of the flame hydrolysis deposition system; Mr. George Boyle for his multirange helpful solutions; Mr. Kaz Piechowiak for the excellent polishing of the waveguides; Mr. Jimmy Young for the gas and hydraulic related work; Mr. Ray Hutchins for his help in the early stage of the project; Mr. Robert Artkins for the mask making facilities; Miss Joan Carson for kindly teaching me photolithography and Mrs. Lois Hobbs for teaching me how to be clean in the cleanroom; Mr. Ray Darkin and Mr. Dave Clifton for the valuable help in the dry etching work; Miss Ann Mc Kinnon for the computer facilities; Mr. Harry Anderson and Mr. George Thornton for the mechanical part of the project; also many thanks to Mr. Tom Wright, Mr. Dave Gourlay and Mr. Douglas MacIntyre.

A special thank goes to Mr. John Cochrane and Mr. Lawrence Bradley who have been always very kind with me.

Very many thanks to my industrial supervisor Dr. Colin Millar, of BT Labs, who encouraged me throughout the course of my project showing his positive

interest and by continuously suggesting brilliant solutions and original ideas. Also many thanks to Dr. Graeme D. Maxwell, with whom I shared the enthusiasm for this project, for the incessant and creative discussions, for his constructive criticism and plain speaking. Also many thanks to Jim J. Ainslie who showed constant interest in my ideas and fully appreciated my efforts. Thanks also to Dr. Steve Hubbard for the implementation of the mask designs.

Also thank to all my friends John Bebbington, Ken Thomas, Armando Loni, Philippe Nadal, Ivair Gontijo, Zhou Yen, Pisu Yang, Haiping Zhou and Scott Roy.

Financial support was provided by a Science and Engineering Research Council CASE award with BT Labs, which is gratefully acknowledged.

A special thank goes to Professor Mario N. Armenise of the University of Bari, Italy, who put me on the road to Glasgow.

Last, but not least, I am grateful to my parents and my brother for their continual support and encouragement during my prolonged education.

Giovanni Barbarossa
Glasgow, December MCMXCII

Summary of work

This thesis is concerned with the technological aspects of the flame hydrolysis deposition (FHD) technique for the fabrication of high-silica content passive planar lightwave circuits and with the research and development of useful and original solutions for telecommunications applications.

A FHD apparatus has been engineered, assembled and maintained in clean, good working order by the author. A series of solutions has been adopted for the sake of the operator safety and of the fabrication reproducibility and reliability.

$\text{SiO}_2\text{-P}_2\text{O}_5$ optical waveguides have been successfully fabricated on Si substrate using FHD for the first time. P_2O_5 has been used to decrease the sintering point of silica as well as to increase its refractive index. The deposition parameters and the sintering process have been optimised in order to achieve low-loss, bubble-free waveguides. $\text{SiO}_2\text{-P}_2\text{O}_5\text{-GeO}_2$ optical waveguides have been also fabricated.

The influence of the temperature range and gradient on the evolution of the sintering of $\text{SiO}_2\text{-P}_2\text{O}_5$ planar films and its consequences on the dopant incorporation, have been investigated. Volatilisation of the P_2O_5 phase from the silica matrix has been observed at different levels as a consequence of different thermal treatments.

Channel waveguides have been fabricated by using a combination of photolithographic patterning and reactive ion etching (RIE) technique. The influence of different dopants on the optical damage threshold of the fabricated channel waveguides has been investigated. By comparisons of experimental results on two silica systems considered, it has been concluded that the P_2O_5 -doped silica waveguides have a greater power handling capability than the $\text{P}_2\text{O}_5\text{-GeO}_2$ -doped silica waveguides.

Symmetrical three waveguide couplers (3WC), consisting of slab-coupled

rib waveguides, have been fabricated in $\text{SiO}_2\text{-P}_2\text{O}_5$ glass on Si substrate. Wideband filtering responses have been achieved by appropriate connection of 3WCs in cascade. This solution has been shown to offer flexibility over the tuning of the passbands, and to achieve high stopband rejection and lends itself to a systematic approach for the synthesis of complicated spectral characteristics. Methods and criteria followed in the filter design have been described, particularly directed towards the improvement in rejection bandwidth of the filter characteristic.

A novel configuration for a wide rejection band optical guided-wave multi-demultiplexer at 1.3 and 1.55 μm , based on cascaded and appropriately connected 3WCs, has been fabricated. For a stopband rejection loss of 20 dB, rejection bandwidths of 160 and 170 nm have been achieved for the 1.3 and 1.55 μm wavelength regions respectively.

Finally, $\text{P}_2\text{O}_5\text{-GeO}_2$ -doped silica channel optical waveguides have been vertically integrated on a Si substrate for the first time by a multi-step combination of FHD, photolithographic patterning and RIE.

Contents

		page
	Acknowledgements	IV
	Summary of work	VI
Chapter	1. Introduction	1
	1.1 Optical telecommunications	1
	1.2 Planar lightwave circuits	3
	1.3 Silica-based planar lightwave circuits	4
	1.4 Motivation and aim of research	5
	1.5 Review of the contents of the thesis	7
Chapter	2. Flame hydrolysis deposition (FHD)	9
	2.1 Introduction	9
	2.2 FHD	11
	2.3 FHD apparatus	16
	2.3.1 The gas supply assembly	17
	2.3.2 The bubbler cabinet	19
	2.3.3 The mass flow control cabinet	20
	2.3.4 The deposition chamber	22
	2.3.5 The scrubber system	32
	2.4 Deposition procedure	34
Chapter	3. Fabrication and characterisation of planar waveguides	37
	3.1 Introduction	37
	3.2 Substrate preparation	40
	3.3 Fabrication of SiO ₂ -P ₂ O ₅ films by FHD	42
	3.4 Investigation of sintering of SiO ₂ -P ₂ O ₅ films	46
	3.5 Fabrication of SiO ₂ -GeO ₂ -P ₂ O ₅ films by FHD	54

	3.6	Fabrication considerations	55
	3.7	Rare-earth aerosol doping of $\text{SiO}_2\text{-P}_2\text{O}_5$ films	64
	3.8	Characterisation of planar waveguide	69
Chapter	4.	Channel waveguide fabrication	86
	4.1	Introduction	86
	4.2	Photolithography	87
	4.3	Reactive ion etching	91
	4.4	Investigation into the optical damage threshold of $\text{SiO}_2\text{-P}_2\text{O}_5$ and $\text{SiO}_2\text{-GeO}_2\text{-P}_2\text{O}_5$ channel waveguides	98
	4.4.1	Optical damage in silica based waveguides	98
	4.4.2	Experimental	100
	4.4.3	Results and discussion	103
	4.5	Summary	105
Chapter	5.	Three-waveguide-coupler (3WC) based devices	106
	5.1	Introduction	106
	5.2	The 3WC and its peculiarities	107
	5.3	Cascading 3WC	109
	5.4	3WC-based devices	116
	5.4.1	Power splitter	116
	5.4.2	Filter	123
	5.4.3	Wavelength division multi-demultiplexer	129
	5.5	Summary	133
Chapter	6.	Vertical integration (VI) of high-silica content channel waveguides	134
	6.1	Introduction	134
	6.2	Examples of VI reported in literature	135
	6.3	Requirements for VI of channel waveguides	137
	6.4	FHD peculiarities in a VI context	138
	6.5	Multi-nonidentical step fabrication process	139
	6.6	Multi-identical step fabrication process	148

	6.7	Patent pending	151
Chapter	7.	Conclusions and further work	152
	7.1	Conclusions	152
	7.2	Outlines for further work	154
Appendices			
	A	Four-layer planar optical waveguide theory	158
	B	Effective index method for 3WC	161
	C	Directional coupling in 2WC and 3WC	166
	D	3WC-based WDM and filter design	174
General References			178

Chapter 1. Introduction

Chapter Layout

- 1.1 Optical telecommunications
- 1.2 Planar lightwave circuits
- 1.3 Silica-based planar lightwave circuits
- 1.4 Motivation and aim of research
- 1.5 Review of the contents of the thesis

1.1 Optical telecommunications

Communication, i.e. “the imparting or exchange of information” (from the latin word *communicare* = to share), is certainly a distinctive activity which differentiates animal beings from plants. Telecommunication, i.e. “communication at or over a distance” (from the greek word $\tau\epsilon\lambda\epsilon$ (telé) = far) is a practice which is definitely a prerogative of intelligent beings. Nowadays for telecommunications we intend the science and technology of real-time media for transferring or diffusing information, such as telephone, radio, television, etc., although, in a wide sense of the word, newspapers, music records, letters could be considered telecommunication media.

Telecommunication has always been very important to mankind. More and more advanced telecommunication services are presently considered essential for the economic and social development of an industrialised country. In modern times the revolution in terrestrial telecommunications has been initiated by the almost simultaneous proposals by Werts and Kao et al. in 1966 of using an optical carrier and a dielectric medium to produce high bandwidth (information capacity)

long distance communications links. The advent of the semiconductor laser and of the glass optical fibre triggered the dream of an optical telecommunications network. Although many years were necessary to obtain low loss optical fibres and reliable semiconductor lasers, other intrinsic advantages of an optical fibre telecommunications network, such as electrical isolation, immunity to interference and crosstalk, signal security, potential low cost, system reliability and ease of maintenance, were immediately realised.

About 10^7 Km of glass optical fibre have been installed worldwide in telecommunications applications since the first demonstration of a low loss optical fibre. However, installations have been mainly point to point in the long haul, trunk and feeder sections of the telecommunications outside plant. This has been the scenario in the past two decades in which the optical fibre first proved cost effective and superior in performance with respect to existing metallic cables (Senior '92).

The extension of fibre into the local loop, all the way to the subscriber, could only be justified by the introduction of broad-band subscriber services, most notably broadcast and switched video. One current proposal is for the distribution of up to four 150 Mbit/s channel per subscriber, one of which is a packet switched channel for voice, data, and signalling, and the others are circuit switched and intended for video usage (Linnell '86).

In the event of a completely optical network, loop distribution would be the most cost-sensitive portion of the network, for the simple reason that there is no practical way to share the subscriber-line costs. The passive routing functions which are necessary in bringing the fibre to the subscriber are basically interconnection, furcation, i.e. splitting and coupling, and filtration. The interconnection category can be divided into single or multiple, fibre-to-fibre and fibre-to-device subcategories. From the component viewpoint, the subscriber loop requires massive signal furcation and filtration compared to the trunk and feeder. The implication is that components for the loop must be very cheap relative to what would be tolerable costs in the transmission side of the network. To date,

furcation and filtration functions have been realised in bulk-optic configurations using microlenses and prisms or in fibre-optic configurations using fused-fibre couplers. These bulk-optic and fibre-optic approaches, however appear to have some limitations in terms of productivity, device stability and suitability for integration (Keck '89).

1.2 Planar lightwave circuits

In 1969 Miller, a researcher at Bell Laboratories, introduced the term Integrated Optics (IO), based on the concept that optical circuits could be constructed in close analogy to integrated electronic devices. The idea required the integration of different optical functions on the same chip. Over the last two decades IO has received a great deal of interest by the scientific community because of its potential to offer devices with crucial advantages over conventional bulk and optical fibre based geometries, in terms of mass producibility, low cost, performance and ruggedness.

However, more than 20 years of research have demonstrated that there is no single material for photonic integration which is ideal in all respects, while most applications requires the highest possible joint performance. On the other hand, a number of technologies have proved to satisfy commercial requirements in the different context of simple passive planar lightwave circuits (PLC). In fact some PLCs which perform simple passive optical functions are already available on the market at an affordable price.

There is a number of valuable technologies for the fabrication of passive PLCs. Those which have produced the larger amount of fully characterised PLCs are: ion-exchange in glass (e.g. Ramaswamy '88 a), photopolymerization (e.g. Kurosawa '80) and high-silica content waveguides on Si substrate (e.g. Kawachi '90, Verbeek '88, Valette '89). Once an acceptable threshold performance level is demonstrated, the driving forces for passive PLCs in an optical network, in order of decreasing importance, are: cost, upgradeability, reliability, and incremental performance. However, the total system cost must include not only hardware, but

installation and maintenance as well. Therefore, ease of installation and lifetime of the passive components are also of crucial importance (Keck '89).

1.3 Silica-based planar lightwave circuits

There are several factors, however, which play a key role in determining the successful large scale implementation of a technology for passive PLCs. Beyond just producing waveguides structure with low absorption and scattering losses, which are vital for the performance of any device, the technology should preferably be compatible with the well established microelectronic silicon technology, involve a reasonable number of fabrication steps and ensure a high degree of reproducibility. Moreover, it is vital that a passive PLC be compatible, in terms of optical and structural coupling, with the optical fibres of the existing network, which are silica-based.

It is immediate that the highest degree of compatibility with the existing silica-based optical fibre network is offered by silica-based PLCs. In fact, being based on the same material, they have same optical and structural properties. Fresnel reflections are minimised at the coupling interface with the fibre and the field overlap between the modes of fibre and integrated waveguide with similar size is optimised. Very low fibre to device coupling loss has been reported for these devices < 0.04 dB (Miyashita '88) and also fusion splicing between fibre and silica-based PLC devices has been demonstrated (Shimizu '84), which yields more durable and less labour intensive splicing than epoxy bonding. Consequently low loss permanent coupling is easily achieved. Silica-based waveguides have also shown the lowest propagation loss value reported in literature: 0.01 dB/cm obtained for single mode GeO_2 -doped silica channel waveguides (Kominato '90, Ohmori '90). Low coupling loss together with low propagation loss, yield a very low insertion loss device, which turns in extremely low pigtailling loss (~ 0.05 dB) (PIRI '92).

The dominant cost in the manufacture of integrated optical devices is expected to be the cost of fibre pigtailling and alignment, i.e. packaging. In a

silica-based technology, grooves for holding the input and output fibres can be precisely defined in the Si substrate as part of the waveguide fabrication process, allowing passive fibre waveguide alignment, leading to low cost device assembly.

The reasons which have been mentioned will have a determining role in the success of high-silica technologies in the passive component market for terrestrial telecommunications application and they will mean a real opportunity for the first large scale application of IO.

A number of technologies has been investigated for the fabrication of silica-based planar waveguides. In Table 1.I an exhaustive review of these technologies has been attempted by the author. In the table only those fabrication techniques which have produced optical quality films have been included. Therefore all those technologies developed by the electronic industry to fabricate silica-based dielectric films for passivation, have not been included. For a good review of these technologies the interested reader can consult the particular references (Kern '77, Pliskin '77). Among the technologies listed in Table 1.I, those which have produced the major number of functional devices are certainly: low pressure chemical vapour deposition (LPCVD), developed at AT&T in USA (Verbeek '88), plasma enhanced CVD (PECVD), developed at LETI in France (Valette '88), plasma activated CVD (PACVD), developed at GEC in UK (Nourshargh '85 b) and flame hydrolysis deposition (FHD), developed at NTT in Japan (Kawachi '83).

1.4 Motivation and aim of research

In the telecommunication community it is an established belief that passive silica-based PLCs, supported by continuous improvement in waveguide processing, circuit design and device packaging, will penetrate low-cost commodity markets for fibre to the subscriber applications and will proceed to higher-level integrations of optical functions for the next generation of telecommunications systems. This belief is firmly proved by the financial efforts in these field of the biggest telecommunications companies on a world scale.

Technology	Raw materials	Waveguide materials	T process, °C	Substrate	Note	References
Plasma enhanced CVD	SiH ₄ , PH ₃ , NO	SiO ₂ , P ₂ O ₅	not reported	Si	rf plasma	Valette '88
	SiH ₄ , N ₂ O	SiO ₂ , SiO _x	300	Si	rf plasma	Lai '92
	SiCl ₄ , AsH ₃ , O ₂	SiO ₂ , As ₂ O ₃	not reported	Si, SiO ₂	rf plasma	Hubbard '89
Plasma activated CVD	SiCl ₄ , GeCl ₄ , O ₂	SiO ₂ , GeO ₂	r.t.-1100	SiO ₂	μwave plasma	Nourshargh '85b
Plasma impulse CVD	SiCl ₄ , O ₂ , GeCl ₄ or Freon™	SiO ₂ , GeO ₂ or F	800-1000	SiO ₂	μwave plasma	Kersten '91
	TiCl ₄ , HMDSO	SiO ₂ , TiO ₂	1000	"	"	"
Low temperature CVD	SiH ₄ , PH ₃ , O ₂	SiO ₂ , P ₂ O ₅	390	SiO ₂	spin on cladding	Imoto '87
Low pressure CVD	SiH ₄ , PH ₃ , O ₂	SiO ₂ , P ₂ O ₅	380-450	Si	cladding layer	Verbeek '88
	TEOS, PH ₃ , NH ₃ , O ₂	SiO ₂ , P ₂ O ₅	680	Si	by using TEOS	Henry '89
Vacuum Deposition	not reported	SiO ₂ , TiO ₂	350	SiO ₂	cladding by FHD	Imoto '88
Thermal oxidation	SiCl ₄ , GeCl ₄ , PCl ₃ , BBr ₃ , O ₂	SiO ₂ , GeO ₂ , P ₂ O ₅	900-1100	SiO ₂	sintering 1400 °C	Izawa '81
Thermal growth	Si (substrate), O ₂	SiO ₂	1100	Si	graded index	Zelmon '83
RF reactive sputtering	SiO ₂ -GeO ₂ (target)	SiO ₂ , GeO ₂	not reported	SiO ₂	-	Huang '85
Sol-gel	GELSIL™	SiO ₂	not reported	Si	laser assisted	Ramaswamy '88b
Flame Hydrolysis Deposition	SiCl ₄ , TiCl ₄ , PCl ₃ , BCl ₃ , H ₂ , O ₂	SiO ₂ , TiO ₂ , P ₂ O ₅ , B ₂ O ₃	1250	SiO ₂	Si substrate '90	Kawachi '83
	SiCl ₄ , GeCl ₄ , PCl ₃ , H ₂ , O ₂	SiO ₂ , GeO ₂ , P ₂ O ₅	1270	SiO ₂	-	Kashyap '89
	SiCl ₄ , GeCl ₄ , PCl ₃ , BBr ₃ , H ₂ , O ₂	SiO ₂ , GeO ₂ , P ₂ O ₅ , B ₂ O ₃	not reported	Si	loss 0.01 dB/cm	Kominato '90
	SiCl ₄ , PCl ₃ , H ₂ , O ₂	SiO ₂ , P ₂ O ₅	1260	Si, SiO ₂	-	Barbarossa '91a
Ion implantation	not reported	SiO ₂ , TiO ₂ , B ₂ O ₃	not reported	Si	-	Schneider '91
	fused SiO ₂ (substrate)	SiO _x N _y	150	SiO ₂	-	Naik '83
	fused SiO ₂ (substrate)	SiO ₂ -H ⁺	not reported	SiO ₂	graded index	Schineller '68
Electr. beam irradiation	fused SiO ₂ (substrate)	SiO ₂ -Li ⁺	220	SiO ₂	also Bi, C, Th, He	Standley '72
	fused SiO ₂ (substrate)	SiO ₂	not reported	SiO ₂	graded index	Barbier '91

Table 1.1 Silica and doped-silica optical thin film fabrication technologies

Therefore, the interest in the development of a suitable technology for mass production of cost-effective silica-based PLCs is rapidly increasing.

At Glasgow University and BT Labs (the financial supporter of this research project in conjunction with the SERC), there is a strong belief that FHD technology offers, at this moment in time, the best perspective, in terms of process flexibility, towards the realisation of commercial devices at an affordable price and with high performance.

In this context the aims of the present research were:

- to understand the various stages of the FHD process;
- to engineer and assemble a FHD system for research purposes, capable of guaranteeing a reliable and repeatable fabrication process;
- to establish a flexible and controllable fabrication procedure for the fabrication of low loss planar waveguides by FHD;
- to investigate the possibility of synthesising novel silica-based glass systems by FHD and to resolve eventual fabrication problems;
- to develop a suitable microfabrication process, based on photolithographic and dry etching techniques, for the definition of low loss channel waveguides;
- to research new solutions for basic passive optical functions and to design, fabricate and characterise the resulting guided wave components;
- to investigate the possibility of resolving the dimensional limitations imposed by the substrate size on the development of large scale PLCs.

1.5 Review of the contents of the thesis

As has been already underlined, for more than 20 years the scientific community has devoted a great deal of interest to the theoretical and technological field of IO. Excellent books on the matter are available, which deal with elementary and advanced waveguide theory fundamentals, as well as with the early and latest technological achievements in the field of IO (e.g. Tamir '75, Hunsperger '82, Lee '86, Nishihara '89). Therefore it has been intention of the

author not to remain any longer than necessary on those basic concepts which are essential theoretical and practical tools for the researcher in IO and which should be a well assimilated background of the interested reader. Hence, the dissertation has been intended to deal with original investigations and achievements, although, when it has been believed necessary, a brief account on fundamental topics has been also given for the sake of clarity.

Following this introduction, in chapter 2 the FHD apparatus engineered and assembled by the author is described in its units. The procedure for a safe and reproducible deposition is also explained. In chapter 3 the fabrication of planar P_2O_5 -doped and GeO_2 - P_2O_5 -doped silica optical waveguides is described. The optimisation of the fabrication parameters is discussed, particularly with respect to the sintering process. At the end of the chapter, the combination of aerosol doping technique and FHD is described, which has been proved to be an effective method for incorporation of rare-earth ions in silica-based planar waveguides. The photolithographic and dry etching processes necessary to fabricate channel waveguides are described in chapter 4. In this chapter, a brief account on the experimental results concerning the optical damage threshold of doped silica channel waveguides is also given. Chapter 5 deals with the theory, the fabrication and the assessment of three waveguide coupler based devices, such as wideband filter and high stopband rejection multi-demultiplexer. Chapter 6 is devoted to the vertical integration of high-silica channel waveguides. Experimental details are given and possible modifications to the basic process are discussed. Finally, in chapter 7 the results of the present research work are summarised and suggestions for further study are given.

Chapter 2. Flame hydrolysis deposition (FHD)

Chapter Layout

- 2.1 Introduction**
- 2.2 FHD**
- 2.3 FHD apparatus**
 - 2.3.1 The gas supply assembly**
 - 2.3.2 The bubbler cabinet**
 - 2.3.3 The mass flow control cabinet**
 - 2.3.4 The deposition chamber**
 - 2.3.5 The scrubber system**
- 2.4 Deposition procedure**

2.1 Introduction

FHD (Kawachi '83) has received increasing attention as a technique for the fabrication of high-silica content, low-loss, planar lightwave circuits (PLC) for telecommunications because of its extended compatibility with fibre optics technology. Moreover the possibility of producing cost effective passive devices has shown FHD to be a promising technology for the first large scale application of Integrated Optics in the telecommunications market. Many of the basic components have been developed which form the building blocks of large scale mass-producible PLCs (Kawachi '90). A wide variety of functional devices have been demonstrated employing this technology and some of them are currently available on the market (PIRI '92).

The optical and structural compatibility with the existing fibre optic network derives from the fact that such waveguides are fabricated in a similar

way to fibres and the same materials are employed, the difference being that in FHD the deposition of the glass formers is planar and there is no drawing process.

The presence in the fabrication process of an intermediate sintering stage makes FHD suitable for doping of the glass matrix with, e.g., rare-earth solutions, achieving significant doping concentration levels. Nd- (Hibino '89) and Er- (Kitagawa '91) doped silica CW lasers and amplifiers (Kitagawa '92) have been reported, extending the potential of FHD. So far, rare earth doping of silica based waveguides fabricated by other well developed high-silica technology has not been reported yet, to the author's knowledge.

Unique features which distinguish FHD from other high-silica technologies and contribute to broaden its field of application are: the purity of the glass particles synthesised by the flame process, purity which can easily match that of the raw materials fed to the flame (Ulrich '84) and which enables the production of very low loss glasses; the extended flexibility in the thickness (2-200 μm) and refractive index difference (0.2-3 %) achievable (Piri '92), the low-cost batch-type fabrication process and high deposition rate; the possibility of fabricating completely buried waveguides, i.e. the possibility of burying the waveguides with a thick planarizing cladding layer, which allows successive photolithographic processes. Recently, the possibility has been demonstrated of fabricating circular cross section waveguides by a combination of FHD and selective etching (Sun '91), resulting in a further reduction of the coupling loss to optical fibres.

All these characteristics will probably have a determining role in the success of FHD as preferred technology for the fabrication of high-silica content, optical fibre compatible PLCs. Table 2.I has been compiled for a comparison of the most developed technologies for the fabrication of high-silica content PLCs and it has been based on information which have been reported in literature. Table 2.II is a list of those companies or research laboratories, which, to the author's knowledge, have reported experimental work in the FHD field. The rapid growth in late years is a demonstration of the interest which this technology is continuously generating in the scientific community.

High-silica technology	FHD	LPCVD	PECVD	PACVD	TO
Min. prop. loss * (dB/cm) ¹	0.01	2.6	0.1	0.3 ²	3 ³
Refr. index step range (%)	0.2-3	0-0.9	0-4.8	0-9.5	0.2-0.9
Thickness range (μm)	1-200	0-20	0-30	0-100	0-50
Deposition rate (μm/min)	1	n.a.	0.04	0.5	2.5
Typical process temp. (°C)	1260	450	300	1100	1200
Typical annealing temp. (°C)	1100	1000	1000	n.a.	1350
Low pressure deposition	no	yes	yes	yes	no
Max number of samples *	50	n.a.	n.a.	1	5
CO ₂ laser processing *	yes	no	no	yes	no
Thermo-optic effect *	yes	no	no	no	no
Birifringence control *	yes	no	no	no	no
Glass systems synthesised *	6	1	1	2	1
Rare-earth doping *	yes	no	no	no	no
Planarizing cladding	yes	no	no	no	no
Vertical integration	yes	no	no	no	no

1 at $\lambda=1.55 \mu\text{m}$; 2 planar waveguide value; 3 at $\lambda=1.32 \mu\text{m}$

Table 2.I Comparison of the main technologies for the fabrication of high-silica content PLCs. Those characteristics marked with *, refer to the current status of the technology, to the best of the author's knowledge, i.e. the particular characteristic has been not demonstrated yet, but it is possible in principle. The other characteristics are intrinsic to the particular technology.

In this chapter the FHD system engineered and assembled by the author is described and the procedure for safe and reproducible deposition explained.

2.2 FHD

FHD is a chemical vapour deposition process, where the glass former oxides are synthesised through the hydrolysis of their appropriate high vapour

pressure precursors. The technique was first conceived by J. Hyde whilst working at Corning Glass in 1934 for the fabrication of transparent articles of silica at low temperatures and with a high degree of purity. It was subsequently applied to the fabrication of optical fibre preforms and gave birth to the outside vapour deposition method (OVD) (Keck '72). The technique was further modified in the vapour axial deposition method (VAD) (Izawa '77). FHD was subsequently transferred to planar geometries for the fabrication of high-silica content PLCs on Si substrates (Kawachi '83)[§].

Company/ Research Laboratory	Country	Year started	References
Corning Glass Works	USA	1976	(Keck '74) ¹
Nippon Telephone & Telegraph	Japan	1983	(Kawachi '83)
Hitachi Cable Ltd.	Japan	1988	(Imoto '88)
Photonic Integration Research, inc.	USA	1988	(PIRI '91) ²
BT Labs	UK	1989	(Kashyap '89)
Furukawa Electric Co. Ltd.	Japan	1989	(Yanagawa '89)
National Optics Institute	Canada	1991	(Croteau '91)
Siemens AG	Germany	1991	(Schneider '91)
IBM	USA	1992	(Jackson '92) ³

¹ Patent pending; no experimental work reported; ² Commercial devices; ³ Optical interconnects

Table 2.II Flame hydrolysis deposition worldwide activity

A simplified schematic (gas tubing and electrical wiring are not totally shown) of a FHD system for planar deposition, is shown in Fig. 2.1 (its key is in the following page). This schematic represents the FHD system engineered and

[§] Despite the first demonstration of the fabrication of planar waveguide using FHD was reported by Kawachi et al. of NTT in 1983, a U.S. patent had been previously granted to Keck et al. of Corning Glass in 1974.

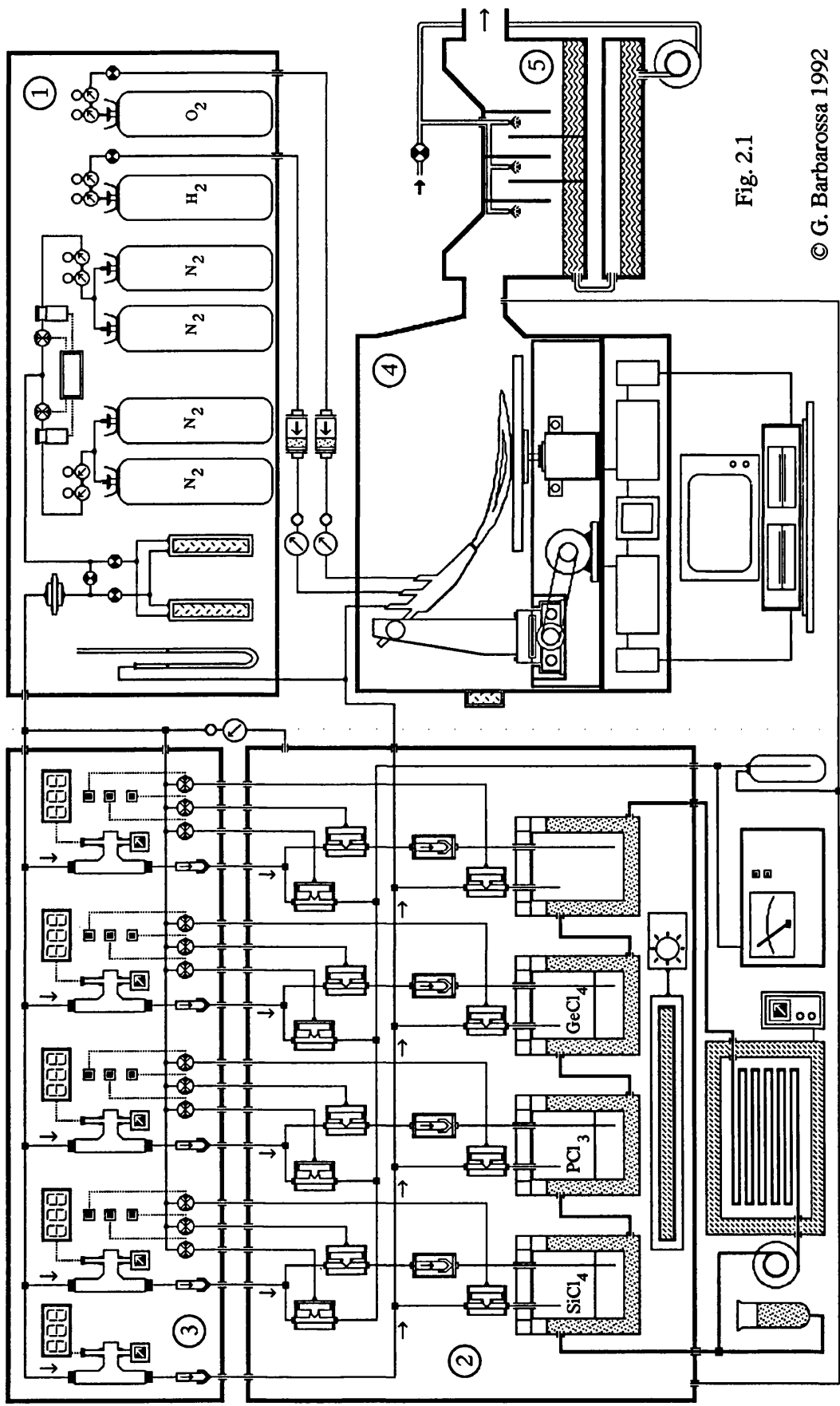
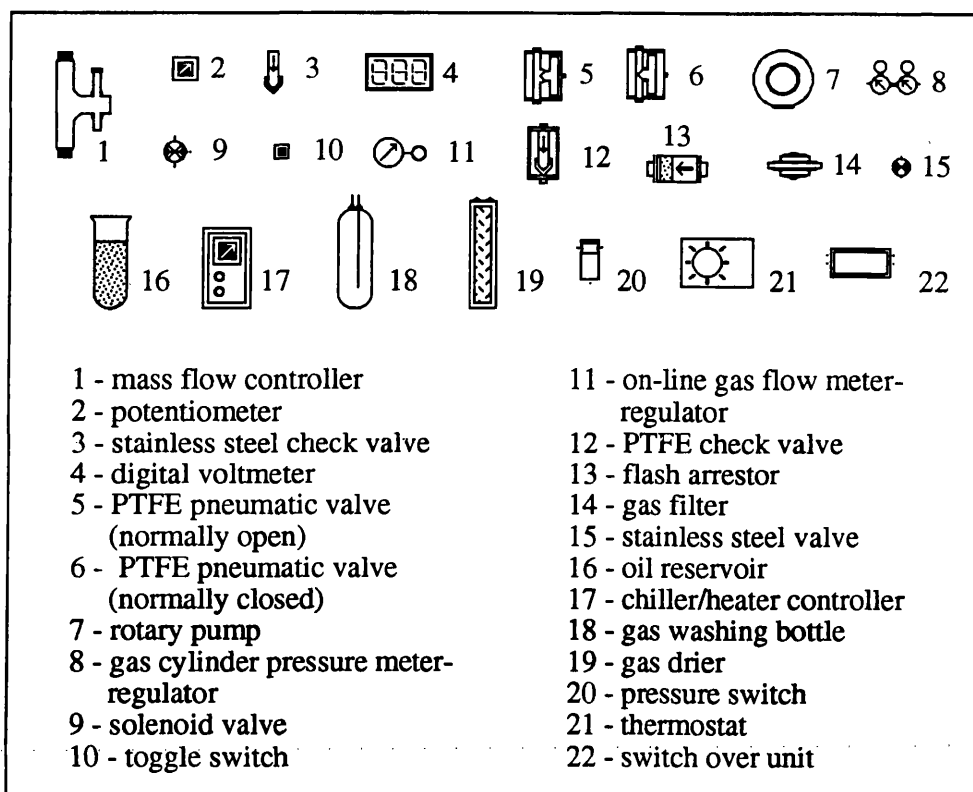


Fig. 2.1

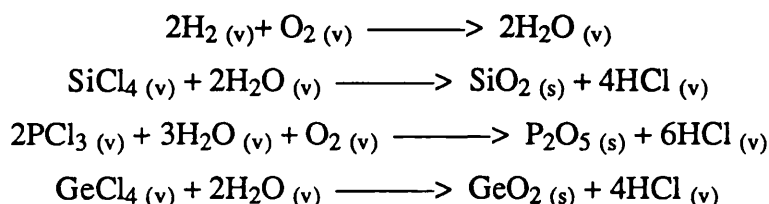
© G. Barbarossa 1992

assembled by the author, which will be described in its subsystems in the following paragraphs.



Key of Fig. 2.1

Submicron oxide particles are synthesised by a heterogeneous hydrolysis reaction of the corresponding halides (typically SiCl_4 , PCl_3 or POCl_3 , BCl_3 or BBr_3 , GeCl_4 , TiCl_4), the vapours of which are collected by bubbling an ultra dry gas through temperature controlled Drechsel's bottles which contain the particular liquids, and fed to an oxy-hydrogen torch. The heterogeneous hydrolysis reactions for the chlorides used by the author are



It has to be noted that the reaction for PCl_3 can be stoichiometrically balanced only in presence of an excess of oxygen. Oxygen rich flames are then preferable to favourably promote the synthesis of P_2O_5 .

The high purity of the low density glass "soot", which easily matches that of the raw materials, is guaranteed by the flame synthesis (Ulrich '84). The technique allows the production of high-silica content glasses and enables the fabrication of very low-loss waveguides. The oxide particles are deposited on Si or SiO_2 substrates, held on a turntable. The deposited oxide soot is subsequently sintered to produce the transparent doped silica film. The number of substrates to be coated, in principle, depends only on the size of the turntable employed and the capacity of the furnace for the consolidation of the deposited soot. The HCl waste gas produced is extracted from the deposition chamber and neutralised.

To achieve uniform deposition the torch is traversed repeatedly in the radial direction of the rotating turntable. Control of the refractive index of the glass is achieved by adjusting the relative flow rates of the halides, which determine the silica doping level and consequently the desired refractive index step. The thickness of the deposited film and the deposition rate are preferably controlled by the traverse speed of the torch, the rotation speed of the turntable and the number of traversals, rather than by the halide flow-rates which also determine the mass-flow of the glass oxides produced.

This is because once the deposition has been calibrated, i.e. the thickness per traversal is known at certain torch and turntable speeds, a double thickness can be simply obtained by doubling the number of traversals. However, doubling the flow rates of the chlorides does not double the thickness obtained. This is due to the fact that the amount of oxide synthesised is not linearly proportional to the flow rates of the nitrogen bubbling through the halides, but rather depends on the flame hydrolysis reaction efficiency for fixed H_2/O_2 gas flow rates (Niizeki '85).

Deposition parameters such as traverse speed of the torch and rotation speed of the turntable have to be optimised to achieve homogeneous and constant, precisely controlled, thickness films. We have achieved a better uniformity and homogeneity by using slow deposition speeds (typical values: torch starting speed 25 mm/min, turntable speed 25 rev/min) and few traversals, rather than high speeds and many traversals, and by keeping constant the mass flow of oxides synthesised. For example, with SiCl_4 and PCl_3 flow rates of 150 and 160 cm^3/min , and H_2 and O_2 flow rates of 12 and 8 l/min, a typical thickness of 1 μm per traversal has been obtained at the mentioned deposition speeds.

Flame flow rates affect the efficiency of the hydrolysis reaction and the uniformity of the deposition. Although higher flame flow rates promote the hydrolysis reaction for fixed halide flow rates, it is preferable to use relatively lower rates because otherwise the uniformity of the deposition would be adversely affected by the turbulence of the flowing gases. This is an important factor which is absent in the fabrication of fibre preform, where possible dimensional irregularities are scaled down by the drawing process during which the preform cross section is reduced by two orders of magnitude. In FHD irregularities in the thickness of the deposited soot layers are found in the consolidated film. Consequently deposition parameters, such as torch and turntable speed, halide and oxygen-hydrogen flow rates, have to be optimised in order to favourably promote the hydrolysis reaction and to achieve the best compromise between uniformity of the soot layer and deposition rate.

2.3 FHD apparatus

The deposition apparatus constructed consists of five units which will be described separately; they are numbered in the schematic of Fig. 2.1 as follow: 1) Gas supply assembly, 2) Bubbler cabinet, 3) Mass flows control cabinet, 4)

Deposition chamber and 5) Scrubber system. A complete view of the FHD apparatus is shown in Fig. 2.2.

2.3.1 The gas supply assembly

The gases which are necessary for a FHD system are H_2 and O_2 to obtain the hydrolysing flame, an inert ultra dry gas for the transport of the halide vapours and for the purging of the pipework and bubbler cabinet, and a cheap inert gas for the control of the pneumatic valves. Zero grade, i.e. ultra dry (< 10 ppm of H_2O), nitrogen is a good inert carrier and purging gas as it is also cheap. Running costs of the purging operation are important as this has to be carried on 24 hours a day to ensure a dewpoint at least of -70 °C, which is necessary to prevent hydrolysis of the halides in the pipework and its consequent blocking. The gas supply assembly includes the necessary control valves, pressure indicators and regulators for each of the gas cylinders as well as pressure switches, solenoid valves and control electronic circuit for the switch over-unit.

To obtain a certain purging autonomy the N_2 gas supply system has been furnished with an automatic switch-over unit. This gives an autonomy of 4 N_2 cylinders for a total of ~ 40 m³ of gas, which guarantee approximately 8 days of continuous purging at ~ 3 l/min. The nitrogen is also used to purge the inside of the bubbler cabinet to maintain a dry atmosphere around the bubblers, and to cleanse residual halide vapours, which remain after refilling operations of the bubblers. Nitrogen dryers have been also incorporated, with the eventual aim of using standard grade N_2 . They can be by-passed when using zero grade N_2 . A 2 μ m particulate filter has been included in the pipeline to remove any contaminants in the gas. Nitrogen is also used as controlling gas for the pneumatic bellows valves which direct the path of the carrier gas through the bubblers. Fig 2.3 shows a photograph of the N_2 supply assembly on the left and the drying filter unit on the right.

The hydrogen and oxygen lines incorporate control valves, pressure regulators, indicators and flowmeters to allow accurate settings. Both lines



Fig. 2.2 FHD apparatus.

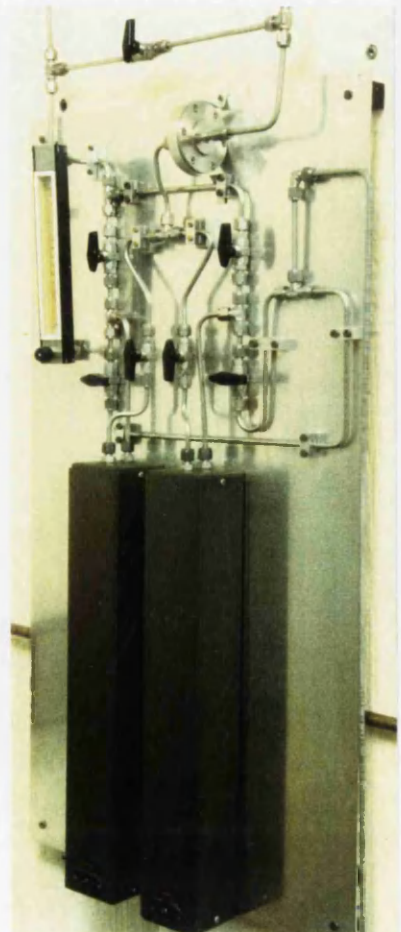


Fig. 2.3 Nitrogen gas supply assembly (left) and drying filter unit (right).

include flash arrestors for safety precautions. Flashback has occurred once during operation of the system and the flash arrestors have proved to be effective in preventing explosion of the H₂ cylinder. Stainless steel piping has been used throughout the supply system and piping lines to the bubbler and mass flow control cabinet.

2.3.2 The bubbler cabinet

The bubblers used are glass, jacketed Drechsel's bottles. They are contained in a sealed glove cabinet which is constantly purged with dry nitrogen. The cabinet is sealed for two main purposes: to ensure safety of the operator during refilling operations of the bubblers, preventing nasty chloride vapours being inhaled, and to keep a dry atmosphere around the bubblers to prevent hydrolysis of the chlorides in the pipework, in the event of leaky joints. There are four bubblers: three for SiCl₄, PCl₃ and GeCl₄, and a spare one. The vapour pressure of the chlorides is kept constant by controlling the temperature of the low viscosity oil circulating in the outer jackets of the bubblers. This is achieved by means of a heater/chiller unit. A rotary pump circulates the oil in the four bubbler jackets and heater/chiller unit complex tubing. An oil reservoir has been included in the oil circuit to facilitate air bubble removal during oil refilling operations.

The bubblers are maintained at a constant temperature of 20 °C. At this temperature SiCl₄, PCl₃ and GeCl₄ have a saturated vapour pressure of 250, 36 and 87 mbar, respectively. The carrier gas bubbling through the liquid chloride, picks up an amount of vapour = $FV/(P - V)$, where F is the carrier gas flow, P is the pressure above the liquid and V is the saturated vapour pressure. The chloride flow rates mentioned in the following paragraphs are referred to the N₂, as they are directly read on the mass flow controller monitor display. Therefore the real chloride flow rate is obtained by multiplying the N₂ flow rates by a conversion factor that is 0.29, 0.034 and 0.086 for SiCl₄, PCl₃ and GeCl₄, respectively (having considered P = 1.1 bar).

The bubbler cabinet and the mass flow control cabinet constitute the chloride vapour delivery apparatus which is shown in Fig. 2.4. The heater/chiller unit and dewpoint meter are also visible below it. A close view of the bubbler cabinet is shown in Fig. 2.5. The vapour path tubing is entirely made of polytetrafluorethylene (PTFE). The bubbler cabinet has been provided internally with an electric heater and thermostat, to keep the pipework warmer than the carried vapour, in such a way preventing any condensation of chloride vapours in the pipework. The purging line of the cabinet is provided with a flow regulator to temporarily increase the nitrogen flow after bubbler refilling operations.

Pneumatic bellows valves control the path of the carrier gas. These are arranged in such a way that purging of the whole piping is possible when the bubblers are excluded and the required chlorides flow rates can be set up while the gas flows to waste. For this purpose two normally closed and one normally open valves are necessary for each bubbler. The valves have PTFE taps and polyvinylidene fluoride (PVDF) coated stainless steel pistons to resist corrosion by the chlorides. The valves have also an internal switch that indicates their status. A PTFE check valve has been included on each bubbler output line to prevent sucking of the liquid, in case of a faulty valve, by the purging gas.

It is good practice to have inside the cabinet some sodium carbonate for neutralisation of an eventual spillage and a complete set of bubblers lids which would be necessary to seal the bubblers, having disconnected and removed them in the event of an accident. A gas washing bottle has been mounted on the purging line, externally to the bubbler cabinet and below it. This bottle is for safety precautions and its purpose is to collect eventual chlorides drained into the piping.

2.3.3 The mass flow control cabinet

Flows of the carrier gas through the bubblers are controlled by mass flow controllers (MFC), which are contained in a cabinet above that of the bubblers. A

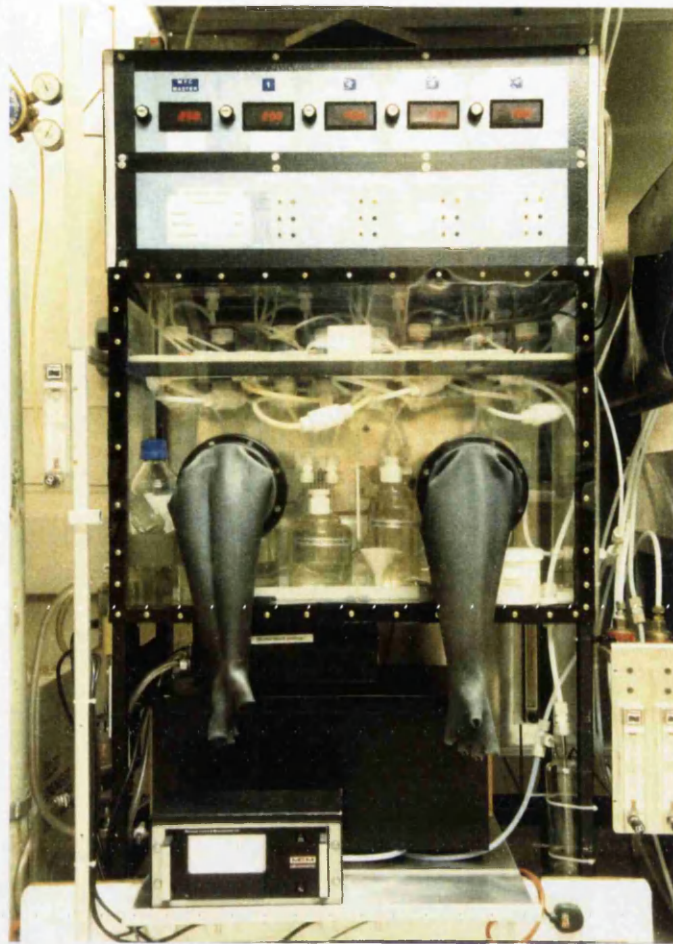


Fig. 2.4 Chlorides vapour delivery apparatus.

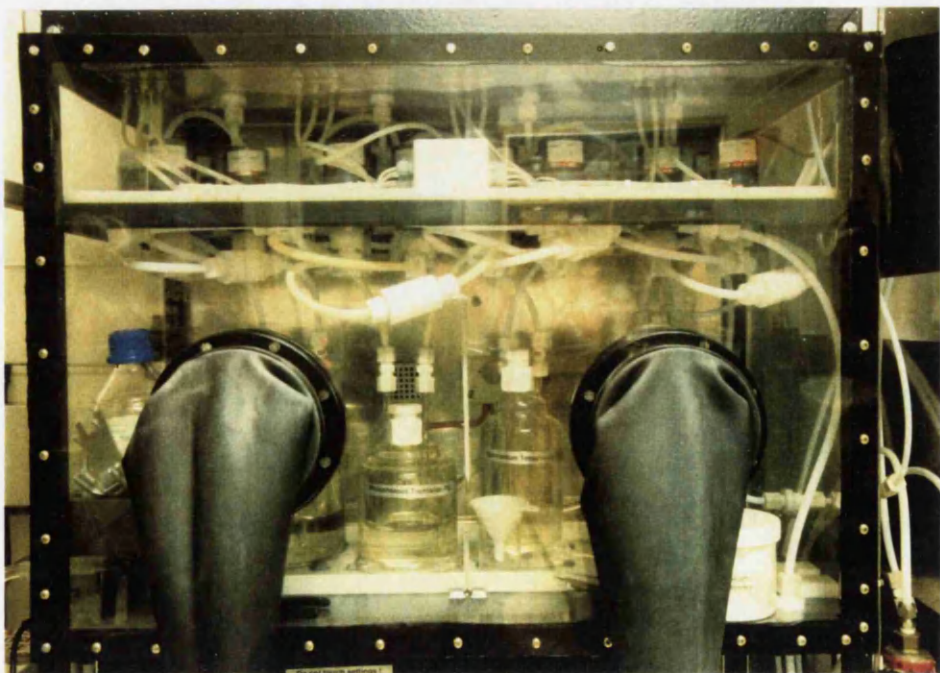


Fig. 2.5 Bubbler cabinet.

photograph of the mass flow control cabinet is shown in Fig. 2.6. Potentiometers and digital voltmeters are also included as they are necessary to set and monitor the gas flows before and during the deposition. A separate MFC is used to control the gas flow purging the line which feeds the torch. A positive pressure is thus maintained in the vapours path and it prevents moisture infiltration from the open end of the line which is represented by the torch. This pressure is measured relatively to the atmospheric pressure by mean of a glass manometer and its increase gives indication of eventual blocking in the inner orifice of the torch.

Each MFC is followed in the gas path by a stainless steel check valve to protect it from eventual reflow of corrosive vapours. The cabinet also contains the solenoid valves and switchgear which operate the pneumatic bellows valves in the bubbler cabinet. A single power supply is used for all the electronic components present in the cabinet, which has been also provided of a cooling fan.

2.3.4 The deposition chamber

This chamber consists of a free standing rectangular box with a sliding transparent Perspex™ panel, which allows access to the interior and observation during deposition (Fig. 2.7). The remaining panels are of hard anodised aluminium. Aluminium has been chosen because is cheap and resists to high temperature. Anodization is necessary to protect the aluminium from corrosion by the HCl vapours produced by the hydrolysis reaction. Waste vapours (HCl, residual H₂O and unreacted reagents) are extracted from a rectangular aperture which is in line with the turntable and reproduce the shape of the opposite entrance aperture.

The latter is provided with filters to block dust, thus keeping the chamber as cleaner as possible. The apertures of the chamber are arranged in such a way as to establish a quasi laminar flow. The uniformity of the deposited film strongly depends on the turbulence of the flame and all the precautions have to be taken to obtain the most steady flame combustion. Similar criteria have been also followed in the design of exhaust system in VAD apparatus (Izawa '87). The need for a



Fig. 2.6 Mass flow control cabinet.

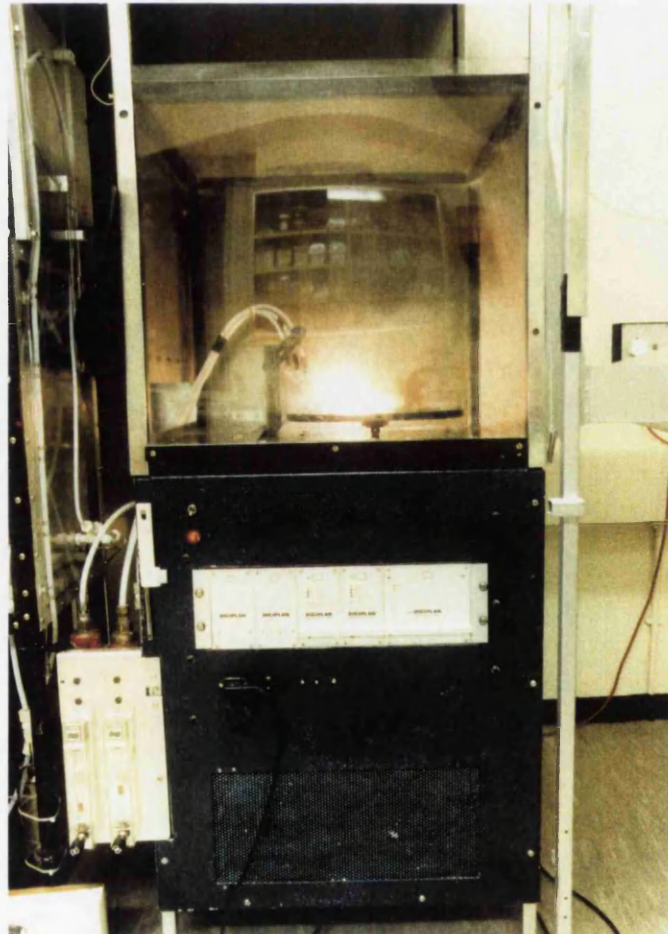


Fig. 2.7 Deposition chamber.

laminar air flow is shown with the aid of Fig. 2.8 a and b. As soon as the entrance aperture is closed the shape of the flame is altered by the eddies which chaotically develop inside the chamber, with consequent nonuniformity of the deposited film. The aspect of the deposited soot after a dummy deposition carried out by keeping the entrance aperture shut is shown in Fig. 2.9.

The extraction aperture can be also equipped with a stainless steel funnel, which is shown in Fig. 2.10. This funnel reduces the size of the extraction aperture and it concentrates the extraction draught along the traverse path of the torch. Moreover, being in close proximity to the flame, it keeps the flame as steady as possible. The use of this funnel eliminates the need for a laminar air flow inside the deposition chamber, as the stronger and localised extraction draught prevents the flame from fluctuating. A similar arrangement has been adopted for the exhaust system in VAD apparatus for fibre preform fabrication (Izawa '87).

The chamber houses the linear drive mechanism on which the torch is mounted. The torch platform allows precise positioning of its inclination and horizontal-vertical distance from the turntable edge. The torch, which is shown in Fig. 2.11, is made of fused quartz and it is a modified Wickbold burner, usually employed for flame spectrometry. It has three ports for H_2 , O_2 and N_2 plus the chloride vapours. The torch feeding lines use PTFE tubes inside the deposition chamber, allowing the flexibility required for the torch traversal.

Basically, the torch consists of three tapered concentric tubes, which are independently fed. O_2 is fed to the outer tube and N_2 plus the chloride vapours are fed to the inner tube. H_2 is fed to the middle tube. This arrangement serves two purposes. First, by jacketing the H_2 with O_2 there is less chance to free unburnt H_2 in the atmosphere. Second, the hydrolysis reaction is more efficient as the reagents are fully enclosed by the hydrolysing flame. A four port torch has also been used and it will be discussed in the next chapter. Different nozzles have been employed to shape the flame. Some of them are shown in Fig. 2.12. The nozzle has a focusing effect on the flame which loses its turbulent aspect and assumes a

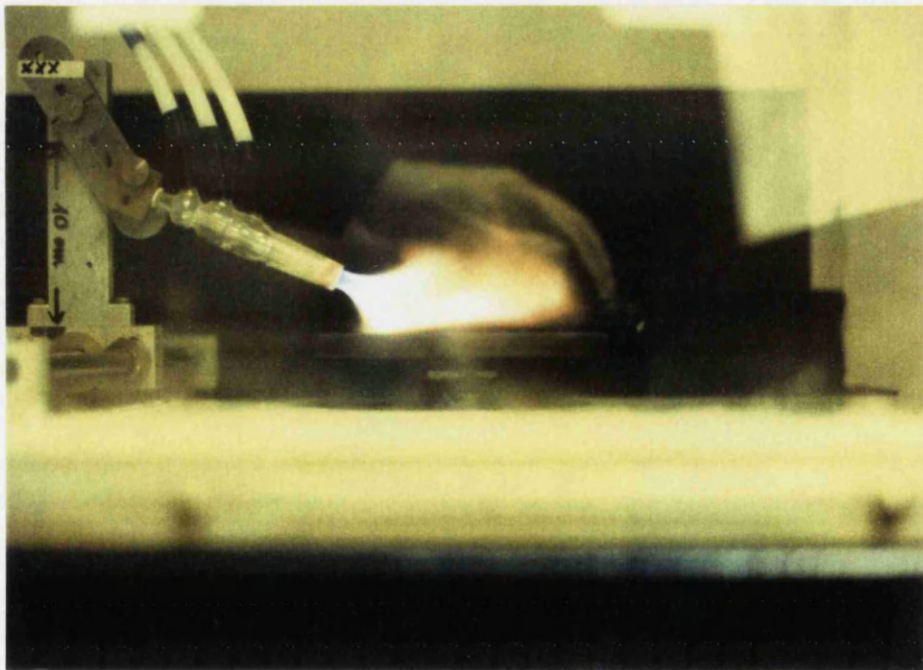
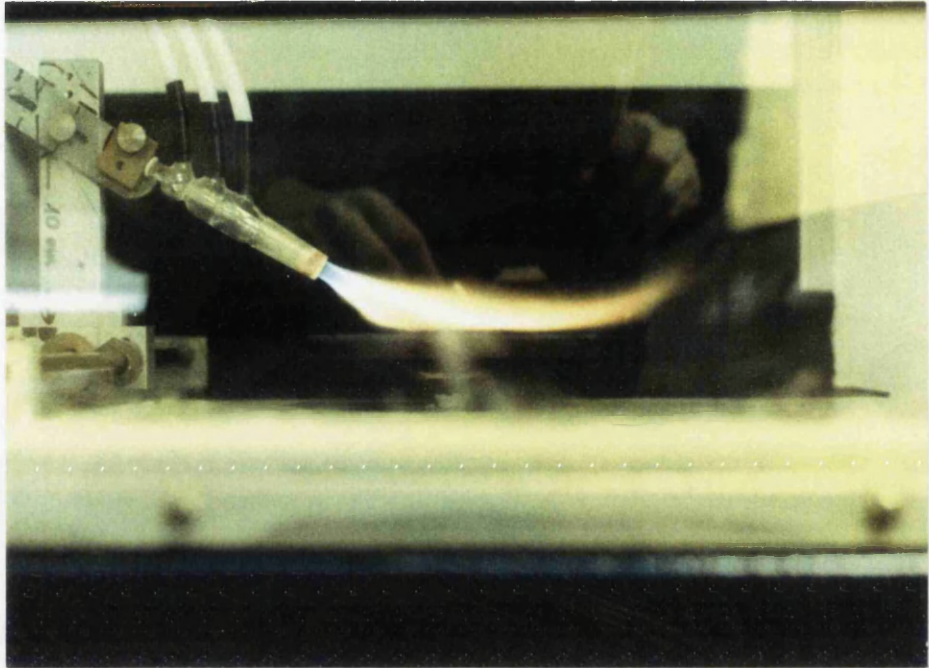


Fig. 2.8 Flame shape in quasi laminar flow condition (a, top) and when the entrance aperture of the deposition chamber is shut (b, bottom).

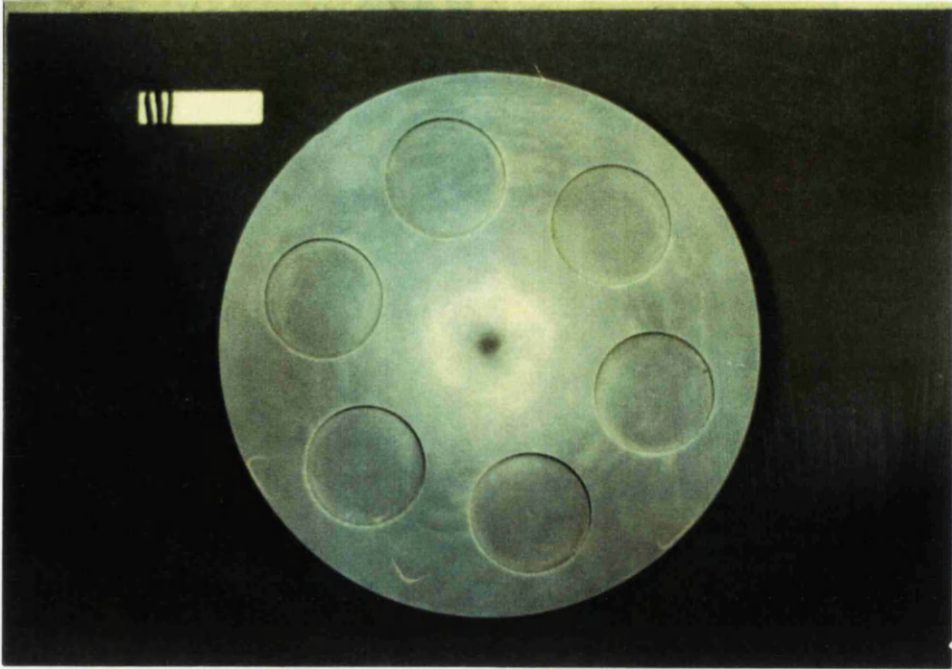


Fig. 2.9 Deposited soot appearance after a dummy deposition carried out by keeping shut the entrance aperture of the deposition chamber.



Fig. 2.10 Waste vapours extraction funnel. The narrower part of the funnel is hinged to allow removal of the turntable.

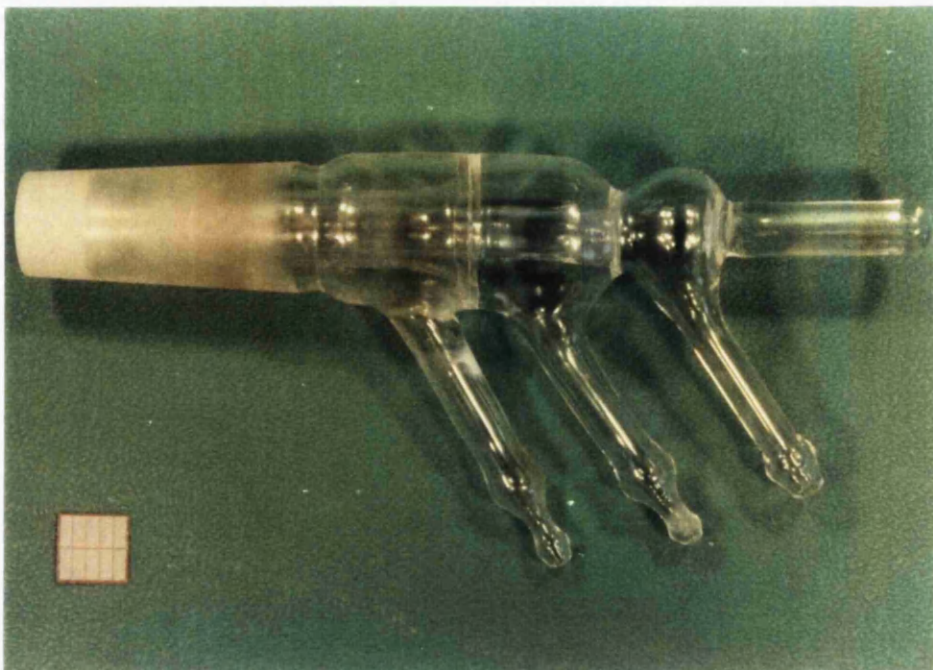


Fig. 2.11 Three-port fused quartz torch. From the left: the first tube feeds the outermost orifice of the torch, the second feeds the central orifice and the third feeds the innermost orifice.

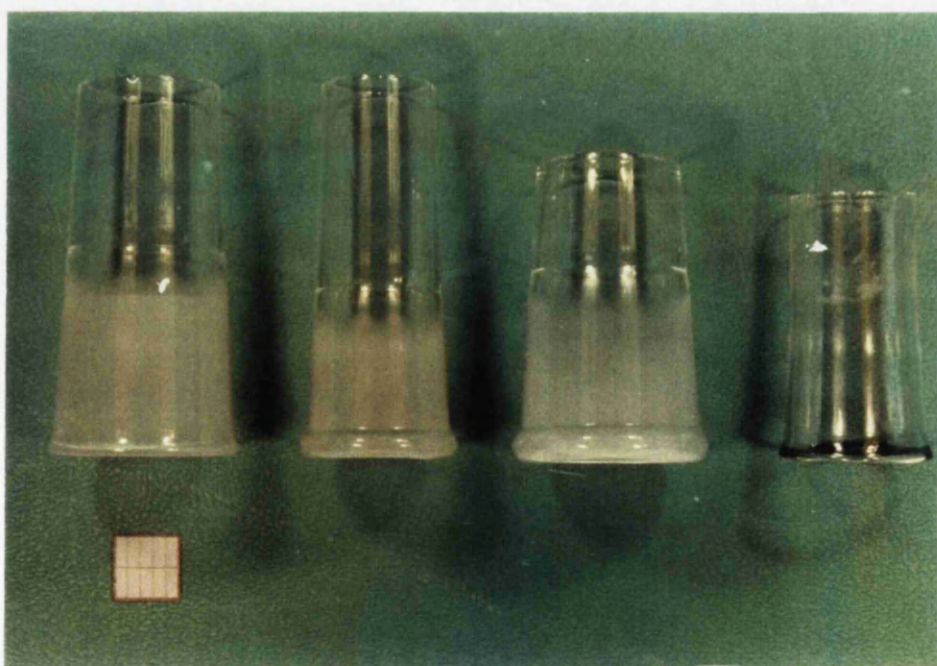


Fig. 2.12 Fused quartz nozzles for torch.

narrower deposition spot. This effect is clearly visible by comparing Fig. 2.13 a and b.

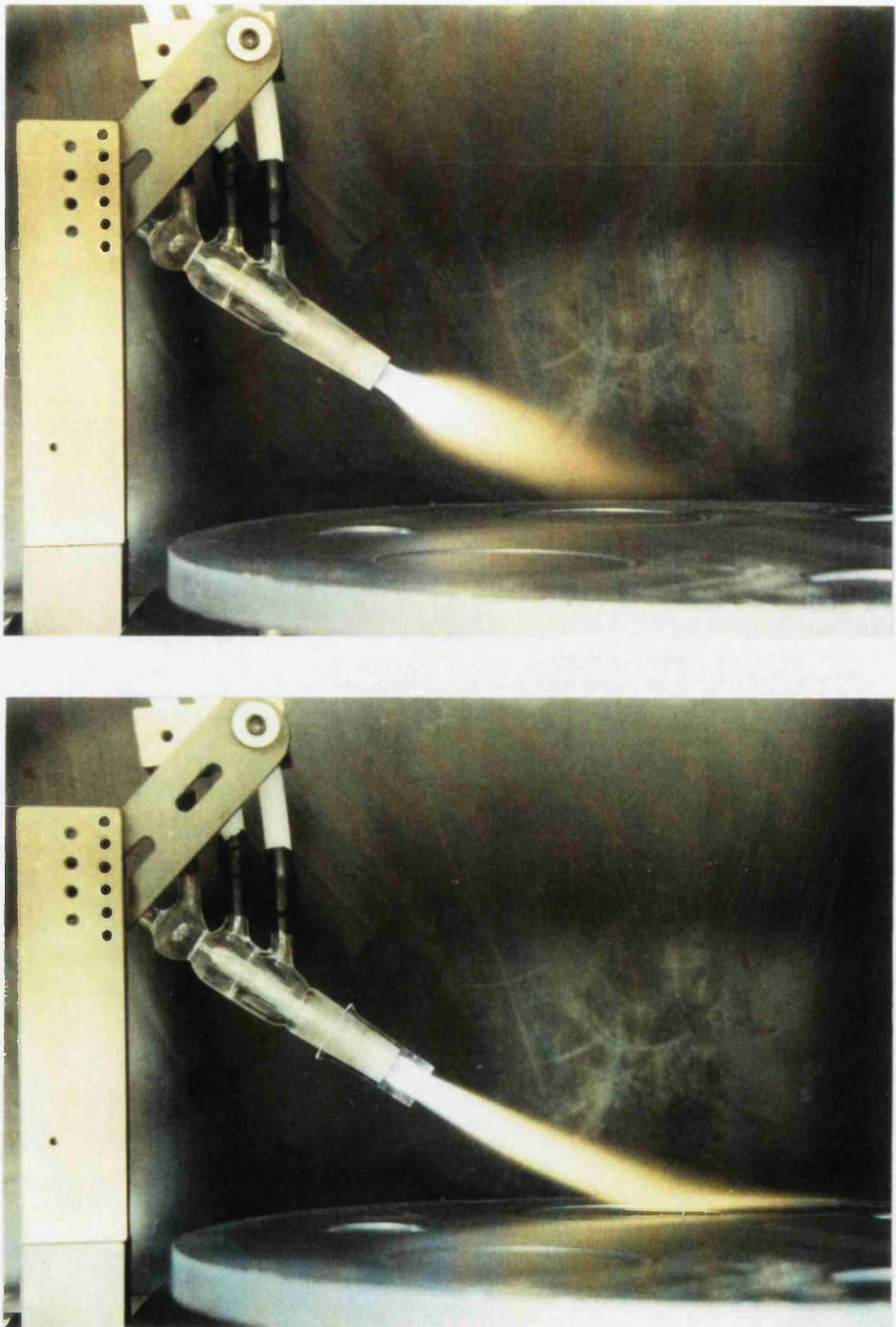


Fig. 2.13 Flame shape without (a, top) and with nozzle (b, bottom).

The turntable is interchangeable. Three turntables have been used. One can accommodate three 75 mm ϕ wafers and three 20 mm ϕ discs and it is made of SiC (Fig. 2.14). A smaller one can accommodate six 20 mm ϕ discs (Fig. 2.9). A third one accommodates three 20 mm ϕ discs and its bottom has a series of concentric ridges to facilitate heat exchange with a cooling liquid (Fig. 2.15). This turntable has been used, in conjunction with a stainless steel tank and a cooling unit, for experiments regarding depositions carried out at low temperature. Both the small turntables are made of hard anodised aluminium. Both SiC and anodised aluminium stand up well to corrosion by HCl and to the high temperature of the flame. All the turntables have the necessary recesses to hold the samples in position during the deposition.

The turntable and the linear drive mechanism are moved by two separate stepper motors. The stepper motors, their electronic drivers and power supplies are housed underneath the deposition chamber. The whole is controlled by a personal computer through a general purpose interface card. A program in BASIC language allows independent variation of the torch traversal starting position, length and rate, number of traversals and rotation speed of the turntable. The program includes a routine to vary the traverse speed of the torch during the deposition to obtain a constant deposition thickness. In fact, for a constant volume of synthesised oxides in unit time and with constant traverse speed, the thickness increases towards the centre of the turntable, as smaller ring areas are swept by the torch deposition spot in unit time. This effect is clearly visible in Fig. 2.16 where a dummy deposition has been effected by keeping the traverse speed of the torch constant. By varying the traverse speed of the torch during the deposition it is possible to keep the area of the turntable swept by the deposition spot in unit time constant. The torch will move slower at the edge and faster towards the centre of the turntable. This guarantees a more uniform thickness of deposited soot. The result obtained by using this routine is shown in Fig. 2.17.

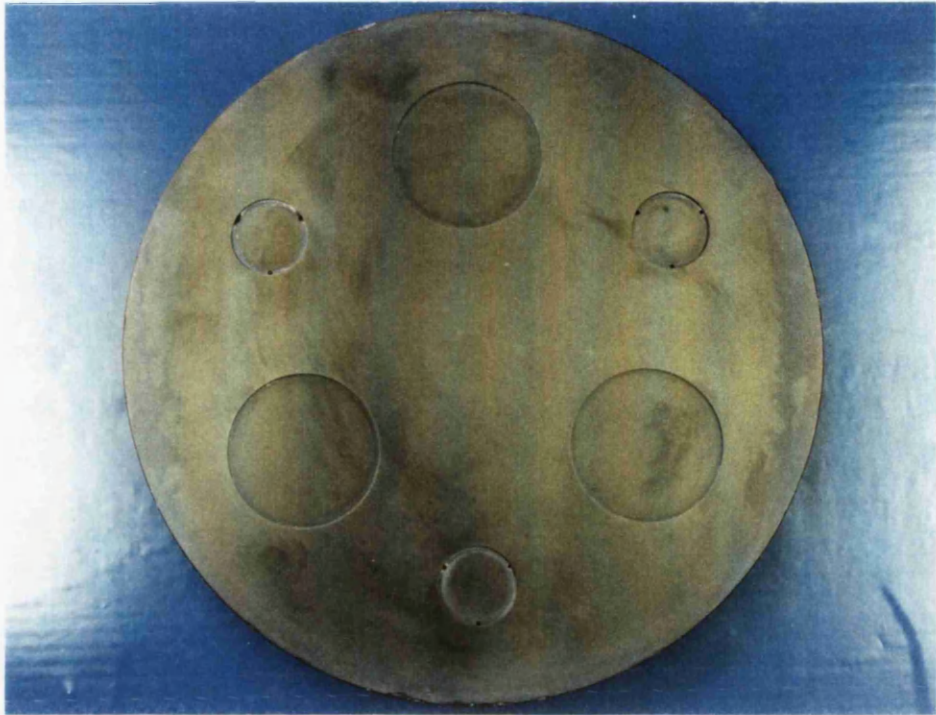


Fig. 2.14 SiC turntable.



Fig. 2.15 Hard anodised aluminium turntable (top and bottom view) and stainless steel tank.

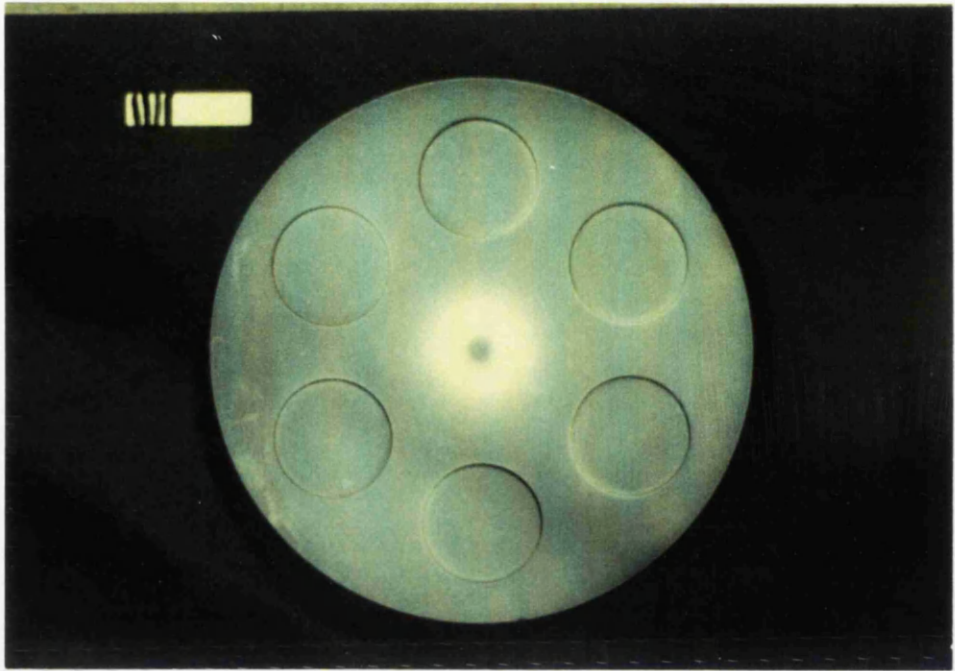


Fig. 2.16 Deposited soot appearance after a dummy deposition carried out by keeping the traverse speed of the torch constant along the traversal length.

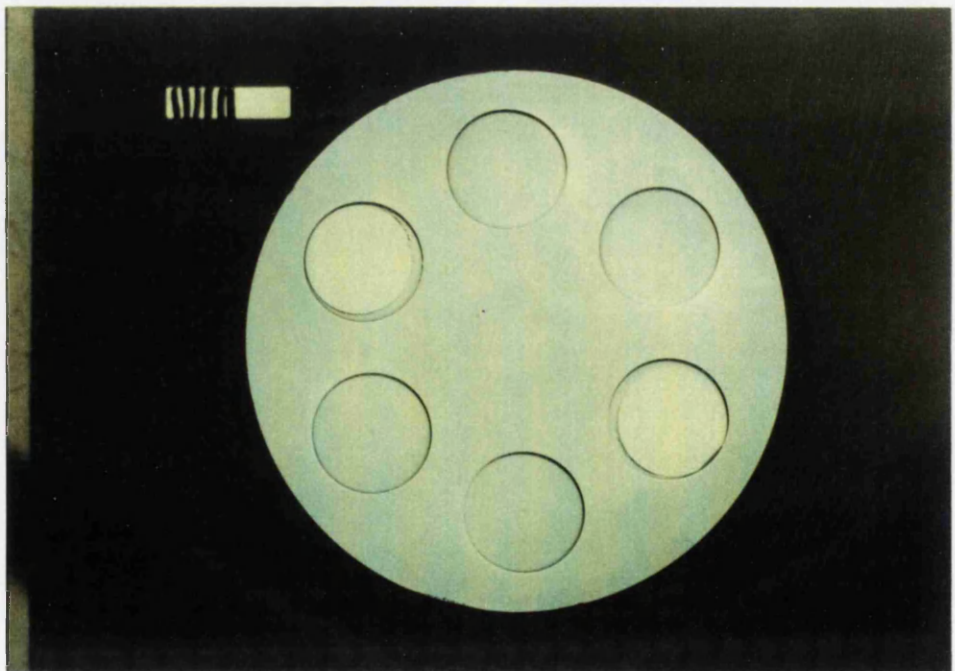


Fig. 2.17 Deposited soot appearance after a deposition carried out by increasing the traverse speed of the torch along the traversal length.

2.3.5 The scrubber system

Waste vapours (HCl, residual H₂O and unreacted reagents) are extracted from the deposition chamber by means of a centrifugal fan. Interposed between the deposition chamber and the fan, there is a scrubber system, where the vapours are neutralised for safety and ecological reasons. The scrubber, which is shown in Fig. 2.18, is made of stainless steel and it consists of a series of baffles over which the vapours are drawn. Spray bars are mounted between each successive baffle and provide a wet atmosphere of a water solution in which the vapours can easily dissolve. The water solution is then passed into a separate storage tank below the scrubber. The water solution circuit is closed and it is run by a rotary pump.

Neutralisation of the strong hydrochloric acid is obtained by dissolving sodium carbonate (Na₂CO₃) in the circulating water. An acid-base indicator such as phenolphthalein is also dissolved, which shows by a change in the colour of the solution, when sodium carbonate has to be added to reestablish the basicity of the solution. Periodically, the water tank has to be refilled, because of natural evaporation and baffles have to be cleaned from encrustation by the dissolved salt. It is a good practice to flush them after every operation with tap water.

The whole of the bubbler/mass flow control cabinet and deposition chamber are enclosed in an extracting canopy for safety reasons. In the eventuality of spillage of chlorides, nasty fumes would be readily extracted.

After deposition, consolidation of the low density glass film is achieved in an electrical furnace (Severn Science Ltd. SC 105/4.5/1600) (Fig. 2.19). It has a fused quartz tube and a programmable temperature controller. To support the sample a fused quartz "table" is employed, which consists of a 76 mm ϕ , 5 mm thick disc and three legs which hold the table top at the level of the furnace tube centre.

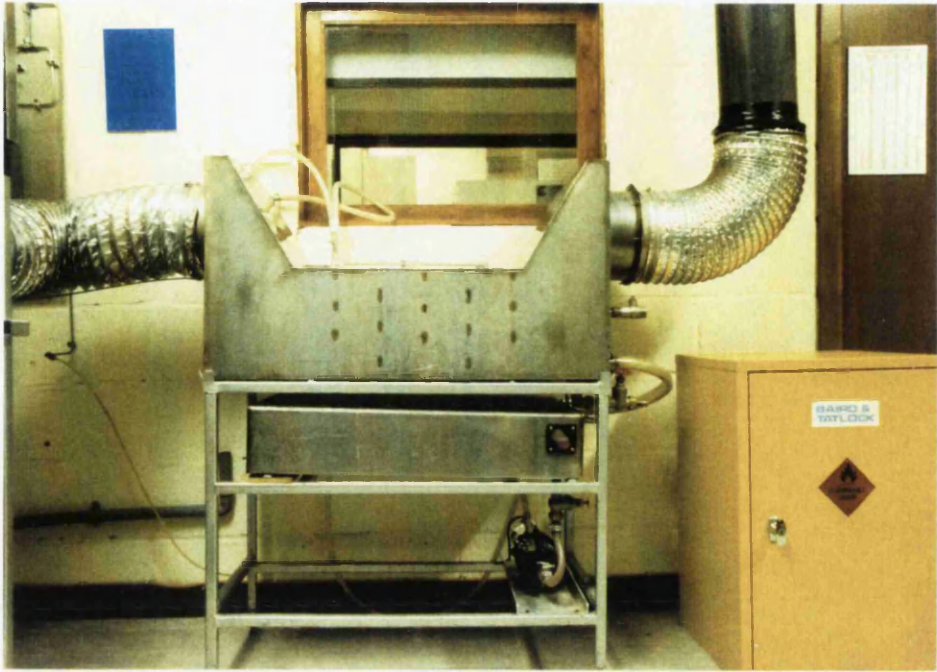


Fig. 2.18 Scrubber system for neutralisation of waste vapours.

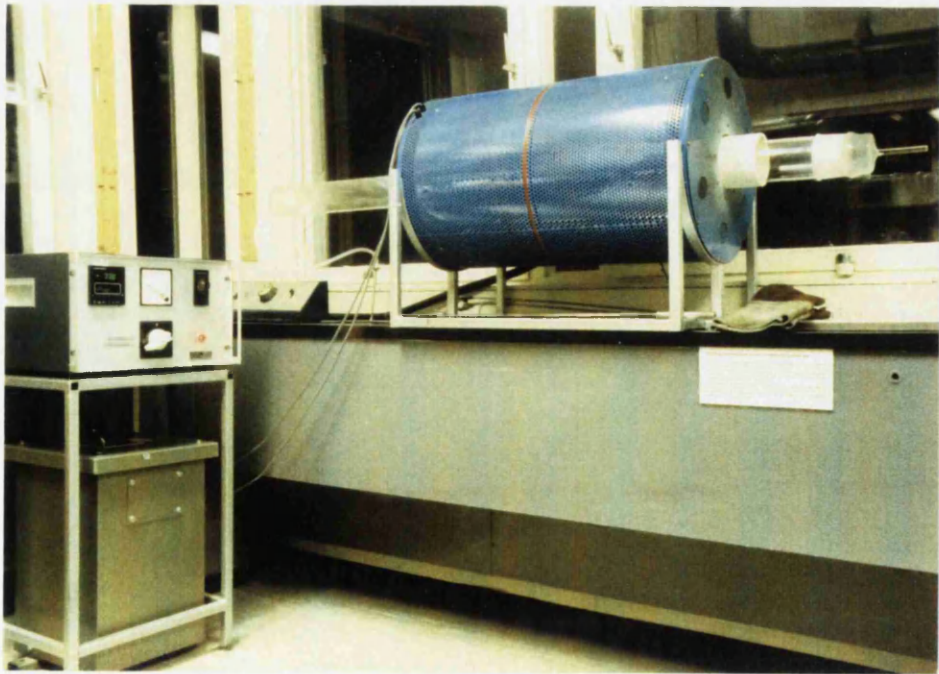


Fig. 2.19 Programmable electrical furnace for sintering of deposited oxide soot.

2.4 Deposition procedure

A deposition procedure is now described, which addresses three main requirements: safety of the operator, reproducible results, and longevity of the whole deposition apparatus.

- 1 Check, by switching on the dewmeter, that the dewpoint inside the pipeline equals the reference value; if not, temporarily increase the purging N₂ flow rate and wait until the required level is reached
- 2 Slowly open the valves on the H₂ and O₂ gas cylinders
- 3 Check that the cylinder pressures allow completion of the deposition; if not, replace the cylinders
- 4 Open the valves on both gas lines and set the pressure regulators of both cylinders at the desired pressure
- 5 Set the desired flow conditions for the chlorides to be employed by using the potentiometers and digital voltmeter readings on the mass flow control cabinet
- 6 Check the pressure present at the torch on the glass manometer; if it is different from the reference value, clean the torch
- 7 Check the temperature inside the bubbler cabinet; if it is less than the reference value check that the heater is on; if not, switch it on
- 8 Check that the chloride levels inside the bubblers allow completion of the deposition; if not, refill
- 9 Check that the extraction fan is operating; if not, switch it on
- 10 Check basicity of the scrubber water solution by its colour; if not, add sodium carbonate inside the scrubber tank
- 11 Switch on the scrubber pump
- 12 Switch on the stepper motors control unit
- 13 Switch on the computer
- 14 Load and run fabrication program

- 15 Input the pertinent data, i.e. starting position, number of traversals, traverse speed for the torch and rotation speed for the turntable for the warm up procedure
- 16 Open the sliding Perspex™ panel of the deposition chamber
- 17 Slowly open the valve on the H₂ flowmeter and continuously produce sparks in close proximity to the torch by using the piezoelectric lighter until the torch is ignited
- 18 Close the sliding panel
- 19 Slowly open the valve on the O₂ flowmeter and set both gas flow rates at the desired levels for the turntable warm up
- 20 Set the turntable and torch in motion by pressing the appropriate computer keys and wait until warm up is finished
- 21 Turn down the H₂ and O₂ flow rates, extinguishing the torch by closing the H₂ flowmeter valve first
- 22 Input deposition data on the computer
- 23 Wearing dust free gloves place substrates on the turntable
- 24 Ignite torch as at point 17 and set H₂ and O₂ flow rates to deposition values
- 25 Throw the toggle switches controlling the valving for the carrier gas flows through the chloride bubblers
- 26 Wait until hydrolysis begins and equilibrium is obtained. This can be confirmed by observing a change in brightness and length of the flame, and takes approximately one minute
- 27 Set the turntable and torch in motion
- 28 During the deposition do not leave the apparatus unattended. If it is necessary to abandon the room (e.g. fire alarm) immediately close the H₂ and O₂ flowmeter valves (H₂ first) and shut the N₂ flow through the bubblers
- 29 Once the deposition is completed, switch off chloride vapour transport and allow flame to return to original colour. This ensure full reaction of any chlorides left in the pipeline and it takes approximately one minute
- 30 Close valves on H₂ and O₂ cylinders

- 31 Wait until flame is extinguished, so as not to leave any H₂ in the pipeline, then close H₂ and O₂ flowmeter valves
- 32 Set H₂ and O₂ cylinder pressure regulators to closed position, then close the valves on both gas lines
- 33 Switch off the scrubber pump and flush the spray bars by opening the main water supply valve
- 34 Switch off computer and stepper motor controllers
- 35 Remove substrates for sintering
- 36 Allow the turntable to cool, then wash, dry and mount it in the deposition chamber.

Chapter 3. Fabrication and characterisation of planar waveguides

Chapter Layout

- 3.1 Introduction
- 3.2 Substrate preparation
- 3.3 Fabrication of $\text{SiO}_2\text{-P}_2\text{O}_5$ films by FHD
- 3.4 Investigation of sintering of $\text{SiO}_2\text{-P}_2\text{O}_5$ films
- 3.5 Fabrication of $\text{SiO}_2\text{-GeO}_2\text{-P}_2\text{O}_5$ films by FHD
- 3.6 Fabrication considerations
- 3.7 Rare-earth aerosol doping of $\text{SiO}_2\text{-P}_2\text{O}_5$ films
- 3.8 Characterisation of planar waveguide

3.1 Introduction

Doping of SiO_2 deposited by FHD for planar optical waveguide applications is necessary for two reasons. The first is to obtain a suitable refractive index step with respect to the surrounding medium. The second is to lower the sintering temperature of pure silica to allow its consolidation without affecting the integrity of the substrate used.

A variety of silica based glass systems have been synthesised by FHD (Table 3.1). TiO_2 (Kawachi '83) and GeO_2 (Maxwell '89, Kominato '90) have been used to increase the refractive index of silica, whilst small amounts of P_2O_5 and B_2O_3 have been included in the glass matrix to decrease its sintering temperature. The effect on the refractive index of silica of various dopants (Beales '80) is shown in Fig. 3.1. The variation of softening temperature with dopant content for $\text{SiO}_2\text{-P}_2\text{O}_5$, $\text{SiO}_2\text{-GeO}_2$ and $\text{SiO}_2\text{-B}_2\text{O}_3$ binary glasses (Hammond '78) is shown in Fig. 3.2.

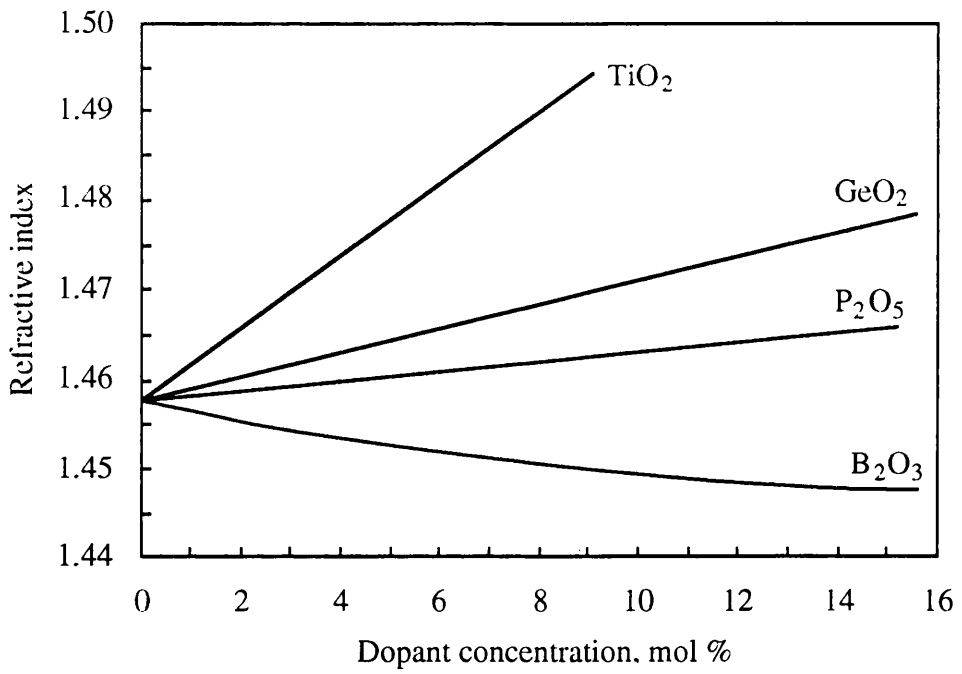


Fig. 3.1 Refractive index versus dopant content for SiO₂-P₂O₅, SiO₂-GeO₂, SiO₂-B₂O₃ and SiO₂-TiO₂ binary glasses (Beales '80).

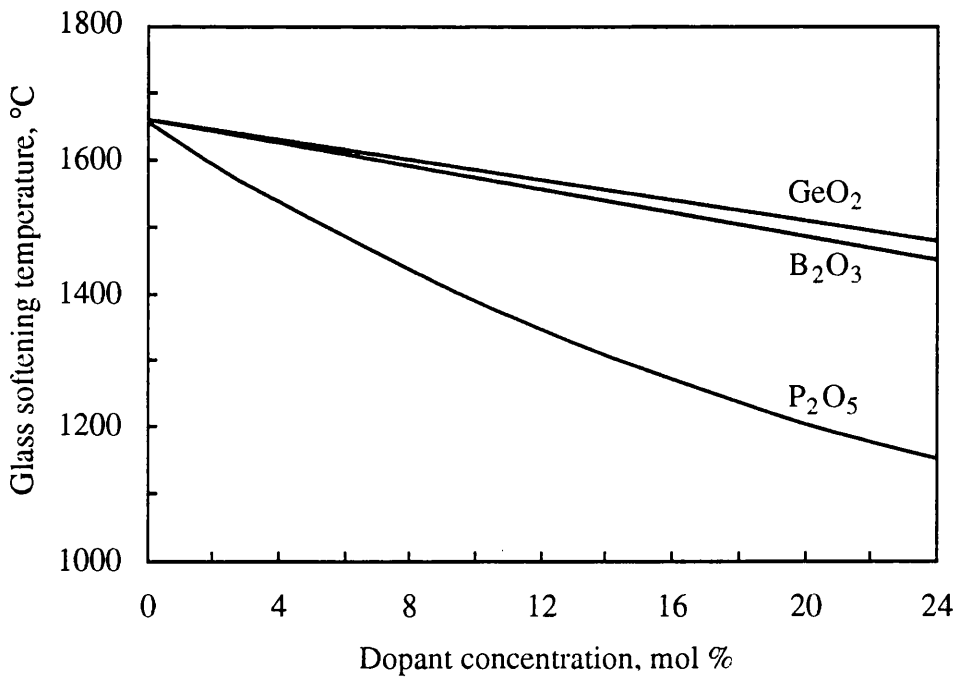


Fig. 3.2 The variation of softening temperature with dopant content for SiO₂-P₂O₅, SiO₂-GeO₂ and SiO₂-B₂O₃ binary glasses (Hammond '78).

We have doped silica only with P_2O_5 , obtaining a simple binary glass (Barbarossa '91 a). In this case P_2O_5 plays a double role, increasing the refractive index of silica and decreasing its sintering temperature.

Glass system	Phases	Scientif. Instit.	Reference
$SiO_2-TiO_2-P_2O_5-B_2O_3$	4	NTT Labs	Kawachi '83
$SiO_2-GeO_2-P_2O_5$	3	BT Labs	Maxwell '89
$SiO_2-GeO_2-P_2O_5-B_2O_3$	4	NTT Labs	Kominato '90
$SiO_2-P_2O_5$	2	Glasgow Univ.	Barbarossa '91 a
$SiO_2-TiO_2-B_2O_3$	3	Siemens	Schneider '91

Table 3.I Silica-based glass systems synthesised by FHD (in chronological order); the phases responsible for the refractive index increment of silica are in bold; the phases responsible for the decrease of the sintering temperature of silica are in italic.

In this chapter the fabrication of $SiO_2-P_2O_5$ and $SiO_2-P_2O_5-GeO_2$ planar waveguides by FHD is described in terms of deposition parameters and sintering process, which have been optimised to achieve low-loss, bubble-free waveguides. In particular, investigations regarding the sintering process for $SiO_2-P_2O_5$ films are described and an explanation of the results obtained is attempted. Rare-earth incorporation by aerosol doping technique is also presented. Characterisation of the fabricated waveguides has been carried out in terms of refractive index, thickness, wavelength dispersion and propagation loss.

It is stressed at this point that the main aim of the author was to find a suitable "recipe" which yielded inclusion free, homogeneous films with a reproducible thickness and refractive index, which could be used for further processing. Therefore, many of the results are described in general terms, indicating qualitative observations made on deposited films. As a consequence, detailed investigation into the causes of the observed phenomena was not carried out beyond the level necessary to surmount the problems encountered.

3.2 Substrate preparation

The substrates used were mainly of two types; 1) 76.2 mm (3") ϕ , 1 or 0.75 mm thick, polished Si wafers (from Wacker-Chemitronic, Germany), orientation (100), p-type, with a 10 μm thick SiO_2 buffer layer thermally grown by high pressure steam oxidation. 2) 30 mm ϕ , 1 or 2 mm thick Homosil™ grade (from Heraeus, Silica and Metals Ltd., U.K.) polished fused silica. Other substrates used were 32 or 38 mm ϕ , 0.4 mm thick, polished Si wafers, orientation (100), p-type, unoxidized and 50 mm ϕ , 3 mm thick Homosil™ grade polished fused silica. A set of different substrates employed is shown in Fig. 3.3.

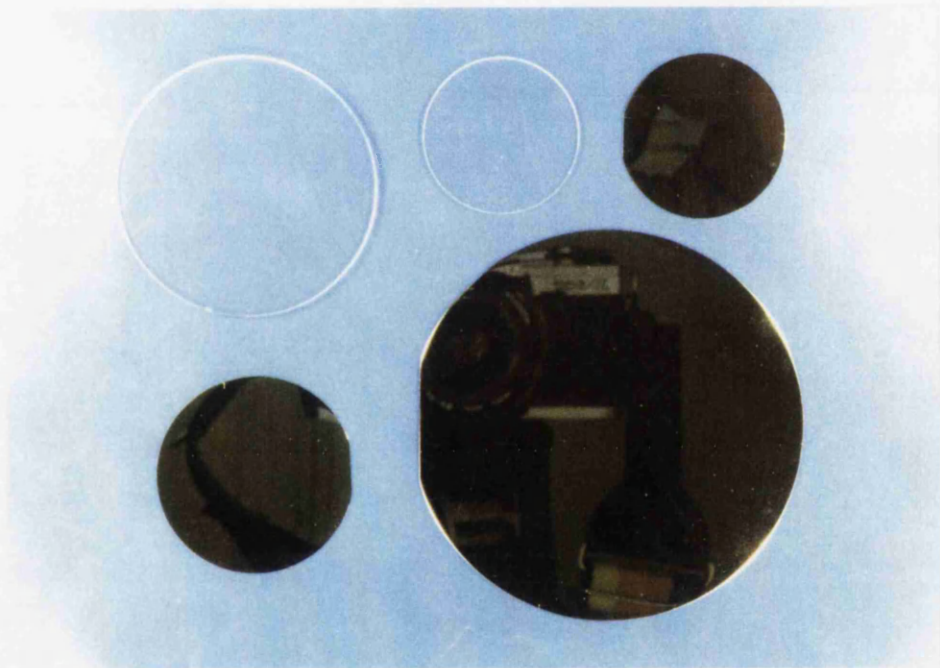


Fig. 3.3 Set of different substrates employed by the author.

The buffer layer on Si wafers is required to prevent coupling of the guided light in the highly absorbing substrate. This buffer layer has to be thick enough to give an attenuation value due to substrate coupling well below the value of the waveguide intrinsic propagation loss. Thermal growth of thick SiO_2 layers is a time-consuming process mainly because the oxidation rate of Si is inversely

proportional to the grown thickness (Sze '83). For example a 10 μm thick SiO_2 layer is grown under high pressure steam oxidation at 1300 $^\circ\text{C}$ in about a week (Maxwell '91). Consequently it is important to determine the minimum thickness of the buffer layer which would guarantee a tolerable attenuation. An adequate buffer thickness has been determined by using the four layer planar optical waveguide theory which is illustrated in Appendix A. At an operating wavelength of 1.55 μm , a 10 μm thick layer of thermal SiO_2 is sufficient to give an attenuation due to substrate coupling less than 10^{-4} dB/cm, which is three order of magnitude smaller than the average value reported for low loss high silica content planar waveguides.

The alternative is to deposit on the Si substrate a lightly doped silica buffer layer. Thickness of the buffer layer deposited by FHD can be determined in a similar way to thermal SiO_2 . However even in this case a thin oxide layer is necessary on the Si surface to improve its wettability. This point will be examined in more detail later in the chapter.

Prior to deposition, substrates were cleaned to remove organic and inorganic contaminants by employing the following procedure

- 1 Wash substrates individually with soapy water using a sponge
- 2 Five minutes in soapy water in ultrasonic bath (UB)
- 3 Rinse in deionized water
- 4 Five minutes in trichloroethane in UB
- 5 Rinse in methanol
- 6 Five minutes in methanol in UB
- 7 Rinse in acetone
- 8 Five minutes in acetone in UB
- 9 Flush with plenty of deionized water without extracting the sample from the beaker
- 10 Blow dry with filtered nitrogen
- 11 Dry on hot plate

The sequence for the solvents employed is not casual. It is arranged in such a way that each solvent is soluble in the following one. Alternatively, a water solution (1:20) of Decon™ can be used instead of the trichloroethane bath (step 4).

3.3 Fabrication of SiO₂-P₂O₅ films by FHD

Although P₂O₅ has an expansion coefficient some 25 times larger than SiO₂, in combination, for concentrations up to 45 wt% (Gambling '76), they form a stable glass having an expansion coefficient compatible with that of pure silica. The glass obtained exhibits very low loss at telecommunication wavelengths, presents the same refractive index dispersion, absorption and scattering properties of pure silica and shows no tendency either to phase separation or to devitrification, as well as good resistance to attack by water (Lee '88).

The inclusion in SiO₂ of modest amounts of P₂O₅ dramatically reduces the temperature required to liquefy the resulting glass. This can be evinced by observing the phase diagram of the SiO₂-P₂O₅ system in Fig. 3.4 (Tien '62), in which the liquidus line, being the boundary on a phase diagram between the solid and liquid phases, presents a steep slope for low concentrations of P₂O₅. It should be stressed that the liquidus line represents the transition between solid crystal and liquid, and as such may not strictly apply to the glasses under consideration. However, it serves as a useful guide to understanding the behaviour of such glasses.

A problem in the fabrication of SiO₂-P₂O₅ waveguides by FHD is the high volatility of the P₂O₅ phase, which requires the deposition and sintering processes to be optimised in order to prevent its volatilisation. It is worthwhile to mention at this point that P₂O₅ has a saturated vapour pressure higher than 760 torr in the 1300-1500 °C range, and therefore it cannot exist in the solid form at this temperature (Niizeki '85). Consequently, care was taken during the deposition to prevent the volatilisation of the P₂O₅ phase by using deposition speeds such that the high temperature flame (~1300 °C) would not overheat the deposited soot and cause the evaporation of the P₂O₅. Alternatively, a water cooled turntable was

designed for this purpose. The temperature of the water bath was kept constant at 80 °C, this temperature being low enough to prevent P₂O₅ from evaporating. The sintering process of SiO₂- P₂O₅ films will be examined in more detail in the next section.

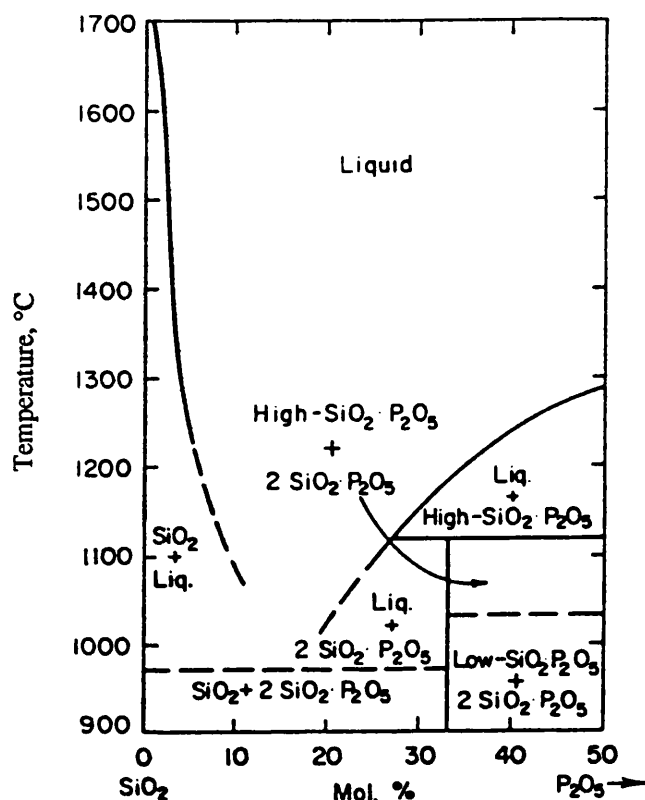


Fig. 3.4 Phase diagram of SiO₂-P₂O₅ system (Tien '62).

Chloride flow rates ranged from 75 to 180 cm³/min for SiCl₄ and from 95 to 200 cm³/min for PCl₃. Typical flame flow rates used ranged from 4-12 and 6-10 l/min for H₂ and O₂, respectively, achieving a flame temperature of about 1300 °C. The average size of the oxide particles, which is determined by the temperature of the flame, by the halide flow rates and their residence time in the flame, was about 60 nm in diameter (see scanning electron microscope (Hitachi 800) (SEM) micrographs in Fig. 3.5). Torch traverse speed and turntable rotational speed were typically 25 mm/min and 30 rev/min, obtaining, with flow rates of 150 cm³/min for SiCl₄ and 160 cm³/min for PCl₃, a 1.5 μm thick film per traversal (after sintering).

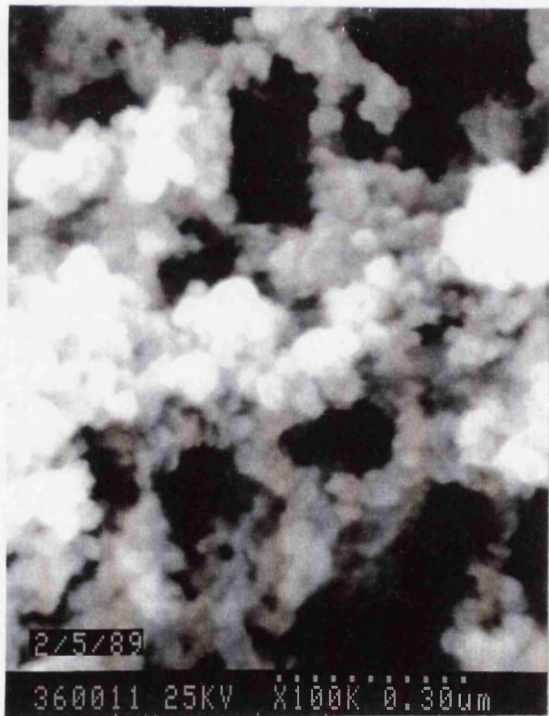


Fig. 3.5 SEM micrographs of as-deposited SiO₂-P₂O₅ soot.

We have fabricated P_2O_5 -doped silica films with a relative refractive index difference ranging from 0.35 to 1 %. The index increment versus the PCl_3 flow rate is reported in Fig. 3.6. These values refer to $SiCl_4$, H_2 and O_2 flow rates of $150\text{ cm}^3/\text{min}$, 4 and 7 l/min, respectively (Barbarossa '92 h). In Fig. 3.6 a negative intercept between the ordinate axis and the regression line can be noted.

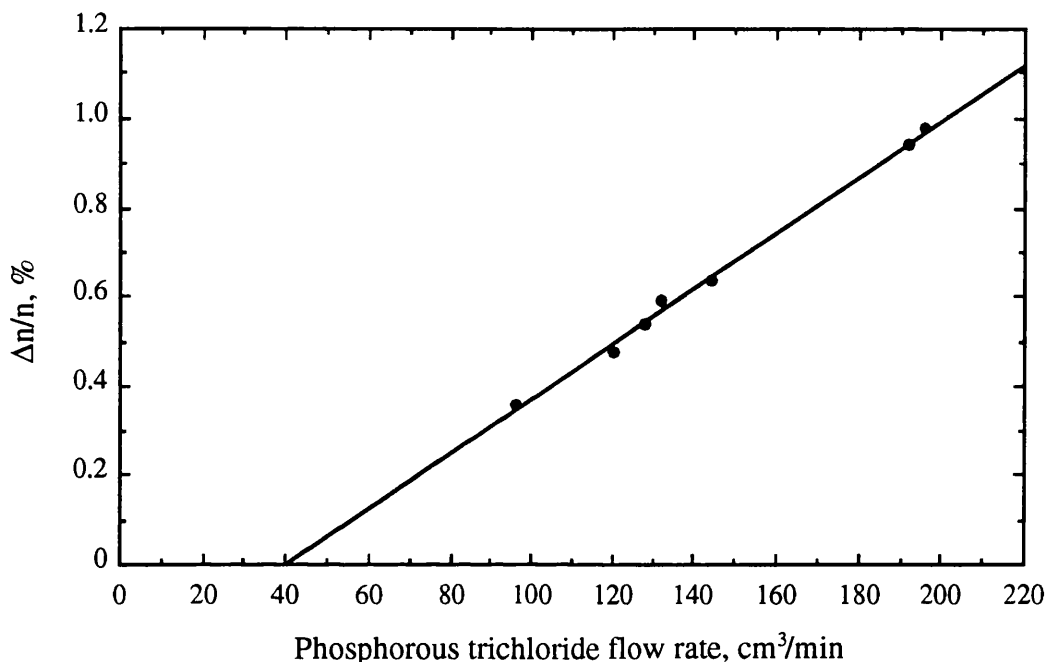


Fig. 3.6 Refractive index change versus the PCl_3 flow rate. ($SiCl_4$ flow rate $150\text{ cm}^3/\text{min}$ and H_2 and O_2 flow rates 4 and 7 l/min).

Besides eventual experimental errors, this effect can be explained in two ways. The first is that the refractive index of the SiO_2 synthesised by FHD is lower than that of the thermally grown SiO_2 . This explanation could be proved only by fabricating bulk sample of SiO_2 by FHD, as sintering of pure SiO_2 on a substrate can not be accomplished at temperatures below $1400\text{ }^\circ\text{C}$. The second is that there is a threshold flow rate of PCl_3 which is necessary for the incorporation of solid P_2O_5 particles in the deposited soot. This threshold flow rate appears to be dominated by the saturated vapour pressures of the oxide components in the flame (Niizeki '85). Thus, for the H_2 and O_2 flow rates used, a value of $\sim 40\text{ cm}^3/\text{min}$ could be regarded as the minimum PCl_3 flow rate for P_2O_5 formation in the flame. It is stressed here that films deposited by using PCl_3 flow rates less than $90\text{ cm}^3/\text{min}$ could not be sintered completely at temperatures below $1400\text{ }^\circ\text{C}$. Therefore the existence of a refractive index change, and consequently of the

formation and incorporation of P_2O_5 in the silica matrix, could not be directly verified.

3.4 Investigation of sintering of SiO_2 - P_2O_5 films

In ceramics, sintering is the process of consolidation of oxide powders by heating without melting (Scherer '77). Sintering kinetics play an important role in determining the structural and optical properties of silica based planar waveguides fabricated by FHD. Despite the fabrication process being a modification of the VAD or OVD methods for the fabrication of optical fibre preforms, and the glasses synthesised being basically the same, planar deposition suffers from critical restrictions in sintering temperature range and gradients imposed by the presence of the substrate.

Whilst fibre preforms fabricated by VAD, for example, are normally sintered at temperatures of about 1500 °C and drawn at temperatures above 1900 °C (Sudo '80), the planar films can only be processed at temperatures below 1300 °C, because higher temperatures would inevitably cause the warping and the bowing of the Si or SiO_2 substrates. Residual gas trapping, evaporation of the silica dopant, thermal shock of the substrate, and unreleased stresses of the deposited layer after the consolidation process, due to the difference in thermal expansivities between film and substrate (Scherer '85), are other problems that need to be addressed in a planar deposition. Finally, the planar sintering process, evolving as it does on a substrate, behaves in a different way from the isotropic case of the fibre preform. This results in a viscosity-slowed coalescence of the soot. All these problems, which are absent in the fabrication of fibre preform, govern the reliability and repeatability of the planar fabrication process and the conclusions obtained for the fibre preform fabrication do not systematically apply to planar deposition.

Extensive literature exists dealing with the sintering of fibre preform fabricated by VAD (Niizeki '85) or OVD (Morrow '85), but not with regard to the fabrication of planar waveguides. We have investigated the influence of the temperature range and gradient of the heating-up ramp on the evolution of the sintering of P_2O_5 -doped silica low density soot and its consequences on the dopant incorporation of the resulting glass (Barbarossa '92 g). An optimum sintering process has been determined which guarantees bubble free, low loss

waveguides, prevents the warping of the substrate and inhibits the volatilisation of the silica dopant. Thermal shocks and forbidden temperatures are avoided, gas trapping is prevented and the target refractive index step is obtained. Volatilisation of the P_2O_5 phase from the silica matrix has been observed at different levels after different thermal treatments.

SiO_2 - P_2O_5 low density glass soot was deposited on fourteen 76.2 mm ϕ , 0.75 mm thick, Si substrates. $SiCl_4$ and PCl_3 flow rates were 150 and 140 cm^3/min , respectively. Flame flow rates were 10 and 5 l/m for H_2 and O_2 , respectively (flame temperature $\sim 1300^\circ C$). A film approximately 40 μm thick (before sintering) was obtained after 4 traversals.

After deposition, seven samples were independently introduced into the furnace for consolidation at seven different starting temperatures during successive identical sintering programs. The programs were implemented on the furnace temperature controller and consisted of a common part going from point G (see Fig. 3.7) to the end of the program, whilst they differed in the starting temperature (points A-G) of the first ramp.

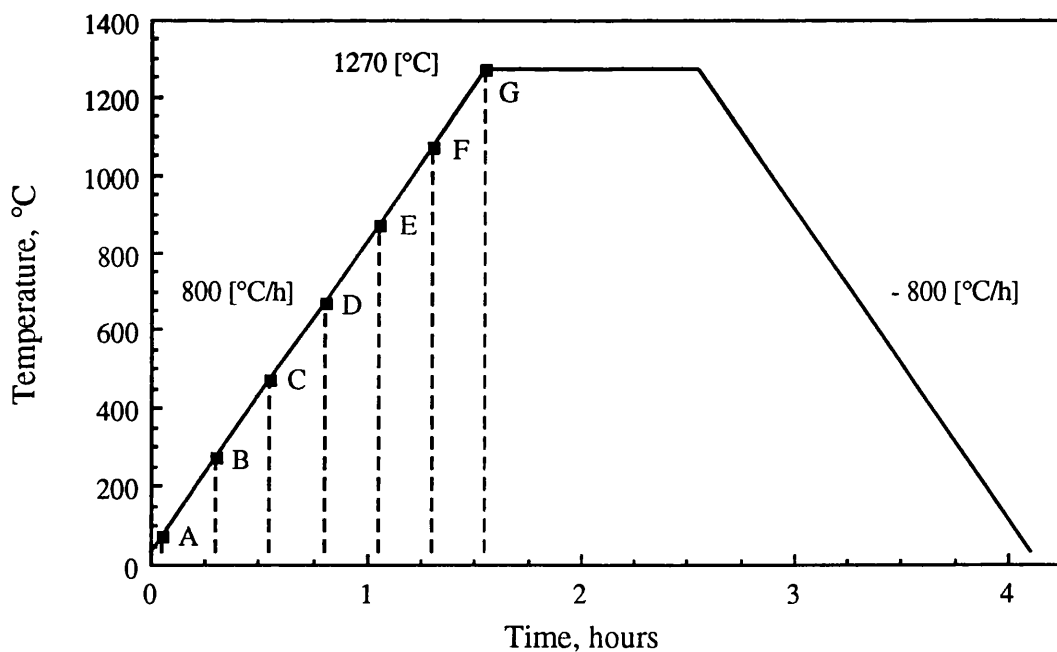


Fig. 3.7 Diagram grouping the seven different sintering processes for the first seven samples.

The temperature gradient of the first ramp was 800 °C/h, the dwell was at 1270 °C for 1 hour, and the gradient of the second ramp was -800 °C/h. It is worthwhile emphasising that each sample was subjected to the heating treatment going from point G (representing the highest temperature reached during the program) to the end of the process.

We observed that only the sample introduced into the furnace at 1270 °C (point G) completely sintered. An increasing degree of sintering, qualitatively evaluated from the average pores size of the layers (see SEM micrographs in Fig. 3.8 a-f), was noted from the sample introduced at room temperature (point A in Fig. 3.7), towards the sample introduced at 1270 °C (point G). So, despite all the samples having been subjected to the highest temperature part of the process, i.e. the dwell at 1270 °C for 1 hour, which by itself caused complete sintering of the sample introduced at 1270 °C, they did not reach the same degree of consolidation. Indeed, samples which underwent longer heating treatments were less sintered.

The remaining seven samples were submitted to sintering processes having different gradients of the heating-up ramp (Fig. 3.9). The dwell and the cooling ramps were the same as the previous experiment. The gradient of the heating-up ramp ranged from 200 to 1400 °C/h, by increments of 200 °C/h. All the samples were introduced into the furnace at room temperature. After completion of each sintering process, we observed a different degree of sintering of the samples. The less sintered sample was that submitted to the process with the slower heating-up ramp. The fastest heating-up ramp produced a completely sintered layer. SEM micrographs showing the different degree of sintering are similar to those relative to the previous experiment. From the experimental results it can be inferred that the warm up preceding the highest temperature of the heat treatment affects the final result of the whole sintering process. As has been previously described, only P₂O₅ was used as dopant to increase the refractive index of silica, as well as to decrease its sintering temperature. Consequently, it is reasonable to deduce that during the heating-up ramp of the process some of the P₂O₅ was lost to the gas phase by evaporation (P₂O₅ melts at 580 °C and sublimates at 300 °C). The decrease in P₂O₅ concentration increased the sintering point of the doped silica, and the temperature and duration of the dwell were not high enough and long enough to achieve complete consolidation.

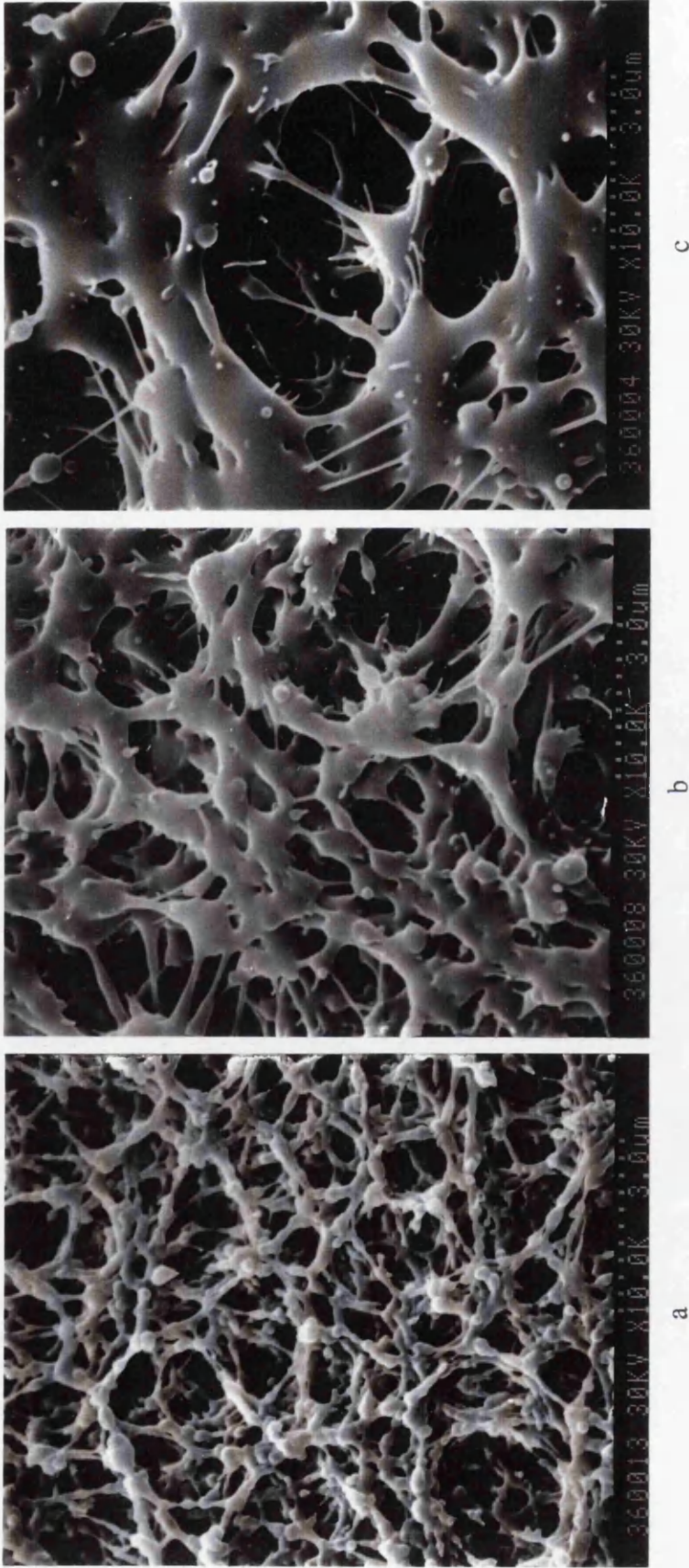


Fig. 3.8.1 SEM micrographs of samples introduced into the furnace at points A-C (a-c) of the sintering program in Fig. 3.7, showing their different degree of sintering. Photos were taken after completion of the sintering program.

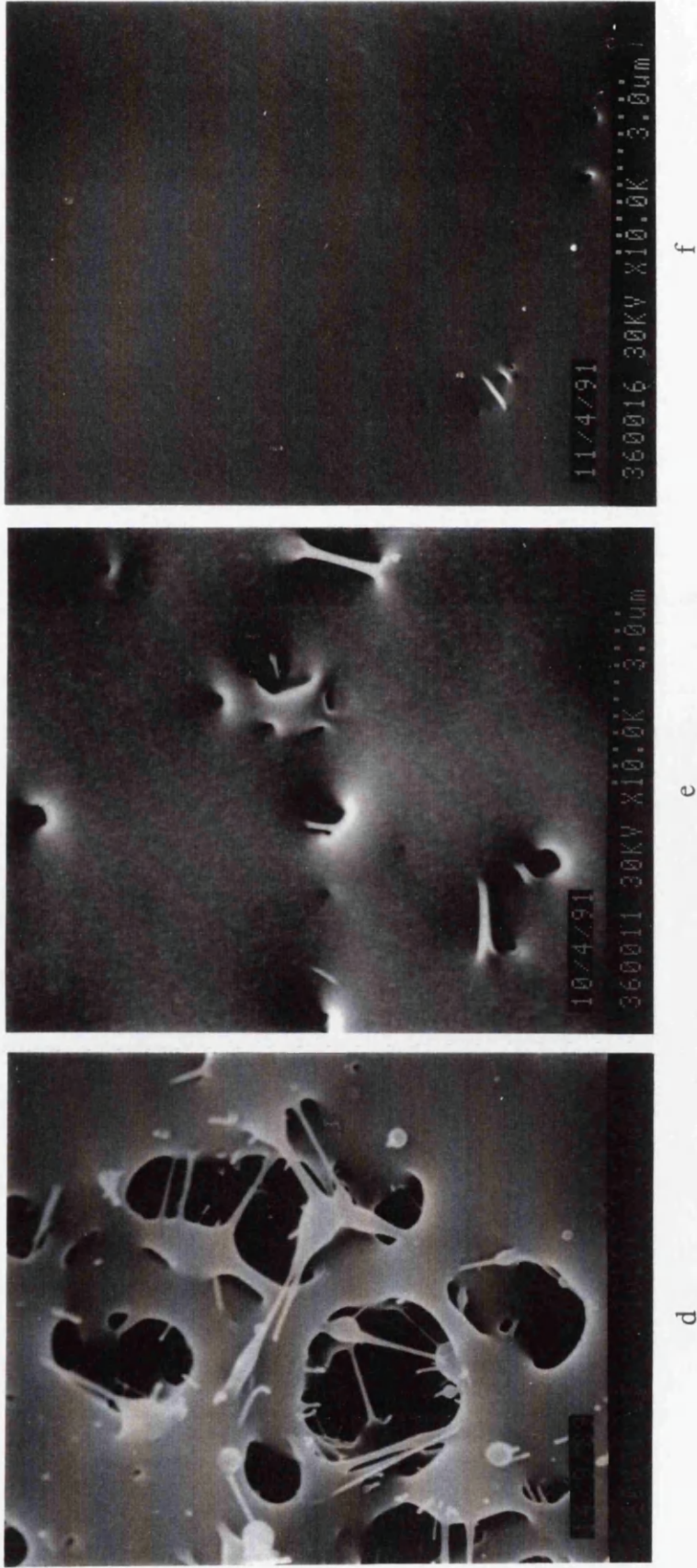


Fig. 3.8.2 SEM micrographs of samples introduced into the furnace at points D-F (d-f) of the sintering program in Fig. 3.7, showing their different degree of sintering. Photos were taken after completion of the sintering program.

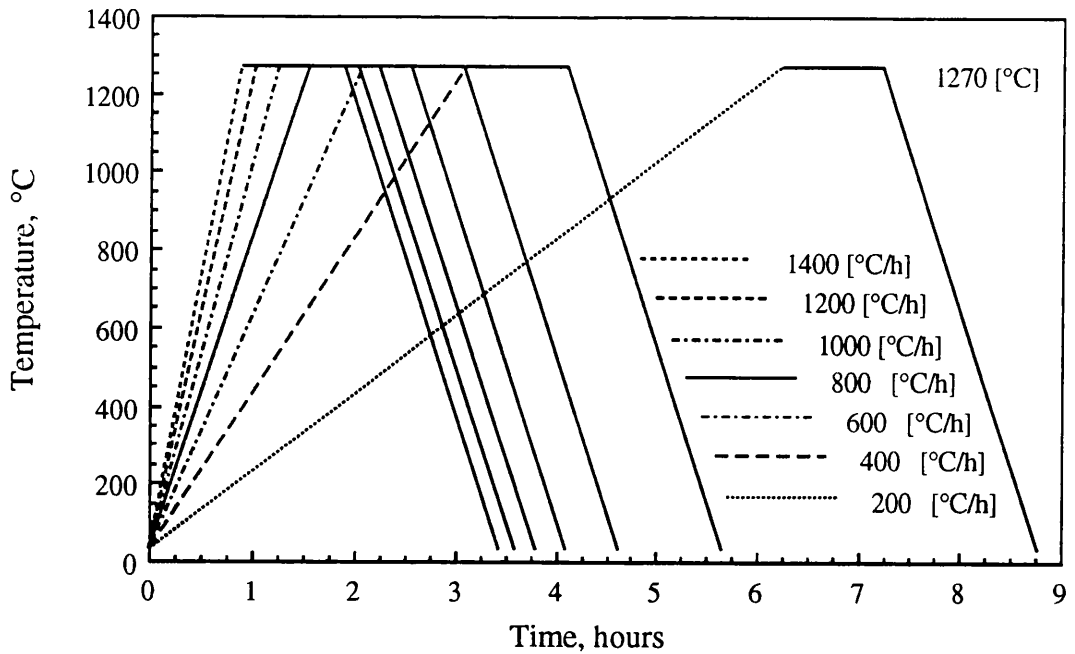


Fig. 3.9 Diagram grouping the seven different sintering processes for the second set of seven samples.

Diffusion processes of phosphorous oxide and related species in silica films have been studied extensively. Ghoshtagore ('75) found that above 1150 °C, the P_2O_5 phase diffuses through the SiO_2 matrix in a solid state and that for concentration below 0.5 mol%, its diffusivity in SiO_2 is concentration-independent. $xP_2O_5-ySiO_2$ species also diffuse through the silica matrix but in a liquid state and their mobility is greatly affected by traces of moisture. Volatile P_2O_5 formed by the decomposition of this species at the exposed surface should be regarded as responsible for the out-diffusion of the P_2O_5 . Precautions, such as the use of sealed platinum tubes, have also been adopted to prevent loss of P_2O_5 from the silica matrix during the investigation of phase relations in the $SiO_2-P_2O_5$ binary system (Tien '62). Eldridge et al. ('68) deliberately heat treated phosphosilicate films to lose P_2O_5 to the gas phase by evaporation, and produce films of controlled polarizability for surface stabilisation of Si MOS structures. Volatilisation of P_2O_5 has been also experienced from the centre of the core region during the collapsing of phosphosilicate glass fibre preforms. Gambling et al. ('76) suggested a means to overcome the problem by increasing the P_2O_5 concentration during the deposition of the innermost layer to counterbalance the loss by diffusion.

Because the densification rate of low density glass is a strong function of the sintered density and decreases as the glass approaches its theoretical density (Yan '80), a complete sintering of the samples was attempted by extending the duration of the dwell at 1270 °C. Samples corresponding to point E and F were fully sintered after 3 hours. However, samples from A to D could not be completely sintered, even for a dwell duration of 10 hours and it is believed that higher temperature would have been necessary, which would have caused warping of the substrate. It is worthwhile to point out that fusion temperatures of the SiO₂-P₂O₅ system (see Fig. 3.2) do not strictly apply to the sintering of fine oxide powders. In fact consolidation of fine particles takes place at temperature well below the fusion temperature of the corresponding solid material, the driving force arising from the excess free energy of the surface area of the powder particles over that of the solid material (Mackenzie '49).

From the flow rates of SiCl₄ and PCl₃ used, the doped silica film was estimated to have a nominal composition of 3 mol% of P₂O₅. To verify the evaporation of the P₂O₅ the refractive indexes of sample E and F were derived from the mode synchronous coupling angles (details of waveguide characterisation will be given in the next paragraph). From the refractive index change, a decrease of 0.07 and 0.05 mol % was estimated for sample E and F, respectively. Therefore, the sintering process affects the dopant concentration and its effects on the refractive index of the synthesised glass have to be taken into account. It has been pointed out that the sintering rate affects dopant incorporation by regulating the length of time over which dopant diffusion occurs (Digiovanni '89). It is desirable, however, to have a sintering process that does not affect the film composition, which would preferably be controlled, in a direct manner, by the flow rates of the halides.

From the experimental results it is clear that any fast heating-up ramp (>1400 °C/h) would allow complete consolidation of the deposited soot and prevent loss by evaporation of the P₂O₅ from the silica matrix. This is confirmed by the first experiment. However a too steep temperature gradient is not desirable as it causes gas trapping in the consolidating layer and generates thermal shock in the Si substrate, which has a thermal expansion coefficient one order of magnitude lower than that of the synthesised glass.

Evaporation of the dopant from films fabricated by FHD is helped by the slowness of planar sintering, as this is retarded with respect to bulk sintering (Scherer '85). Sintering of a low density soot layer comprises of two processes: densification of the glass soot, where the transition from open pore state to closed pore state occurs, and closed pore collapsing. Pore collapsing depends not only on the permeability of the trapped gas but also on the temperature increasing speed. In fact, bubble free preforms fabricated by VAD have been obtained in impermeable gas atmosphere, with a low temperature increasing speed of less than 400 °C/s (Sudo '80). This means that a slow sintering process would be helpful in obtaining bubble free and more uniform films by allowing complete pore collapse. However, as we have observed, too slow a sintering rate causes volatilisation of the silica dopant, which is more accentuated with a more volatile dopant.

A platinum box, which is shown in Fig. 3.10, was used to seal the sample and create a partial pressure of P_2O_5 on the sample. Samples still did not sinter. This is thought to be due to the open structure of the low density glass soot that facilitates the P_2O_5 evaporation with respect to other experiments reported in literature (Tien '62) where bulk P_2O_5 was heat treated.

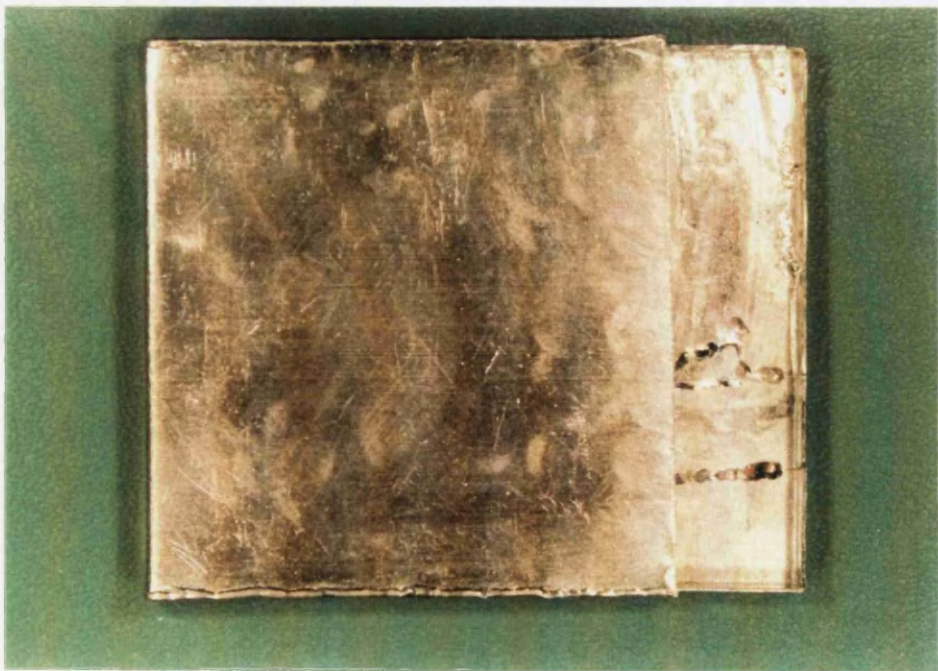


Fig. 3.10 Platinum box used for sintering experiment.

A good compromise was found to be a heating-up rate of 1400 °C/h up to 1270 °C, a 1 hour dwell and a cooling ramp of 800 °C/h, which produced completely sintered, bubble free, low-loss films, in a reproducible manner.

Further studies are necessary for a more comprehensive understanding of the subject. For example, structural microanalysis of the doped silica films would allow a quantitative evaluation of the amount of P₂O₅ lost in the gas phase during the consolidation. Also, mercury or gas porosimetry would help in a precise correlation between the degree of sintering and the thermal process adopted.

3.5 Fabrication of SiO₂-P₂O₅-GeO₂ films by FHD

SiO₂ and GeO₂ form a stable monophase glass for any their relative concentration (Schafer '64). Temperatures required for a single phase solution are higher than those for the SiO₂-P₂O₅ system. In SiO₂-GeO₂ films fabricated by FHD, P₂O₅ codoping is necessary to lower the glass sintering temperature below the value allowed by the substrate integrity. We have fabricated P₂O₅-GeO₂-doped silica films with a relative refractive index difference ranging from 0.5 to 1.1 %. The index increment versus the GeCl₄ flow rate is reported in Fig. 3.11. These values refer to SiCl₄, PCl₃, H₂ and O₂ flow rates of 150 and 108 cm³/min, 4 and 7 l/min, respectively. The ordinate axis intercept on the diagram in Fig. 3.11, which corresponds to a GeCl₄ flow rate equal to zero and to a PCl₃ flow rate of 108 cm³/min, is slightly lower than the value in the diagram in Fig. 3.6 corresponding to the same value of PCl₃ flow rate for SiO₂-P₂O₅ glass. This difference of 0.07 % in refractive index change for identical values of SiCl₄ and PCl₃ flow rates can be attributed, besides eventual experimental errors, to the same reasons already exposed in the previous paragraph for SiO₂-P₂O₅ films, which regards the chlorides threshold flow rates.

Sintering of SiO₂-P₂O₅-GeO₂ films was achieved by following the same optimum heat treatment adopted for SiO₂-P₂O₅ films. There is to say, however, that less problems than in sintering of SiO₂-P₂O₅ films were generally encountered in this case, due mainly to the fact that GeO₂ has, at the temperatures involved, a saturated vapour pressure several orders of magnitude smaller than that of P₂O₅ (Niizeki '85).

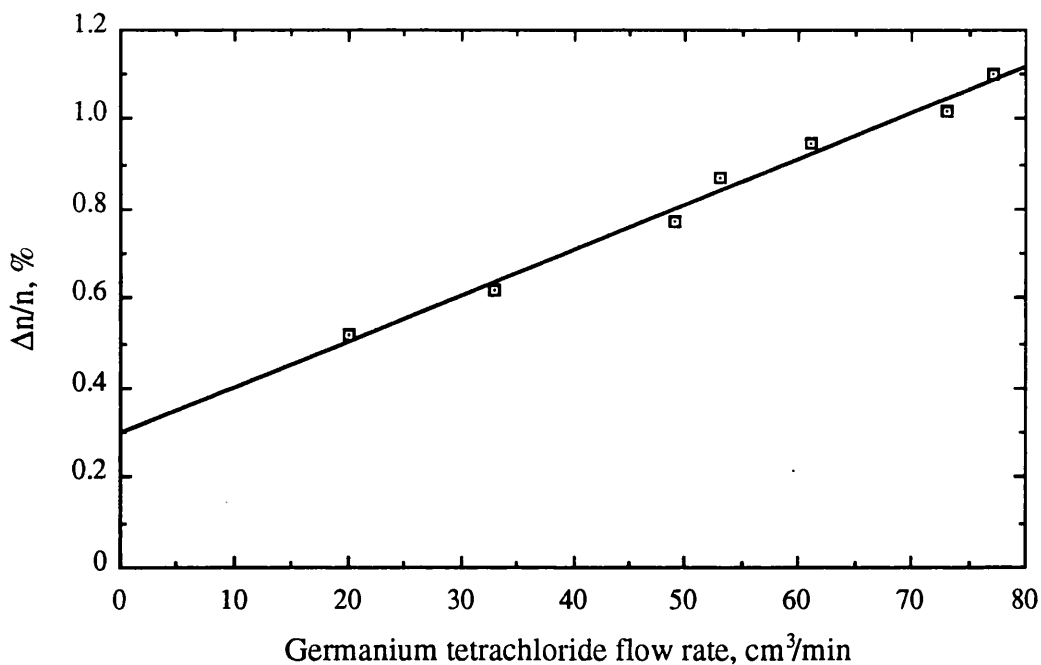


Fig. 3.11 Refractive index change versus GeCl_4 flow rate (SiCl_4 and PCl_3 flow rates 150 and 108 cm^3/min , H_2 and O_2 flow rates 4 and 7 l/min).

3.6 Fabrication considerations

Particulate contaminants, such as dust or even reaction products, in the chloride vapour stream or on the substrate surface during the deposition or sintering can result in void, thin spots, pinholes or hillocks. Localised defects include embedded foreign particles, microcrystallites or precipitates caused by reactions in the solid state. Silica based glasses may also devitrify, i.e. convert their state from amorphous to crystalline, in local regions under certain conditions. Devitrification of pure silica at atmospheric pressure occurs as cristobalite formation from 1000 °C to the cristobalite liquidus at 1723 °C with a maximum growth rate at 1600 °C. Crystals form and grow from nuclei found predominantly at the glass surface and internal crystallisation is rarely seen (Kirk-Othmer '72).

At the temperatures involved in the sintering of films fabricated by FHD, devitrification can represent a problem. Devitrification has been sometime

experienced by the author on the surface of $\text{SiO}_2\text{-P}_2\text{O}_5$ films. The surface defects originated by such a devitrification are clearly visible in Fig. 3.12. However their nature is not well understood. In fact cristobalite crystals have a cubic or tetragonal unit cell. However, as is evident from Fig. 3.12, the crystals formed have a clear hexagonal symmetry, which is typical of silica in the natural quartz crystalline state.

The devitrification rate is extremely sensitive to both surface and bulk impurities, especially alkali. The water content of the glass also affects the devitrification rate. A high hydroxyl content in the glass as well as water vapour and oxygen in the atmosphere enhance devitrification. However, it is thought that such microcrystals are originated from impurities such as microparticles flaking from the fused quartz torch and nozzle during the deposition or from the furnace fused quartz tube during the sintering. Etching of the torch and nozzle in a buffered hydrofluoric acid (HF) solution was periodically carried out to remove devitrified particles from their surface, which developed due to the inevitable thermal cycle which they experienced for each deposition run. A platinum box was found to be effective in protecting the film during sintering from chips of silica landing on its surface.

The composition of the glass to be deposited on silica substrates is restricted to lower dopant contents because of the tensile stresses which would develop caused by the positive difference in thermal expansion coefficient between doped silica ($0.5 \cdot 10^{-6} \text{ deg}^{-1}$) and silica ($0.35 \cdot 10^{-6} \text{ deg}^{-1}$) and which cause film cracking (Kawachi '90). An example of such cracking is visible in Fig. 3.13, where SEM micrographs of a heavily $\text{GeO}_2\text{-P}_2\text{O}_5$ -doped film deposited on a silica substrate are shown (cracking in P_2O_5 -doped films on silica substrate have the same appearance). From the sharp nature of the cracking edge it can be evinced that it occurred when the film had a hard consistency, i.e. upon quenching from the high sintering temperatures. This kind of cracking affects the whole extent of the film. Because of the negative difference between the thermal expansion coefficients of doped silica and Si ($2.5 \cdot 10^{-6} \text{ deg}^{-1}$), when Si substrates are used, the stresses in the doped silica layers are compressive and they do not tend to crack.

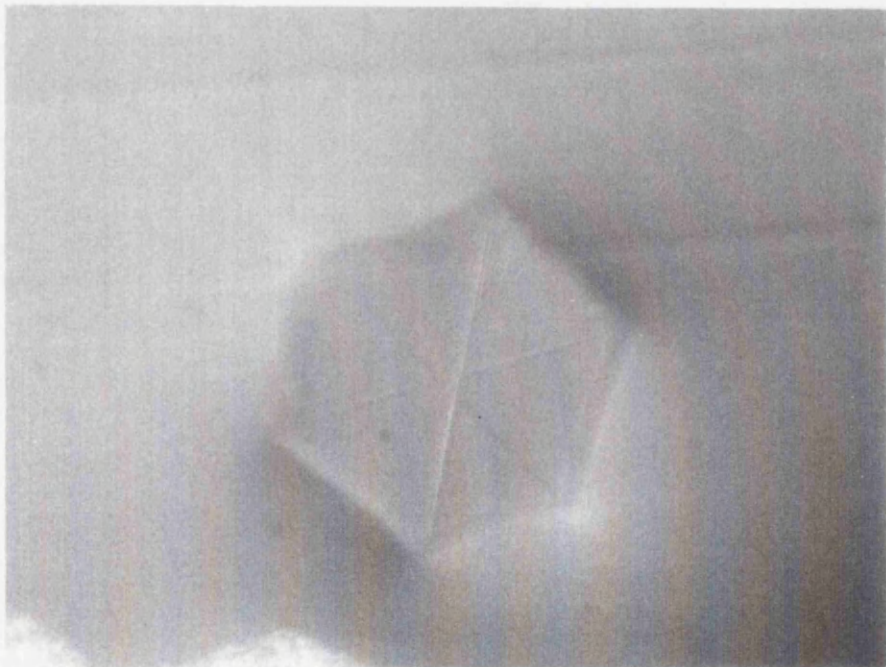


Fig. 3.12 Photographs of surface defects caused by devitrification; the hexagonal symmetry of the microcrystallites is clear.

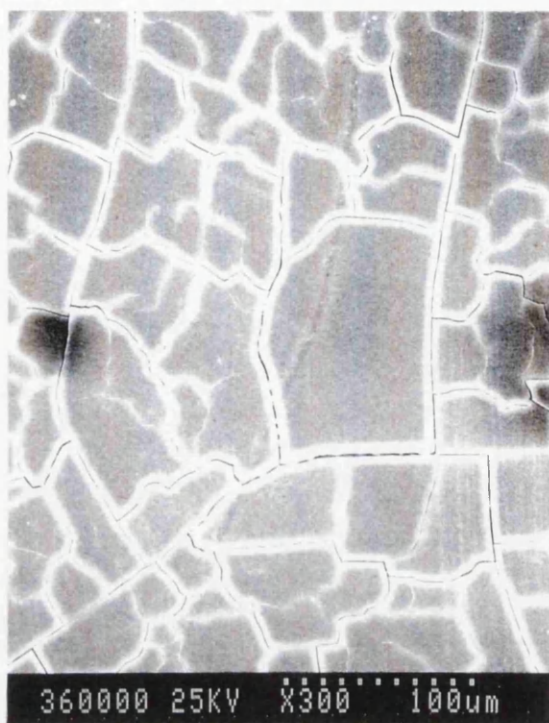


Fig. 3.13 SEM micrographs of cracking of heavily $\text{GeO}_2\text{-P}_2\text{O}_5$ -doped silica film deposited on silica substrate.

Although the nature of the stresses generated by the mismatch in thermal expansivities between doped silica film and Si substrate is compressive, when thick ($> 15 \mu\text{m}$) films are deposited, a kind of superficial cracking can be easily experienced even on Si substrate. The nature of this kind of cracking illustrates the manner in which sintering develops in thick layers. In fact, shrinkage of thick films occurs not only normally to the plane of the substrate (thickness shrinkage), but also in its plane (Scherer '85). In thin films this planar shrinkage does not happen because of the lateral constraint imposed by the substrate on the whole thickness of the film.

At the high sintering temperature involved, surface tension of the underlying layers plays an important role in pulling apart soft sintered areas of the superficial layer. As the SEM micrograph in Fig. 3.14 shows, cracking occurs even when complete consolidation has not been yet achieved, and it is not erased when the film is completely sintered (Fig. 3.15). This kind of cracking is different in appearance from cracking due to tensile stresses developed between film and silica substrate (see Fig. 3.13). First, cracking in thick films does not extend all over the substrate. Second, it is a sort of ramifying groove with smooth edges and it is limited to the superficial part of the film. The superficial extension of the groove is visible in the SEM micrograph in Fig. 3.14, which shows that below the cracked layer there is a uniform partially sintered layer. Crack-free thick films have been fabricated in successive stages by multiple thin film depositions. This point will be reconsidered in chapter 6.

Another problem which it is possible to incur during FHD is the formation in the deposited glass soot of voids by flaking of oxide particle agglomerates. These voids, an example of which is shown in Fig. 3.16, are responsible subsequently for surface defects of the sintered film. This kind of problem can be more easily experienced when the flame during the deposition is far from the substrate. In fact, in this case, the flame does not help in compacting the soot as when it is in close proximity. It is preferable that the flame produces a partial degree of sintering of the deposited film, as this increases its mechanical strength. Similar precautions are also taken in the fabrication of fibre preforms by VAD, where considerable mechanical strength of the porous preform is necessary to support its own weight during upward pulling (Izawa '87).

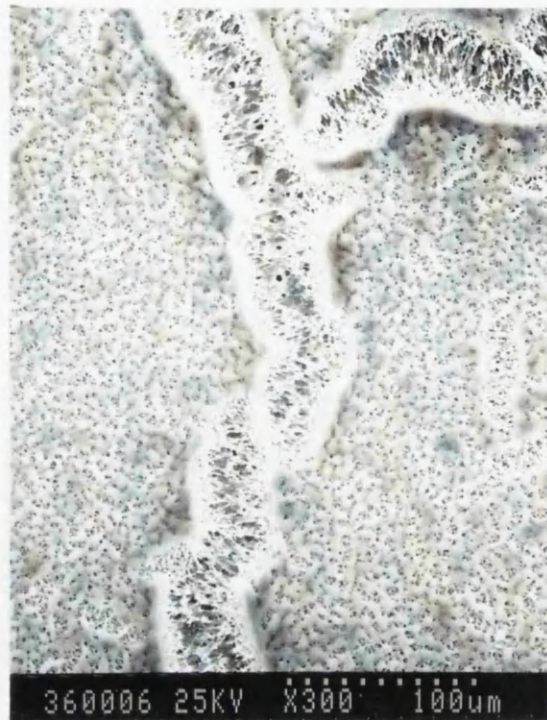


Fig. 3.14 SEM micrograph revealing that cracking in thick films deposited on Si substrate occurs even when complete consolidation has not been achieved and it affects only the superficial part of the film.



Fig. 3.15 Photograph of cracking in thick film deposited on Si substrate after complete sintering.

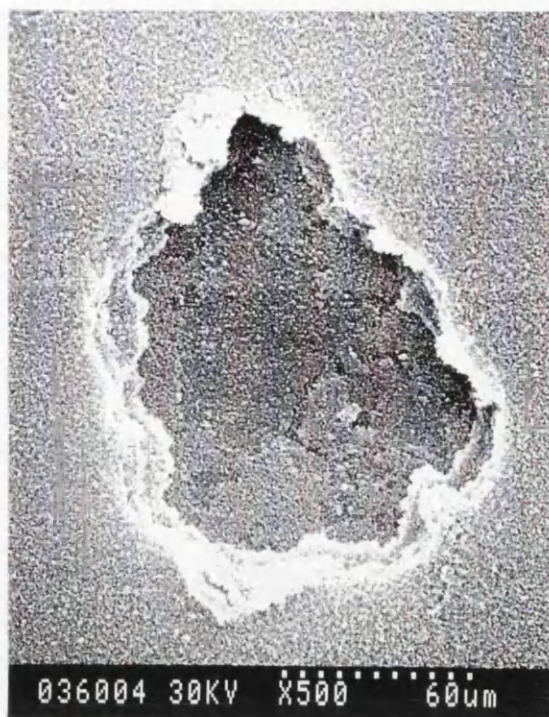


Fig. 3.16 SEM micrograph of void in deposited soot prior to sintering.

Gas trapping has also been experienced, especially in the fabrication of thick films (thicker than $10\ \mu\text{m}$). SEM micrographs of gas bubbles on the surface of a sintered film are shown in Fig. 3.17. The problem can be solved by depositing thinner films or by using as sintering atmosphere a gas, such as He, more permeable than air. Also reducing the heating up gradient of the sintering process, as has been already discussed in paragraph 3.4, helps in obtaining bubble-free films by allowing the trapped gases time to escape from the film in the closed pore state (Sudo '80).

It has been already pointed out that Si substrates require a thick, low-refractive index buffer layer to prevent coupling of the guided light into the highly absorbing substrate. This is obtained by thermally growing a SiO_2 layer by high pressure steam oxidation. The alternative is to deposit the buffer layer by FHD. However, a thin SiO_2 layer is always required because of the poor wettability of the Si substrate during the viscous sintering. In fact, because of the elevated surface tension of the glassy layer during the high temperature sintering process, voids can be experienced in films deposited on unoxidized Si substrates. This effect is visible in the SEM micrographs shown in Fig. 3.18.

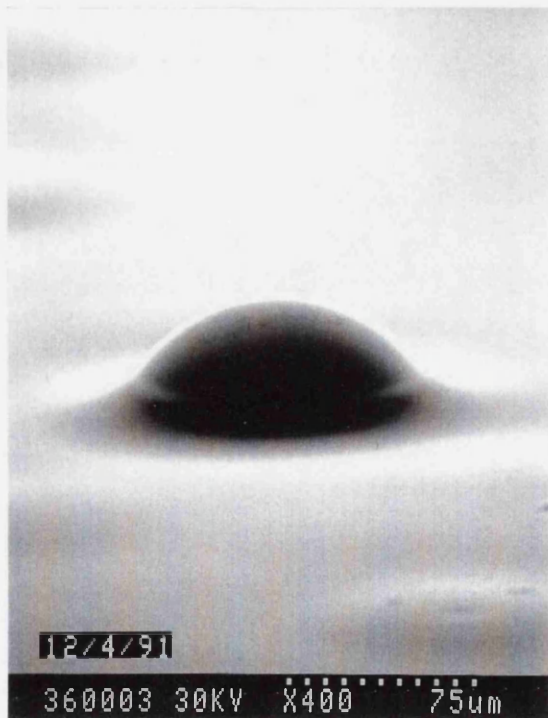
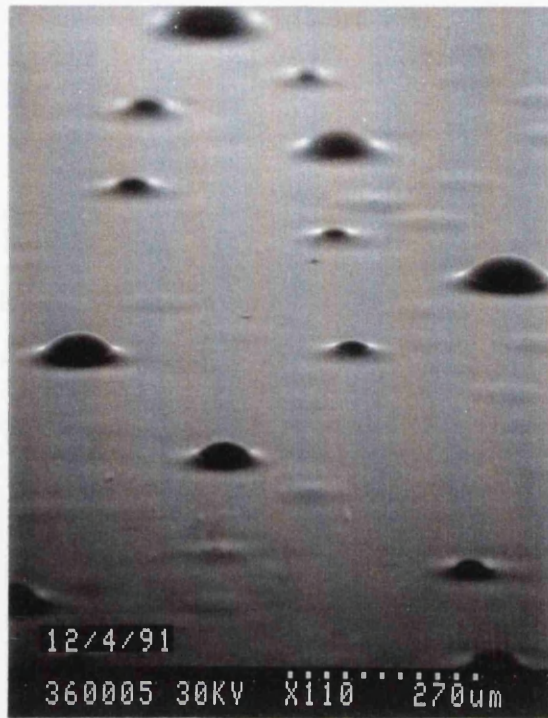


Fig. 3.17 SEM micrographs of gas bubbles on the surface of a sintered film.

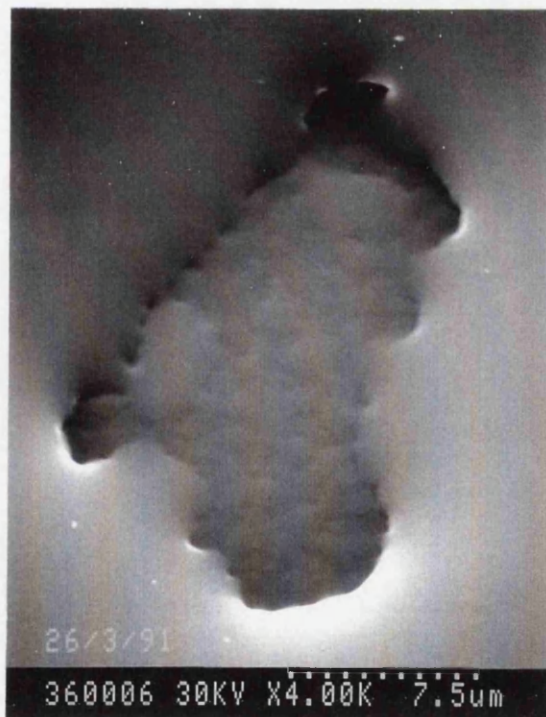
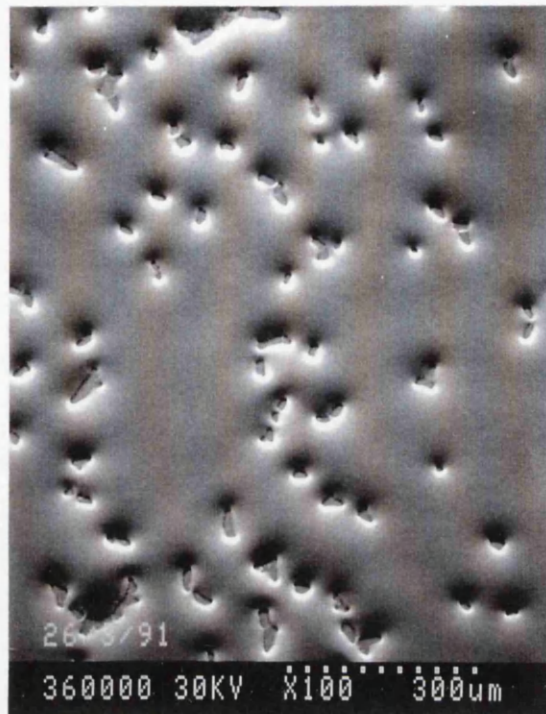


Fig. 3.18 SEM micrographs of voids experienced in sintered films deposited on unoxidized Si substrate.

3.7 Rare earth aerosol doping of SiO₂-P₂O₅ films

Recently there has been a growing interest in the fabrication of integrated optical waveguide lasers and amplifiers. Several techniques have been developed to incorporate rare earth ions in optical fibres (Ainslie '91), which, in principle, could be transferred to planar high-silica waveguides. To date, rare earth doped planar silica waveguides (Hibino '89, Kitagawa '91) have been fabricated by partially sintering the deposited soot and incorporating the rare earth ions into the porous structure using the solution doping technique (Townsend '87) or by introducing the rare earth ions during deposition using vapour phase transport of a rare earth chelate (Tumminelli '91).

The aerosol doping technique, originally developed to fabricate multicomponent glass fibres by VAD or OVD (Sanada '80, Takahashi '82) and rare earth doped silica fibre by MCVD (Morse '91), has been successfully adapted by the author to the planar format, achieving high doping levels of both Nd and Er ions. The aerosol doping technique used has the advantage over solution doping of incorporating the rare earth ions into the glass in a single fabrication step during deposition, thus making redundant the control of the degree of partial sintering and the drying of the sample after immersion, as is the case for solution doping. Moreover, being carried out at microscopic level, the doping promotes an homogeneous distribution of the rare-earth ions, reducing clustering, which increases the scattering losses (Morse '91). Finally, the chemicals used are relatively inexpensive and the delivery system less complex in comparison to the method involving the vapour phase transport of low vapour pressure rare earth chelates (Tumminelli '91).

Although silica has many excellent properties, the solubility of rare earth ions in it is low. The poor solubility can be relieved to some extent by the addition of a few mole % of P₂O₅ or Al₂O₃ (Arai '86). Hence the SiO₂-P₂O₅ glass system discussed in the previous paragraph is highly appropriate for rare earth doping, as it enables the fabrication of low-loss waveguides with high rare-earth ion concentration.

Rare earth ions were incorporated in the low density $\text{SiO}_2\text{-P}_2\text{O}_5$ glass soot by feeding a four port fused quartz torch (Fig. 3.19) with the aerosol of 0.5 molar Nd or Er anhydrous chloride in aqueous solutions. After deposition, sintering of the doped glass soot was carried out following the same process used for the undoped films.

The aerosol was generated by mean of a stainless steel pneumatic atomiser; N_2 gas was used to pressurise the solution and as the aerosol carrier to the torch. The aerosol generator was reproduced from a PVC atomiser for aerosol therapy, and its components are shown in Fig. 3.20. With a N_2 pressure of 1.5 bar, the atomiser was capable of producing a monodispersed distribution of aerosol droplets, the size of which was not influenced by gravitational settling, and enabled convective transport to the torch, without causing accretion along the feeding duct. The aerosol delivery rate was 0.3 ml/min of solution for a N_2 flow rate of 4 l/min. When the aerosol entered the reaction zone, the water evaporated leaving sub-micron particles of rare-earth chloride, which were oxidised in the oxygen rich flame.

Fig. 3.21.1 and 3.21.2 show flames obtained by feeding the four port torch with an aerosol of NaCl , BaCl_2 , NdCl_3 and ErCl_3 water solutions, respectively. Their different colour is a clear indication of the different dopant.

Accurate control of the doping levels can be easily achieved by changing the solution concentration or varying the N_2 flow rate. This can be done even when deposition is in progress, which could allow the fabrication of both active and passive region on the same substrate (Bebbington '92 a). This represents a real advantage over the solution doping technique, in the context of an integrated optical circuit, because it allows the lossy active area of the circuit to be confined only to the laser section. Moreover, vertical selective doping has been demonstrated, which allows the peak doping level to be coincident with the maximum intensity of the waveguide mode (Bebbington '92 b). The aerosol doping technique has been extensively developed in the course of another project in the same Department, and the results will be published elsewhere (Bebbington '92 c).

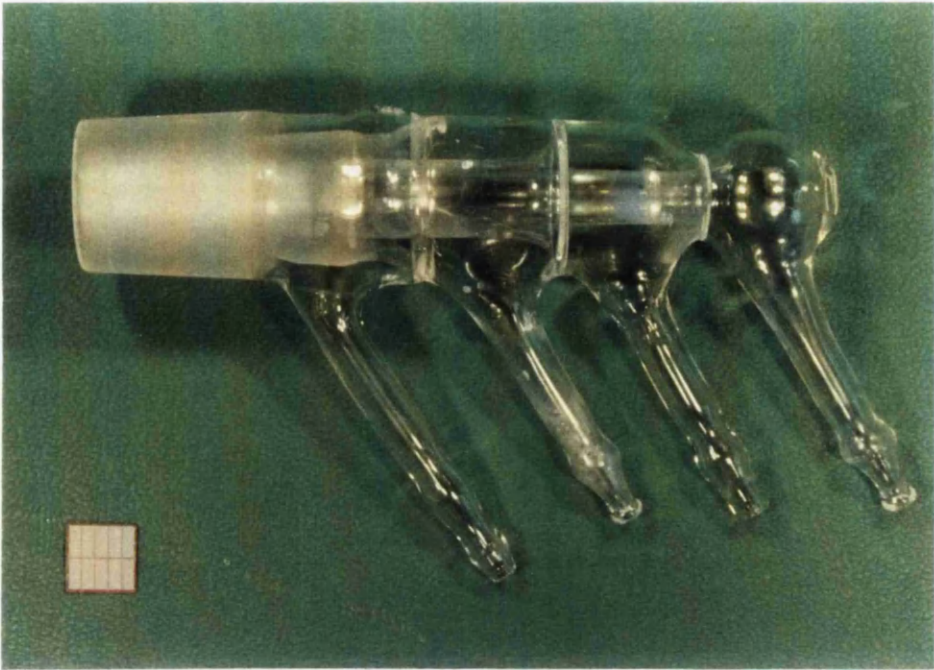


Fig. 3.19 Four-port fused quartz torch employed for aerosol doping.

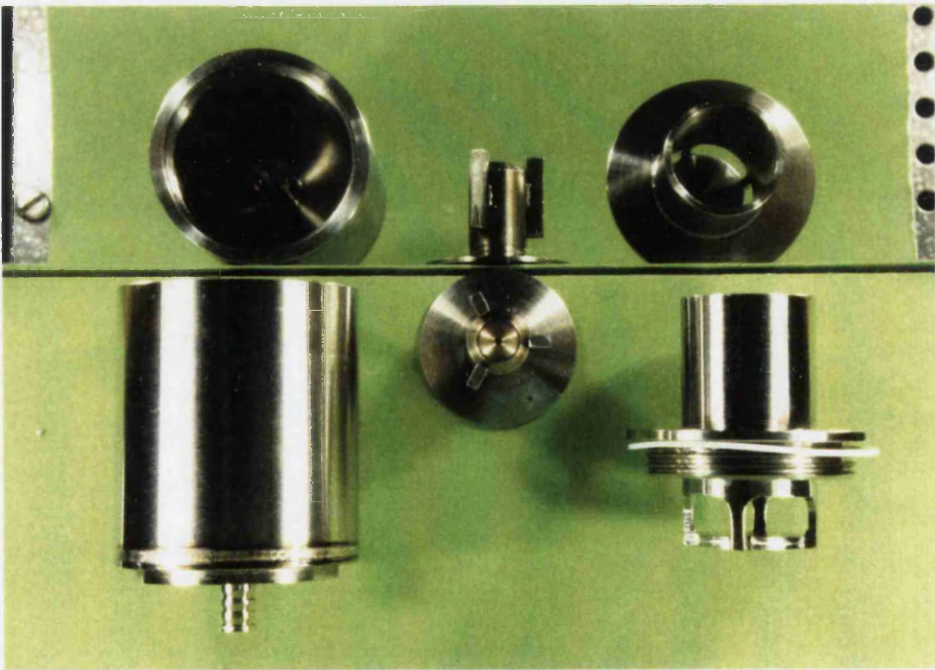


Fig. 3.20 Stainless steel pneumatic atomiser used for aerosol generation.

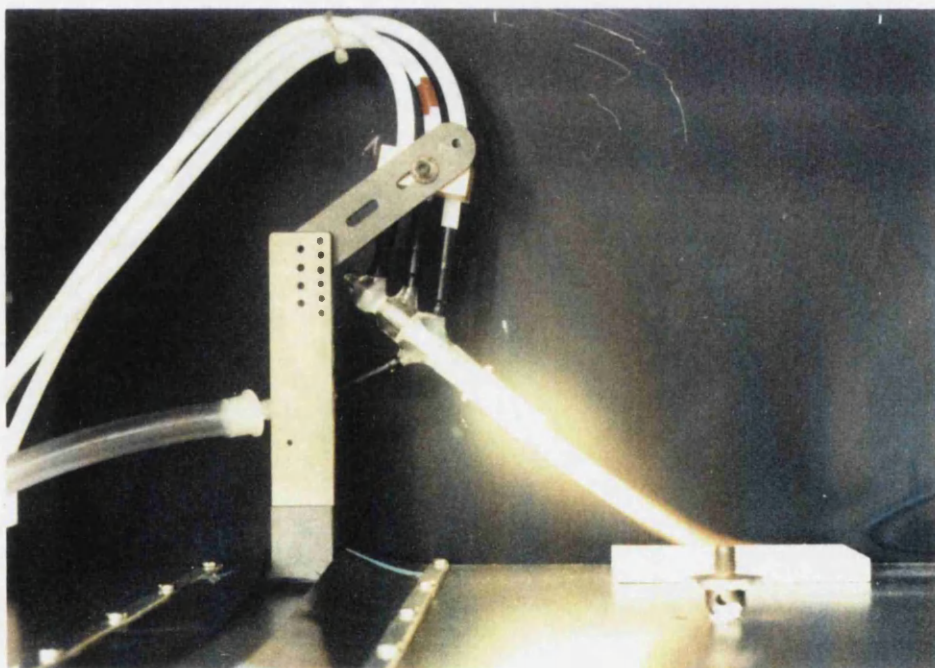
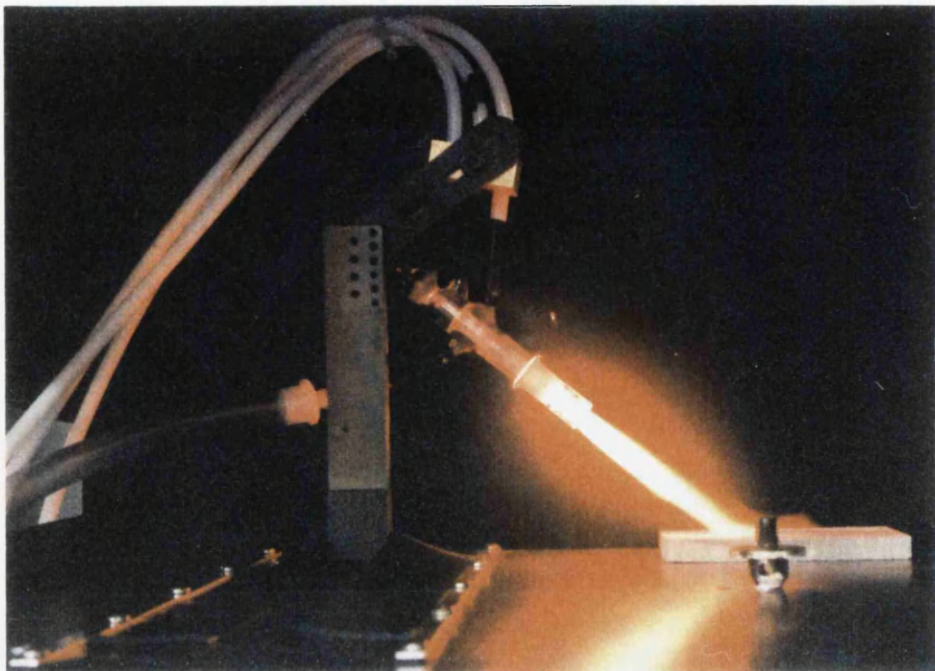


Fig. 3.21.1 Flames obtained by feeding the four port torch with aerosol of NaCl (top) and BaCl₂ (bottom)

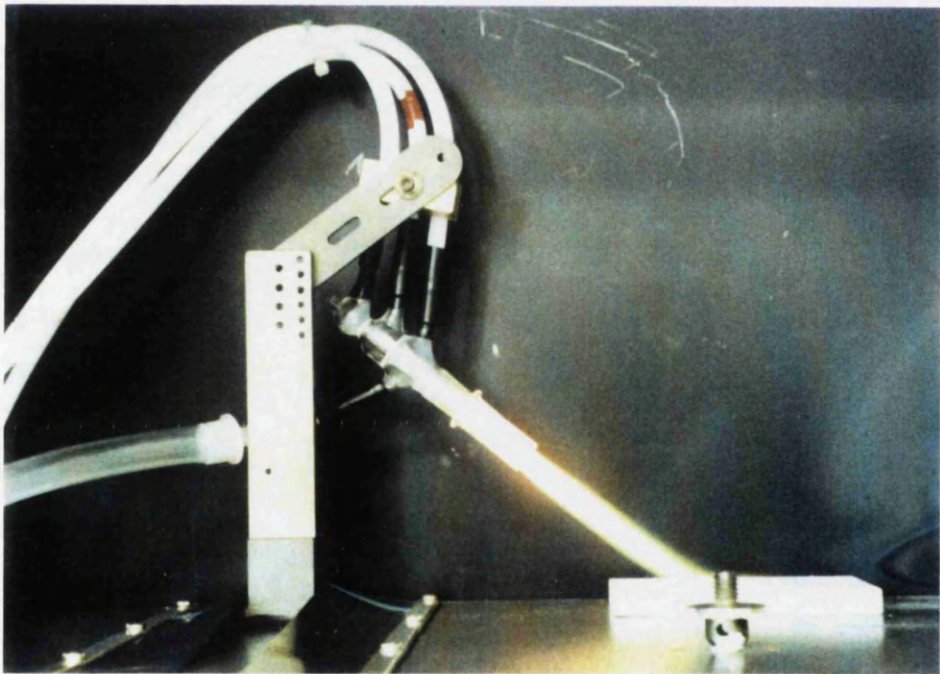
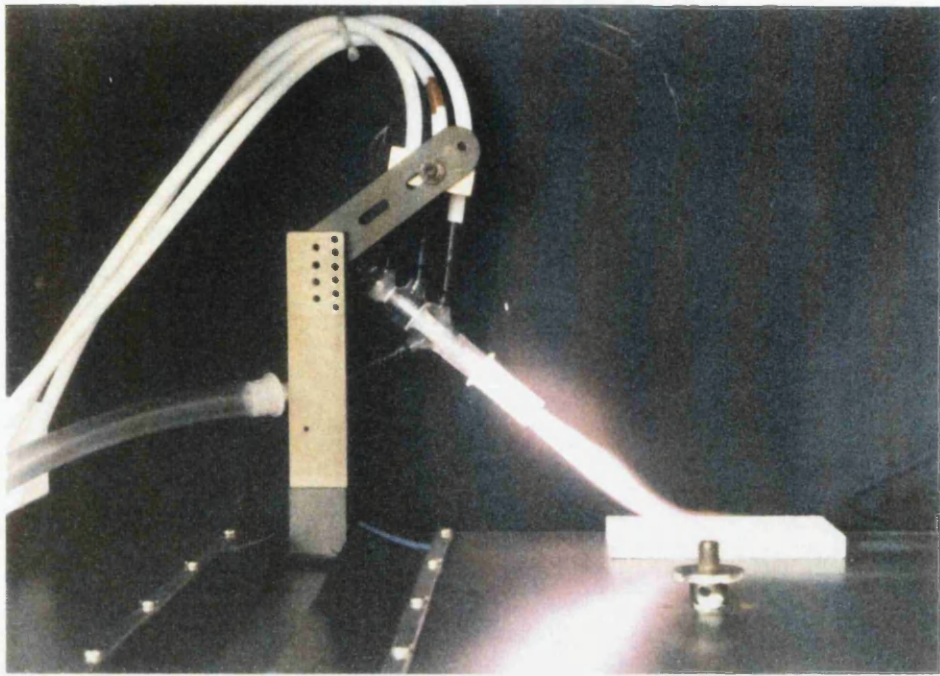


Fig. 3.21.2 Flames obtained by feeding the four port torch with aerosol of NdCl_3 (top) and ErCl_3 (bottom)

3.8 Characterisation of planar waveguide

Characterisation of planar waveguides involves the determination of those parameters which affect the waveguide propagation characteristics. These are the refractive index of the waveguide, its thickness and its attenuation, assuming that the optical parameters of the surrounding media are already known. The waveguide parameters can be measured directly or indirectly. Direct measurement techniques are described in the reference (Nishihara '89). An effective and practical method is to determine the waveguide parameters indirectly from the results of waveguiding characteristics such as propagation constant, guided-mode number and propagation losses. The importance of waveguide characterisation lies in the fact that feedback of the results to the design and fabrication processes enables performance improvements.

In order to evaluate the waveguiding characteristics of a planar film, a guided wave has to be excited. There are several methods of excitation, certainly the prism-coupling method being by far the most widely used. This method is exhaustively discussed elsewhere (Ulrich '73), whilst it is briefly described here. Planar waveguiding theory is well known; the interested reader can consult any book dealing with the matter (e.g. Nishihara '89, Lee '86).

Light waves incident onto the planar face of a waveguide cannot propagate as a guided wave in the waveguide because they belong to the radiation modes of the structure (Tien '77). The prism coupling method employs a high-index prism to excite a guided wave through phase matching between the incident wave and a guided mode (Harris '70). A prism with a refractive index higher than that of the waveguide to be measured is put in close proximity to the waveguide, as is shown in the schematic diagram of Fig. 3.22. If a laser beam strikes the base of the prism at an angle greater than the critical angle, it is reflected by total internal reflection and evanescent fields extend from the base of the prism into the waveguide. When the angle of incidence of the laser beam is such that the horizontal component of the wave vector for the wave in the prism is equal to the propagation constant of one of the guided modes, then the corresponding mode is excited and light is coupled into the waveguide.

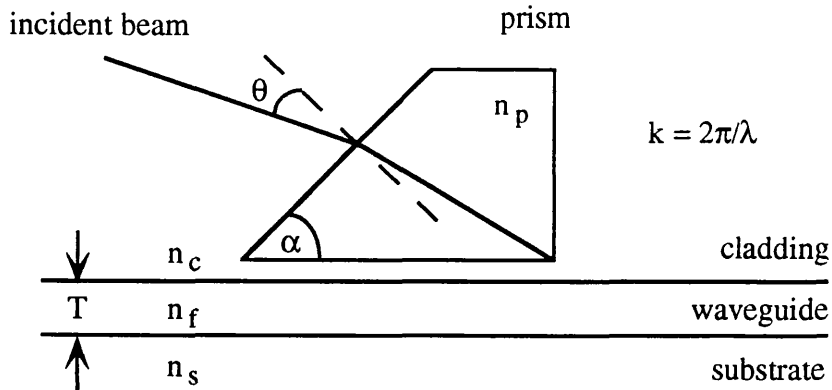


Fig. 3.22 Schematic of prism coupling geometry.

It can be shown (Ulrich '73) that the normalised propagation constant N , or "effective index", of the mode excited at a particular incidence angle is given by

$$N = \beta/k = n_p \sin(\alpha - \sin^{-1}(\sin\theta / n_p))$$

where all the terms are explained in Fig. 3.22. By evaluating the propagation constants for two or more modes is possible to numerically determine the refractive index and the thickness of the film by mean of the dispersion equation of the planar dielectric waveguide (Ulrich '73)

$$kT(n_f^2 - N_m^2)^{1/2} = m\pi + \Phi_s(n_f, N_m) + \Phi_c(n_f, N_m) \quad m = 1, 2, 3...$$

where

$$\Phi_s(n_f, N_m) = \arctan \left[\frac{n_f^2(N_m^2 - n_s^2)}{n_s^2(n_f^2 - N_m^2)} \right]^{1/2}$$

$$\Phi_c(n_f, N_m) = \arctan \left[\frac{n_f^2(N_m^2 - n_c^2)}{n_c^2(n_f^2 - N_m^2)} \right]^{1/2}$$

Initially laser light was coupled into the planar waveguides using a prism coupler made from SF15 Schott glass ($n=1.69425$, 60° included angle) (Schott '90). Because of the easy splintering of this glass, new prisms were designed using a BaK4 Schott glass ($n=1.56670$). This glass has a Knoop hardness coefficient greater by a factor of 100 than the SF15 glass. Because of the lower refractive index a 75° included angle was necessary to achieve the synchronous coupling condition.

The thickness values obtained numerically from prism coupling measurements were compared with the values measured mechanically using the Talystep (from Taylor Hobson, U.K.) on a step produced by etching the films in HF, which notoriously does not etch the Si, and taking in account the SiO_2 buffer layer. The thickness was also evaluated on a step obtained by removing an area of soot from the coated disc using a razor blade and measuring the step after the sample had been sintered as usual. One had to ensure that a sufficient longitudinal length was used during the measurement. This to reach the base of the lip on the unscraped film side caused by the shrinkage occurred during sintering (Fig. 3.23).

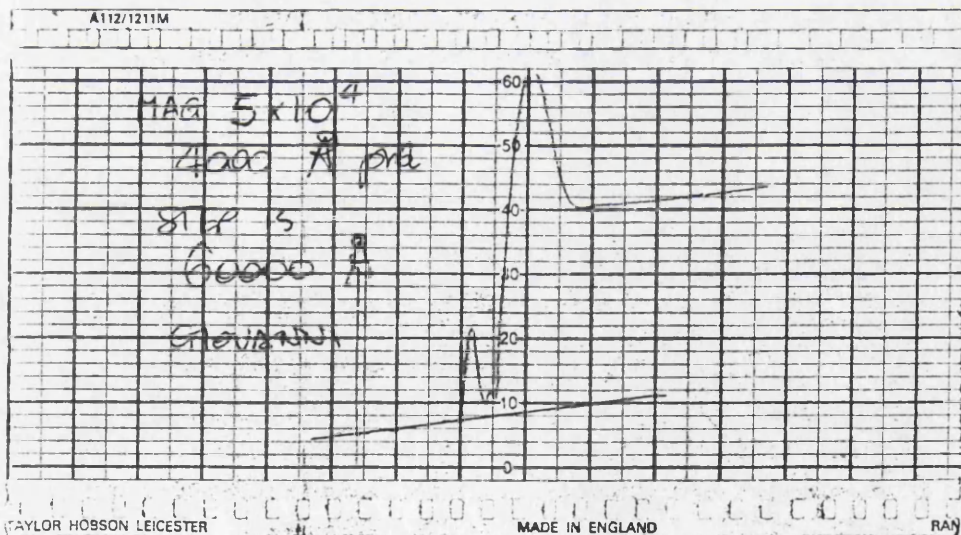


Fig. 3.23 Example of Talystep measurement showing lip at scraped edge.

Moreover care had to be taken to ensure complete removal of the soot from the substrate, otherwise any remaining material would have affected the Talystep result in such a way as to indicate a thinner film than had actually been deposited.

Differences in thickness of max $\pm 4\%$ have been found between the two methods (Table 3.II).

Sample	Prism coupling, μm	Talystep, μm	Difference, %
31-5-1	5.41	5.2	- 3.8
31-5-2	4.87	5.0	+ 2.6
31-5-3	5.81	6.0	+ 3.2
2-6-1	8.49	8.8	+ 3.6
2-6-2	7.48	7.2	- 3.7
2-6-3	5.42	5.2	- 4.0
2-6-4	4.08	4.2	+ 2.9
3-6-1	6.23	6.0	- 3.7

Table 3.II Example of thickness measurements of fabricated films effectuated by prism coupling method and Talystep direct method.

Talystep was also used to evaluate the relation between deposition thickness (after sintering) per traversal and torch traverse speed (starting value) (Fig. 3.24).

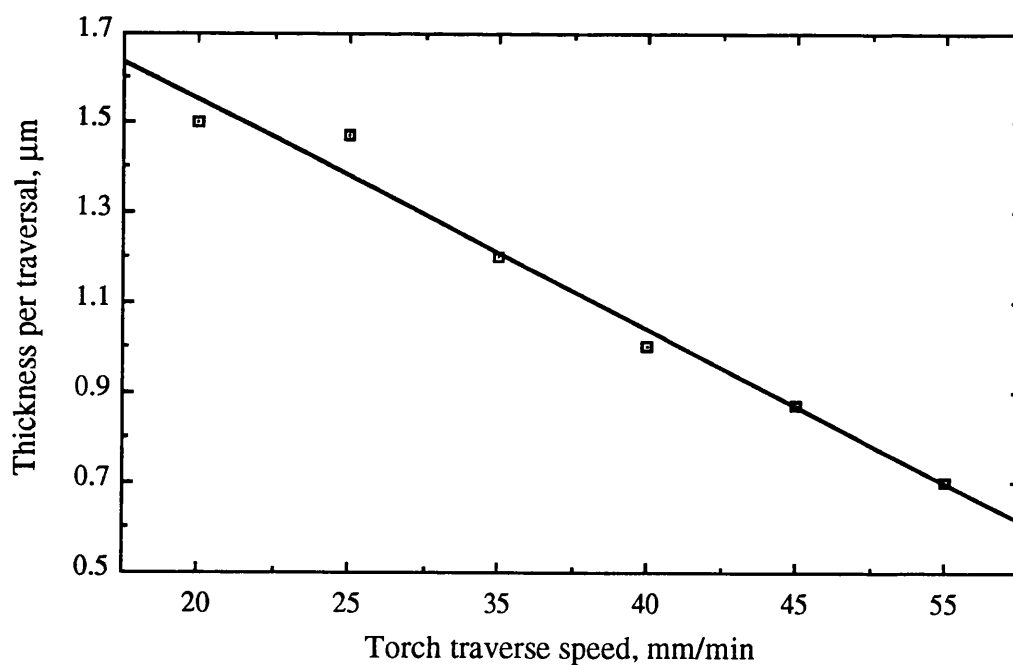


Fig. 3.24 Deposition thickness (after sintering) per traversal versus the torch traverse speed for $\text{SiO}_2\text{-P}_2\text{O}_5$ films (turntable rotation speed 30 rev/min; flow rates: H_2 and O_2 : 4 and 6 l/min; SiCl_4 and PCl_3 : 150 and 160 cm^3/min).

Talystep only was employed to evaluate the thickness uniformity of deposited films. This because the prism coupling method implicitly assumes that the film has a uniform thickness. After removal of the sample from the turntable the deposited soot was scraped with the razor blade along an imaginary line which corresponded during the deposition to the radial direction of the turntable, i.e. the direction of traverse of the torch. Talystep measurements were made at five places (A-E in Table 3.III) along the scored edge. By using a variable traverse speed during the deposition, the best uniformity which could be achieved was better than 7% over a distance of 6 cm across the substrate. Incidentally, the uniformity which could be obtained by using a constant traverse speed for the torch was not better than 13 %.

Sample	A	B	C	D	E	Var. %
2-6-1	9.3	9.0	8.8	8.7	8.7	6.4
2-6-2	7.3	7.3	7.2	7.1	6.8	6.8
2-6-3	5.3	5.2	5.2	5.1	5.0	5.6
2-6-4	4.5	4.3	4.2	4.2	4.2	6.6

Table 3.III Example of Talystep measurements for film thickness uniformity evaluation. All thickness values are in μm .

Thickness measurements were carried out to evaluate the influence on the deposition rate of the torch inclination angle with respect to the turntable. The angle reported in Table 3.IV is that between the torch axis and the turntable plane.

Sample	Torch angle deg	Thickness μm	Comments on film quality
1-5-2	70	6.7	partially sintered
1-5-3	60	6.2	partially sintered
1-5-4	45	5.8	very good
1-5-5	30	4.6	good
1-5-6	20	3.9	poor

Table 3.IV Deposited film thicknesses (after sintering) for various torch inclination angles. Deposition parameters are identical to those cited for Fig. 3.24. The torch traverse speed was 25 mm/min and the number of traversals was 4.

It has to be said that, although higher deposition rate could be achieved for angle greater than 45° , films deposited with 60° and 70° inclination resulted partially sintered and detaching of the film from the substrate could be experienced. This can be explained by an overheating of the deposited soot by the flame, whilst the substrate is kept cooler being in contact with the turntable. This mismatch in temperature could be argued as the cause of poor adhesion of the partially sintered film. The preferred angle at which most of the depositions were carried out was 45° .

The effect of flame temperature on the refractive index of the deposited film has been also investigated. Flame temperatures were measured with an infrared thermometer. From Fig. 3.25 it can be evinced that higher temperature flame causes the refractive index to decrease. This may be attributed to the fact that the saturated vapour pressure of both silica dopants used, P_2O_5 and GeO_2 , increases with temperature. Therefore the amount of oxide retained in the vapour phase stream (which is extracted through the exhaust aperture), increases with the flame temperature, whilst the amount of solid oxide deposited decreases. This flame temperature effect has been already observed in fibre preform fabrication by VAD (Izawa '87).

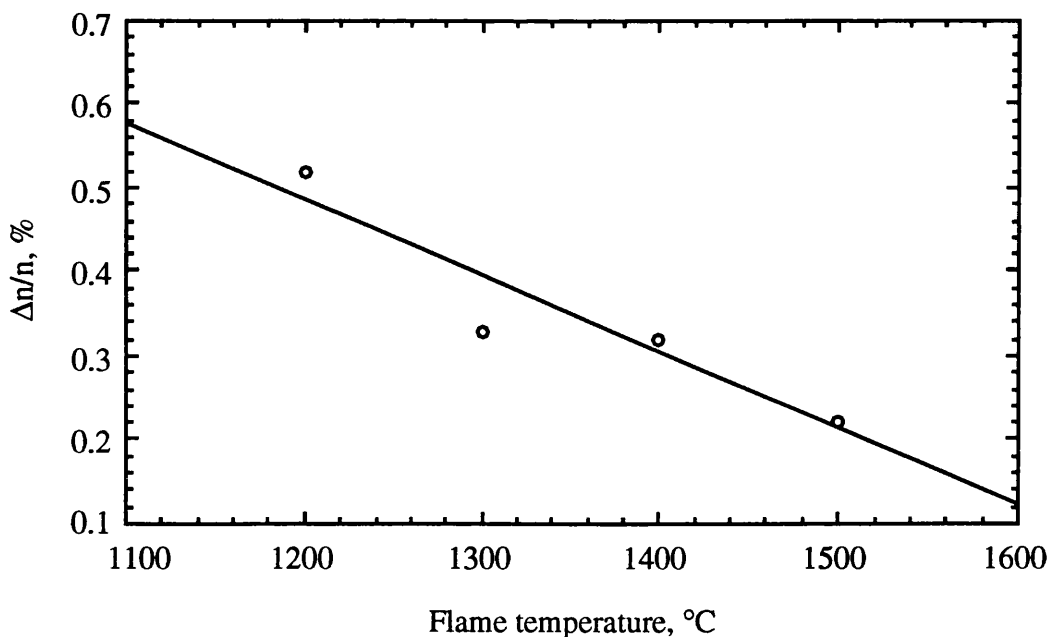


Fig. 3.25 Flame temperature dependence of refractive index change for $SiO_2-P_2O_5-GeO_2$ films.

For a multimode waveguide where many measured effective index values are available, approximate calculation based on the inverse WKB method (White '76) enables the determination of the refractive index profile of the waveguide. An example of refractive index plot is shown in Fig. 3.26, where a step index profile fits well the Δn values obtained by using such a method for waveguides fabricated by FHD (Loni '90).

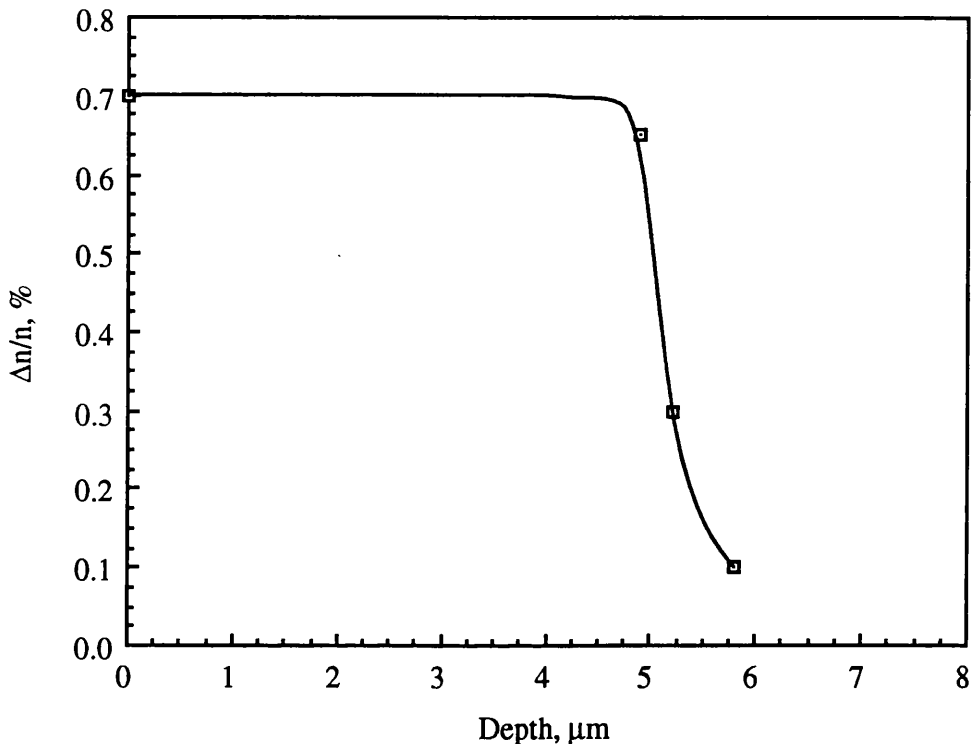


Fig. 3.26 Refractive index change profile obtained using the inverse WKB method. The solid line is a smoothly fitting curve to measured values.

The refractive index dispersion of the fabricated waveguides has been evaluated using the prism coupler method. In Fig. 3.27 (a) the wavelength dispersion of $\text{SiO}_2\text{-P}_2\text{O}_5$ waveguides is shown for samples having 8 and 9 (wt. %) of P_2O_5 (concentrations were determined by Energy Dispersive X-ray Analysis). In Fig. 3.27 (b) the wavelength dispersion of $\text{SiO}_2\text{-P}_2\text{O}_5\text{-GeO}_2$ waveguides is shown for samples fabricated with a GeCl_4 flow rate of 50 and 70 cm^3/min . The measurements have been performed at the following wavelengths: 0.633 and 1.150 μm (He-Ne), 0.800 and 0.930 μm (Ti-Sapphire), 1.066 and 1.320 μm (Nd-YAG). Fig. 3.27 (a) evidences a clear similarity between the dispersion curve of $\text{SiO}_2\text{-P}_2\text{O}_5$ waveguides and that of fused silica (Malitson '65) also shown for

comparison, whilst this similarity is less evident in Fig. 3.27 (b) for $\text{SiO}_2\text{-P}_2\text{O}_5\text{-GeO}_2$ waveguides.

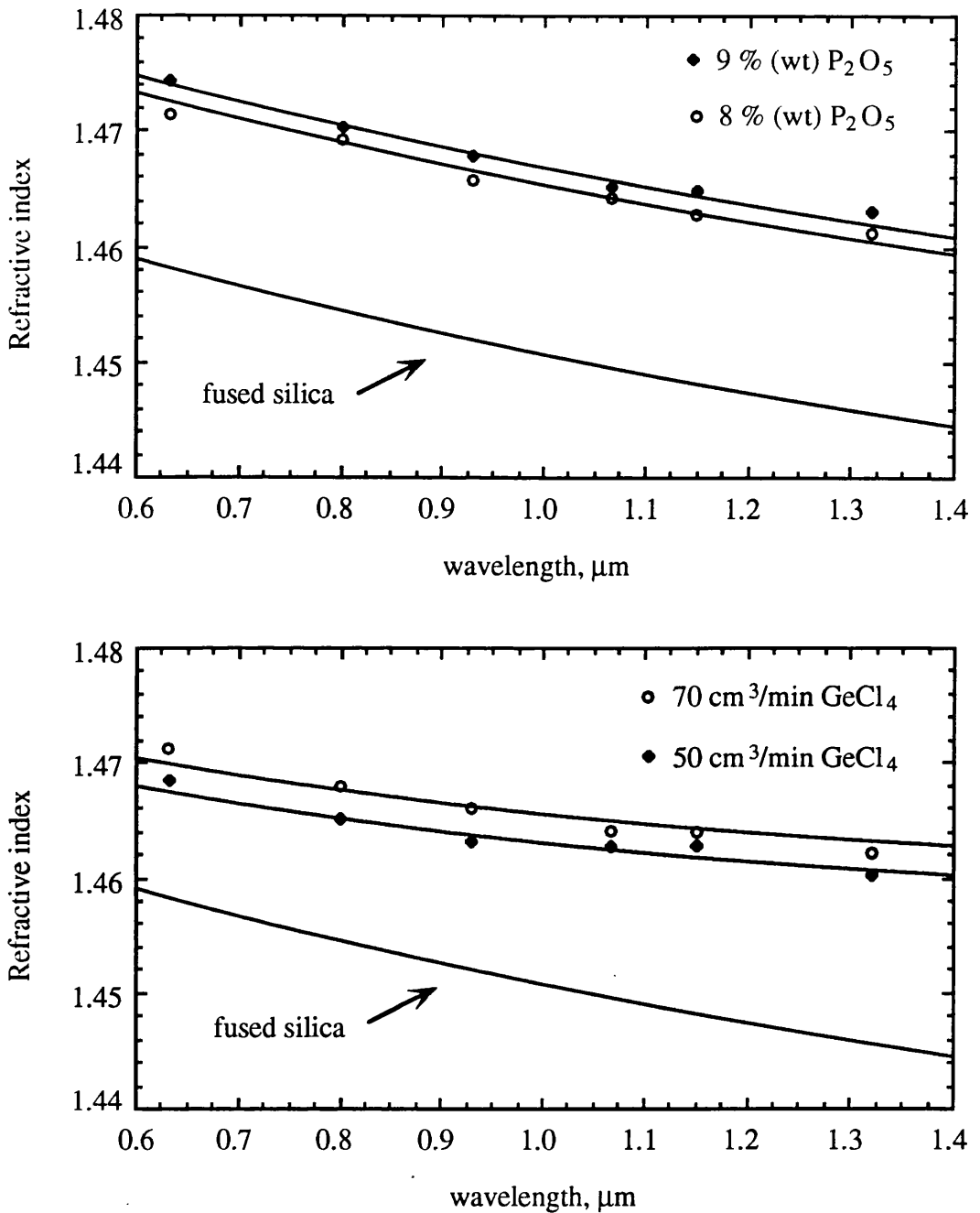


Fig. 3.27 (a, top): refractive index dispersion with wavelength of P_2O_5 -doped silica waveguides for different P_2O_5 (wt %) concentrations; (b, bottom): refractive index dispersion with wavelength of $\text{GeO}_2\text{-P}_2\text{O}_5$ -doped silica waveguides fabricated with different GeCl_4 flow rates. The dispersion curve for pure fused silica is also shown for comparison (Malitson '65). The curves are based on measurements at 0.633, 0.8, 0.93, 1.066, 1.15 and 1.32 μm .

All the passive waveguides fabricated, P_2O_5 or $GeO_2-P_2O_5$ doped, did not show out of plane scattering when visible laser light was coupled in. On the other hand, rare-earth doped waveguides were very lossy and scattered light out from the plane of propagation. The difference is clearly visible in the photographs shown in Fig. 3.28. By taking a photograph of the passive $SiO_2-P_2O_5$ waveguide, the light line of the excited mode shining on a screen (visible on the left of the waveguide) has been included in the picture, to prove that the He-Ne laser light is really travelling in the waveguide.

Propagation loss of planar waveguides is one of the most important parameters for the evaluation of their utility for integrated optical circuits. Three non-destructive techniques have been used by the author: the three prism technique (Won '80), the mercury drop technique (Jackel '84) and the fibre probe technique (Nourshargh '85 a).

a) Three prism technique

The three prism technique involves a fixed prism coupling light into the waveguide. A second movable prism couples out a certain amount of the guided light at different positions along the waveguide. A third fixed prism couples out a certain amount of the remaining guided light after the second prism. The experimental set-up prepared by the author is shown in Fig. 3.29. In Fig. 3.30 the three prisms positions on a 3" Si wafer are shown. The input prism is the rightmost.

It is necessary to calibrate the system before any measurement. The calibration involves measuring the output power P_3^0 from the third prism when no power is coupled out by the second prism. Then for each position of the second prism the out-coupled power from the second and third prism, $P_2(z)$ and $P_3(z)$ respectively, and the separation between the second and third prism, are measured. It can be shown that the power of the guided light at a certain position z along the waveguide is equal to the following ratio

$$P(z) = \frac{P_2(z)P_3^0}{(P_3^0 - P_3(z))}$$

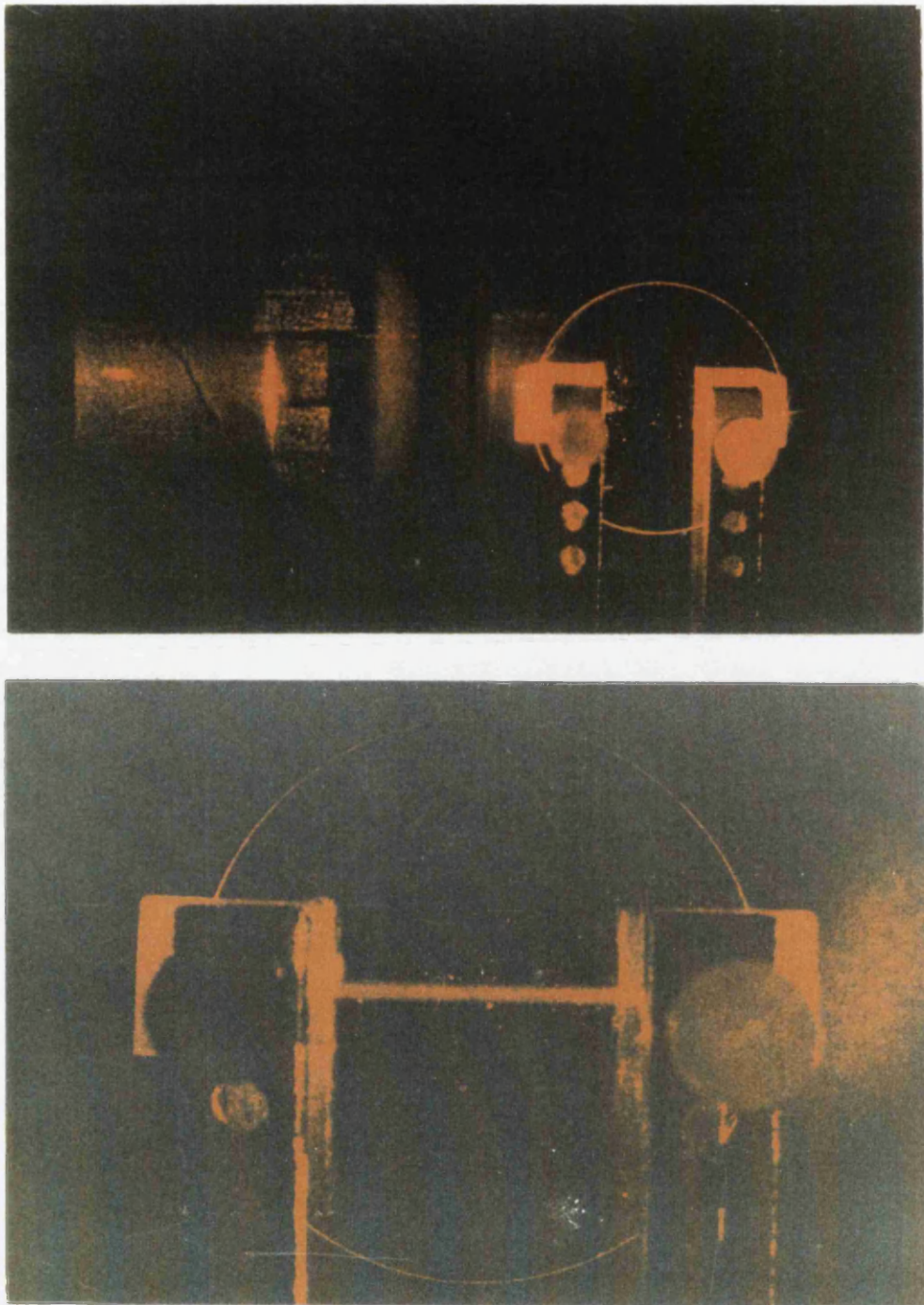


Fig. 3.28 Photographs of He-Ne ($0.6328 \mu\text{m}$) light coupling in passive (top) and rare-earth doped (bottom) $\text{SiO}_2\text{-P}_2\text{O}_5$ waveguides. By taking the photograph of the passive waveguide (top) the light line of the excited mode shining on a screen (visible on the left side of the photo) has been included, to prove that the He-Ne laser light is really travelling into the waveguide. On the other hand, the rare-earth doped waveguide (bottom) was very lossy and scattered light out of the plane of propagation.

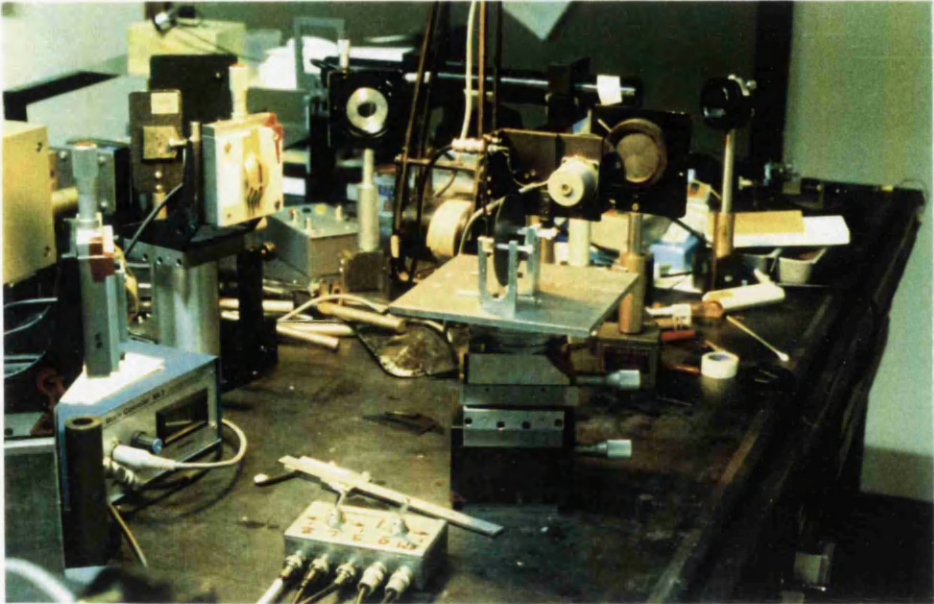


Fig. 3.29 Experimental set-up prepared by the author for loss measurement of planar waveguides by the three-prism technique.

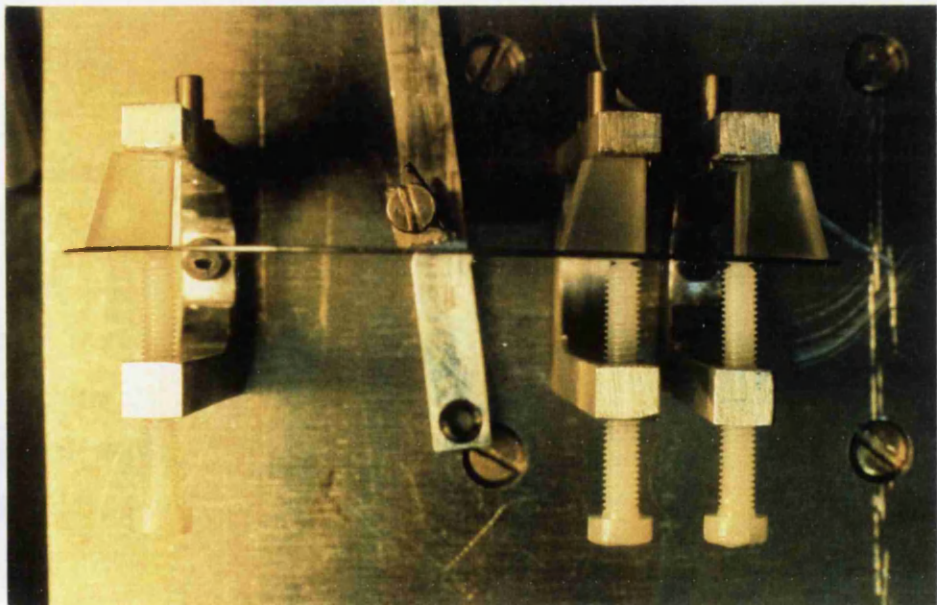


Fig. 3.30 Positions of the three prisms on a 3" Si wafer for loss measurement. The input prism is the rightmost.

that is independent on the outcoupling efficiency of the movable prism. However the experimental error will be minimal if the outcoupling efficiency of the movable prism is 50% (Won '80).

Some precautions have to be taken during the measurements. This technique works if the first and third prism are fixed, i.e. their position and coupling efficiency are, for each position of the movable prism, rigorously the same. Consequently care must be taken to ensure that during the measurement, both first and third prism are not affected in anyway. For this reason, the respective clampers were connected to the rotating plate which was blocked at the coupling angle.

It is good practice to check, after each displacement of the second prism, that the power coupled out by the third prism is always equal to the calibration value. A small metal mirror was necessary to deflect the light coupled out by the second prism, which otherwise would have been shadowed by the third prism. A calliper with a 0.02 mm resolution was used to measure the progressive separation. Lock-in technique was used for power measurement. Loss measurements were performed only on 3" wafers, as smaller substrates did not allow sufficient experimental data due to the size of the prisms.

Losses of 4 μm thick P_2O_5 and $\text{GeO}_2\text{-P}_2\text{O}_5$ -doped silica waveguides (Δn % of 1 and 0.8, respectively) were measured at the wavelengths of 0.633 and 1.32 μm (Fig. 3.31). The scattering in the measured values can be imputed to small changes in coupling efficiency caused by touching the prisms with the calliper and moving the substrate during the reclamping of the movable prism. Least squares fit to the experimental data gave for the P_2O_5 -doped waveguides losses of 0.08 and 0.05 dB/cm and for the $\text{GeO}_2\text{-P}_2\text{O}_5$ -doped waveguides losses of 0.07 and 0.06 dB/cm at 0.633 and 1.32 μm , respectively. Lower loss figures should be expected at longer wavelengths.

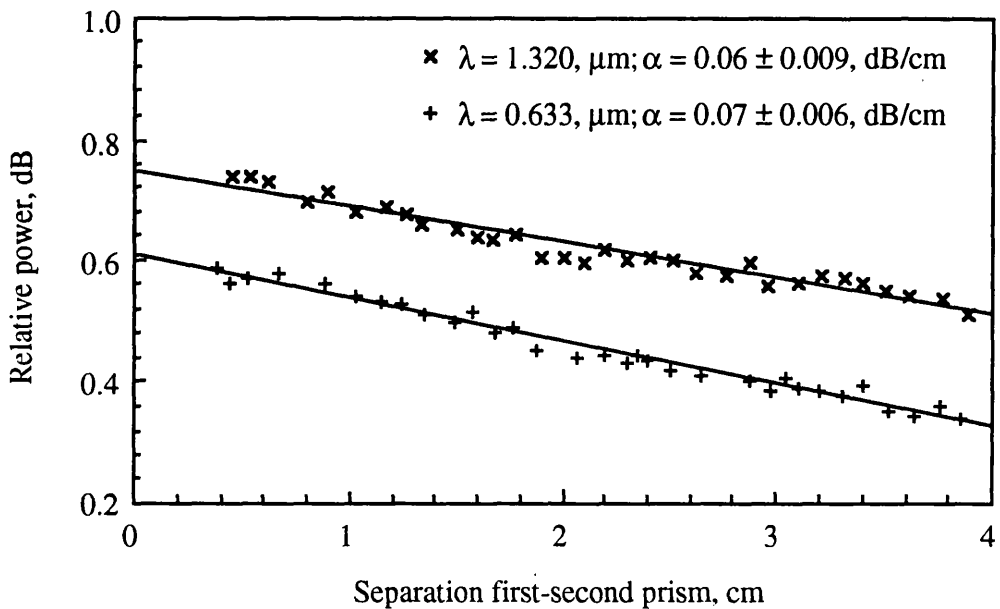
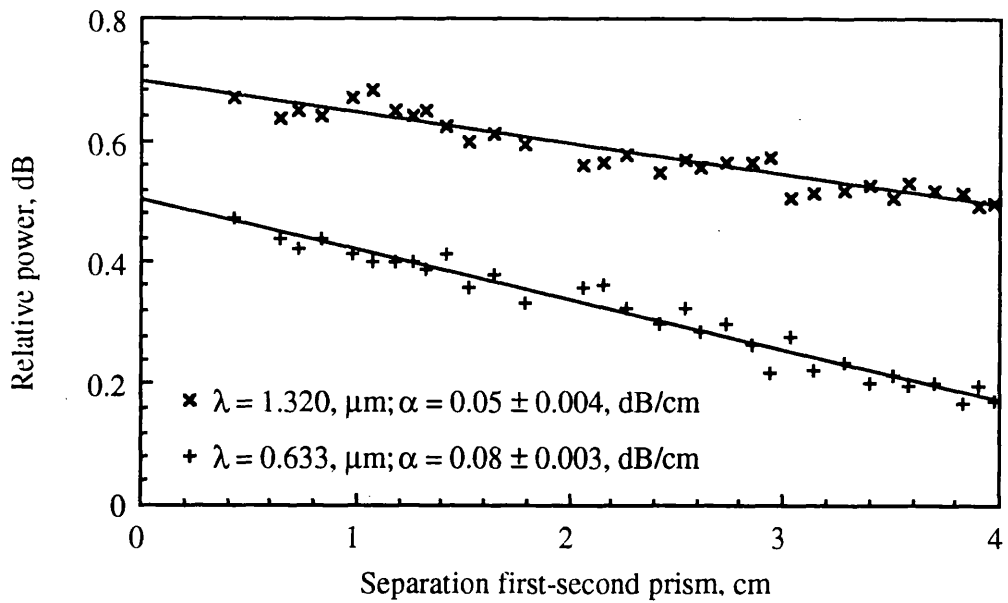


Fig. 3.31 Loss measurements at two different wavelengths for a P_2O_5 -doped (top) and GeO_2 - P_2O_5 -doped (bottom) silica planar waveguide obtained by using the three-prism method. The lines represent least-squares fits to the data.

b) Mercury drop technique

This technique involves temperature measurements. The experimental set-up prepared by the author is shown in Fig. 3.32. The measurement device, which is shown in Fig. 3.33, consists of a Perspex™ fixture containing a mercury reservoir and a small channel through which the mercury can be forced using the nylon screw on the top. A 0.025 mm ϕ chromel-constantan (E type) thermocouple is placed at the centre of this channel, so to be immersed in the mercury. The thermocouple wires were coated with a plastic paint to prevent short circuit in the mercury. The E type thermocouple was chosen because it has the highest sensitivity. The Perspex™ fixture was mounted on a micropositioner to easily control the distance from the waveguide and the position respect to the guided light.

When the mercury drop protruding from the hole is placed in contact with the waveguide, a portion of the light travelling under it is absorbed. Then the mercury is heated and the thermocouple measures the rise in temperature which is very small. Therefore lock-in detection is needed. The chopping rate is limited by the thermal response of the mercury. It can be shown that for the mercury, the characteristic depth for heat penetration is about 0.5 mm at 5 Hz (Jackel '84). Consequently, using a 1 mm diameter drop, a chopping rate of 5 Hz, or less, is necessary to make sure that the thermocouple is within a penetration depth at any point of the drop.

Mercury is chosen for different reasons. Because it is liquid, it can touch the waveguide without scratching it. Because it does not wet the surface of the waveguide, the contact area can be easily controlled by adjusting pressure and position. Because it is a metal, it absorbs the guided light and transmits the resulting temperature increase to the thermocouple.

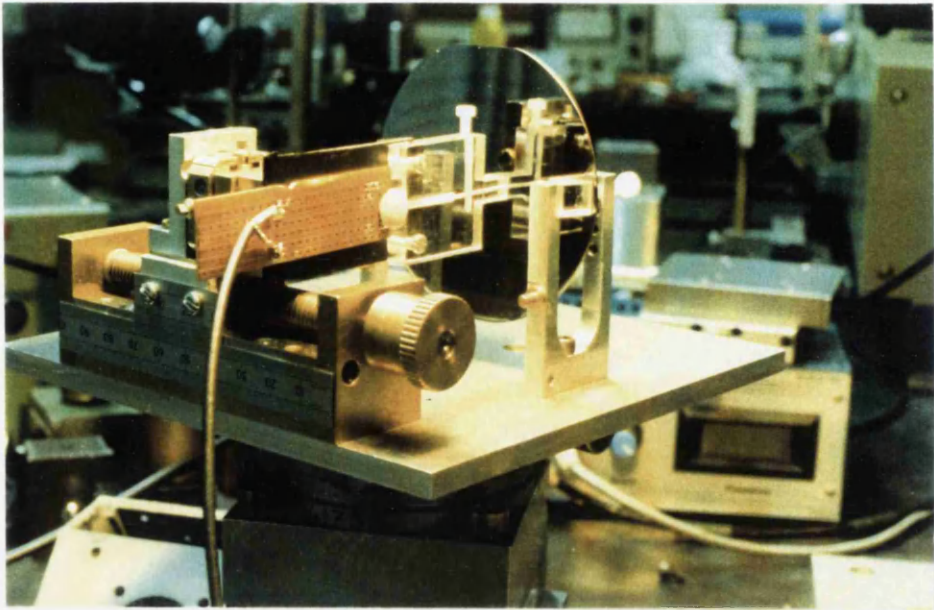


Fig. 3.32 Mercury drop technique set-up prepared by the author for loss measurements of planar waveguides.

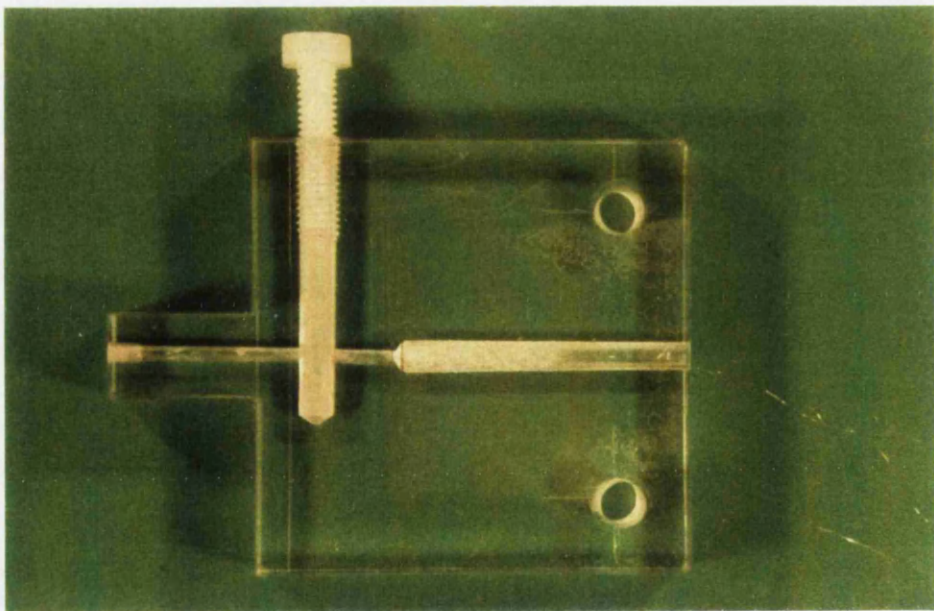


Fig. 3.33 Perspex™ fixture for mercury drop loss measurement technique.

Measurements were carried out using a reference junction at 0 °C. During the measurements it was necessary to maximise the signal by moving the mercury drop perpendicularly to the direction of propagation. However the thermal signal obtained using a 4.8 mW He-Ne laser was very low and unstable. Data measured were much too uncorrelated to give meaningful results. This may be due to various reasons such as the low power of the laser used, the loss of the waveguides examined which was expected to be low, cumulative effect in the temperature build up of the waveguide, the difficulty in maximising the signal along the propagation direction.

c) Fibre probe technique

This technique measures the variation of scattered light with length for the waveguide. A plastic fibre with a core diameter of 1 mm and $NA = 0.47$ is connected to a photodetector whose output goes to a chart recorder. The other end of the fibre is polished flat and it is mounted on a xyz positioning stage by mean of an aluminium holder. The experimental set-up prepared by the author is shown in Fig. 3.34.

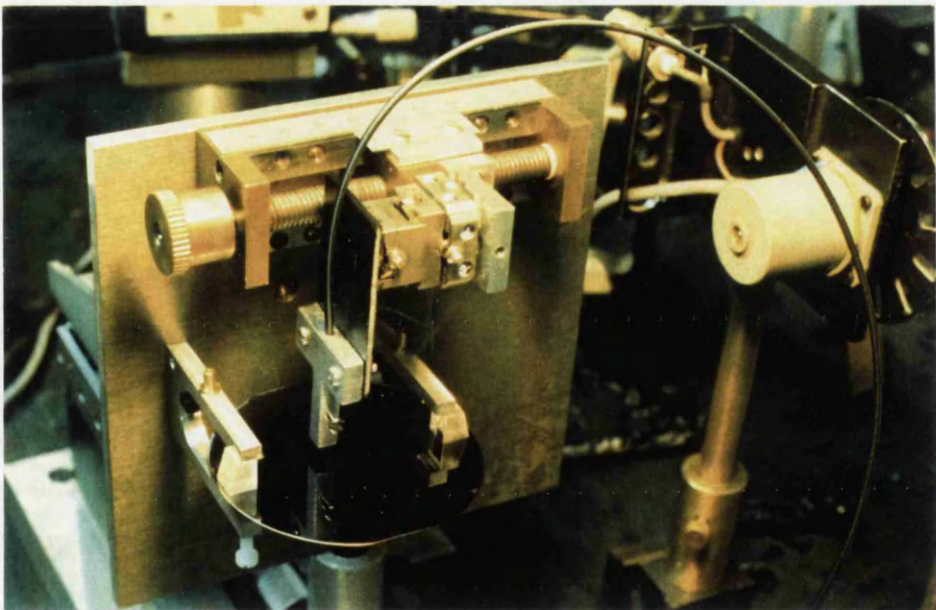


Fig. 3.34 Fibre probe technique apparatus prepared by the author for loss measurements of planar waveguides.

The fibre end is positioned at about 2 mm from the surface of the waveguide and parallel to it. The fibre end is scanned across the width of the guided light until a maximum intensity reading is obtained. The chart recorder is then switched on and the fibre end is moved towards the waveguide by small increments. Decreasing the separation between the fibre and the waveguide the recorded signal becomes larger. A significant rise is observed as soon as contact is made between the fibre and the waveguide. The fibre is then slowly withdrawn. By repeating the measurement at different points along the waveguide one can obtain the attenuation by plotting the relative scattered power versus the length.

This technique revealed itself to be inadequate for loss measurement of our low-loss passive waveguides. The apparent absence in the passive waveguides examined of out-of-plane scattering was probably the reason for the lack of consistency in the measured data.

The loss measurement techniques which have been described, are time consuming as they require point by point measurements and the accuracy increases by increasing the number of measurement points. They are also very sensitive to experimental errors. Moreover, all of them implicitly assume that there are no isolated scattering centres along the interested guiding region of the planar waveguide and that measuring conditions are identical for each measurement point. It is believed by the author that only reflectometric techniques are adequate in giving consistent figures for low loss optical waveguides (e.g. Takada '90). However, the implementation of these techniques is rather complicated and goes beyond the aim of this thesis. The three prism technique was by far the most used by the author for loss measurements of passive waveguides. The set-ups prepared by the author were used in the course of another project undertaken in the same Department, for loss measurements of lossy rare-earth doped waveguides (Bebbington '92 b).

Chapter 4. Channel waveguide fabrication

Chapter Layout

- 4.1 Introduction
- 4.2 Photolithography
- 4.3 Reactive ion etching
- 4.4 Investigation into the optical damage threshold of $\text{SiO}_2\text{-P}_2\text{O}_5$ and $\text{SiO}_2\text{-GeO}_2\text{-P}_2\text{O}_5$ channel waveguides
 - 4.4.1 Optical damage in silica based waveguides
 - 4.4.2 Experimental
 - 4.4.3 Results and discussion
- 4.5 Summary

4.1 Introduction

Functional PLCs include waveguides which confine light in two dimensions, called in a wide sense 'channel waveguides'. In this chapter the microfabrication techniques involved in the definition of channel waveguides will be taken into consideration. High-silica content planar waveguides fabricated by FHD can be patterned in a channel waveguide circuit by mean of lithographic processes and etching techniques. We have used a combination of photolithography and reactive ion etching (RIE) to fabricate channel waveguides. The photolithographic practice will be described in its various stages and the RIE process parameters, which allow one to obtain channel waveguides with smooth and vertical walls, will be summarised.

Finally, we will present an investigation of the optical damage threshold in P_2O_5 -doped and GeO_2 - P_2O_5 -doped silica channel waveguides. The damage threshold levels obtained will be presented and discussed, emphasising the difference in power handling capability between the two different doped silica systems considered.

4.2 Photolithography

Photolithography is the patterning process of a photosensitive polymer by mean of ultraviolet light. It has been developed for the microelectronics industry and it has been adopted in IO for the definition of optical circuits. The two patterning processes mainly used by the author are schematised in Fig. 4.1. Comprehensive details on photolithography can be found in any book on microelectronic fabrication technology (e.g. Sze '83). Here we will briefly describe the processes adopted and report the physical parameters involved, which are listed in Table 4.I and II.

A photosensitive polymer (photoresist) film is applied to the planar waveguide to be patterned, dried, and then exposed to ultraviolet light through a photomask in which the proper geometrical patterns are defined. After exposure, the sample is soaked in a solution that develops the images in the photoresist. Depending on the type of photoresist used, positive or negative, exposed or non exposed areas of photoresist are removed in the developing process.

Once the pattern has been defined in the photoresist, it can be transferred to the planar waveguide through etching techniques by mean of two methods. In the first or direct method the photoresist pattern is used as a protective pattern and unmasked portions of the waveguides are removed by etching. In the second method or "lift-off", an appropriate metal mask is deposited on top of the photoresist and unmasked waveguide areas. The photoresist is then removed, taking with it the metal layer on its top. This leaves the remaining metal mask on the waveguide surface, and the unmasked areas, which were previously covered by photoresist, are removed by etching. The second method is called lift-off since the metal is lifted off with the photoresist.

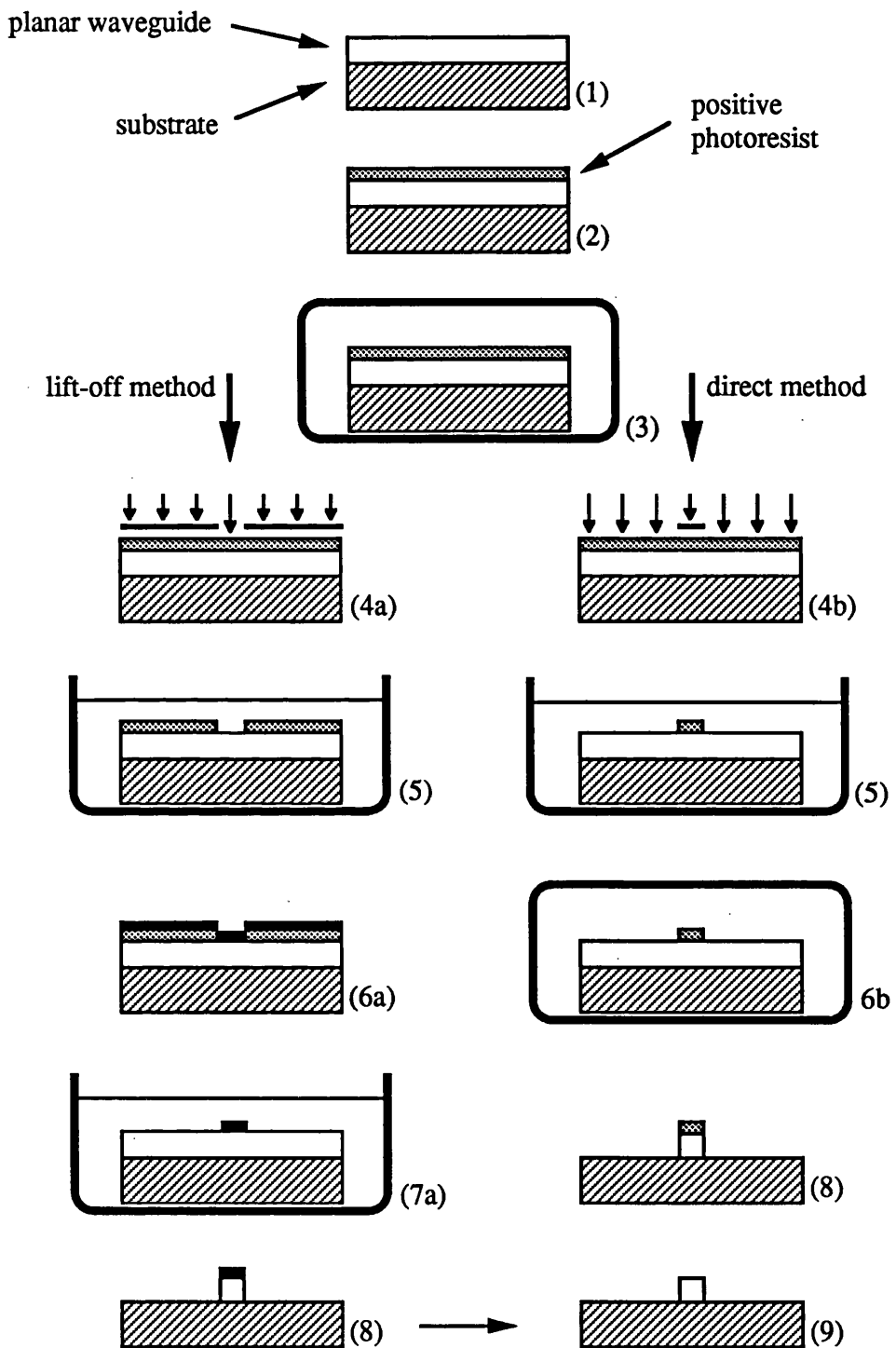


Fig. 4.1. Photolithographic and etching steps to fabricate channel waveguides; lift-off method (left) and direct method (right): 1) Sample cleaning; 2) Photoresist spinning; 3) Photoresist prebaking; 4) Photoresist UV exposure through a) dark-field mask or b) light-field mask; 5) Photoresist developing; 6a) Metal evaporation; 6b) Photoresist hard baking; 7a) Lift-off; 8) Etching; 9) Removal of metal or photoresist mask

Resist primer	Hexamethyldisilazine
Primer spin	4000 rpm - 60 sec
Photoresist	Shipley™ 1400 - 31 (positive) *
Photoresist spin	4000 rpm - 30 sec
Prebake	90 °C - 30 mins
Exposure time	6 sec (HTG mask aligner) or 5 mins (contact printer)
Developer	Microposit™ : deionized water (1:1)
Developing time	75 sec
Postbake	120 °C - 20 mins

Table 4.I Typical positive photoresist patterning parameters for direct method.
(* Technical data from Hoechst U.K. Ltd., Electronics Products Division).

Resist primer	Hexamethyldisilazine
Primer spin	4000 rpm - 60 sec
Photoresist	Shipley™ 1400 - 31 (positive) *
Photoresist spin	3500 rpm - 20 sec
1st Prebake	90 °C - 15 mins
Soaking	Chlorobenzene - 15 mins
2nd Prebake	90 °C - 15 mins
Exposure time	7 sec (mask aligner) or 8 mins (contact printer)
Developer	Microposit™ : deionized water (1:1)
Developing time	90 sec
Metal evaporation	Aluminium - 0.05 µm
Lift-off	Acetone - 4 hours

Table 4.II Typical positive photoresist patterning parameters for lift-off method.

Masks can be light-field, in which the desired pattern is defined by the optically opaque areas, or dark-field, in which the pattern is defined by the transparent areas. The choice of the mask depends on the pattern transfer method and resist type to be used. The four possibilities are summarised in Table 4.III. The combination mainly used by the author has been that of positive photoresist and light-field mask. Although this combination limits the depth obtainable by dry etching techniques, as will be described in the following paragraph, it is certainly the quickest as it involves the minimum number of steps.

Method	Positive photoresist	Negative photoresist
Direct	<i>light-field mask</i>	dark-field mask
Lift-off	<i>dark-field mask</i>	light-field mask

Table 4.III Possible combinations of photoresist, mask and transfer method; the two combinations mainly used by the author are in italic.

Sample preparation prior to coating with photoresist plays an important role in determining the quality of the photolithography. In fact any residue of grease or inorganic particulate, can affect the adhesion of the photoresist and lead to uneven contact between the mask and the photoresist surface. For this purpose the procedure adopted prior to depositing the oxide soot by FHD, already explained in the previous chapter, was followed.

The printing has always been of the contact type. In the lift-off method, prior to metal coating by evaporation, it was found effective to carry out an O₂ RIE for 1 minute to improve adhesion of the metal to the unmasked areas. The O₂ RIE in fact, partially removes the photoresist pattern revealed but also traces of photoresist which may have been left by uncompleted developing.

After etching the photoresist or metal masking can be removed to leave the etched pattern behind. The kind of photoresist used is easily removed by acetone in ultrasonic bath. However, sometime this technique revealed itself to be

insufficient. In that case the following specific acid cleaning procedure was adopted:

- 1 Wear plastic apron, plastic gloves and safety glasses
- 2 Prepare in two separate beakers the necessary quantities of H_2O_2 and H_2SO_4 for a 1:5 solution such that the sample can be completely immersed in it, and in a third beaker deionized water
- 3 Slowly add small quantity of H_2O_2 to the beaker of H_2SO_4
- 4 Continuously stir the solution by using a glass thermometer and check that the temperature does not go beyond $80\text{ }^\circ\text{C}$
- 5 Once $80\text{ }^\circ\text{C}$ has been reached, immerse the sample in the solution by using plastic tweezers and leave it for 10 minutes
- 6 Extract the sample from the solution by using plastic tweezers and immerse it in the H_2O beaker then flush with deionized water
- 7 Fill the cabinet sink with water then immerse the beaker containing the solution in it; flush with plenty of water

Aluminium masking was effectively removed by using a solution consisting of orthophosphoric acid (H_3PO_4), nitric acid (HNO_3) and water in the ratio of 16:1:2. Complete removal of $0.05\text{ }\mu\text{m}$ thick aluminium masking could be achieved in about 20 minutes.

4.3 Reactive ion etching

Photoresist or metal patterns, after having been photolithographically defined, are not permanent elements of the final device but only replicas of circuit features. Patterns must be transferred into the planar waveguide to produce an optical circuit. One method of transferring the patterns is to selectively remove unmasked portions of the planar waveguide, a process generally known as etching. Dry etching or plasma-assisted etching techniques, which are commonly used in the microelectronics industry, have been adopted in IO because of their potential for very high fidelity transfer of resist patterns and accentuated anisotropy. In particular, reactive ion etching (RIE), also known as reactive

sputter etching, has been proved to be an effective technique in the microelectronic industry for the etching of SiO₂ films (Steinbruchel '85, Matsuo '80). For this reason, RIE has been initially used for the etching of high-silica content optical waveguides with excellent results (Kawachi '83).

Etching has been carried out on a Plasma Technology μ P 80 machine. Various gases have been tried as etchants. In Table 4.III the characteristics of the various etching processes experimented by the author are summarised for the 3 gas combinations used. CHF₃ has been found to give the best results in terms of etched wall roughness (average surface roughness < 50 nm) and anisotropy, although C₂F₆+O₂ and C₂H₄+C₂F₆ give much faster etching rates. An etching rate ratio of film : resist equal to 5:2 was achieved for all the gases, whilst the etching of the Al mask was negligible. The sidewall quality obtained for the three etchant gases used are shown in Fig. 4.2. Reflow at 1100 °C for 1 hour is used to smooth the sidewall roughness caused by the etching process, and hence to reduce the scattering losses, thus improving the overall propagation loss of the waveguides.

Etchant gas	CHF ₃	C ₂ F ₆ +O ₂	C ₂ F ₆ +C ₂ H ₄
Mask material	photoresist	Al	photoresist
Flow rates (cm ³ /min)	8	24/15	15/3
Pressure (mTorr)	8	102	19.5
RF Power (forward/reverse)	100/0	100/0	100/0
DC Bias (V)	240	240	240
Etch rate SiO ₂ -P ₂ O ₅ (Å/min)	350	1000	650
Etch rate SiO ₂ -GeO ₂ -P ₂ O ₅ (Å/min)	320	900	n.a.
Etch smoothness	excellent	good	good
Etch anisotropy	excellent	good	good
Polymer redeposition	yes	no	no

Table 4.III Etching process parameters for the various etchant gases used

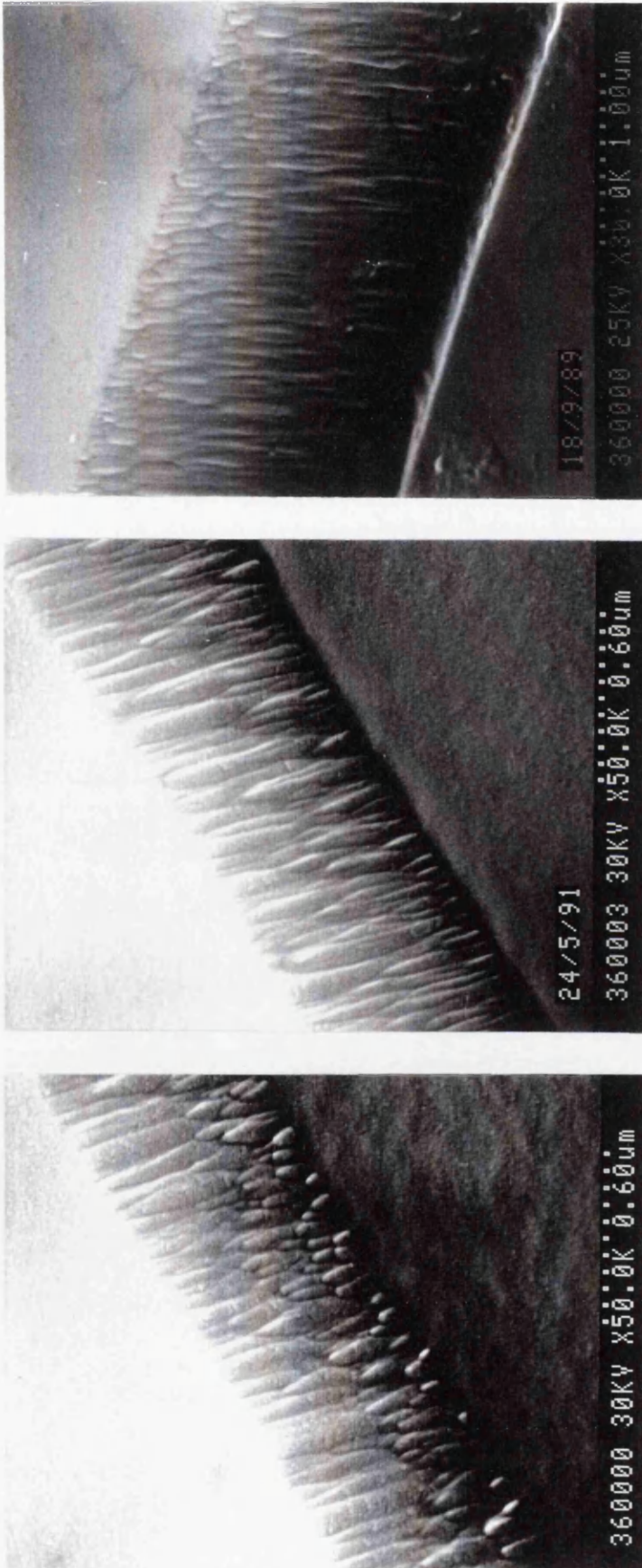


Fig. 4.2 SEM micrographs of reactive ion etched waveguides, showing the different sidewall qualities obtained by using as etchant gases: $C_2F_6+O_2$ (left), $C_2F_6+C_2H_4$ (center) and CHF_3 (right).

As can be seen in Fig. 4.2 and 4.3, trench formation can be observed at the base of the side wall of ridges obtained by using CHF_3 as etchant gas. Trenching results mainly from an enhanced ion flux at the base of a step due to ion reflection off the side of the step. The etch rate resulting both from physical sputtering and ion assisted reactions increases at the location of the trench because of the greater ion flux there (Sze '83).

Etching results obtained by using $\text{C}_2\text{F}_6+\text{O}_2$ and $\text{C}_2\text{F}_6+\text{C}_2\text{H}_4$ have been obtained in the late part of the research period. Therefore, these results should not be considered conclusive, as it is the belief of the author that better etching quality could be obtained by investigating a suitable recipe involving gas pressures, mass flow rates and RF power.

Both cladded ridges and slab coupled ribs have been fabricated. The cladded ridges offer lower coupling loss to the optical fibre of similar core size than the slab coupled ribs, because of the vertical symmetry of the guided mode which more closely matches the fibre mode, although they require extra cleaning, deposition and sintering stages. The slab coupled ribs, however, require a precise knowledge of the doped silica etch rate, which depends on the doping level, in order to achieve the exact thickness for the slab coupling region between the ribs. SEM micrographs of a $\text{SiO}_2\text{-P}_2\text{O}_5$ ridge waveguide before cladding deposition are shown in Fig. 4.3. Typical single mode guides were $4\ \mu\text{m}$ wide and $4\ \mu\text{m}$ high, as measured by Talystep. Slab coupled rib waveguides were typically $3.3\ \mu\text{m}$ high leaving a $0.7\ \mu\text{m}$ thick coupling slab.

Substrates are cut by using a diamond circular saw. It has to be said that cleavage of Si substrates was not found effective. The direct cleavage often resulted in catastrophic breakage of the sample. The reason for such failure is to be found in the high degree of dislocation which occurs in the Si crystal at the high temperatures involved in the sintering process.

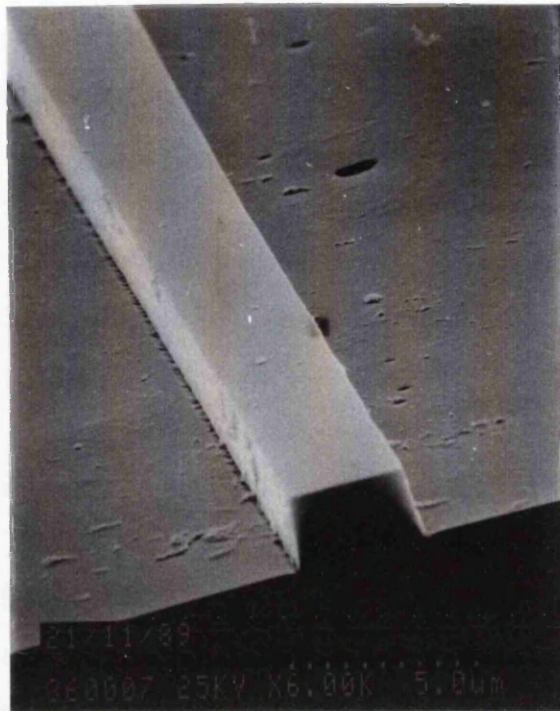


Fig. 4.3 SEM micrographs of P_2O_5 -doped silica channel waveguide.

Polishing of the end facets of the waveguides is required for efficient light coupling. This is achieved by a three-stage process. To prevent the waveguide ends from being chipped during the whole polishing process, the sample is bonded up-side down to a glass plate using Shellac, which fills in the gaps between the waveguide ridges. A first roughing down is obtained by using carborundum (SiC) 100 μm fine powder. Then Al_2O_3 3 μm fine powder is used to remove scratches left by the previous stage. The final polish is obtained using a colloidal silica solution (Syton W15).

In order to achieve accurate pattern reproduction in contact printing, it is important that the fanning out of the light between the mask and photoresist be zero. To this end the photoresist surface must be perfectly flat. By the spinning process the photoresist conformally reproduces the film surface and its defects. Sometime these defects precluded a perfect contact between the mask and the photoresist surface, the effect of which on the transferred pattern is visible in Fig. 4.4. For major clearness it has to be said that the central waveguide in the etched structure shown in Fig. 4.4, which evidently presents a taper in its width, had instead a constant width on the mask. In the next chapter some SEM micrographs regarding the same pattern transfer will be shown to prove the elimination of such a problem.

Micromasking is another problem that can be encountered. It happens sometime that, because of a wrong exposure or developing time for example, removal of a poorly defined photoresist pattern is necessary to allow a new photolithographic process. If the removal is not complete, microparticles of photoresist are still present on the waveguides surface and act as micromasking areas, obtaining the result shown in Fig. 4.5.

It has been found necessary to interrupt deep etching time with an oxygen etch for cleaning purposes of the chamber.

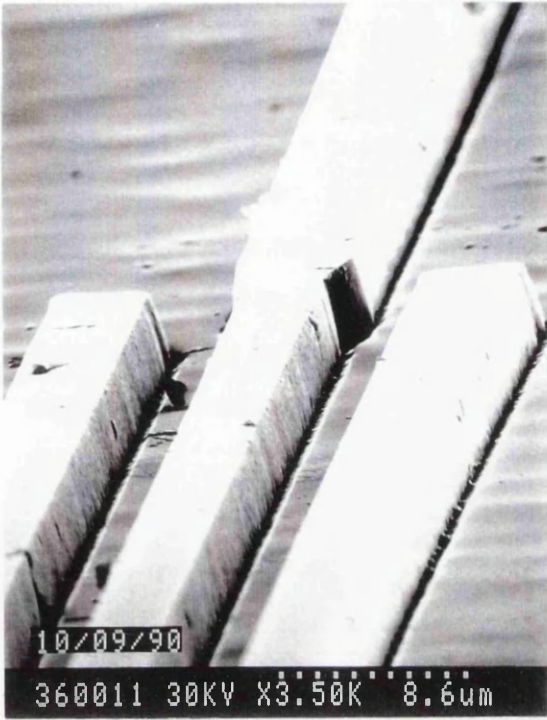


Fig. 4.4 SEM micrograph showing the effect of poor mask contact on the pattern transfer after etching.



Fig. 4.5 SEM micrograph showing the consequence of micromasking on the etched pattern.

In fact, continued long etching time caused polymer redeposition, where organic molecular species of a non volatile nature are formed in the plasma and are deposited on the film surface. The result of such redeposition is visible in Fig. 4.6. An oxygen etch of 15 minutes every hour of CHF_3 etch was found to be effective in cleaning the chamber. O_2 flow rate was $40 \text{ cm}^3/\text{min}$ and the etching pressure was of 100 mtorr (RF power = 100 W). The etching chamber was cleaned after each run with isopropanol. It has to be said that such redeposition could be avoided by choosing suitable feed gas, plasma parameters and masking material so that only volatile products form (Sze '83). In this sense further experimental work should be carried out in future.

4.4 Investigation into the optical damage threshold of $\text{SiO}_2\text{-P}_2\text{O}_5$ and $\text{SiO}_2\text{-GeO}_2\text{-P}_2\text{O}_5$ channel waveguides

Various nonlinear optical phenomena can be observed in silica based glasses when subjected to short light pulses with high power densities (e.g. Stegeman '85). There is interest in these results in integrated optical waveguides as only moderate total optical powers are necessary to produce sufficiently high power densities. However silica based channel waveguides can easily suffer from optical damage at relatively low average powers, as has already been observed in silica based optical fibres. In order to prevent catastrophic failure of these waveguides, it is important to correlate their glass composition and guiding properties to the optical power density at which such a failure occurs.

4.4.1 Optical damage in silica based optical waveguides

Laser induced damage (Allison '85) and self-propelled self-focusing damage (Kashyap '88) in silica based optical fibres have been studied extensively. Optical power handling capability of planar waveguides has also been investigated. For example Hermann et al. ('83) reported on dip coated $\text{TiO}_2\text{-SiO}_2$ waveguides with high optical damage threshold at 488 and 514 nm wavelengths.

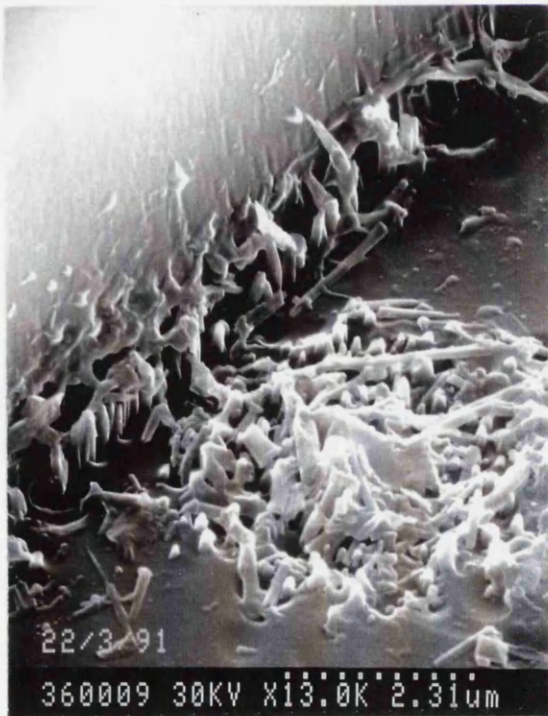
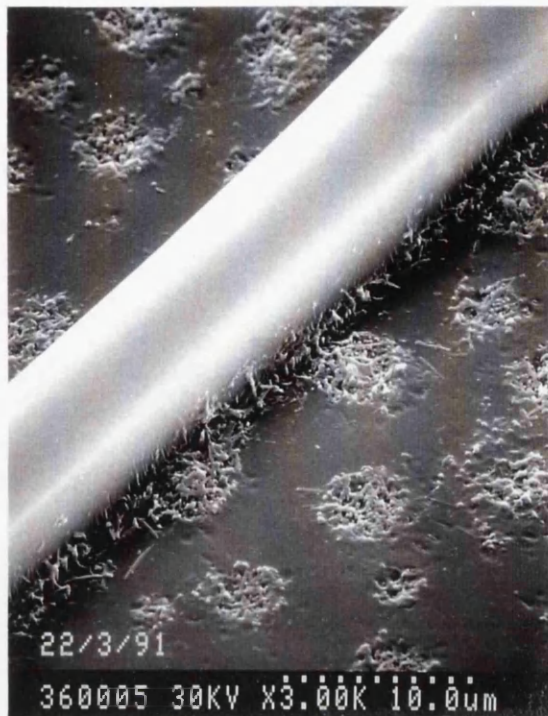


Fig. 4.6 SEM micrographs showing polymer redeposition which was experienced during long RIE run.

Optical damage in $\text{GeO}_2\text{-P}_2\text{O}_5$ -doped high-silica content channel waveguides has been reported by Kashyap et al. ('89) during second harmonic generation experiments, at the wavelength of $1.064\ \mu\text{m}$. Although some explanation was attempted, correlation between silica dopants or Q-switching frequency and optical damage threshold was beyond the purpose of their research.

We have investigated the optical damage threshold of P_2O_5 -doped and $\text{GeO}_2\text{-P}_2\text{O}_5$ -doped high-silica content channel waveguides fabricated by FHD on Si substrate (Barbarossa '92 f). Waveguides were subjected to high peak power pulses from a Q-switched Nd:YAG laser, operating at a wavelength of $1.064\ \mu\text{m}$. The influence of silica dopants on the damage threshold levels has been investigated by comparisons of experimental results on the two silica systems considered. The influence on the damage threshold level of other parameters, such as Q-switch frequency and exposure time, has also been investigated in order to assess the possibility of cumulative effects in the waveguides examined.

4.4.2 Experimental

Details of the fabrication process are important as the results obtained have to be considered in close relation to the structural composition of the synthesised glasses. The channel waveguides were $\text{SiO}_2\text{-P}_2\text{O}_5$ or $\text{SiO}_2\text{-GeO}_2\text{-P}_2\text{O}_5$. High purity of the oxide soot is guaranteed by flame synthesis and it easily matches that of the raw materials. An oxygen rich oxy-hydrogen flame was employed. Si substrates with $10\ \mu\text{m}$ thick, thermally grown, SiO_2 buffer layer were used.

The same refractive index step for the two compositions was obtained by decreasing the P_2O_5 concentration in the $\text{GeO}_2\text{-P}_2\text{O}_5$ -doped waveguides. The relative refractive index difference between core and substrate was 0.5 %. The ridges were formed by RIE of the core using CHF_3 as etchant gas and a resist mask. No cladding layer was deposited, hence the superstrate was air. The guides were $4\ \mu\text{m}$ wide and $4\ \mu\text{m}$ thick and resulted single mode at $\lambda=1.064\ \mu\text{m}$. The length of the waveguides examined, after cutting and polishing of the end faces, was 30 mm.

Scanning electron micrographs of typical damage track and its close view at the damage starting point are shown in Fig. 4.7. An undamaged waveguide is also shown for comparison. The spreading of the damage deep into the substrate can be observed. The micrographs refer to P_2O_5 -doped silica waveguide. No evident difference was noticed in the damage appearance in the two different composition. In most of the waveguides, the damage track extended all the way to the input end.

The experimental set-up used for optical damage threshold measurements is schematically shown in Fig. 4.8. The laser was a Q-switched, Nd:YAG laser (Spectron Laser Systems SL902TQ) operating at $1.064 \mu\text{m}$. P1 and P2 are two polarizers and HWP is a half wave plate, which together constitute an optical attenuator. M1 and M2 are two x40 microscope objective, SMF is a single mode fibre, C is the waveguide chip, D is a power detector and M is a mirror. The infrared camera was used to verify light coupling into a known waveguide on the chip. The mirror was used to deflect the laser beam to the power meter and to prevent blinding of the CCD camera at high power levels. The laser output consisted of Q-switched pulses of 100 ns FWHM at a repetition rate of 1 KHz. The laser operated in the TEM₀₀ mode, with no control over the longitudinal modes, and the pulse reproducibility was typically $\pm 2 \%$, peak to peak. The fibre was butt coupled to the ridge waveguides.

Fibre alignment and launching optimisation were performed at low power level and the insertion loss of the waveguide under examination was measured. Subsequently, the coupled laser power was slowly increased by rotating the half wave plate until the reading of the power meter suddenly dropped. An accurate evaluation of the guided power at the damage threshold was performed after every single experiment by measuring the output power from the fibre at the level at which catastrophic optical damage occurred and by taking into account the insertion loss previously measured.

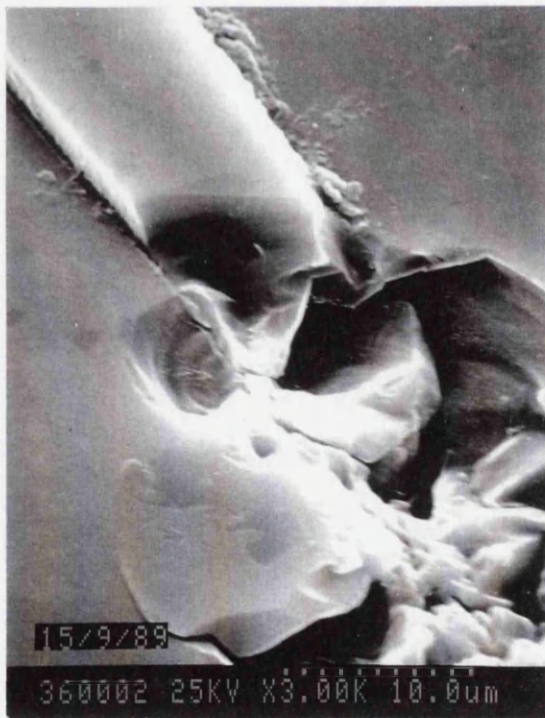
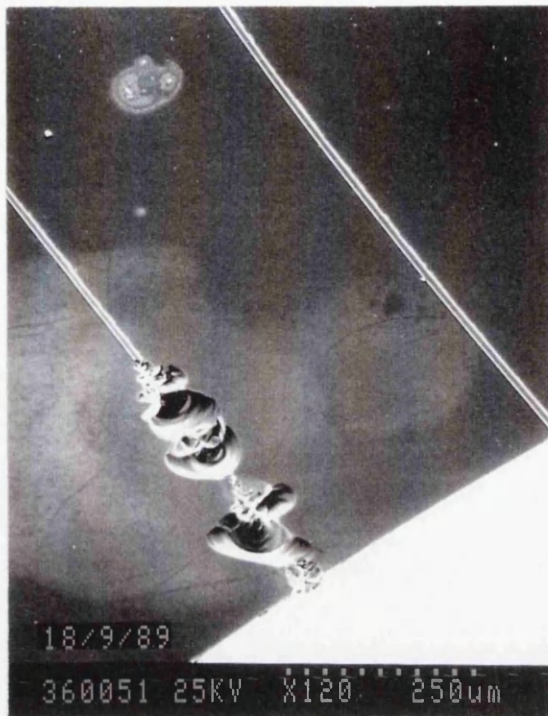


Fig. 4.7 SEM micrographs of catastrophically damaged P_2O_5 -doped silica channel waveguide (top) and close view of the damage starting point (bottom).

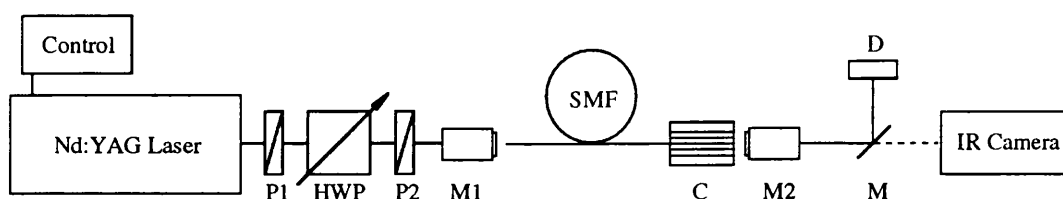


Fig. 4.8 Schematic diagram showing the experimental set-up for optical damage threshold measurement.

4.4.3 Results and discussion

50 waveguides were examined for each composition. As the power damage threshold varied for identical waveguides, we have reported in Fig. 4.9 the number of occurrence of breakage versus the average guided power, where occurrences have been grouped in 60 mW intervals. As the waveguides were not cladded, the high optical field intensities at the surface boundary and surface contamination could be regarded as contributory factors in the initiation of the damage. For the damage to extend over a distance much greater than the wavelengths of operation, we believe that it is similar to self-propelled self-focusing damage (Kashyap '88) observed in optical fibre of similar composition.

By assuming a Gaussian distribution for the probability of damage, the mean damage threshold occurred at 180 mW, corresponding to ~ 1.4 kW of peak power, for the GeO_2 - P_2O_5 -doped silica waveguides, and at 340 mW, corresponding to ~ 2.7 kW of peak power for the P_2O_5 -doped silica waveguides. The waveguide cross-section was $16 \mu\text{m}^2$ which gives, by assuming an uniform mode distribution, an energy density of about 9 and 17 GW/cm^2 for the GeO_2 - P_2O_5 -doped and P_2O_5 -doped silica waveguides, respectively. Characterisation of mode profile of the waveguides examined will help to determine more precisely the damage threshold.

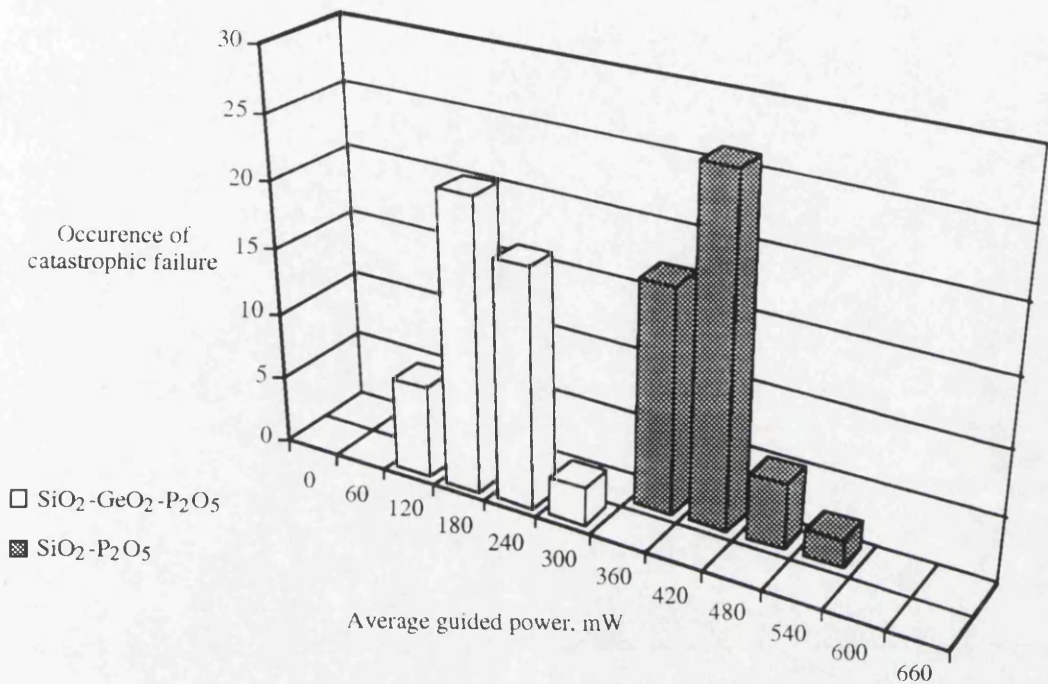


Fig. 4.9 Number of occurrence of catastrophic damage versus average guided power at $\lambda=1.064 \mu\text{m}$ (Q-switch frequency 1 KHz) for P_2O_5 and $\text{GeO}_2\text{-P}_2\text{O}_5$ doped silica channel waveguides.

We also investigated the effect of the repetition rate of the pulses on the damage threshold of both compositions. It seemed that the Q-switch frequency did not have influence on the failure of the waveguides. In fact, by changing the frequency from 1 KHz to 100 Hz, damage occurred at same peak power levels. So although the average power was reduced by an order of magnitude, the physical parameter deciding the waveguide failure was the peak power level. Similar results have been obtained in ion-exchanged waveguides (Albert '91).

For both doped silica waveguides, another experiment was performed to assess any cumulative effects. The waveguides were left guiding for 1 hour at high peak power level but 5 % below the threshold level already observed for identical waveguides. No catastrophic failure occurred although this does not exclude the possibility of a cumulative effect within a Q-switched pulse. Ultra short pulse experiments should clarify this point.

Spectral transmission measurements were performed using a halogen lamp and an optical spectrum analyser. The transmission spectra of both waveguides in the 0.9-1.3 μm wavelength range, were reasonably similar and flat within 2 dB. Consequently, the difference in power handling capability of the two waveguide composition examined, does not find justification in different absorption properties, as these are similar.

4.5 Summary

The microfabrication techniques involved in the realisation of high-silica content channel waveguides have been outlined. Photolithographic patterning and RIE process have been described and the pertinent parameters summarised. Photolithography and RIE have been proved to be an effective combination for the fabrication of channel waveguides with vertical and smooth sidewall.

The influence of different dopants on the power handling capability of high-silica content channel waveguides has been investigated. From the experimental results obtained, it can be concluded that at wavelength of 1.064 μm , the P_2O_5 -doped silica waveguides have a greater power handling capability than the P_2O_5 - GeO_2 -doped silica waveguides. Quantitatively, for the experimental conditions used in this work, the maximum power ratio for the two systems is about 2:1. Q-switch frequency does not seem to affect the optical damage threshold, as this is rather decided by the peak power level. Cumulative effects have not been observed for exposition time up to 1 hour. For the damage to extend over a distance much greater than the wavelengths of operation, we believe that it is similar to self-propelled self-focusing damage observed in silica optical fibre of similar composition. Absorption does not seem to be a relevant factor in the power handling capability of the waveguides examined, as they were transparent at the wavelength considered.

Chapter 5. Three-waveguide-coupler (3WC) based devices

Chapter Layout

- 5.1 Introduction**
- 5.2 The 3WC and its peculiarities**
- 5.3 Cascading 3WC**
- 5.4 3WC-based devices**
 - 5.4.1 Power splitter**
 - 5.4.2 Filter**
 - 5.4.3 Wavelength division multi-demultiplexer**
- 5.5 Summary**

5.1. Introduction

Various kinds of optical circuit elements have been realised based on high-silica content channel waveguides. These include: Y branches, X crosses, curvatures, reflection bends, two waveguide directional couplers, birefringence controllers, waveguide gaps and phase shifters. An excellent review of the subject has been recently published by M. Kawachi ('90) of NTT laboratories in Japan.

We have concentrated our attention on the three waveguide directional coupler (3WC) and demonstrated 3WC-based simple passive devices. A 3WC consists, in its simplest form, of three waveguides which are sufficiently closely spaced that interaction between their evanescent fields allows energy to be transferred from one to another. A schematic of 3WC is shown in Fig. 5.1.

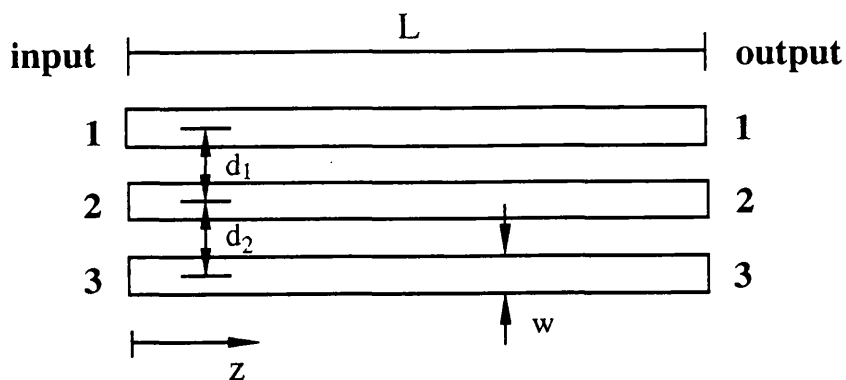


Fig. 5.1 Schematic diagram of a three waveguide directional coupler (3WC).

In the following sections, first, a brief account on the peculiarities of the 3WC, as compared to the 2WC, is given. Then, the cascading of 3WCs is taken into consideration as a viable approach to improve the filtering performance of the single component. Finally, characterisation of 3WC-based power splitter, filter and wavelength multi-demultiplexer, which have been designed and fabricated, is carried out, and the experimental results discussed.

5.2 The 3WC and its peculiarities

The passive 3WC is a key element in various applications because of its own peculiarities. There is an extensive literature (Donnelly '83, '86, '87, Haus '81) dealing with the theoretical aspects of the 3WC. In this section, we briefly summarise its main characteristics, whilst mathematical details are given in Appendix C.

When fed to the central waveguide, the 3WC presents a $1/\sqrt{2}$ time shorter coupling length for 3 dB splitting than the conventional 2WC and, because of the wider separation between the two outer waveguides, it eliminates the need for bends in many systems, thus resolving the conflict between loosely confining waveguides (as those realised in doped silica) and small bend radii (Haus '81). This contributes to reducing the overall loss of the device and to simplifying the

mask design. From this point of view, its use in the fabrication of multiport power splitters would turn advantageous if compared to the use of conventional Y branches or 2WC.

The 3WC is well known also for its superior performance in optical guided-wave filtering compared to the 2WC. An attractive feature, distinguishing the 3WC from the 2WC, is the sharper transfer spectral response, which yields better performance in filtering operations. In fact, it has been pointed out that its spectral response is the square of that of the 2WC, the squaring leading to a very effective sidelobe suppression (Haus '81). The 3WC also presents a rejection band that is more than 3 times wider than that of the 2WC. A wide rejection band is often required, for example, in multi-demultiplexing operations to cover the wavelength variation of light sources in practical conditions (Imoto '87).

Moreover, the 3WC presents six ports, which is the smallest number of ports that enables in-phase and quadrature outputs to be obtained. It can thus be used as a $2\pi/3$ optical hybrid, a key component in phase diversity coherent receiver or in passive stabilisation schemes for fibre interferometers (Sheem '82).

The 3WC has limitations. It has been shown (Donnelly '86) that when the individual isolated guides are single mode, the 3WC can support three different modes and the power transfer efficiency between the two outer guides is maximum only if the propagation constants of its three modes are evenly spaced, which is not in general the case for a 3WC with identical waveguides, unless they are loosely coupled. However, this is not a severe problem when the 3WC is employed as power divider or combiner, i.e. when the input light is fed to the central guide and coupled to the outer guides, or vice versa. In fact, in this case the coupler can support only two modes. Still, in both cases the overall power transfer efficiency is limited by the radiation losses which are due to the imperfect match between the mode of the input and output guides and the optimum linear combination of the three modes of the 3WC.

5.3 Cascading 3WC

By cascading 3WCs it is possible to achieve further improvement in the filtering performance. Simply by the proper choice of the interaction length and number of cascaded 3WC, appropriately connected, it is possible to design suitable spectral responses for filtering operations, tuning the passbands and achieving high stopband rejection. In a cascading context, the larger number of possible combinations in the connection of 3WCs, than of 2WCs, also contributes to make their cascading a flexible design technique.

Cascading of directional couplers has been previously suggested to improve their performance. However, this has been accomplished by cascading 2WCs in a tree structured fashion for multi/demultiplexing purposes (Imoto '87) or cascading of 3WCs has been suggested to improve the sampling windows of a periodic electro-optic sampler (Haus '81). The cascading has been limited to 2 stages in both cases. Cascading of fibre-based 2WC (Yataki '85) and 3WC (Safaai-Jazi '91) has also been suggested.

When three, or more, 3WCs are cascaded, the problem is more complicated. Nevertheless, this allows a more flexible design and it is possible to match ones own requirements. The schematic of 3 cascaded 3WCs is shown in Fig. 5.2, where the dotted lines indicate possible connections; s is the spacing between two successive couplers. s is a function of the numerical aperture of the waveguides, and must be chosen in such a way as to minimize recoupling between adjacent waveguides.

Once the basic coupling structure is designed, i.e. waveguide cross section, separation and refractive index step, and the spectral responses of a single 3WC for different interaction lengths are known, the design of the spectral response does not require new computations for the synthesis of different filtering characteristics. From this point of view, the cascading concept is simple and straightforward, and lends itself to a systematic approach.

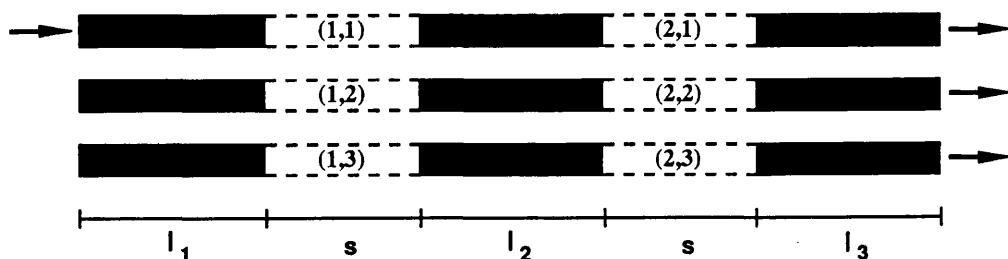


Fig. 5.2 Schematic diagram of 3 cascaded 3WCs: the dotted lines represent possible connections between facing waveguides (configurations of cascaded 3WCs are listed in Table 5.I and 5.II).

For input to one of the outer waveguides, by cascading three identical 3WCs ($l_1=l_2=l_3$), it is possible to originate 49 possible useful configurations of which only 8 ensure full transfer efficiency at selected wavelengths for both outer waveguides and 16 for the same input waveguide (Barbarossa '92 a). These configurations are listed in Table 5.I and 5.II respectively. Full transfer efficiency at selected wavelengths is obtainable for the central waveguide only if this is also the input waveguide (correspondingly the outer waveguides do not present full transfer efficiency). Configurations of Tables 5.II are not employable for multi-demultiplexing purposes because full transfer efficiency is achieved for one waveguide only. Configuration n. 1 is equivalent to considering a single 3WC having a trebled interaction length.

I	Configuration number							
	1	2	3	4	5	6	7	8
(1,1)	□	□	□	□	□	□	□	□
(1,2)	□		□	□			□	
(1,3)	□		□	□	□	□	□	□
(2,1)	□	□	□	□	□	□	□	□
(2,2)	□	□	□		□			
(2,3)	□	□				□		

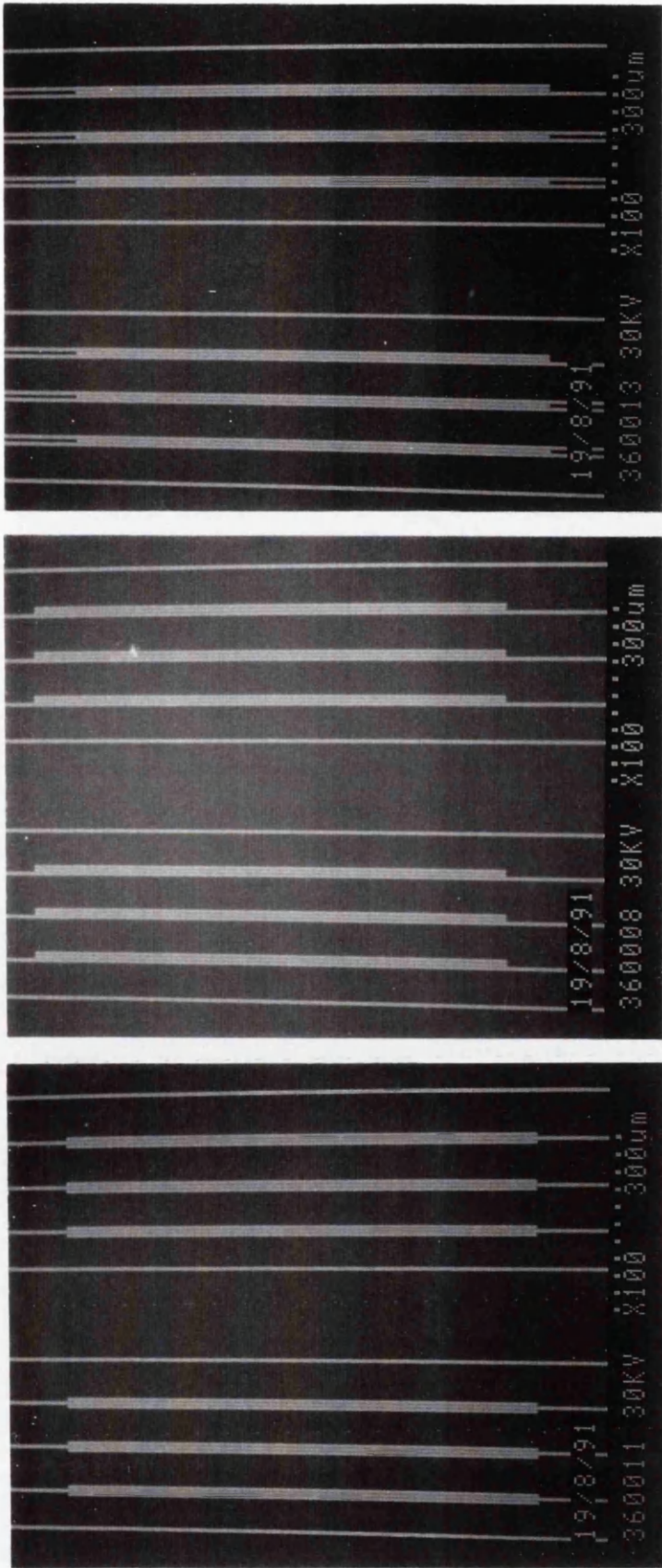
Table 5.I Cascaded configurations of three 3WCs which guarantee, for input to one of the outer waveguides, 100 % transmission for both the outer waveguides.

II	Configuration number															
	9	10	11	12	13	14	15	16	17	18	19	20	21	22	23	24
(1,1)	□		□			□		□			□		□	□		□
(1,2)	□	□	□	□	□			□	□							□
(1,3)		□		□	□		□		□	□		□			□	
(2,1)	□	□	□	□	□	□	□	□	□	□	□	□	□	□	□	□
(2,2)	□	□		□		□	□					□	□			□
(2,3)	□	□	□		□	□	□			□	□					

Table 5.II Cascaded configurations of three 3WCs which guarantee, for input to one of the outer waveguides, 100 % transmission for only the input waveguide.

When cascading implies the use of a 2WC as connection (e.g. configuration n. 3 and 9), this can be taken into account in the design of the spectral response. This intermediate 2WC contributes to improving the overall rejection bandwidths, although it complicates the design of the filter. However, in the case of weak coupling, if the connection involves the two outer waveguides (e.g. configuration n. 5 and 11), which are widely spaced, its influence on the spectral characteristic can be neglected. Configurations involving a single waveguide connection (e.g. configurations n. 2 and 22) can also include 3WCs with different waveguide spacing to achieve more sophisticated filtering characteristics, without requiring bends for the connections. On the contrary, configurations involving two waveguide connections (e.g. configurations n. 6 and 24) would require bends in order to cascade 3WCs with different coupling structures.

Fig. 5.3 shows SEM micrographs of one stage of the fabricated cascaded 3WCs for three different connections: central waveguide (a), one of the outer waveguides (b) and both outer waveguides (c). Fig. 5.4 shows close view SEM micrographs of the three different connections. The remaining possible connection, i.e. by two adjacent waveguides, has not been taken into consideration in this work.

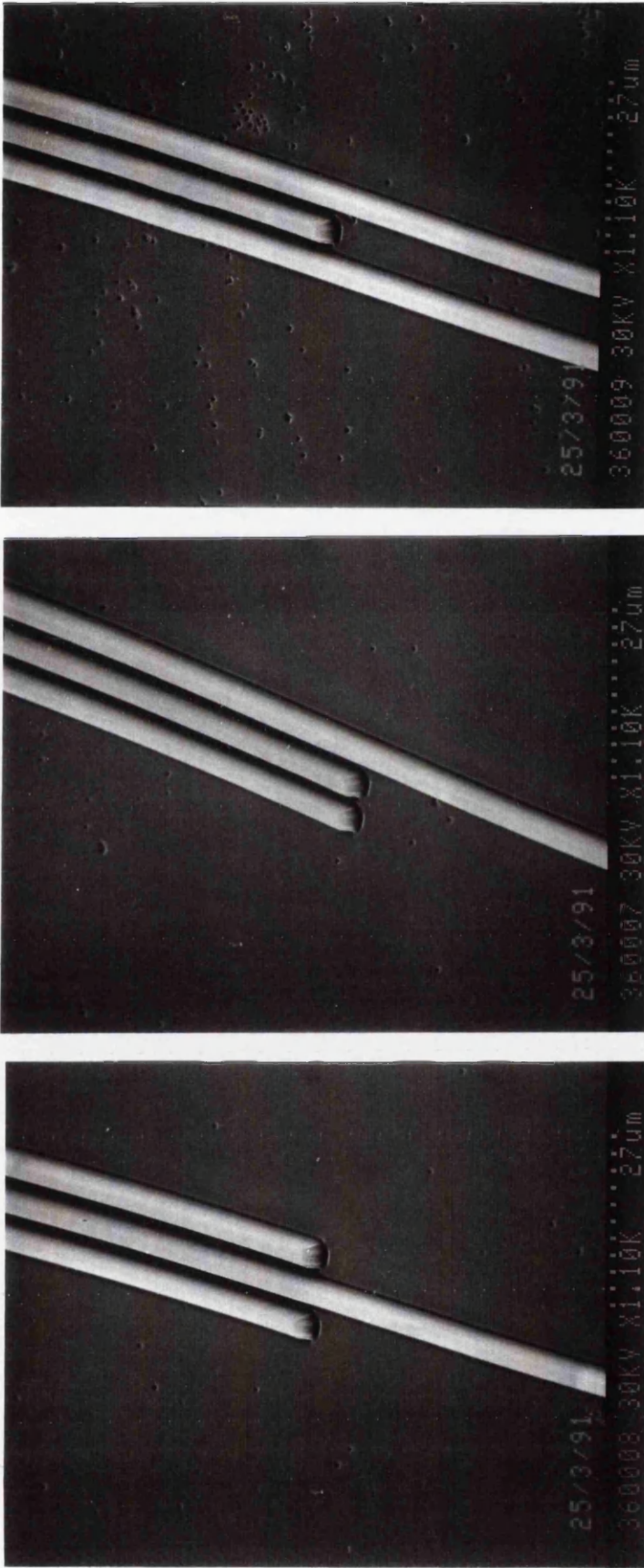


a

b

c

Fig. 5.3 SEM micrographs of one stage of the cascaded 3WCs, for different connections: central waveguide (a), one outer waveguide (b) and both outer waveguides (c). The micrographs have been taken at an angle to include a full stage and the view is foreshortened.



a b c

Fig. 5.4 SEM micrographs of different connections for 3WC (close view):
central waveguide (a), one outer waveguide (b) and both outer waveguides (c).

By cascading 3WCs with different interaction lengths, sophisticated spectral responses can be designed for wideband filtering applications. In the suppression or narrowing of the passbands it is possible, for example, to follow two different approaches. The first is based on the so called “vernier” principle. This consists of cascading 3WCs with slightly different interaction lengths, i.e. having closely matched spectral characteristics, which match only at the desired spectral orders.

The second is based on the cascading of 3WCs having widely different coupling lengths, in such a way that their spectral responses periodically overlap at the desired spectral orders. In Fig. 5.5 a schematic of the two approaches is shown in order to obtain suppression of non corresponding spectral orders, achieving, at the same time, wider rejection bandwidths beside the corresponding spectral orders. These two approaches have also been proposed for the design of compound fibre optical resonators (Urquhart ‘88).

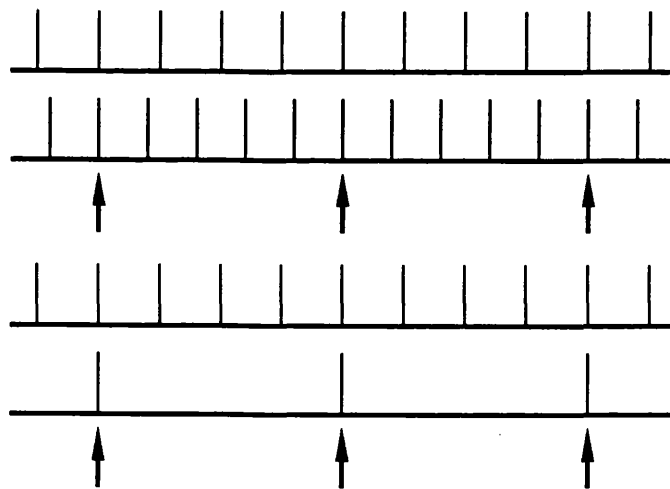


Fig. 5.5 Suppression of undesired spectral orders following the vernier principle (top) or cascading 3WCs with multiple interaction lengths (bottom).

In the synthesis of wideband spectral characteristics, the variation of the coupling efficiency with wavelength should also be taken into account. This results in a chirped spectral behaviour of a single 3WC, which complicates the matching over desired bands of the spectral response between the connected 3WCs. However, in narrowband filtering operation the relationship can be considered linear, simplifying the design.

The cascading of 3WCs finds useful application in other devices such as a multi-demultiplexer for widely spaced channels or when wider rejection bandwidths are required to cover the wavelength variation of laser sources in practical conditions. For example, once the basic coupling structure is designed to obtain duplexing at two wavelengths, wider rejection bandwidths can be obtained by simply connecting identical 3WCs by the two outer waveguides.

The cascading approach has its obvious limitation in the length of the device, as this is constrained by the substrate size. However, long length devices could be realised by folding the optical path following, for example, the arrangement shown in Fig. 5.6. In this design the main limitation in size would be the minimum bend radius compatible with acceptable losses.

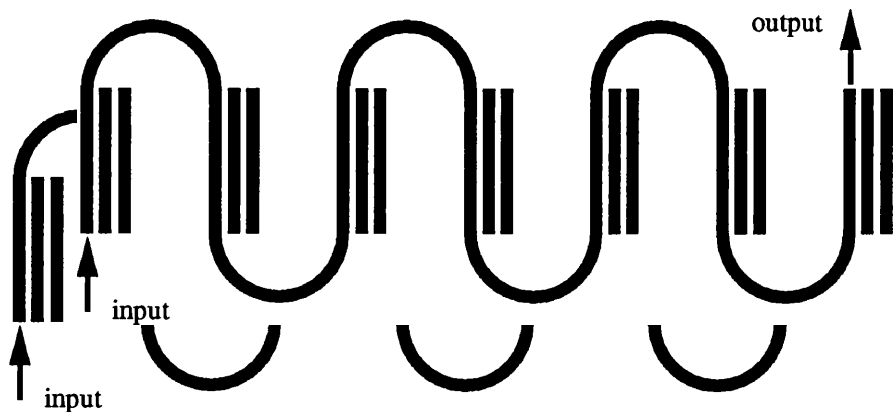


Fig. 5.6 Proposed configuration for cascaded 3WCs to contain the overall length of the device.

5.4 3WC-based devices

The geometry chosen for the implementation of the 3WC has been that of slab-coupled rib waveguides, which, although not perfectly fibre compatible as are the cladded channel guides, are easier to fabricate for the purpose of demonstrating the improvement in filtering performance which can be achieved by using cascaded 3WCs. Fig. 5.7 shows optical microscope photographs of the 3WC polished end facet in reflection and in transmission. The slab coupling region is clearly visible between the ridges. The same 3WC is shown in the SEM micrograph of Fig. 5.8. Fig. 5.9 shows a micrograph of the "branching" section of a 3WC, where the photolithographic problem discussed in paragraph 4.3 has been resolved. A photograph of a finished chip containing several cascaded 3WCs of different length and configuration, is shown in Fig. 5.10.

The 3WC basic structure has been designed using an extension of the effective index method (Donnelly '83) (Appendix B), and numerically simulated by the beam propagation method (BPM) (Lagasse '84) to achieve single mode operation, and to predict the beat length for the prescribed section area and refractive index value. As usual it has been assumed that the mode fields are well confined to the core region of the waveguide and only very little field energy spreads out into the surrounding region.

5.4.1 Power splitter

The waveguides were 4 μm wide with a 4 μm separation. The rib was 3.1 μm high, leaving a 0.9 μm thick coupling slab. The refractive index difference between core and substrate was 0.5 %. With excitation to the centre guide a coupling length of 1.3 mm has been calculated to achieve a 50 % split at $\lambda=1.32$ μm , with the remaining power in the centre guide less than 2%. A length of 0.9 mm was necessary to obtain 33 % splitting. The BPM simulation (Barbarossa '88) has been performed only for the straight coupling region. In Fig. 5.11 relative intensity plots of 1x2 and 1x3 operations, for gaussian input to the central waveguide, are shown. An absorber 4 μm wide was necessary to simulate the evanescent fields outside the waveguides (Lagasse '84).

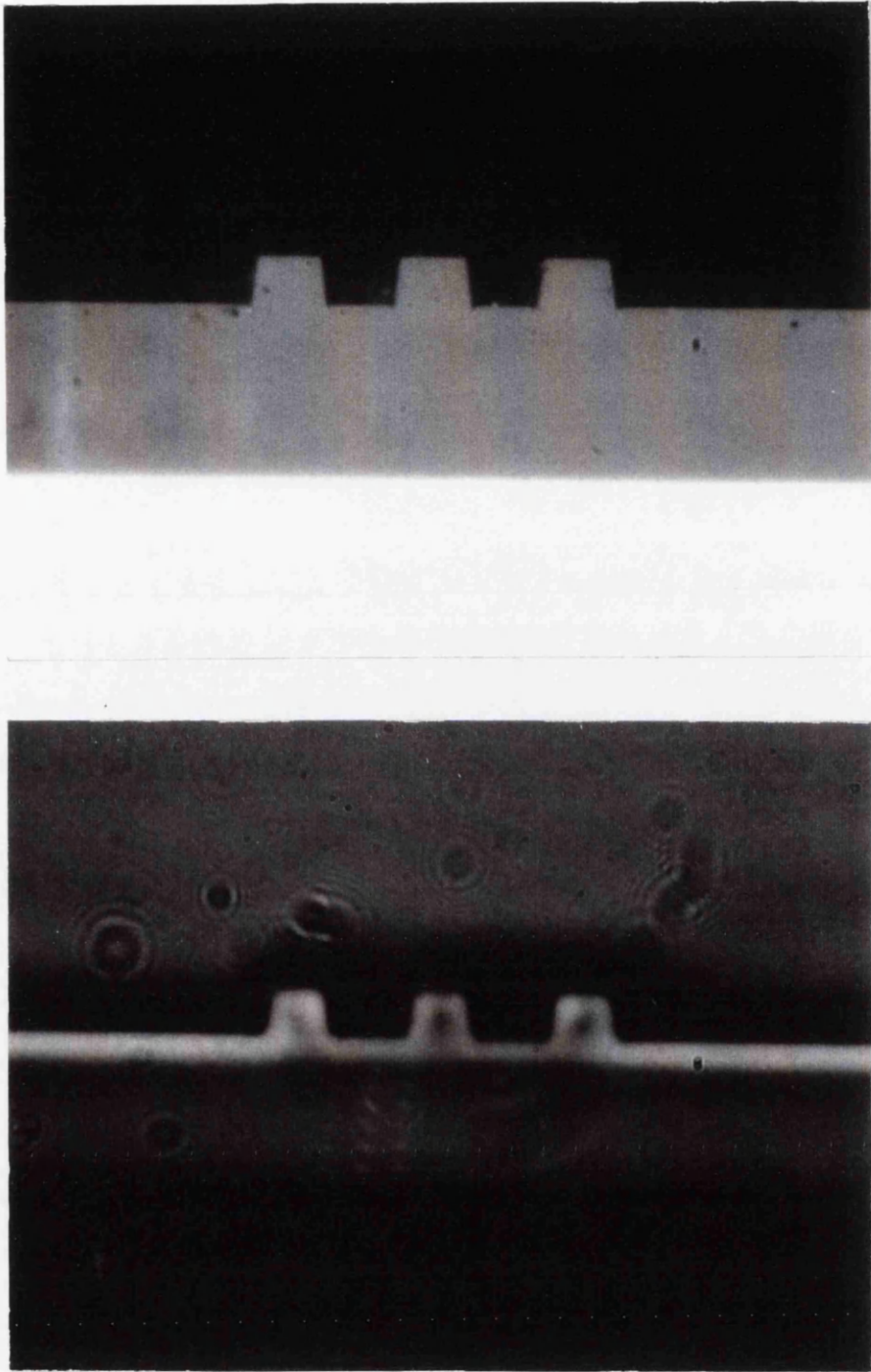


Fig. 5.7 Optical microscope photographs of 3WC polished end facet in reflection (top) and in transmission (bottom): the slab coupling region is clearly visible in between the ridges.

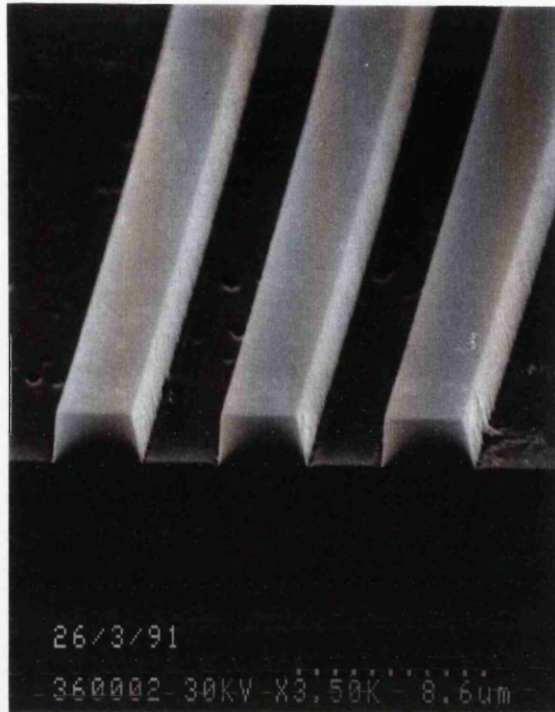


Fig. 5.8 SEM micrograph of polished end facet of 3WC.

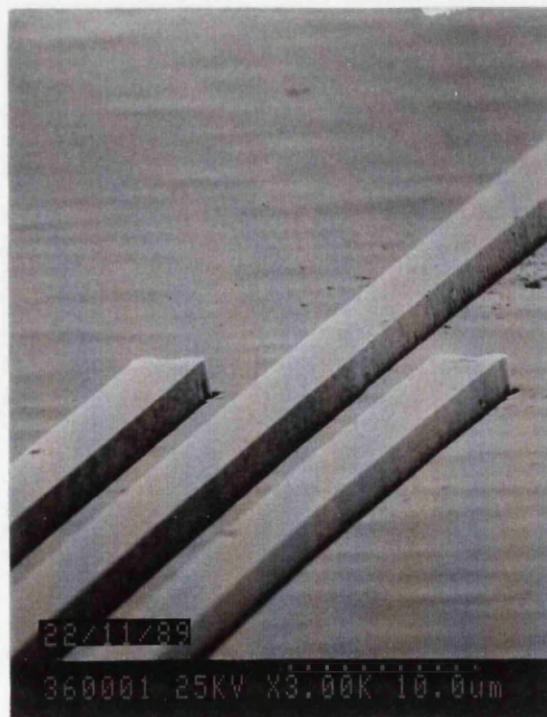


Fig. 5.9 SEM micrograph of 3WC branching section.

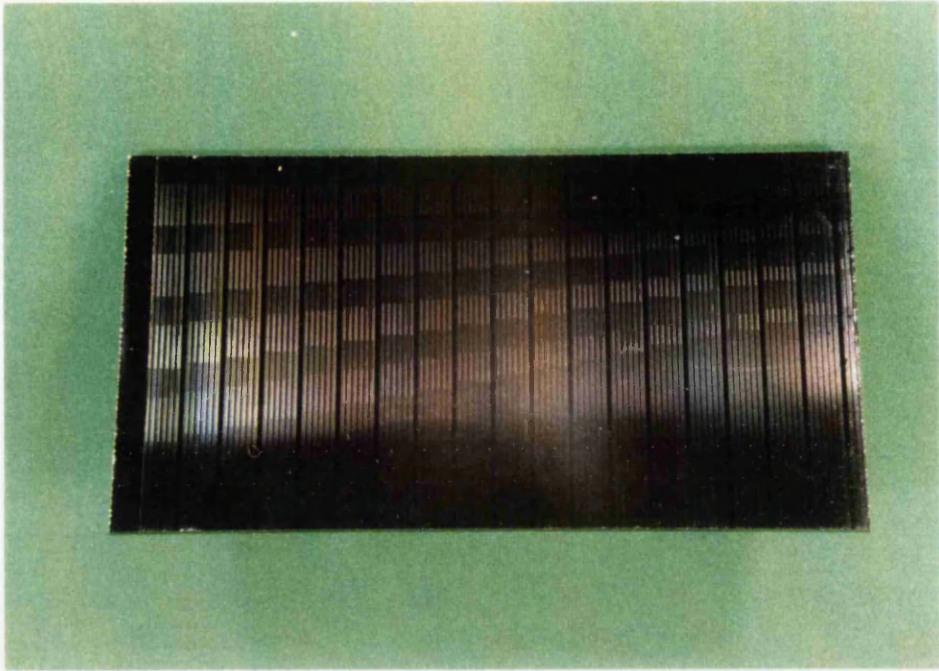


Fig. 5.10 Photograph of finished chip containing several cascaded 3WCs.

For power measurements the experimental set-up in Fig. 5.12 was employed. The Nd:YAG semiconductor pumped laser at $\lambda=1.319 \mu\text{m}$ was coupled into a system fibre, using a 20x microscope objective. The power launched into the fibre was monitored through a 3 dB fibre coupler. The fibre was butt-coupled to the device and the near field output from the device was focused using a microscope objective on an infrared camera, which was connected to a monitor through a video scanner. All the measurements were performed with input coupling to the central waveguide.

In Fig. 5.13 the guided light intensity profiles at the output of 3WC for 1x2 and 1x3 operations are shown. In Fig. 5.14 near field outputs of 3WCs with different interaction length are shown. The interaction length varies from 1.45 to 2.8 mm. As shown in the figure, for the perfect coupling length to achieve 3 dB splitting, which was 1.45 mm, the power remaining in the central waveguide was undetectable. Fig. 5.15 shows the theoretical and experimental relative output power out of each guide as a function of interaction length. An insertion loss of ~ 4 dB has been estimated and the 3 dB coupling length was 8% longer than expected (Barbarossa '91 b).

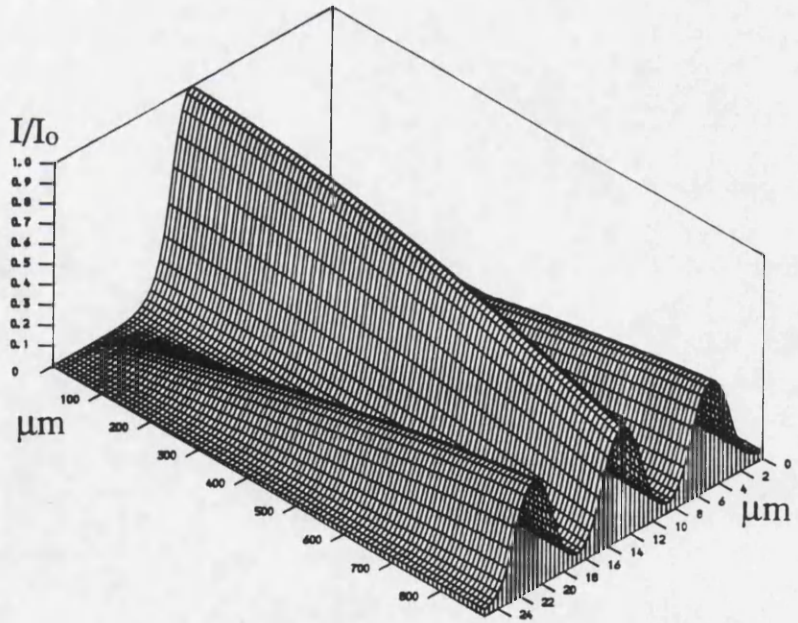
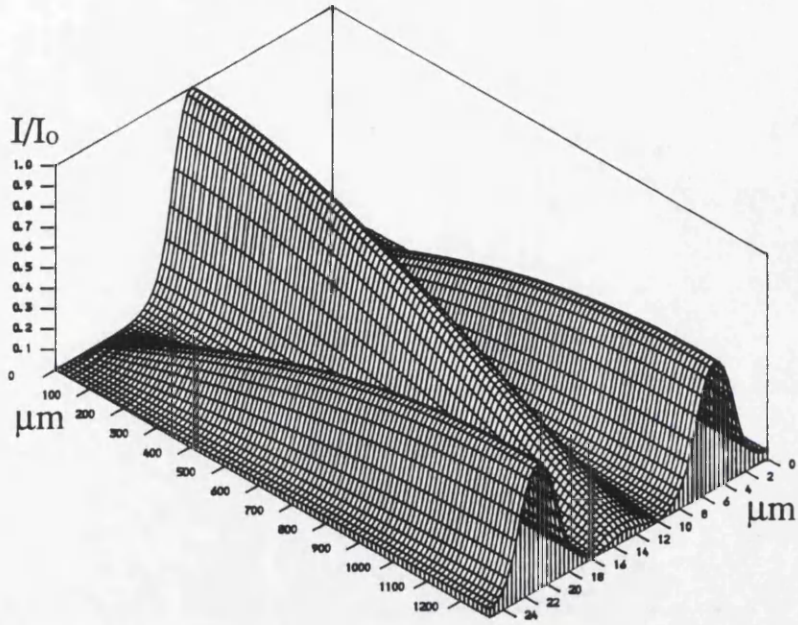


Fig. 5.11 BPM simulations of 3WC: 1x2 and 1x3 operations.

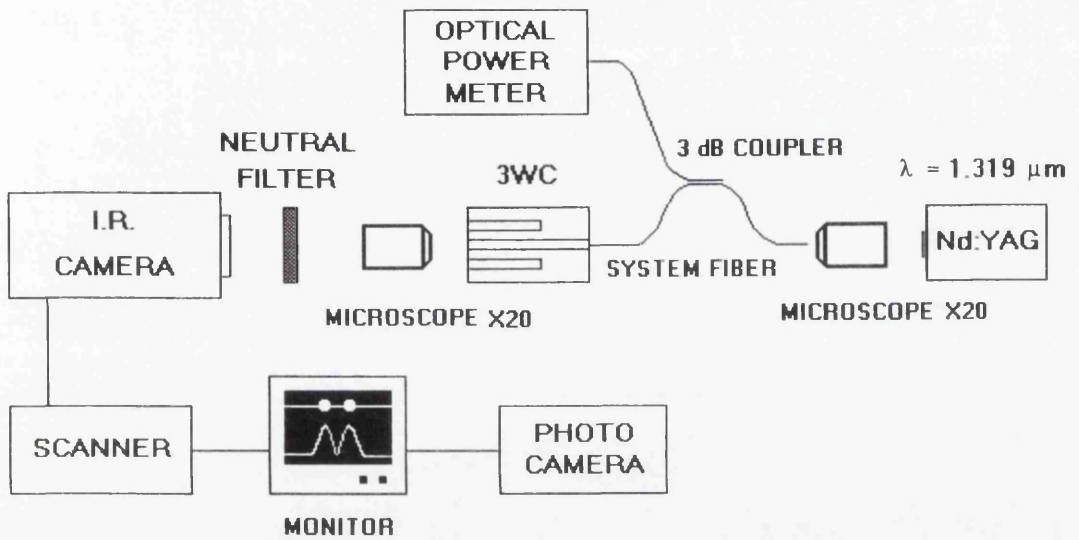


Fig. 5.12 Experimental set-up for power measurements.

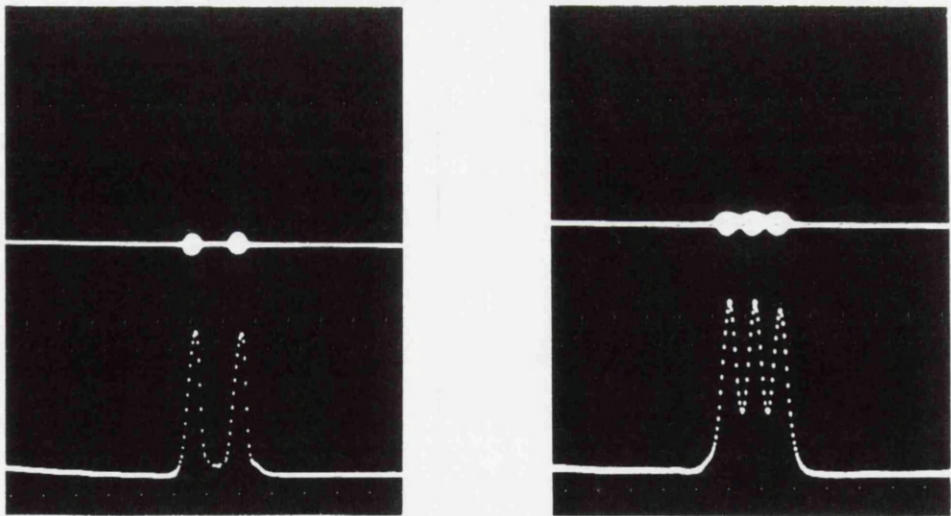


Fig. 5.13 Intensity profiles of near field outputs of 3WC for 1x2 (left) and 1x3 (right) operation (input to the central waveguide).

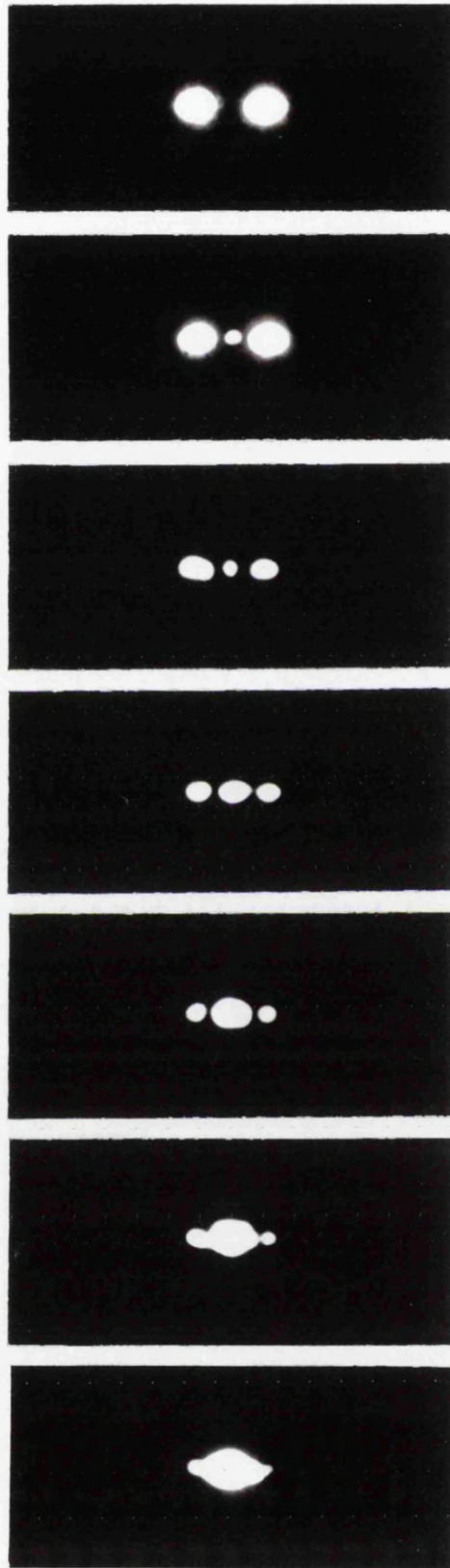


Fig. 5.14 Near field output of 3WCs with different interaction lengths: (top-bottom) 1.45, 1.6, 1.8, 1.9, 2.3, 2.7, 2.8 mm for input to the centre waveguide ($\lambda = 1.32 \mu\text{m}$).

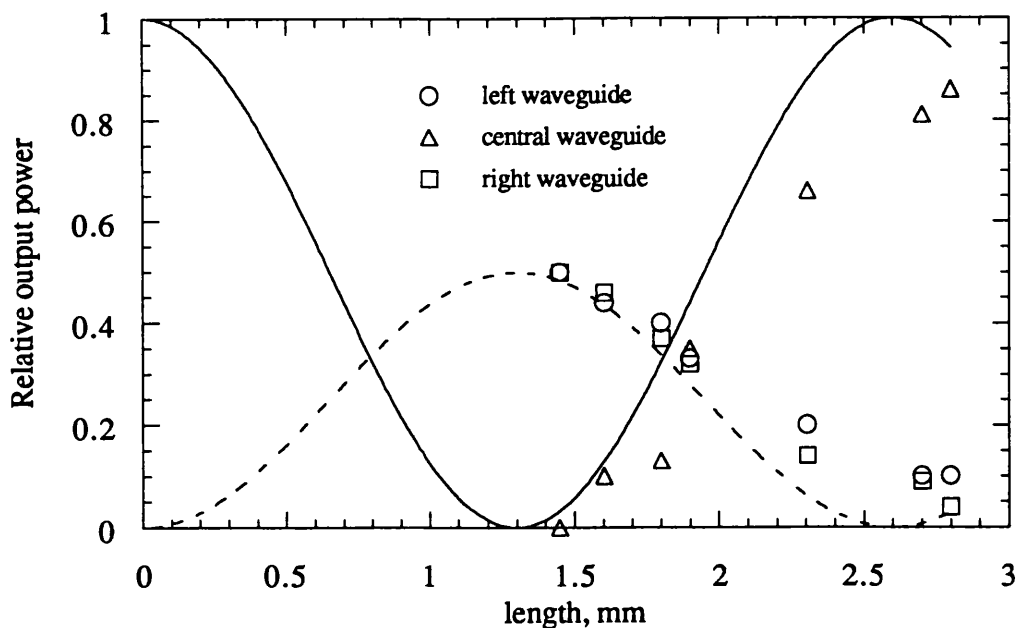


Fig. 5.15 Theoretical and experimental relative output power out of each guide as a function of interaction length for 3WC with input to the central waveguide (solid curve = central waveguide, dotted curve = outer waveguides).

The lighter coupling between the waveguides, which is believed to be the reason for the longer than expected beat length, is probably the result of a deeper etch depth, which left a thinner slab-coupling region, together with a slightly reduced waveguide width obtained after the etching process. Asymmetry in some of the near field patterns is believed to be due to imperfection in the polishing of the output facets, rather than to asymmetries in the 3WC etched geometry, which was imposed by the mask design. The coupling loss was mainly due to the mismatch of the modal fields of fibre and waveguide. Reducing the field mismatch by adjusting the core dimensions and using the cladded geometry will result in lower coupling losses.

5.4.2 Filter

Optical guided-wave filters based on the wavelength selectivity of directional couplers have been already proposed (Alferness '78, Haus '81). Here, we present an example realised by using a 3WC and the improvement in filtering performance achieved by cascading three identical 3WCs.

The design of such a filter (Appendix D) has been directed towards the filtering of the amplified spontaneous emission at $1.05\ \mu\text{m}$ in Nd-doped fluoride fibre amplifiers operating at $1.3\ \mu\text{m}$, which limits the magnitude of the amplifier gain and requires wideband filtering operation to be suppressed (Pedersen '90). The filter at the same time must present large passbands at the pump and lasing wavelength, 0.8 and $1.3\ \mu\text{m}$ respectively. This task can be achieved by using multielectric coatings deposited on the polished end facets of the active fibre, which presents obvious disadvantages of cost and manufacturing (Millar '90). Fig. 5.16 and 5.17 show the theoretical spectral response of such a filter composed of a single 3WC and of three identical cascaded 3WCs, respectively. These spectra correspond to an interaction length of $1.7\ \text{mm}$ for the single 3WC.

For the determination of the spectral response, the experimental set-up in Fig. 5.18 was used. A flat white light source (halogen lamp), whose spectrum is shown in Fig. 5.19, was coupled into a system fibre, which was butt-coupled to the device. A single mode small core ($6\ \mu\text{m}$) fibre was used to guide the output from the device to the optical spectrum analyzer (Advantest Q8381), which was used to record the filter spectral characteristics. This arrangement produced continuous spectral characteristics, rather than scattered experimental points, although the spectral characterisation had to be performed always in high sensitivity mode and employing long averaging time because of the low power spectral density of the white light source employed.

Fig. 5.20 and 5.21 show the filtering characteristics of a single and of three identical cascaded 3WCs, respectively, connected by the outer waveguide (configuration n. 22). The reported spectra correspond to an interaction length of $1.85\ \text{mm}$ for both single and cascaded 3WCs, i.e. a length longer than expected was necessary to obtain a spectral response resembling the theoretical one. All the measurements were performed with input and output coupling to one of the outer waveguides. The spectrum of the white light source, observed through a single straight waveguide, having the same dimensions as those forming the 3WC, is also shown for comparison in Fig. 5.22.

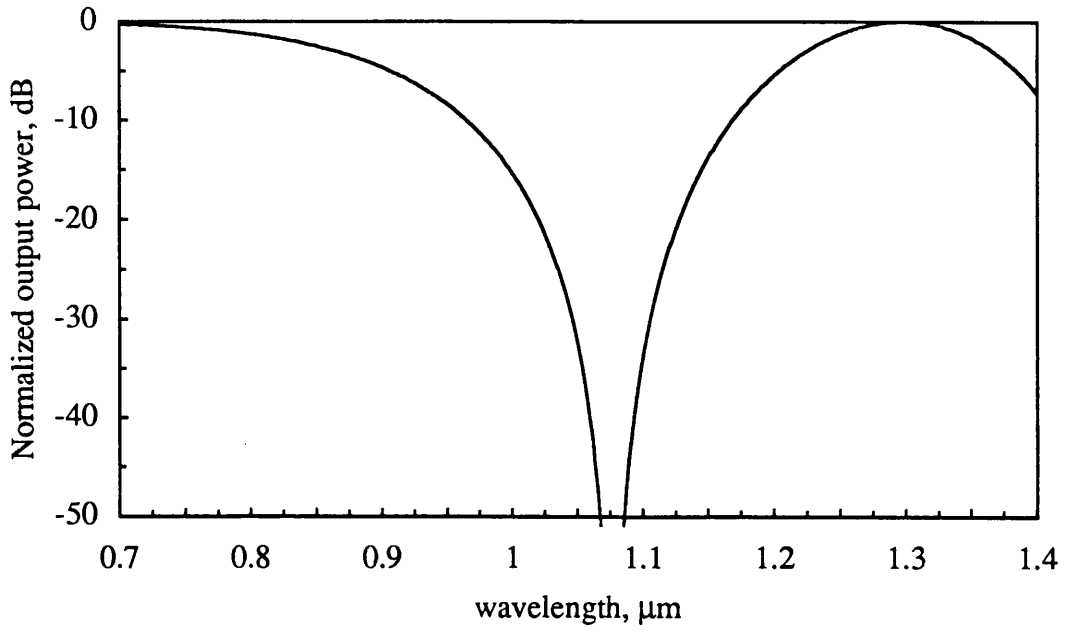


Fig. 5.16 Theoretical normalised spectral response of single 3WC filter for input to one of the outer waveguides and output from the same waveguide.

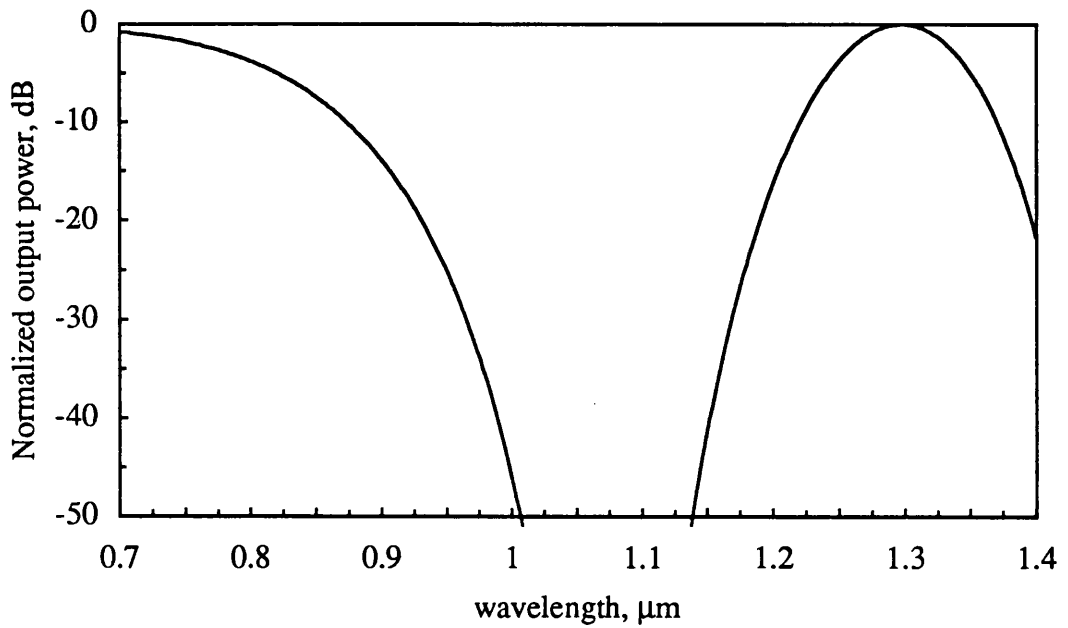


Fig. 5.17 Theoretical normalised spectral response of three cascaded 3WCs (configuration n. 22) for input to one of the outer waveguides and output from the same waveguide.

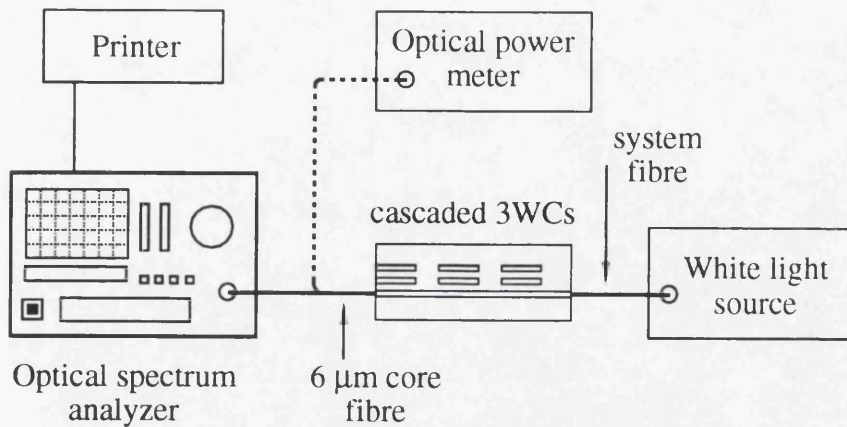


Fig. 5.18 Experimental set-up for spectral response characterisation of 3WC based devices.

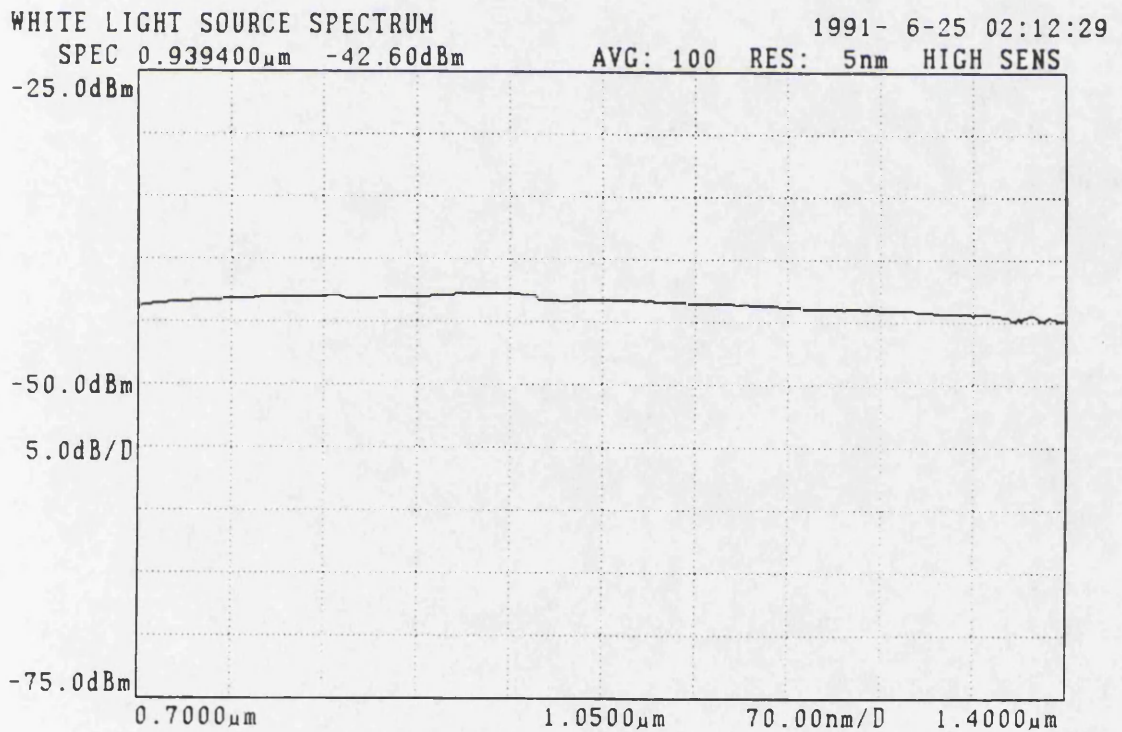


Fig. 5.19 Spectrum of white light source employed for spectral characterisation of 3WC based devices.

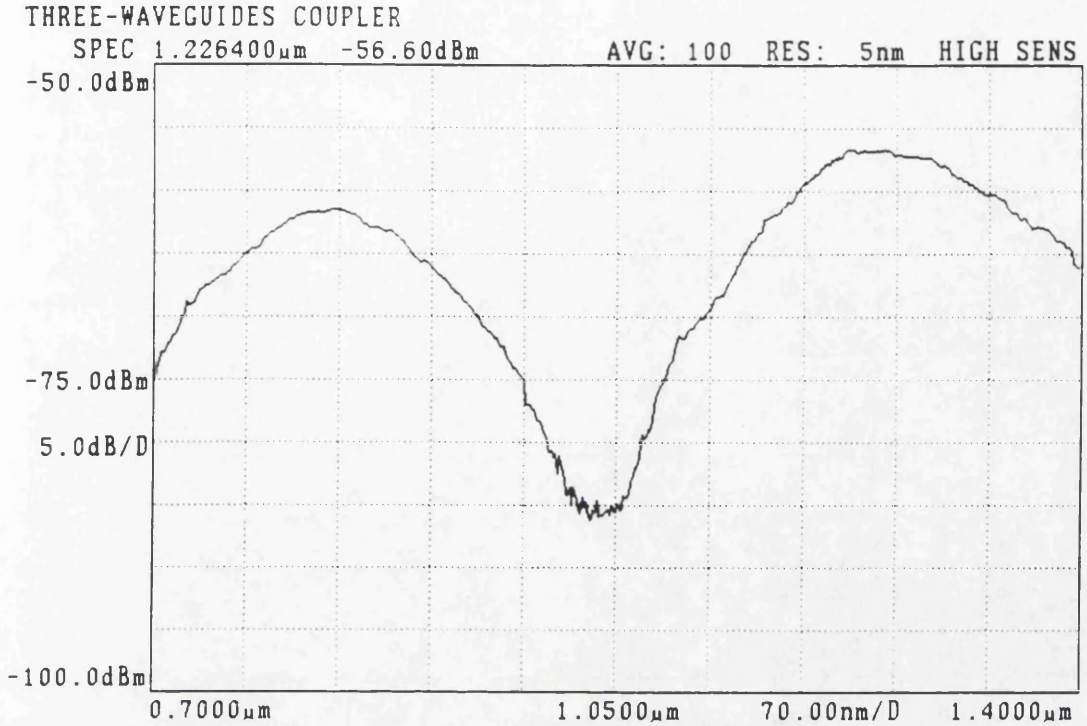


Fig. 5.20 Measured spectral response of a single 3WC for input to one of the outer waveguides and output from the same waveguide.

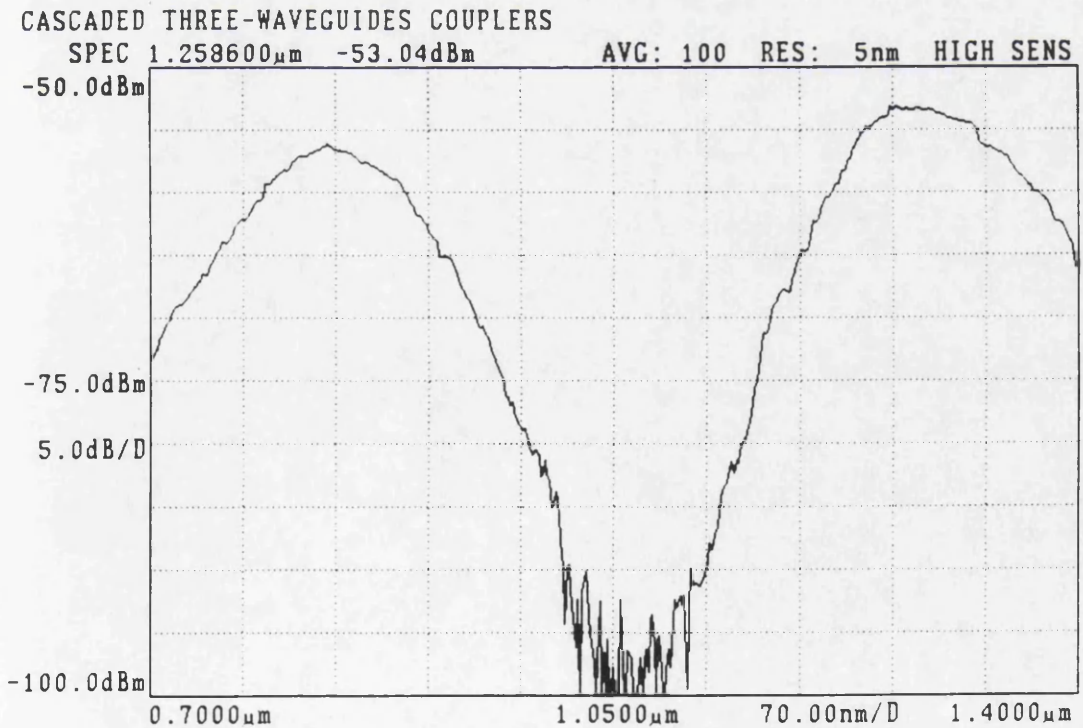


Fig. 5.21 Measured spectral response of three cascaded 3WCs (configuration n. 22) for input to one of the outer waveguides and output from the same waveguide.

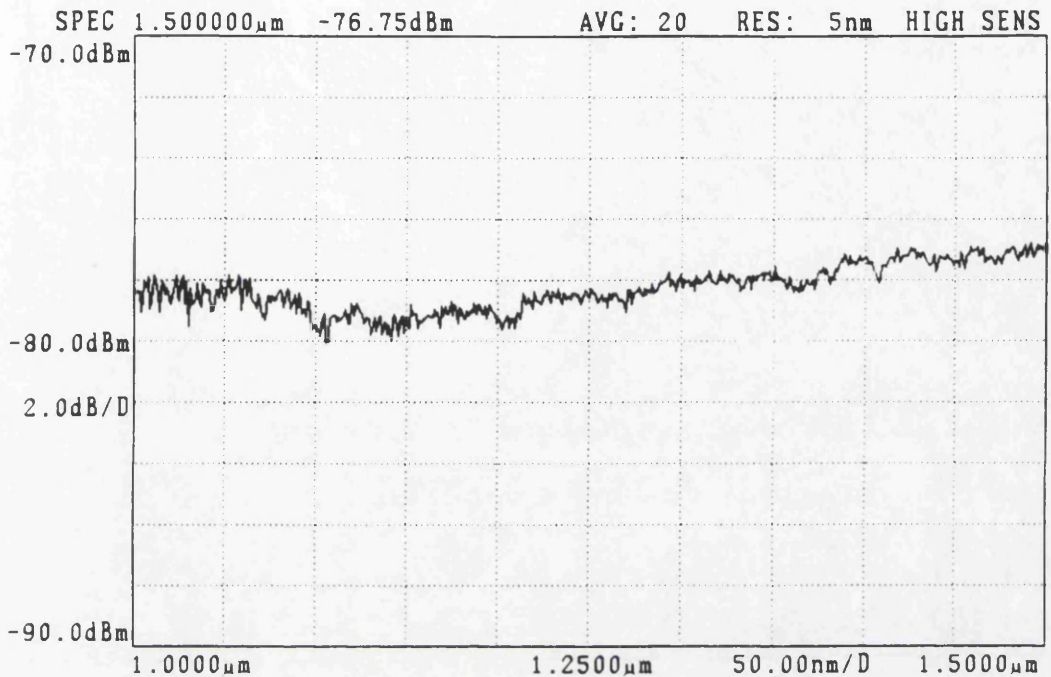


Fig. 5.22 Spectrum of white light source through a straight single waveguide.

For the single 3WC the rejection bandwidth centered at $1.05 \mu\text{m}$, which guarantees loss in excess of 20 dB, when measured with respect to the $0.8 \mu\text{m}$ centered passband maximum, is about 70 nm. This increases to $\sim 190 \text{ nm}$ by cascading three 3WCs. So there is an increase of $\sim 120 \text{ nm}$ in rejection bandwidth at -20 dB. In other words, the loss for a rejection band 100 nm wide increases from $\sim 13 \text{ dB}$ up to $\sim 36 \text{ dB}$ (Barbarossa '92 a).

The insertion loss at $1.3 \mu\text{m}$ increases for the cascaded configuration, rising from 7 to 9 dB. Beside the longer propagation length, a relevant factor in the increase in insertion loss is the radiation losses at the connections between two stages, which are due to the mismatch between the mode of the single input/connecting waveguide and the optimum linear combination of the three modes of the coupler (Donnelly '86), and which limits the power transfer efficiency in the device. Other contributions are given by fibre to channel waveguide coupling loss and waveguide propagation loss. The total insertion loss can be drastically reduced by reducing the fibre field mismatch employing

cladded waveguides with core size matched to the fibre core, which would optimise the fibre coupling efficiency and reduce the propagation loss.

Chirping of the spectra derives from the non linear relationship between coupling efficiency and wavelength. The shift in spectral response between the spectrum of the single 3WC and that of the cascaded 3WCs is thought to be due to a partial recoupling of the light between facing waveguides. Noise in the stopbands derives from the dynamic range limitation of the optical spectrum analyser. It can be demonstrated that wider rejection bandwidths can be achieved by feeding the central waveguide and connecting the cascaded couplers with the same waveguide. However, this configuration does not give full transfer efficiency to two outputs, and consequently is not suitable for multi-demultiplexing purposes.

5.4.3 Wavelength division multi-demultiplexer

Wavelength division multiplexing (WDM) of optical signals is well recognised for its potential in greatly increasing the transmission capacity of optical fibre communication systems (Ishio '84). The key device in a WDM transmission system is the multi-demultiplexer which performs the combining/sorting of the signals according to wavelength. Optical guided-wave multi-demultiplexers for widely spaced channels based on directional coupler wavelength selectivity have been reported for 1.3 and 1.55 μm (Takato '89, Cheng '91).

It has been pointed out that wide rejection bands are required in order to accommodate the wavelength variation and spectral width of ordinary laser sources in practical environmental conditions (Imoto '87). Wide rejection bands have been achieved by connecting three identical 2WC in a tree-structured fashion (Imoto '87), or perturbing the coupling coefficients of a single 3WC by periodically varying the span between the central and the outer waveguides (Kishioka '90). We have reported the realisation of a novel multi-demultiplexer

configuration where a wide rejection band has been achieved by cascading and appropriately connecting high-silica 3WCs (Barbarossa '92 b).

Our device has been designed for the duplexing of 1.3 and 1.55 μm wavelengths (Appendix D). It consists of three cascaded identical 3WCs connected by the two outer waveguides (configuration n. 6). To minimise recoupling of the light between the facing central waveguides of two successive stages, the length of the spacing s between the stages was 2.4 mm. The cross coupling between the outer waveguides in this region is weak due to the exponential decay of the evanescent field and it has not been taken into account in the design of the device. Nevertheless, the spacing s can be appropriately designed in terms of interaction length of an equivalent 2WC, whose spectral response can be included in the filter design. Fig. 5.23 and 5.24 show the theoretical spectral response of a single 3WC and of three identical cascaded 3WCs, respectively. These spectra correspond to an interaction length of 1.9 mm for the single 3WC.

The multi-demultiplexer spectral characteristics were measured using the same arrangement of Fig. 5.18. Fig. 5.25 shows the demultiplexing transmission characteristic for a single 3WC and Fig. 5.26 for the three cascaded 3WC configuration. The reported spectra correspond to an interaction length of 2.15 mm for both single and cascaded 3WCs, i.e. a length longer than expected was necessary to obtain a spectral response resembling the theoretical one. All the measurements were performed with input coupling to one of the outer waveguides. From their measured transmission spectra an extinction ratio lower than 25 and 30 dB has been estimated for single and cascaded configuration respectively.

For the cascaded configuration, the stopband which guarantees rejection loss in excess of 20 dB is wider than 160 nm for both 1.3 and 1.55 wavelength regions, which is about 2.6 times as large as the bandwidth of the single 3WC multi-demultiplexer. The insertion loss increases for the cascaded configuration rising from 5.5 to 7 dB for the 1.3 μm path and from 4 to 6 dB for the 1.55 μm path. Further improvement in filtering performance can be achieved by cascading more than three 3WCs.

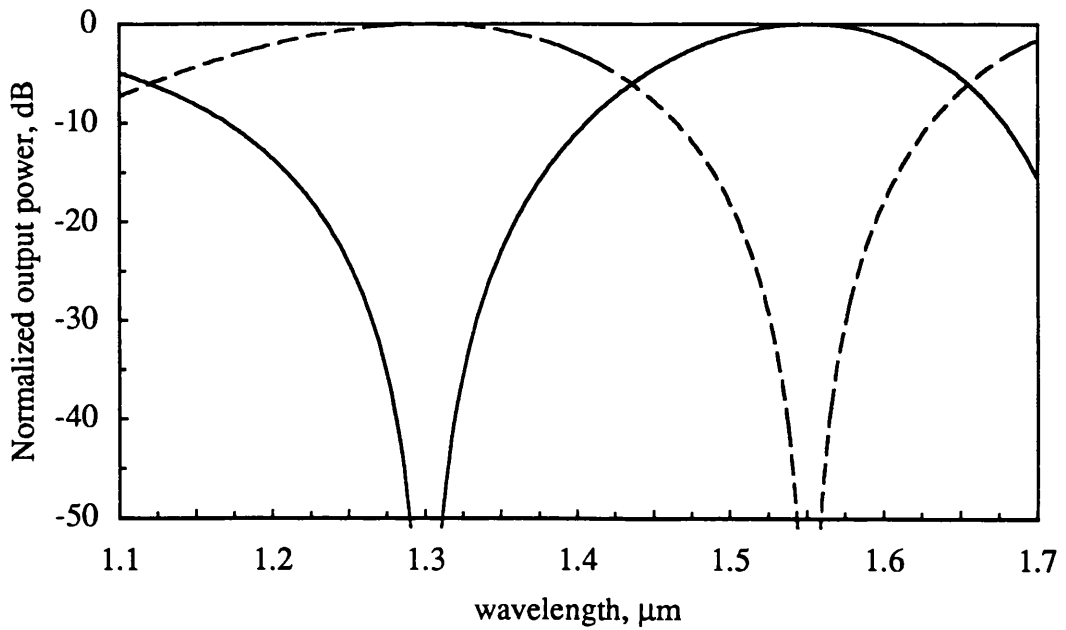


Fig. 5.23 Theoretical demultiplexing characteristic of single 3WC for input to one of the outer waveguides and output from the two outer waveguides (dashed curve = 1.3 μm port, solid curve = 1.55 μm port).

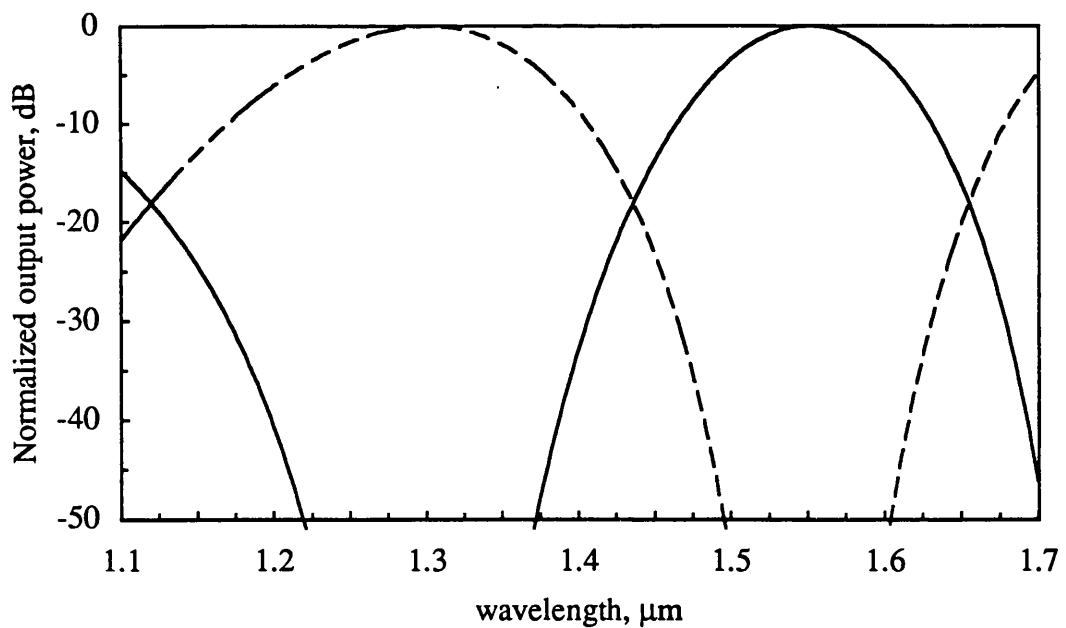


Fig. 5.24 Theoretical demultiplexing characteristic of three cascaded 3WCs (configuration n.6) for input to one of the outer waveguides and output from the two outer waveguides (dashed curve = 1.3 μm port, solid curve = 1.55 μm port).

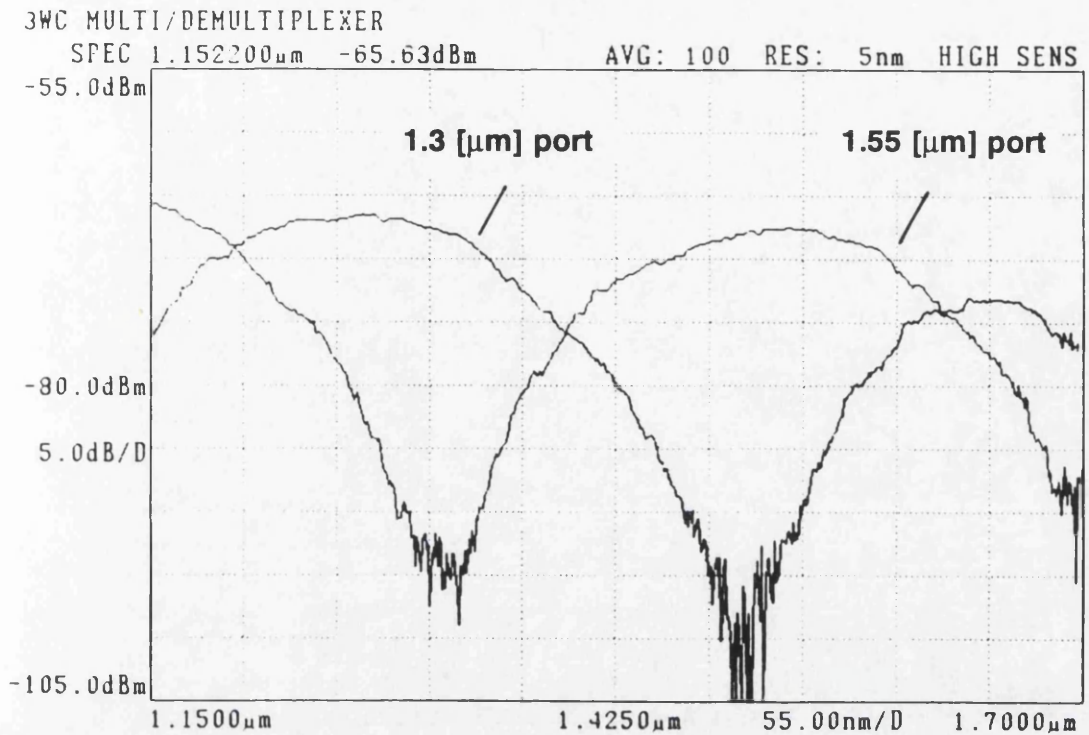


Fig. 5.25 Measured demultiplexing characteristic of single 3WC for input to one of the outer waveguides and output from the two outer waveguides.

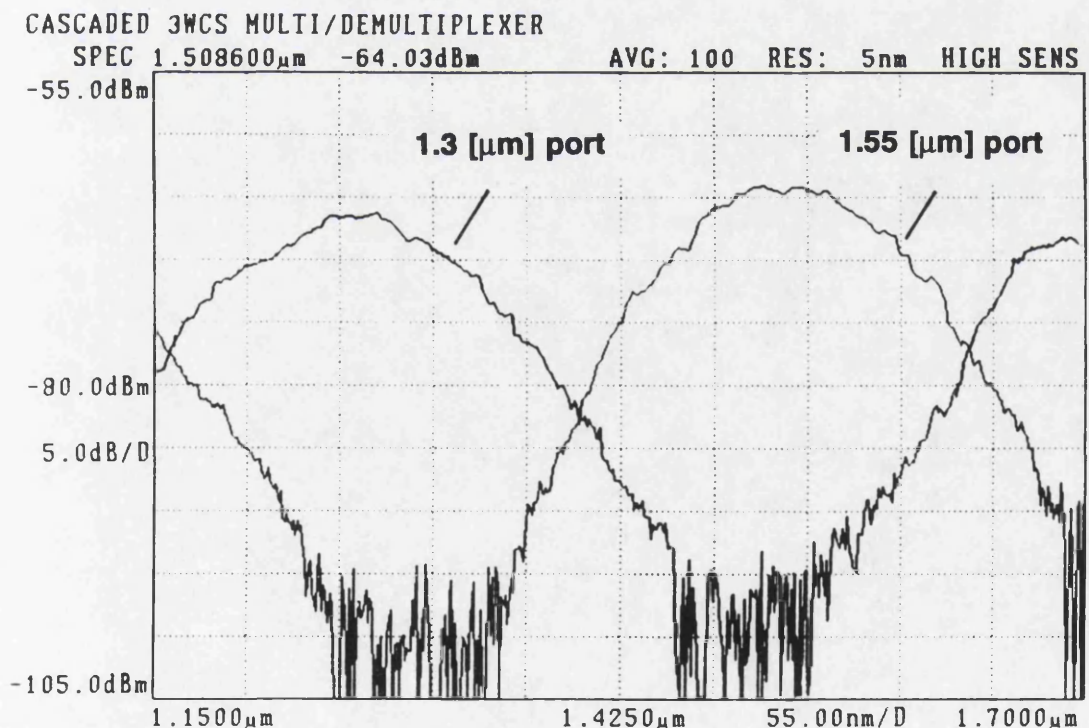


Fig. 5.26 Measured demultiplexing characteristic of three cascaded 3WCs (configuration n.6) for input to one of the outer waveguides and output from the two outer waveguides.

5.5 Summary

In this chapter we have concentrated our attention on the 3WC as a basic optical circuit element. The 3WC because of its own peculiarities lend itself to the realisation of short length power dividers and wide rejection band filters. Methods and criteria followed in the filter design have been described, particularly directed towards the improvement in rejection bandwidth of the filter spectral characteristic.

Wideband optical guided-wave filtering response has been achieved by cascading three 3WCs. This solution offers flexibility over the tuning of the passbands achieving at the same time high stopband rejection. An application has been demonstrated for use in fibre amplifier systems. Further improvement in filtering performance could be achieved cascading more than three 3WCs.

A novel configuration for a wide rejection band optical guided-wave multi-demultiplexer at 1.3 and 1.55 μm has been fabricated. For a stopband rejection loss of 20 dB, rejection bandwidths of 160 and 170 nm have been achieved for the 1.3 and 1.55 μm wavelength regions, respectively. Fibre compatibility of the devices presented can be improved by employing cladded waveguides with a core size compatible with that of the fibre to be connected, which would reduce the insertion loss of the devices.

Chapter 6. Vertical integration of high-silica content channel waveguides

Chapter Layout

- 6.1 Introduction**
- 6.2 Examples of VI reported in literature**
- 6.3 Requirements for VI of channel waveguides**
- 6.4 FHD peculiarities in a VI context**
- 6.5 Multi-nonidentical step fabrication process**
- 6.6 Multi-identical step fabrication process**
- 6.7 Patent pending**

6.1 Introduction

Since 1969, when Miller introduced the concept of IO, PLCs, proposed and fabricated, have been usually confined to a bidimensional extension and interaction. The density of integrable optical functions has been limited to the size of the substrate mainly by curvature radii and branching/bending waveguide angles compatible with acceptable losses, and by the minimum interaction length required to produce useful optical effects, such as directional coupling (Nishihara '89). The optical interaction has also been limited mostly to a planar geometry, i.e. the optical circuits have been essentially developed on the plane of the substrate.

Vertical integration (VI) of PLCs would in principle increase the density of optical functions available on the same substrate and the complexity of IO devices conceivable. By extending the optical interaction to a third dimension, those limits in substrate size, which have already been reached in some devices (e.g. Takahashi '91), could be potentially overcome. Moreover a combination of

horizontal and vertical directional coupling could originate a new generation of complex devices such as, for example, parallel optical signal processors.

In this chapter fabrication details on VI of single-mode waveguides at 1.55 μm are described. Critical parameters related to the FHD technology, such as the sintering temperature and the glass composition of the different deposited layers, are also discussed emphasising their relative limits for a successful VI. An alternative fabrication process is also presented. Potential applications of such a technological development will be discussed in the next chapter.

6.2 Examples of VI reported in literature

As early as in 1981, the fabrication of high density optical waveguide arrays was proposed by stacking two levels of identical patterns (Rose '81). The second level of waveguides was a replica of the first level, and was obtained by filling the gaps in between the waveguides of the first level, where an appropriate low index material was used to optically separate the two core structures (Fig. 6.1). In other words, the gaps in between the waveguides of the first level were of the same size of the waveguides and, after the deposition of a separating layer, the gaps were filled using the same core material of the first level. This solution is rather limited to arrays of parallel waveguides. Moreover, in the technical disclosure, no reference was made to the material employed, neither were fabrication parameters mentioned.

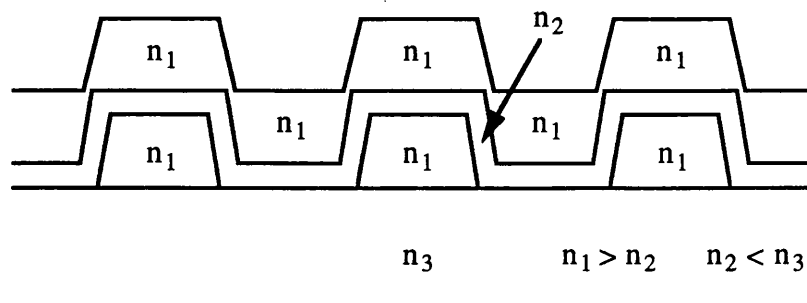


Fig. 6.1 Structure proposed by Rose ('81) for high density optical waveguide array. VI is limited to identical patterns for the two levels.

VI of Si slab waveguides on Si substrate has been recently demonstrated (Soref '91). The Si waveguides are interspaced by a SiO₂ buffer layer and, as it has already been said, they are slab waveguides. In the article, reference has been made by the authors to their patents (Lorenzo '88 a, b) in which the fabrication procedure for VI of Si channel waveguides on Si is proposed but not explained. Also no experimental evidence of such VI of channel waveguides has been reported in literature so far, to the best of the author's knowledge.

VI of ion-exchanged slab waveguides (Noutsios '92) has been also demonstrated. However, the graded-index waveguides of the two levels have different refractive index profile and peak value. A tunable filter based on a vertical coupler on InGaAsP/InP waveguides has been reported (Alferness '92). In this case the waveguides are of the strip loaded type, in which the guided mode of a slab guide is confined transversely by a dielectric or metal strip (Nishihara '89). Moreover, the waveguides have greatly different effective indices because of the different material composition. Therefore, efficient evanescent coupling between the waveguides has been achieved by interposing a phase matching grating. VI of AlGaAs waveguides and GaAs photodetector (Ade '92), or of surface emitting laser and phototransistor (Chan '92) have also been reported. These examples, however, have always realised localised vertical stacking of single on single element, rather than the definition of a second different optical circuit level on top of a first one.

We have reported for the first time (Barbarossa '92 c, d, e) VI of high-silica content channel waveguides on Si substrate. The fabrication process, which has made feasible the VI, is based on a practical multi-step combination of FHD, photolithographic patterning and RIE, and it is strictly related to the FHD peculiarities. We have integrated two levels of vertically uncoupled SiO₂-P₂O₅-GeO₂ based waveguides in SiO₂-P₂O₅ based cladding. It is worthwhile to emphasise that the vertically integrated waveguides are of the channel type, and that the patterns of the two vertical levels have been defined by two completely independent photolithographic and etching processes.

This result opens up a wide range of interesting applications, which could possibly see the extension of the optical guided-wave interaction to three dimensions and rely on bidimensional coupling to perform complex processing. It would certainly increase the density of guided-wave optical functions integrable on a single substrate.

6.3 Requirements for VI of channel waveguides

Although the VI of channel waveguides is an interesting idea, its implementation is not so straightforward. We can analyse those requirements necessary for a successful VI by means of fabrication techniques which involve the deposition of a guiding layer onto a substrate. Diffusion or implantation techniques, which produce a localised refractive index change of the substrate, are not taken into consideration here.

To define a second level of core structure a second “substrate” layer is necessary. This “substrate” layer has to be perfectly flat so as not to affect the propagation characteristics of the second core structure by causing mode conversion or increasing the propagation loss, and, at the same time, it has to allow planar photolithographic processing. This means that the cladding layer besides covering the first core structure has also to planarize itself or, at least, it has to be planarized.

Another point is that the fabrication process of the second level of VI has to involve temperatures which do not affect the core structure of the first level, or alternatively the first core structure has to be able to resist the following heat treatments, to preserve its geometry and composition. Interdiffusion of dopants between core and cladding and deformation of waveguiding structures have to be prevented.

It is also desirable to have identical optical properties for the two core structures and the two cladding layers. In fact, this would facilitate the modelling of vertical interaction, and phase matching between two vertically coupled

waveguides would be possible. Nevertheless, asymmetric waveguiding geometries, in shape and optical properties, would still be possible and could form the basis of particular applications.

Finally, mask alignment for the definition of the second level of core pattern relatively to the first level should be possible. This means that during the photolithographic definition of the second level pattern, the underlying core structure and its alignment marks must be clearly visible through the first cladding layer and second core layer.

6.4 FHD peculiarities in a VI context

FHD presents two peculiarities compared to other technologies for the fabrication of high-silica content waveguides, which in a VI context play an important role. The first peculiarity is the possibility of completely embedding the channel waveguides by the deposition of optical quality, thick cladding layers. At the same time a perfect planarization of the top surface of the cladding layer is achieved if it is thick enough. This peculiarity derives directly from the viscous nature of the sintering of glass microparticles on a rigid substrate (Scherer '85). The surface tension of the doped-silica glass soot which, at the sintering temperature involved in the process, has a low viscosity, tend to minimise the surface area of the cladding layer by planarizing it.

In other high-silica content technologies such as LPCVD (Verbeek '88), PECVD (Valette '88), PACVD (Nourshargh '85), or TO (Izawa '81), the cladding layer is conformal to the core shape, which means that it reproduces the shape of the structure on which it is deposited. Consequently, planarization is hard to achieve. Moreover, thick depositions effected by these technologies generally involve a degradation of the optical quality of the film, which often incurs cracking or flaking. Also, when thick cladding layers are deposited, undesirable cavities are formed between very close waveguides, as is the case with a directional coupler or a branching section (Maxwell '91).

The second peculiarity of FHD is the possibility of synthesising core glasses having the same refractive index but different minimum sintering temperature. This is easily achieved by varying the concentration levels of the silica dopants. We have already discussed in Chapter 3 the influence of the different dopants on the refractive index and sintering temperature of pure silica. Considering for example P_2O_5 and GeO_2 , this peculiarity derives directly from the fact that the rate at which the refractive index of doped silica increases for P_2O_5 doping is lower than for GeO_2 doping, and at the same time the rate at which the softening temperature of doped silica increases for P_2O_5 doping is higher than for GeO_2 doping. In other words, for the same amount of dopant, the increment in the refractive index of silica caused by GeO_2 is higher than that caused by P_2O_5 . On the other hands, the decrement in sintering temperature of silica caused by a certain amount of GeO_2 is lower than that caused by the same amount of P_2O_5 . This is clear if we compare the curves of refractive index and softening temperature of doped silica versus dopant concentration for GeO_2 and P_2O_5 (see Figs. 3.1 and 3.2 in chapter 3).

These two peculiarities allow us to proceed vertically in the fabrication process, as a planarizing cladding layer can be fabricated and can act as a substrate on which a second core layer can be deposited. The second core is afterward sintered at a lower temperature than the first one without adversely affecting the underlying core structure. With FHD it is possible, by varying silica dopants concentrations, to achieve a difference of more than 240 °C in the sintering temperature of the different glasses, as well as a much shorter sintering time, and to deposit up to 200 μm thick layers without incurring film cracking (Kawachi '90).

6.5 Multi-nonidentical step fabrication process

The steps of the fabrication process are summarised in the schematic diagram of Fig. 6.2 (dimensions are not in scale). Fabrication parameters relative to each step are reported in Table 6.I. We have used Si wafers with a thermally grown SiO_2 buffer layer as substrate. However, silica substrates or Si wafers with a suitable deposited buffer layer, can also be used.

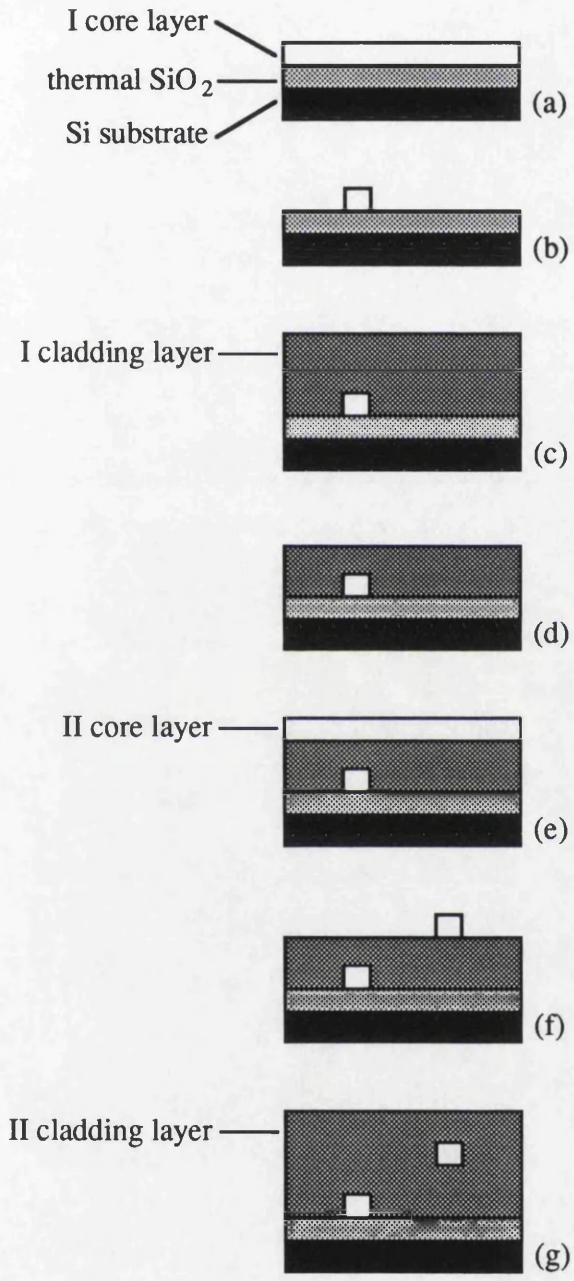


Fig. 6.2 Fabrication steps for vertical integration of high-silica channel waveguides by using different core and same cladding composition for the two levels of vertical integration:

- a) I core layer deposition
- b) I core layer etching
- c) I cladding layer deposition
- d) planar polishing or etching (optional)
- e) II core layer deposition
- f) II core layer etching
- g) II cladding layer deposition

Layer	I	I	II	II
Type	core	clad	core	clad
Thickness (μm)	4	12	4	12
Sintering temperature ($^{\circ}\text{C}$)	1385	1140	1265	1140
Sintering time (minutes)	120	30	10	30
SiCl_4 flow rate (cm^3/min)	120	120	120	120
PCl_3 flow rate (cm^3/min)	16	120	60	120
GeCl_4 flow rate (cm^3/min)	104	-	60	-
Deposition speeds - torch: 25 mm/min, turntable: 25 rev/min				
Flame flow rates - H_2 : 4 l/min, O_2 : 6 l/min				

Table 6.I Fabrication parameters for different deposited layers for VI of channel waveguides by using P_2O_5 and GeO_2 as silica dopants.

A first core layer is fabricated by depositing and sintering low density $\text{SiO}_2\text{-P}_2\text{O}_5\text{-GeO}_2$ glass soot (a). It is preferable to synthesise a core material which has a high softening temperature, in view of the heat treatments which follow. In our case the core was leaner in P_2O_5 and richer in GeO_2 . This first core layer is sintered at a maximum temperature of 1385°C for 2 hours. Patterning of the film is accomplished by a standard combination of photolithographic process and RIE (b), as has already been described in Chapter 4. A first cladding layer, thick enough (>3 times the core height) to achieve perfect planarization, is subsequently deposited by synthesising low sintering point, soft $\text{SiO}_2\text{-P}_2\text{O}_5$ glass (c). Sintering of the first cladding is carried out at 1140°C for 30 minutes. Being consolidated at 245°C below the minimum sintering temperature of the first core glass, the formation of the cladding layer prevents the deformation of the guiding structure previously fabricated. Because of the surface tension at the sintering temperature, the cladding layer distributes itself so to minimise the surface area and, if it is thick enough, perfect planarization of the top surface of the layer is achieved. If coupling between the two levels of integration is required, the cladding thickness can be easily reduced by planar polishing or anisotropic etching to the desired value to obtain effective vertical directional coupling (d). A second $\text{P}_2\text{O}_5\text{-GeO}_2\text{-SiO}_2$

doped silica core layer is afterwards deposited on the first cladding layer, which now acts as a new substrate (e). The doping of the second core is such as to obtain a refractive index as close as possible to that of the first core, and a lower sintering temperature. This is obtained by synthesising a core layer richer in P_2O_5 and leaner in GeO_2 , with respect to the first core. The maximum sintering temperature for the second core is $1265\text{ }^\circ\text{C}$, for a period of 10 minutes. The short time at the maximum temperature and a difference of $120\text{ }^\circ\text{C}$ with respect to the sintering temperature of the first core layer, prevents the deformation of the underlying core structure and reduces the outdiffusion of the core dopants into the cladding material. Finally, after the definition of the second core structure (f), a further P_2O_5 -doped silica cladding layer is deposited on top of the second etched core structure (g). Sintering temperature and time are identical to those of the first cladding layer.

Critical parameters of the fabrication process are: the difference between the minimum sintering temperatures of each core and the cladding glass, and between those of the two cores; the minimum time required for the complete sintering of each layer; the minimum thickness of the intermediate cladding layer in order to achieve a perfect planarization, suitable for the deposition of a further core film.

An optical microscope photograph in transmission relative to the cross section of the vertically integrated waveguides is shown in Fig. 6.3. The core size of the waveguides was $4\text{ by }4\text{ }\mu\text{m}$. The refractive index step relative to the cladding was 0.65% for the first core and 0.6% for the second. These values were estimated by the mode synchronous coupling angles on planar films fabricated in similar conditions. The difference in refractive index between core and cladding, as well as the preservation of the geometry relative to the first core structure, after the subsequent heating treatments, are clearly visible in the photo. The vertical pitch separation between the two guides is $10\text{ }\mu\text{m}$, the horizontal is $25\text{ }\mu\text{m}$.

The VI waveguides shown in Fig. 6.4 have been fabricated using the same parameters of Table 6.I except for the cladding layer thicknesses. These were $26\text{ }\mu\text{m}$ for the first cladding layer and $20\text{ }\mu\text{m}$ for the second.

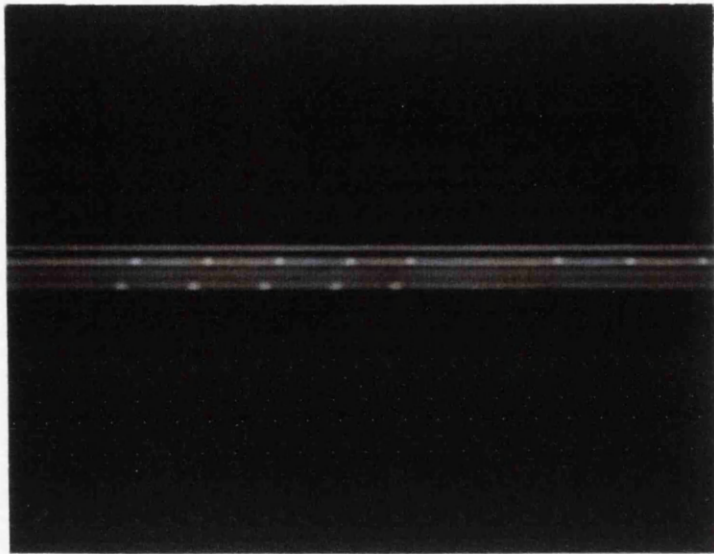


Fig. 6.3 Optical microscope photograph in transmission of cross sectional view of VI high-silica channel waveguides (fabrication parameters as in Table 6.I).

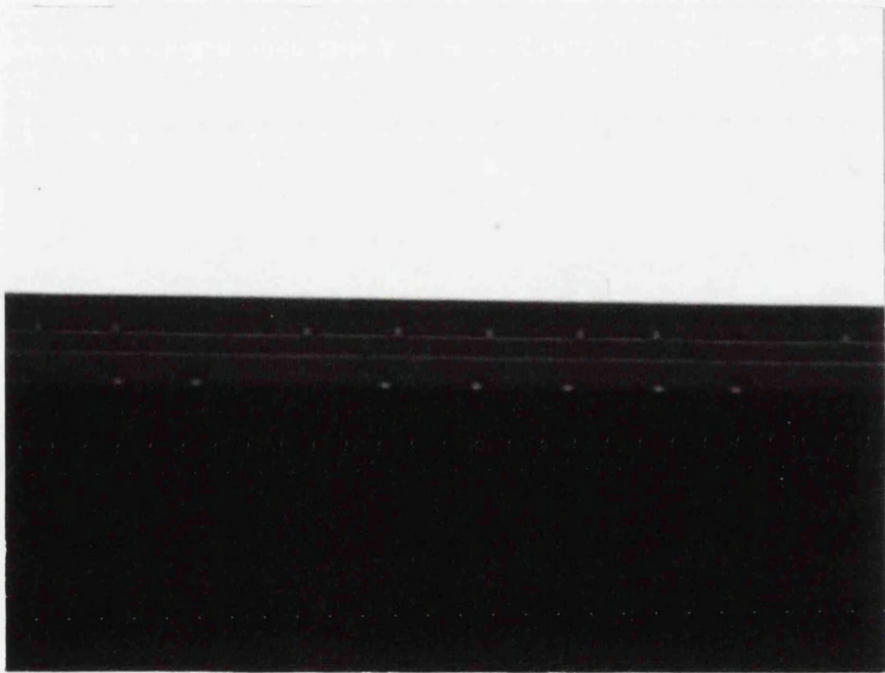


Fig. 6.4 Optical microscope photograph in transmission of cross sectional view of VI high-silica channel waveguides (cladding layer thicknesses: first 26 μm , second 20 μm).

A view from the top of the VI waveguides is shown in Fig. 6.5 a and b. In the top photo the microscope has been focused on the second level of waveguides. By defocusing the objective, both levels of waveguides are visible in the bottom photo. To enhance the contrast a Nomarski interferometer is essential on the microscope. This is also advantageous during mask alignment for the photolithographic definition of the second core pattern to enhance the contrast of the buried first core structure and relative alignment marks. In fact, we found it quite hard to align the patterns of the two layers, because of the poor depth of field of the microscope of the mask aligner. The small refractive index step ($\sim 0.6\%$) between core and cladding also did not help in this sense.

The two arrays of waveguides were deliberately misaligned to demonstrate that it is possible to obtain a VI which can not be obtained via a single, deep etching of stacked planar waveguides. This means that different patterning can be etched onto the two levels.

The horizontal banding visible in the cladding derives from deposition that has been achieved in separate steps. We found it in fact preferable, in terms of planarization and film quality, to fabricate thick layers by multiple thin depositions rather than by a single thick one. Because of surface tension, the thickness of a cladding layer deposited on top of an etched core structure, after sintering, is smaller than beside it. This effect is clearly visible in Fig. 6.3. The first black stripe from the bottom, which corresponds to the deposition limit of the first cladding layer, is parallel to the substrate line. I.e., during the sintering process, glass soot is pulled by surface tension from the top of the etched core structure and the cladding layer is reasonably planarized. Therefore, an acceptable planarization occurs even if the thickness of the deposited cladding layer is comparable with that of the etched structure. A further cladding layer is afterward deposited to obtain perfect planarization. Direct deposition of too thick ($>15\ \mu\text{m}$) cladding layers is not desirable as cracking can be easily experienced (see chapter 3, paragraph 6).

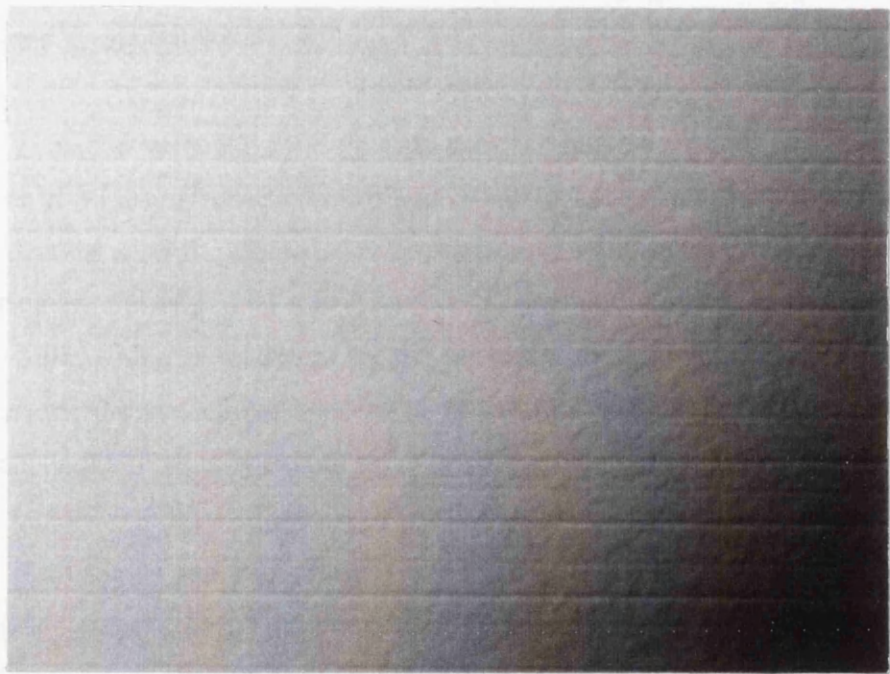
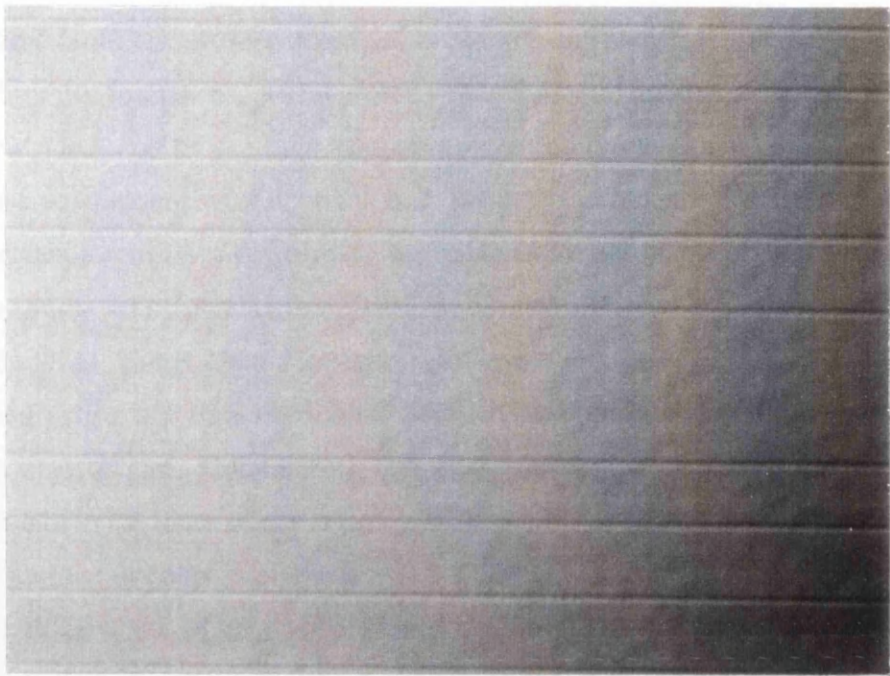


Fig. 6.5 Optical microscope photographs of VI waveguides view from the top. The microscope has been focused on the second level of waveguides in the top photo and then it has been defocused in the bottom photo, showing in this way both levels of waveguides.

Although the different cladding layers have been deposited by using identical fabrication parameters (as is shown in Table 6.I) a discontinuity was noted at the interfaces, which means that P_2O_5 diffusion occurred. This was probably induced by the high temperature of the flame at the beginning of each successive cladding layer deposition. A similar phenomenon has been observed in the fabrication of fibre preform by the VAD and it has been attributed to the same cause (Sudo '81). Also it is clear that the first core dopant is somehow diffused in the cladding, rather than deformed. However, this does not seem to affect the guiding properties in a significant manner, as both layers of cores were single mode at $1.55 \mu\text{m}$. Considering that there is almost one order of magnitude difference in the thermal expansion coefficient between the Si substrate ($2.5 \cdot 10^{-6} \text{ }^\circ\text{C}^{-1}$) and the doped silica layers ($\sim 0.5\text{-}1 \cdot 10^{-6} \text{ }^\circ\text{C}^{-1}$), the total absence of cracking in the thick stack of deposited glass layers and the compressive nature of the stress caused by such a difference of expansion coefficients highlights the tight fusion which must take place between the thermally grown SiO_2 layer and the deposited layers (Kawachi '90).

VI based on such a fabrication process has two major limits: first, the number of VI levels achievable without incurring core structure deformation. This limit derives directly from the restricted range of temperature over which the sintering is allowed. The second limit is the maximum refractive index step achievable, which is restricted by the necessity to achieve a lower temperature process for the successive level to be fabricated. The availability of alternative dopants could eventually extend these limits.

Both GeO_2 and P_2O_5 raise the refractive index of silica and decrease its sintering temperature. However, the refractive index step between core and cladding derives only from the GeO_2 , because the higher content of P_2O_5 in the cladding, with respect to the core, contributes to reducing the relative refractive index step. The lower doping level of P_2O_5 into the core is necessary to give it sufficient rigidity during the subsequent heat treatments. It is necessary to synthesise for the second core a softer glass with respect to the first core glass,

having a higher content of P_2O_5 , counterbalanced, in order to obtain the same refractive index step between core and cladding for the two levels of integration, by a lower GeO_2 doping level. The uppermost limit of P_2O_5 and GeO_2 content in SiO_2 , which in films deposited by FHD is determined by film degradation due to residual stress (Kawachi '83), imposes the lowest limit in sintering temperature of successive cores and consequently the number of integrable levels.

In this sense, a useful degree of freedom would be certainly offered by the use of B_2O_3 or F as cladding dopants, which both decrease the refractive index of silica and lower its sintering temperature, or of TiO_2 as core dopant, which increase both refractive index and sintering temperature of silica (Barbarossa '92 c). This would give the possibility of achieving higher refractive index steps between core and cladding, while simultaneously obtaining a larger difference in the sintering temperatures of the two core layers. A possible recipe for a two level VI with high refractive index step waveguides, is indicated in Table 6.II.

Layer	I	I	II	II
Type	core	clad	core	clad
Thickness (μm)	4	12	4	12
Sintering temperature ($^{\circ}C$)*	1390	1120	1240	1120
Sintering time (minutes)*	60	30	30	30
P_2O_5 (wt %)	5	8	10	8
B_2O_3 (wt %)	-	9	-	9
TiO_2 (wt %)	3	-	-	-
GeO_2 (wt %)	-	-	7	-
Deposition speeds - torch: 25 mm/min, turntable: 25 rev/min				
Flame flow rates - H_2 : 4 l/min, O_2 : 6 l/min				

Table 6.II Proposed fabrication parameters for different deposited layers for VI of high Δn channel waveguides by using as silica dopants P_2O_5 , B_2O_3 , TiO_2 and GeO_2 (* supposed values).

The necessity of having the same refractive index step for two or more levels of VI, in order to have phase matching and hence efficient coupling from one level to another, can be removed by modifying the geometry of the core structures. Marcuse ('87) has demonstrated that for vertically coupled asymmetric planar waveguides, phase matching is possible by opportunely sizing the core dimensions. Consequently, the range of glass composition at low sintering point for the second level of fabrication can be extended, not being limited to those compositions which have the same refractive index as the underlying core structure. Theoretical modelling has been reported for dielectric channel waveguides in different layers (Matsumura '86). However, the treatise is limited to identical core size and refractive index and the calculations have been performed in the millimetre wavelength range.

6.6 Multi-identical step fabrication process

As an alternative to the process just described, we propose now an approach of step and repeat type, where all the vertical levels are identical. That is, the refractive index and composition of the second core and cladding are identical to those of the first core and cladding, respectively. Having the same refractive index and the same composition, the fabrication parameters are also the same. The inconveniences regarding core deformation and refractive index are resolved in this proposal by using a PECVD SiO₂ "capping" layer.

The steps of this alternative fabrication process are summarised in the schematic diagram of Fig. 6.6. After the deposition (a) and etching (b) of the first core layer, a first PECVD SiO₂ layer is deposited on top of it (c). This layer, as schematised in Fig.6.6, is conformal to the etched core and is only few microns thick. Silicon planar electronic technology relies on the SiO₂ as a masking material to prevent diffusion of impurity atoms into Si (Sze '83). Moreover, at the sintering temperatures involved (<1400 °C), pure silica is in the solid state (melting point 1610 °C). Hence, the purpose of this layer is to contain the deformation of the core geometry and to minimise dopant interdiffusion between core and cladding during the following high temperature treatments.

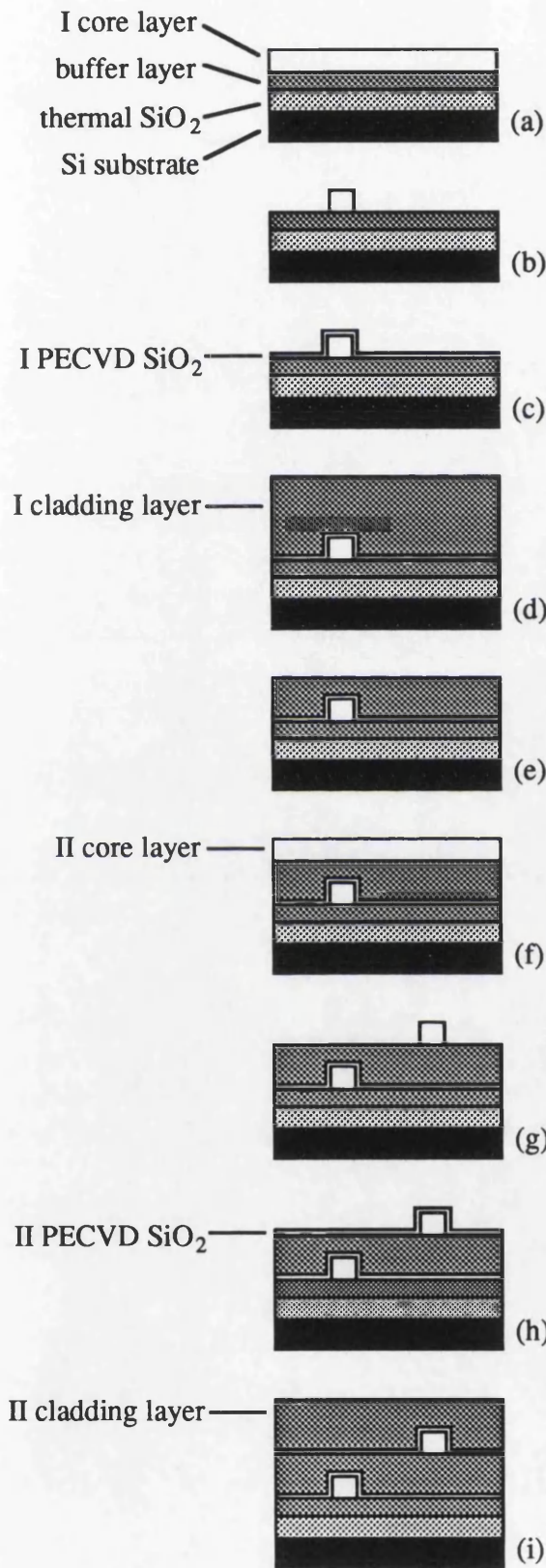


Fig.6.6 Proposed fabrication steps for vertical integration of high-silica channel waveguides by using same core and cladding composition for the two levels of integration:

- a) I core layer deposition
- b) I core layer etching
- c) I PECVD SiO₂ layer deposition
- d) I cladding layer deposition
- e) planar polishing or etching (optional)
- f) II core layer deposition
- g) II core layer etching
- h) II PECVD SiO₂ layer deposition
- i) II cladding layer deposition

The refractive index of SiO₂ deposited by PECVD is generally higher than that of fused silica and it can be higher than that of the cladding layer to be deposited. Annealing has been proved to be an effective way of reducing it (Maxwell '92 a). This can be accomplished during the sintering of the first cladding layer which is deposited afterwards (d). As in the previous process, depending on the requirements, planar polishing or anisotropic etching can be necessary if coupling between the different vertical levels is required (e). Then the steps are repeated identically (f, g, h, i) obtaining a second cladded core structure having the same refractive index and composition as the first one.

This fabrication process has the obvious advantage that the steps for each vertical level are identical and consequently, at least in theory, it could be extended to a larger number of levels of integration than the previous process. Moreover, the limitation on the refractive index step achievable, as it has already been discussed, is removed. Fabrication parameters are the same which are used for a single cladded core level. The disadvantage, with respect to the first process, is the presence of an extra step per level for the deposition of the PECVD SiO₂ layer, which also involves a different technology.

A further step could be the deposition of a thin PECVD SiO₂ layer after the deposition of the first cladding layer and before that of the second core layer (Barbarossa '92 c). This PECVD SiO₂ layer in fact should act as a barrier to dopant interdiffusion between the second core and the underlying clad at the temperature involved in the following fabrication steps.

This process has also been attempted by the author. A 3 μm SiO₂ layer was deposited using a Plasma Technology PECVD reactor. However, because of the poor quality of the SiO₂ layer deposited, the integration could not proceed vertically. In fact, the material deposited using the PECVD reactor available in the Department, is rather a mixture of SiO₂ and SiN (Wilkinson '92), deriving from a partial reaction between SiH₄ and N₂O. The resulting material had consequently, as the experiments have shown, a very different thermal expansion coefficient

than the underlying $\text{GeO}_2\text{-P}_2\text{O}_5$ -doped silica, which caused the flaking and peeling off of the deposited layer. Also poor adhesion can be argued between the deposited PECVD layer and the etched structure. So deposition of the cladding and following layers by FHD could not be carried out. Also, the PECVD layer deposited had a much higher refractive index than the underlying core material synthesised by FHD (being 1.97 the refractive index of SiN at infrared wavelengths). It has to be said that the departmental reactor has always been used for electronic dielectric passivation or masking, and little attention had been paid to obtaining pure, optical quality, SiO_2 layers.

6.7 Patent pending

Both fabrication processes and further details described in this chapter have been invented by the author of this thesis and they have been protected by a patent application (n°. 9202463.7, priority (0)) to the U.K. Patent Office, which has been filed on the 5th of February 1992 on behalf of British Telecommunications plc. (IPD case n°. A24443). At the time of writing this thesis the patent application has not yet been published.

Chapter 7. Conclusions and further work

Chapter Layout

- 7.1 Conclusions
- 7.2 Outlines for further work

7.1 Conclusions

This thesis has been concerned with the technological aspects of FHD regarding the fabrication of high-silica content waveguides for the development of passive planar lightwave circuits.

A FHD system for research purposes has been engineered and assembled, which has allowed us to carry out, until the time of writing this thesis, more than 1500 depositions without incurring exceptional problems and by carrying out only ordinary maintenance work. Improvements of the system in terms of flexibility, reproducibility and yield are possible and necessary, and they will be illustrated in the next paragraph.

Phosphosilicate glass slab and channel waveguides have been fabricated for the first time by FHD (Barbarossa '91 a). Difficulties inherent in the glass composition which have been encountered in the fabrication process have been understood and resolved. The influence of the sintering process on the dopant incorporation has been investigated (Barbarossa '92 g). Volatilization of the P_2O_5 phase from the silica matrix has been observed at different levels after different thermal treatments. An optimum sintering process has been determined in order to produce bubble free, low loss, completely sintered waveguides. Also SiO_2 - P_2O_5 -

GeO₂ slab and channel waveguides have been fabricated. Typical loss values achieved for both P₂O₅ and P₂O₅-GeO₂-doped silica planar waveguides were < 0.06 dB/cm at $\lambda = 1.32 \mu\text{m}$.

The optical power handling capability of both types of silica-based glass channel waveguides has been assessed (Barbarossa '92 f). The experimental results, which should be strictly related to the fabrication process and experimental condition used, have demonstrated an optical power threshold before catastrophic damage for SiO₂-P₂O₅ waveguides almost double that for SiO₂-P₂O₅-GeO₂ waveguides at $\lambda = 1.064 \mu\text{m}$. Q-switch frequency does not seem to affect the optical damage threshold, as this is rather decided by the peak power level. Cumulative effects have not been observed for exposure times up to 1 hour. For the damage to extend over a distance much greater than the wavelengths of operation, we believe that it is similar to self-propelled self-focusing damage observed in silica optical fibre of similar composition (Kashyap '88).

3WC-based simple devices have been designed and fabricated. A power splitter (Barbarossa '91 b), a filter and a wavelength multi-demultiplexer have been realized by using high-silica 3WCs on Si substrate. It has been demonstrated that by cascading 3WCs it is possible to achieve significant improvement in filtering performance in terms of rejection bandwidth. By cascading three 3WCs, a rejection bandwidth at -20 dB more than 2.7 times as large as the bandwidth of a single 3WC has been achieved (Barbarossa '92 a). A wide rejection band WDM at 1.3 and 1.55 μm , based on cascaded 3WCs has been also demonstrated. For a stopband rejection loss of 20 dB, rejection bandwidths of 160 and 170 nm have been achieved for the 1.3 and 1.55 μm wavelength regions respectively (Barbarossa '92 b).

Vertical integration of high-silica channel optical waveguides has been demonstrated for the first time (Barbarossa '92 d, e). The fabrication process, which has made the vertical integration feasible, consists of a practical multi-step combination of FHD, photolithographic patterning and RIE. Geometrical and optical characteristics of the guiding structures are preserved after the successive

heat treatments, which are necessary to build up the stacked structure, by proper choice of the doping levels of GeO_2 and P_2O_5 . We have described the successful application to a double integration of single-mode waveguides at $1.55 \mu\text{m}$ and suggested variations to the process regarding the use of further silica dopants to improve the results obtained. An alternative fabrication process, which employs the use of a PECVD SiO_2 capping layer, has been also proposed. Both fabrication processes and further details have been protected by a patent application on behalf of the industrial sponsor of this research project (Barbarossa '92 c). This result, which has been possible thanks to the FHD peculiarities, by extending the optical interaction to a third dimension, opens up a wide range of original and promising applications, such as vertically coupled devices or parallel optical signal processors, and it can effectively increase the density of optical guided-wave functions integrable on the same substrate.

7.2 Outlines for further work

Flexibility in the fabrication process can be significantly increased by using further silica dopants such as B_2O_3 , TiO_2 and F. By employing these glass formers, an extended range of refractive index steps and sintering temperatures could be obtained. The availability of these silica dopants would be an essential requirement especially in the fabrication of high Δn clad waveguides and in a VI context.

A temperature controlled turntable, which could be heated up to few hundred $^\circ\text{C}$, would allow one to carry out depositions at different substrate temperatures in a more reproducible manner. Also flame-turntable relative position, H_2/O_2 flow rates, deposition speeds and exhaust extraction power should be investigated in such a way as to minimise their effect on the turntable temperature and consequently the substrate temperature.

Different sintering atmospheres should also be investigated. The use of a He atmosphere, for example, by increasing the permeability through the glass of the trapped gases, would certainly be beneficial in achieving bubble free films,

independently from their thickness and the sintering temperature gradients adopted. Contamination problems of the sample surface from silica chips deriving from the inevitable devitrification of the fused quartz furnace tube, could be probably eliminated by using an internal jacket made of a different material such as platinum or alumina.

The yield of the planar fabrication process could be definitely improved by housing the whole system, furnace included, in a clean room, not necessarily of a very low class. This would reduce film inclusions and surface defects caused by an uncontrolled environment. Also, because of the strong moisture sensitivity of the materials employed and with the deposition being carried out at atmospheric pressure, a humidity-controlled environment would be beneficial for the reproducibility of the results.

Microanalytical investigations should be carried out to quantitatively correlate the optical characteristics of the glasses deposited and their compositions. Structural analysis would also be helpful for a more quantitative definition of glass composition as a result of different sintering processes. For example, it would allow a quantitative evaluation of the amount of P_2O_5 lost in the gas phase during the consolidation of SiO_2 - P_2O_5 films. Also, mercury or gas porosimetry would be helpful in a precise correlation between the degree and rate of sintering and the thermal process adopted.

The development of fully fibre compatible channel waveguides should also be addressed. For this purpose a suitable etching process should be developed to allow a faster ($> 0.1 \mu\text{m}/\text{min}$) and deeper etching ($> 6 \mu\text{m}$) with vertical and smooth walls. Also cladded geometries should guarantee better field matching between fibre and channel waveguide and would drastically reduce the scattering losses due to sidewall roughness caused by the etching process. In this context, the availability of silica refractive index depressants, such as B_2O_3 and F, would be essential.

Investigations on optical damage power threshold could be carried out also

for TiO₂-doped silica waveguides and the influence of B₂O₃ or F co-doping could also be addressed. Higher power damage threshold should be expected for annealed or cladded waveguides. Waveguide mode profile characterisation will also be necessary to precisely evaluate the peak power level at the damage threshold.

The incorporation in the glass matrix by aerosol doping technique of transition metals like Cr, Fe, Cu etc. , could be researched for the fabrication of novel waveguide materials for non-linear optical applications.

Further improvement in the rejection bandwidth of 3WC-based WDM could be obtained by increasing the number of cascaded stages. Long length cascaded 3WCs could also be investigated. Folded architectures could be regarded as a viable means of achieving very narrow aperiodic passbands, thus resolving the length constraints imposed on the optical circuit by the substrate size. 3WC-based multiple power splitters could also be realised, thus exploiting the shorter 3 dB coupling length of the 3WC compared to the 2WC.

Beside an increased flexibility in the fabrication process, the use of further silica dopants would also be advantageous in a VI context. By using TiO₂ instead of GeO₂ as core dopant, a more rigid core structure could be synthesised, achieving at the same time higher refractive index steps. Also by using B₂O₃ or F as cladding dopants, lower sintering temperatures and higher refractive index steps could be achieved. The use of B₂O₃ and F in the core material could also be investigated. For example, doping of core material with B₂O₃ counterbalanced by an increase of GeO₂ or P₂O₅ could be a viable means of decreasing the sintering temperature of the second core structure, without increasing its refractive index. Use of Al₂O₃ substrates would allow the fabrication of high sintering temperature core materials (≈ 1500 °C) for the first core level, thus allowing one to obtain a larger difference between the sintering temperatures of first and second core structures.

Fabrication of simple two waveguides vertical couplers could be the next

step in the investigation of the possibilities offered by VI. Complicated multi-waveguides coupled structures could be successively addressed in a parallel signal processing context. An interesting application of VI could be the development of a passive circuit on one level and of an active rare-earth doped layer on another level, thus overcoming the problem of high losses induced by the rare-earth doping and by the absorption of a three level laser system as Er.

Vertical folding of long length devices could be a promising avenue of investigation. For this purpose, a viable means of optical interaction between different levels, beside directional coupling, should also be investigated. Gratings and vertical 90° reflection corners at the edges of the chip could be examples of vertical interconnection. They would have the advantage that coupling between the layers can be obtained in a more restricted area and the circuits would be completely uncoupled in other areas. The disadvantage would be a more complicated fabrication process involving extra photolithography and etching for the gratings and accurate polishing and metal evaporation for the 90° reflection corner.

Theoretical modelling of vertically coupled channel waveguides could also be addressed as future work. The influence on the phase matching of coupled waveguides with different core size, different core refractive index, and their relative horizontal position should be addressed. Multiple coupled waveguides and grating to grating vertical coupling could also be further fields of research.

Appendix A. Four-layer planar optical waveguide theory

In this Appendix the theory regarding four-layer planar optical waveguides is briefly illustrated. The numerical solution of the eigenvalue equation reported at the end of the Appendix has allowed to determine the waveguide loss values due to substrate coupling which have been stated in Chapter 3.

The waveguide geometry that we consider is the four layer planar structure shown in Fig. A.1. In this structure the uppermost medium has a low refractive index, and it corresponds to air or a very thick cladding layer. The second layer corresponds to the guiding layer and has a refractive index larger than that of the first and third layer. The third layer is a buffer layer that has the role of isolating light in the guiding layer from the fourth layer. This is very thick, has a refractive index higher than the other layers and may be absorbing at the wavelength of interest. Since one of the outer semiinfinite layers in the structure being considered here has a larger refractive index than the other layers, the waveguide modes are not strictly bound modes, but instead leaky modes (Tamir '86).

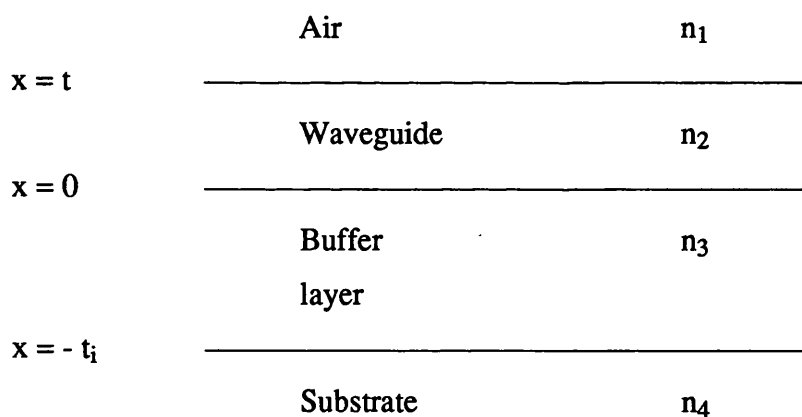


Fig. A.1

The modes are thus characterised by a complex propagation constant, with the imaginary part corresponding to attenuation due to energy radiating away from the guiding layer. In order to describe the modal behaviour in this structure,

Maxwell's equations must be solved in the four regions with the appropriate boundary conditions applied at each interface. Since the structure in Fig. A.1 is composed of planar layers that are homogeneous and isotropic in the y and z directions, we consider propagation in the z direction and ignore field variations in the y direction.

We consider TE mode solutions that are specified by solutions for the y component of electric field E_y and TM mode solutions that are specified by solutions for the y component of magnetic field H_y . These fields will be of the form

$$\Phi_y(x,z,t) = \Phi_y(x)\exp(-j(\beta z - \omega t)) \quad (\text{A.1})$$

where β is the mode complex propagation constant. For fields of this form, the scalar wave equation reduces to

$$\frac{d^2\Phi(x)}{dx^2} - (\beta^2 - k^2 n^2)\Phi(x) = 0 \quad (\text{A.2})$$

where $k=2\pi/\lambda$ is the free-space wavenumber, λ is the wavelength, n_i is the refractive index of the i th layer and $\Phi(x)$ is $E_y(x)$ or $H_y(x)$ for TE or TM modes respectively. We seek solutions of (A.2) in the four-layer structure shown in Fig. A.1 where $n_3 < \text{Re}[\beta/k] < n_2$, assuming $n_3 > n_1$. We consider these solutions because they correspond to guided modes for the three-layer structure in the limiting situation where the fourth layer is omitted and the third layer becomes semiinfinite. For the situation where the previous inequality is satisfied and where we impose radiation conditions at $x = \pm\infty$, solutions of (A.2) have the form

$$\Phi(x) = A \exp(-qx) \quad \text{Region 1 } (x > t) \quad (\text{A.3a})$$

$$\Phi(x) = B \sin(hx) + C \cos(hx) \quad \text{Region 2 } (0 < x < t) \quad (\text{A.3b})$$

$$\Phi(x) = D \exp(px) + F \exp(-px) \quad \text{Region 3 } (-t_1 < x < 0) \quad (\text{A.3c})$$

$$\Phi(x) = G \exp(jsx) \quad \text{Region 4 (} x < t_i \text{)} \quad (\text{A.3d})$$

where

$$q = (\beta^2 - k^2 n_1^2)^{1/2} \quad (\text{A.4a}) \quad h = (k^2 n_2^2 - \beta^2)^{1/2} \quad (\text{A.4b})$$

$$p = (\beta^2 - k^2 n_3^2)^{1/2} \quad (\text{A.4c}) \quad s = (k^2 n_4^2 - \beta^2)^{1/2} \quad (\text{A.4d})$$

Imposing boundary conditions and radiation conditions at $x = \pm\infty$, requires that β for each mode must satisfy the following eigenvalue equation (Borland '87)

$$\tau (\gamma \tan ht - \mu) + \exp(-2pt_i) [\eta \tan ht - \rho] = 0 \quad (\text{A.5})$$

where

$$\tau = (\sigma_3 p + j\sigma_4 s) \quad \gamma = (\sigma_2^2 h^2 - \sigma_1 \sigma_3 p q) \quad \mu = \sigma_2 h (\sigma_1 q + \sigma_3)$$

$$\eta = (\sigma_2^2 h^2 + \sigma_1 \sigma_3 p q)(\sigma_3 p - j\sigma_4 s) \quad \rho = \sigma_2 h (\sigma_1 q - \sigma_3 p)(\sigma_3 p - j\sigma_4 s)$$

$$\sigma_i = 1 \quad i = 1, 2, 3, 4 \quad (\text{TE modes})$$

$$\sigma_i = 1/n_i^2 \quad i = 1, 2, 3, 4 \quad (\text{TM modes})$$

Physical interpretation of this transcendental equation is not generally immediately accessible. For the limiting case of an infinitely thick buffer layer, the second addend disappears, leaving an equation which is identical to that obtained by applying a similar mathematical treatment to the three-layer configuration (Hunsperger '82).

By numerically solving the eigenvalue equation A.5, the mode complex propagation constant β can be determined, the imaginary part of which represent the attenuation due to energy coupled out of the waveguide through the buffer layer into the substrate.

Appendix B. Effective index method for 3WC

In this Appendix the main theoretical aspects resulting from the application of the effective index method to the 3WC are briefly illustrated.

The geometry of the problem is shown in Fig. B.1. Since an exact analytical solution is not available for this problem, an extension of the effective index method (Ramaswamy '74) has been used by Donnelly et al. ('86) to obtain an approximate analytical solution. According to this method, the 3WC is divided into regions 1 and 2, as shown in Fig. B.1b. Each region is assumed to be a three-layer slab waveguide of infinite extent in the x direction, consisting of a substrate with index n_s , a guiding layer with index n_g and a cladding with index n_c (Fig. B.1c). Region 1 is assumed to have a thickness h , whilst region 2 to have a thickness $h-t$. The effective waveguide indexes n_{g1} and n_{g2} are thus calculated for each region by using the eigenvalue equation for the asymmetrical three-layer slab waveguide, which is presented in Chapter 3.

Then the slab coupled 3WC can be analysed by modelling it as a seven layer structure of infinite extent in the y direction with index n_{g1} in the guiding regions and n_{g2} outside the guiding regions (Fig. B.1d). If the individual isolated guides are single mode, the 3WC supports three modes, two symmetric and one antisymmetric in x (Fig. B.2). The eigenvalue equation for each mode is found by equating the tangential components of the field at each boundary (Donnelly '86). For the two symmetric modes A and B, the resulting eigenvalue equation is

$$\frac{(k \tan(kw/2) - r\gamma)^2(k + r\gamma \tan(kw/2))}{(k \tan(kw/2) + r\gamma)(k^2 + r^2\gamma^2) \tan(kw/2)} = e^{-2\gamma d}$$

where k is the transverse wavenumber in the x-direction, $\gamma=(k_1^2-k_2^2-k^2)^{1/2}$ is the transverse attenuation coefficient, $k_1=2\pi n_{g1}/\lambda$, $k_2=2\pi n_{g2}/\lambda$, $r=1$ for TE modes and $r=(n_{g1}/n_{g2})^2$ for TM modes and λ is the wavelength of light. The propagation constant is $\beta=(k_1^2-k^2)^{1/2}$.

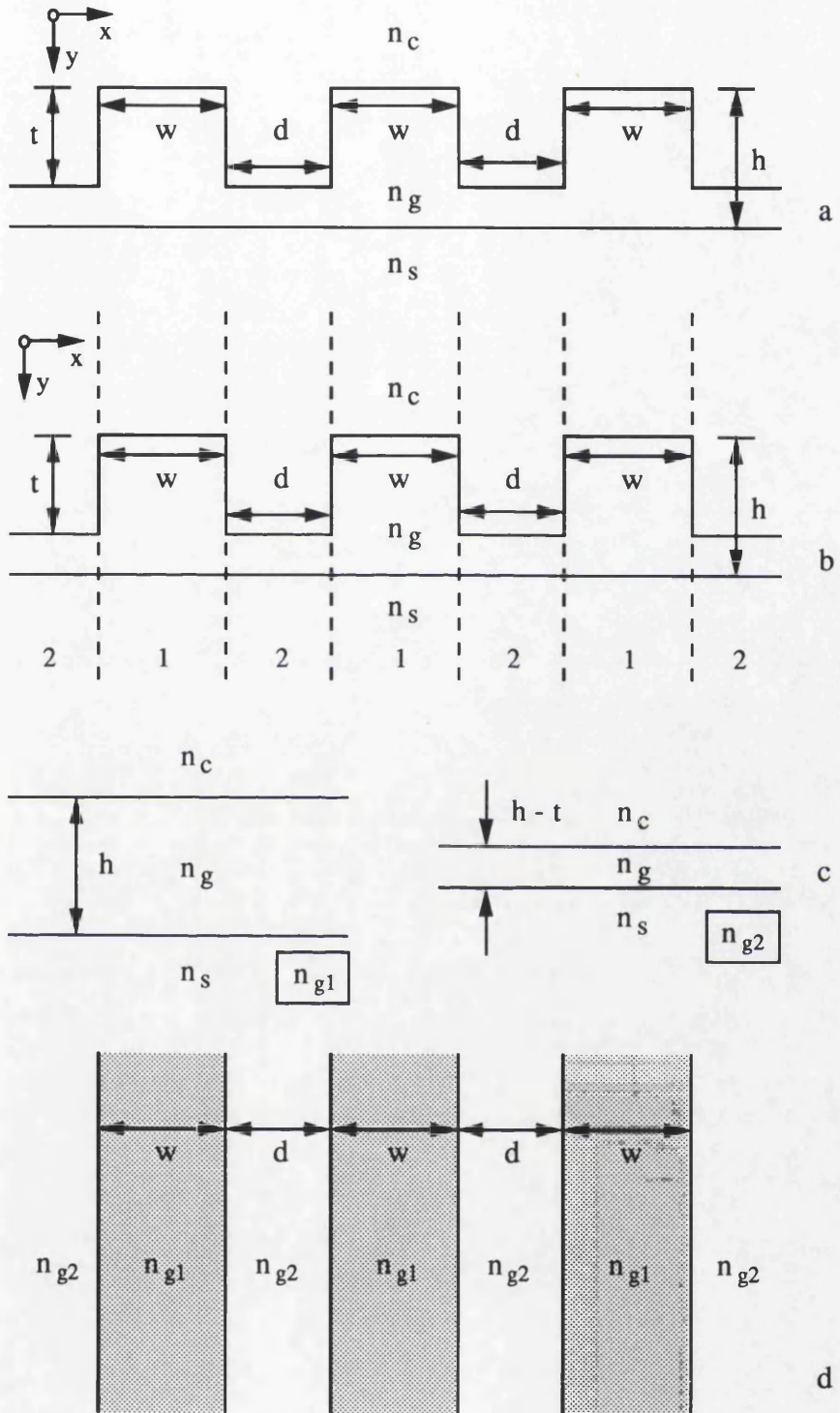


Fig. B.1 Effective index model for 3WC

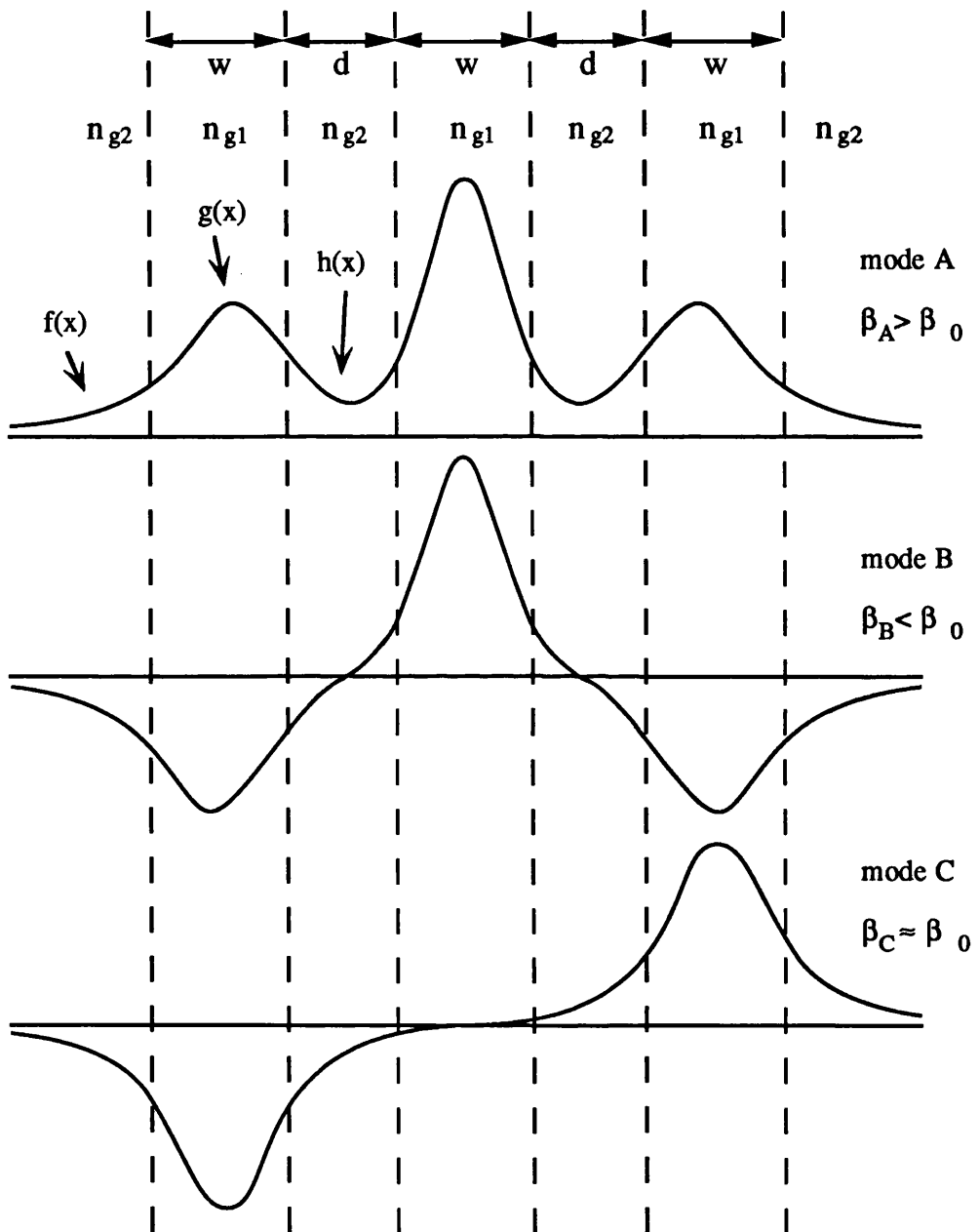


Fig. B.2 Three modes of the 3WC: A and B symmetric, C antisymmetric. The field distributions outside the 3WC, in the single waveguide and in between two waveguides are $f(x) = F \exp(-\gamma |x|)$, $g(x) = D \cos(kx) + E \sin(kx)$ and $h(x) = A \cosh(\gamma x) + B \sinh(\gamma x)$, respectively.

The above equation has two solutions. For the A mode $k_A < k_0$, $\gamma_A > \gamma_0$ and $\beta_A > \beta_0$, where the subscript 0 refers to the mode of a single isolated guide of index n_{g1} in the guiding region and n_{g2} outside the guiding region (Taylor '74). For the B mode $k_B > k_0$, $\gamma_B < \gamma_0$ and $\beta_B < \beta_0$.

The eigenvalue equation for the antisymmetric mode is

$$\frac{(k \tan(kw/2) - r\gamma)(k + r\gamma \tan(kw/2))^2}{(k - r\gamma \tan(kw/2))(k^2 + r^2\gamma^2) \tan(kw/2)} = e^{-2\gamma d}$$

This equation has one solution.

For loose coupling, as a first approximation we can assume that the propagation constants are only slightly perturbed from those of a single isolated guide. I.e., $\beta \approx \beta_0 \pm \Gamma$, $k \approx k_0 \pm \Gamma \beta_0 / k_0$ and $\gamma \approx \gamma_0 \pm \Gamma \beta_0 / \gamma_0$. The expression for Γ is obtained substituting the above expressions in the expressions of β and γ and in the eigenvalue equation for the symmetric modes

$$\Gamma = \frac{2\sqrt{2}rk_0^2\gamma_0^2}{\beta_0[2r(k_0^2 + \gamma_0^2) + (k_0^2 + r^2\gamma_0^2)\gamma_0 w]} e^{-\gamma_0 d}$$

having supposed $\beta_A = \beta_0 + \Gamma$ and $\beta_B = \beta_0 - \Gamma$.

Similarly for the antisymmetric mode we can express $\beta_C \approx \beta_0 + \sigma$ where

$$\sigma = \frac{2rk_0^2\gamma_0^2(k_0^2 - r^2\gamma_0^2)}{\beta_0(k_0^2 + r^2\gamma_0^2)[2r(k_0^2 + \gamma_0^2) + (k_0^2 + r^2\gamma_0^2)\gamma_0 w]} e^{-2\gamma_0 d}$$

With power input into the centre guide, only the two symmetric modes A and B are excited, such that at $z=0$, their fields are in phase. Since the two modes have different propagation constants, at some point l_{3WC} they will be out of phase, i.e. $\beta_A l_{3WC} = \beta_B l_{3WC} + \pi$, and the two modes will be subtractive in the centre guide and additive in the two outer guides. In the loose coupling approximation

$l_{3WC} = \pi/2\Gamma$. It should be noted that Γ assumes in this sense the meaning of a coupling coefficient and it has been demonstrated that it is $\sqrt{2}$ times larger than the coupling coefficient obtained when the same type of analysis is performed on a similar 2WC (Iwasaki '75). This argument is treated in more detail in Appendix C, where the same conclusion is obtained by using the coupled-mode formalism.

Appendix C. Directional coupling in 2WC and 3WC

The theory of directional coupling in cylindrical dielectric waveguides is exhaustively explained in any book on Integrated Optics (e.g. Nishihara '89, Lee '86). In this appendix, power directional coupling in 2WC and 3WC is developed briefly, with the purpose of emphasising the differences existing between the 2WC and the 3WC, in terms of coupling length and power spectral response.

A 2WC consists of two waveguides which are sufficiently closely spaced that interaction between their evanescent fields allows energy to be transferred from one to another. A schematic of a 2WC is shown in Fig. C.1.

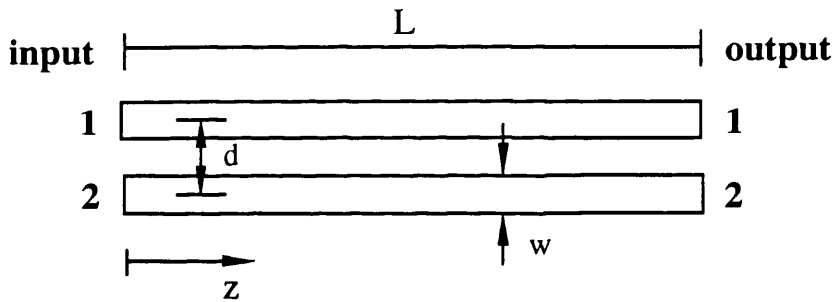


Fig. C.1 Schematic diagram of two waveguide directional coupler (2WC).

The normalised complex field amplitudes $E_1(z)$ and $E_2(z)$ of the modes in the two parallel identical waveguides are governed by the system of equations (Yariv '73)

$$\frac{dE_1(z)}{dz} = -jK(\lambda)E_2(z)$$

$$\frac{dE_2(z)}{dz} = -jK(\lambda)E_1(z)$$

where $K(\lambda)$ is the coupling coefficient between the waveguides, which depends on the wavelength of operation λ , and we have supposed lossless

waveguides. With the boundary conditions $E_1(0) = 1$ and $E_2(0) = 0$, i.e. the input is fed into the waveguide 1, the solution of the system is

$$E_1(z) = \cos(Kz)$$

$$E_2(z) = -j\sin(Kz)$$

The 2WC coupling length l_{2WC} , which is usually defined as the length of interaction necessary to obtain full energy transfer from one waveguide to the other, can be obtained by considering the following conditions

$$E_1(l_{2WC})E_1^*(l_{2WC}) = 0$$

$$E_2(l_{2WC})E_2^*(l_{2WC}) = 1$$

where * denotes complex conjugate. In other words, after an interaction length l_{2WC} all the power is completely transferred from waveguide 1 to waveguide 2. The above conditions are both satisfied if

$$l_{2WC} = n\pi/(2K) \quad n = 1, 3, 5\dots$$

The 3 dB power splitting length, which we indicate by h_{2WC} , can be obtained by considering the following conditions

$$E_1(h_{2WC})E_1^*(h_{2WC}) = \frac{1}{2}$$

$$E_2(h_{2WC})E_2^*(h_{2WC}) = \frac{1}{2}$$

i.e. after an interaction length h_{2WC} the power is equally split in the two waveguides. The above conditions are both satisfied if

$$h_{2WC} = n\pi/(4K) \quad n = 1, 3, 5\dots$$

The power spectral response for the input waveguide 1 of the 2WC is readily expressed by including the wavelength dependence of the coupling coefficient K in the expression of the power for a given interaction length l

$$T_{2WC}(\lambda) = E_1(\lambda)E_1^*(\lambda) = \cos^2(K(\lambda)l)$$

A 3WC consists, in its simplest form of three waveguides which are sufficiently closely spaced that interaction between their evanescent fields allows energy to be transferred from one to another. A schematic of a 3WC is shown in Fig. C.2.

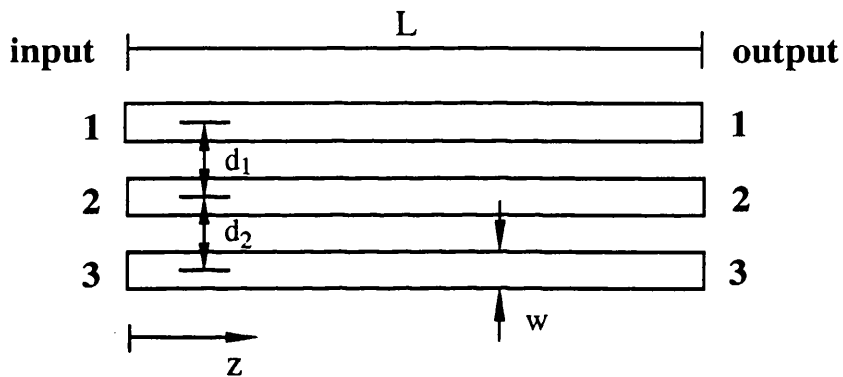


Fig. C.2 Schematic diagram of three waveguide directional coupler (3WC).

The normalised complex field amplitudes $E_1(z)$, $E_2(z)$ and $E_3(z)$ of the modes in the three parallel identical waveguides are governed by the system of equations

$$\frac{dE_1(z)}{dz} = -jK_{12}(\lambda)E_2(z)$$

$$\frac{dE_2(z)}{dz} = -jK_{12}(\lambda)E_1(z) - jK_{23}(\lambda)E_3(z)$$

$$\frac{dE_3(z)}{dz} = -jK_{23}(\lambda)E_2(z)$$

where $K_{12}(\lambda)$ and $K_{23}(\lambda)$ are the coupling coefficients between the adjacent waveguides, which depends on the wavelength λ . We have supposed lossless waveguides and that coupling between non adjacent waveguides is negligible ($K_{13} = 0$). If the 3WC is symmetrical, i.e. the spacing between adjacent waveguides is the same, then $K_{12}(\lambda) = K_{23}(\lambda) = K(\lambda)$. We consider two sets of boundary conditions.

1) $E_2(0) = 1$ and $E_1(0) = E_3(0) = 0$, i.e. the input is fed to the central waveguide 2. In this case the solution of the system is

$$E_1(z) = E_3(z) = -j \frac{1}{\sqrt{2}} \sin(K\sqrt{2}z)$$

$$E_2(z) = \cos(K\sqrt{2}z)$$

For the 3WC the coupling length l_{3WC} can be defined as the length of interaction which is necessary to obtain full energy transfer from the input waveguide to the two output waveguides. It can be obtained by considering the following conditions

$$E_1(l_{3WC})E_1^*(l_{3WC}) = E_3(l_{3WC})E_3^*(l_{3WC}) = \frac{1}{2}$$

$$E_2(l_{3WC})E_2^*(l_{3WC}) = 0$$

i.e. after an interaction length l_{3WC} the power is equally split in the two outer waveguides with no power remaining in the central waveguide. The above conditions are all satisfied if

$$l_{3WC} = \frac{n\pi}{2\sqrt{2}K(\lambda)} \quad n = 1, 3, 5...$$

In the 3WC, for input to the central waveguide, the coupling length, as it has been defined, coincides with the 3 dB power splitting length, i.e. $l_{3WC} = h_{3WC}$.

Comparing the 3 dB power splitting lengths of the 2WC and of the 3WC, we can conclude that

$$h_{3WC} = \frac{h_{2WC}}{\sqrt{2}}$$

Hence the 3WC, for input to the central waveguide, requires a length about 0.7 times shorter than the 2WC to obtain 3 dB power splitting. This is clear in Fig. C.3, where the normalised power distributions in the input waveguide for the 2WC and 3WC have been plotted versus the normalised interaction length Kz .

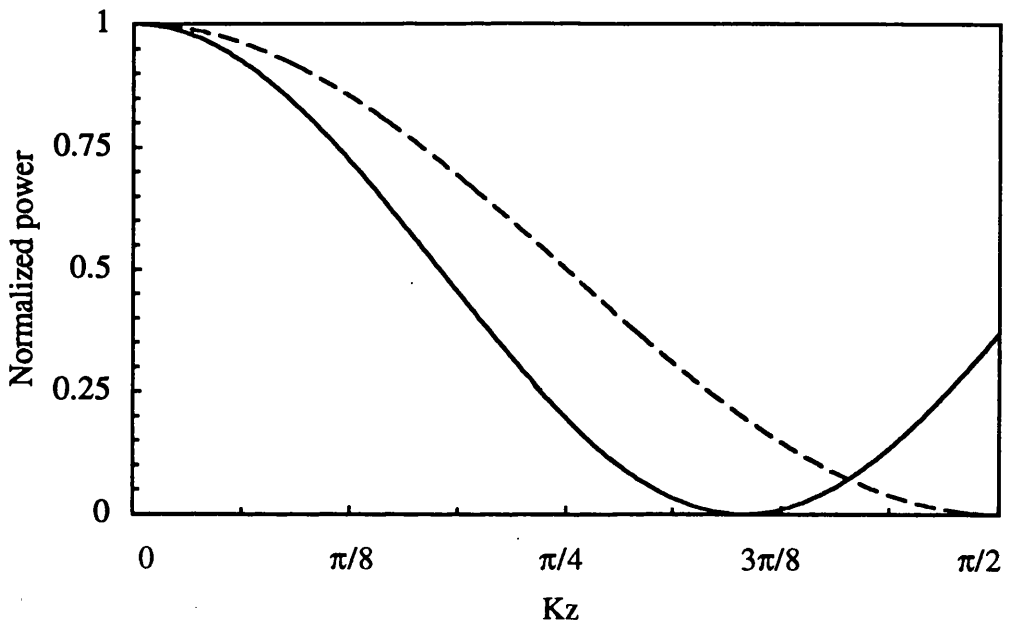


Fig. C.3 Normalised power distribution in the input waveguide as a function of the normalised interaction length Kz for the 2WC (dashed curve) and the 3WC (solid curve, input fed into central waveguide).

The power spectral response for the input central waveguide 2 of the 3WC is readily expressed by including the wavelength dependence of the coupling coefficient K in the expression of the power for a given interaction length l

$$T_{3WC}(\lambda) = E_2(\lambda)E_2^*(\lambda) = \cos^2(K(\lambda)\sqrt{2}l)$$

2) $E_1(0) = 1$ and $E_2(0) = E_3(0) = 0$, i.e. the input is fed to the outer waveguide 1. For these boundary conditions, the solution of the system is

$$E_1(z) = \cos^2\left(\frac{Kz}{\sqrt{2}}\right)$$

$$E_2(z) = -j \frac{1}{\sqrt{2}} \sin(K\sqrt{2}z)$$

$$E_3(z) = -\sin^2\left(\frac{Kz}{\sqrt{2}}\right)$$

In this case the coupling length l_{3WC} can be defined as the length of interaction which is necessary to obtain full energy transfer from the input outer waveguide 1 to the outer waveguide 3. It can be obtained by considering the following conditions

$$E_3(l_{3WC})E_3^*(l_{3WC}) = 1$$

$$E_1(l_{3WC})E_1^*(l_{3WC}) = E_2(l_{3WC})E_2^*(l_{3WC}) = 0$$

After an interaction length l_{3WC} the power is completely transferred from waveguide 1 to waveguide 3, with no power remaining in waveguide 2. The above conditions are all satisfied if

$$l_{3WC} = \frac{n\pi}{\sqrt{2}K(\lambda)} \quad n = 1, 3, 5, \dots$$

The power spectral response for the input outer waveguide 1 of the 3WC is readily expressed by including the wavelength dependence of the coupling coefficient K in the expression of the power for a given interaction length l

$$T_{3WC}(\lambda) = E_1(\lambda)E_1^*(\lambda) = \cos^4\left(\frac{K(\lambda)l}{\sqrt{2}}\right)$$

In weak-coupling operation, we can suppose that the coupling coefficient is linear with wavelength, i.e. $K(\lambda) = K\lambda$ (Kishioka '90). Under this assumption, we can compare the rejection bandwidths of the 2WC and 3WC centred on a rejected

wavelength λ_r . For this wavelength to be rejected at the output from waveguide 1 of the 2WC, it must result that $T_{2WC}(\lambda_r) = 0$, which is satisfied if the 2WC has a length t_{2WC}

$$t_{2WC} = n\pi/(2K\lambda_r) \quad n = 1, 3, 5\dots$$

For the same wavelength to be rejected from waveguide 1 of the 3WC, it must result that $T_{3WC}(\lambda_r) = 0$, which is satisfied if the 3WC has a length t_{3WC}

$$t_{3WC} = \frac{n\pi\sqrt{2}}{2K\lambda_r} \quad n = 1, 3, 5\dots$$

Therefore to reject the same wavelength the 2WC and 3WC must have lengths such that

$$t_{3WC} = \sqrt{2} t_{2WC}$$

Let us find the rejection bandwidth at -20 dB of the 2WC centred on λ_r . We must satisfy

$$T_{2WC}(\lambda_r) = \cos^2(K\lambda_r t_{2WC}) = 0.01$$

From the two solutions of the above equation in the unknown λ_r , we obtain

$$\Delta\lambda_{2WC} \approx 0.2/(Kt_{2WC})$$

For the 3WC

$$T_{3WC}(\lambda_r) = \cos^4\left(\frac{K\lambda_r t_{3WC}}{\sqrt{2}}\right) = 0.01$$

from which we obtain in a similar way

$$\Delta\lambda_{3WC} \approx \frac{0.643\sqrt{2}}{Kt_{3WC}} = \frac{0.643}{Kt_{2WC}}$$

If we take the ratio of the two rejection bandwidths, we obtain

$$\frac{\Delta\lambda_{3WC}}{\Delta\lambda_{2WC}} \approx 3.215$$

i.e. the rejection bandwidth at -20 dB of the 3WC is more than 3 times wider than that of the 2WC. This is clear in Fig. C.4, where the normalised transmissions for the 2WC and the 3WC have been reported versus the product $K' = K\lambda l$.

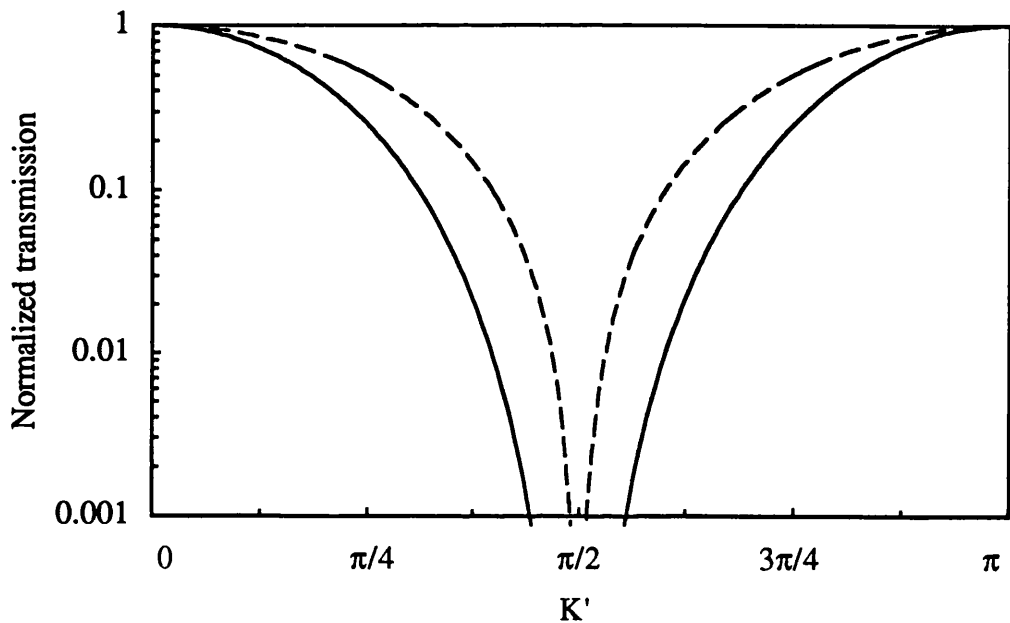


Fig. C.4 Comparison of rejection bandwidth of the power spectral responses between the 2WC (dashed curve) and 3WC (solid curve).

Appendix D. 3WC-based WDM and filter design

In this Appendix examples of design of 3WC-based wavelength division multi-demultiplexer (WDM) and filter are illustrated. Results refer to quasi TE modes. Due to the isotropy of the medium considered, there is little difference from the same analysis performed for quasi TM modes.

It has already been underlined in Appendix C that the coupling coefficient of a 3WC is wavelength dependent. Consequently, the coupling length l_C is also wavelength dependent. At longer wavelengths l_C decreases due to stronger coupling between the modal fields. For a given interaction length L , the wavelength-dependent behavior of l_C results in different amount of power being transferred at different wavelengths to the output ports.

The input port for the WDM considered here is the outer waveguide 1 (see 3WC schematic in Fig. C.2 page 168). For duplexing at wavelength λ_1 and λ_2 we require complete power transfer to port 2 at wavelength λ_1 and to port 1 at wavelength λ_2 , or viceversa. In general, the number of coupling lengths in the region of interaction must be an odd number for λ_1 and an even number for λ_2 . In other words, we require that $(2m_1-1)l_C(\lambda_1)=2m_2l_C(\lambda_2)$, where m_1 and m_2 are positive integers.

For a WDM at 1.3 and 1.55 μm , the condition above is satisfied for many different values of m_1 and m_2 . The minimum length for a WDM operating at 1.3 and 1.55 μm is achieved when the interaction length equals one coupling length at 1.3 μm and twice the coupling length at 1.55 μm , i.e. $l_C(1.3 \mu\text{m}) = 2l_C(1.55 \mu\text{m})$. It has been shown in Appendix B that $l_C(\lambda)=\pi/(2K(\lambda))$. Then the previous condition, in terms of coupling coefficient, becomes $K(1.3 \mu\text{m})/K(1.55 \mu\text{m})=0.5$.

At a fixed wavelength, the coupling coefficient between waveguides having a fixed core geometry depends on the waveguide separation and refractive index step. It is therefore possible to choose these values in such a way that the previous

condition is satisfied. Here we consider slab coupled rib waveguides $4 \mu\text{m}$ wide and we fix the waveguide pitch separation at $6 \mu\text{m}$. The ribs are $3.1 \mu\text{m}$ high leaving a $0.9 \mu\text{m}$ thick coupling slab. We plot now the ratio $R=K(1.3 \mu\text{m})/K(1.55 \mu\text{m})$ versus the refractive index step for the waveguides geometry chosen (Fig. D.1).

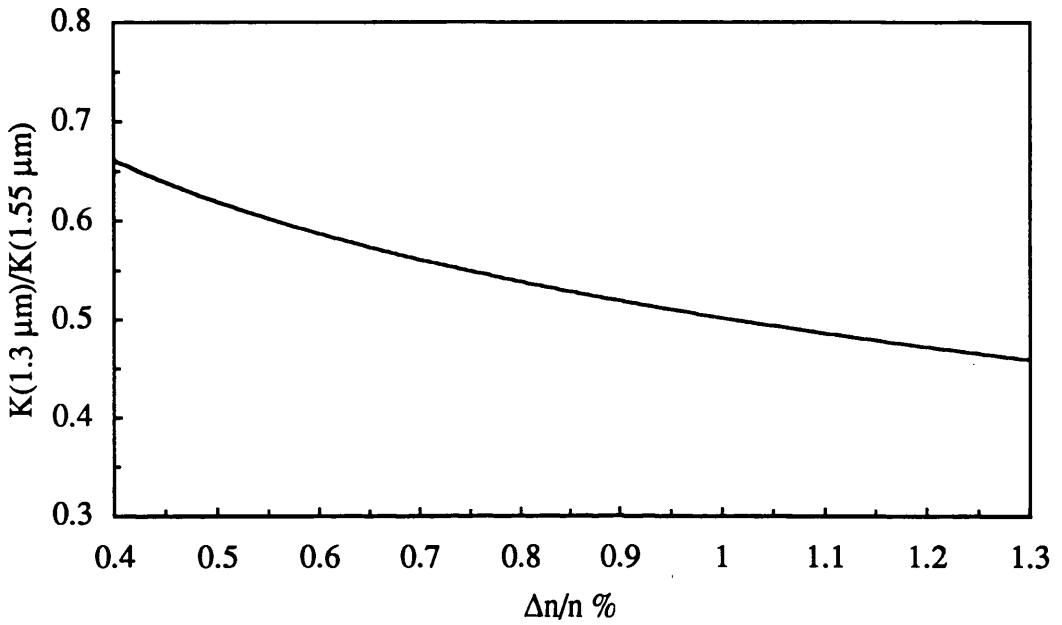


Fig. D.1 Ratio $K(1.3 \mu\text{m})/K(1.55 \mu\text{m})$ versus relative refractive index difference.

At the point of $\Delta n \approx 1 \%$ the value of R becomes 0.5 . We can plot now the spectral response of such a 3WC versus the wavelength and verify that the output peak wavelengths for the two ports corresponds to $\lambda_1=1.3 \mu\text{m}$ and $\lambda_2=1.55 \mu\text{m}$. (Fig. D.2).

In a similar way we can design a filter with two passband peaks at two fixed wavelengths. The input port for the filter considered here is the central waveguide 2. We require complete power transfer to port 2 at wavelengths λ_1 and λ_2 . In general, the number of coupling lengths in the region of interaction must be an odd number for both λ_1 and λ_2 or an even number for both λ_1 and λ_2 . In other words, it is required that $(2m_1-1)l_C(\lambda_1)=(2m_2-1)l_C(\lambda_2)$ or $2m_1l_C(\lambda_1)=2m_2l_C(\lambda_2)$, where m_1 and m_2 are positive integers.

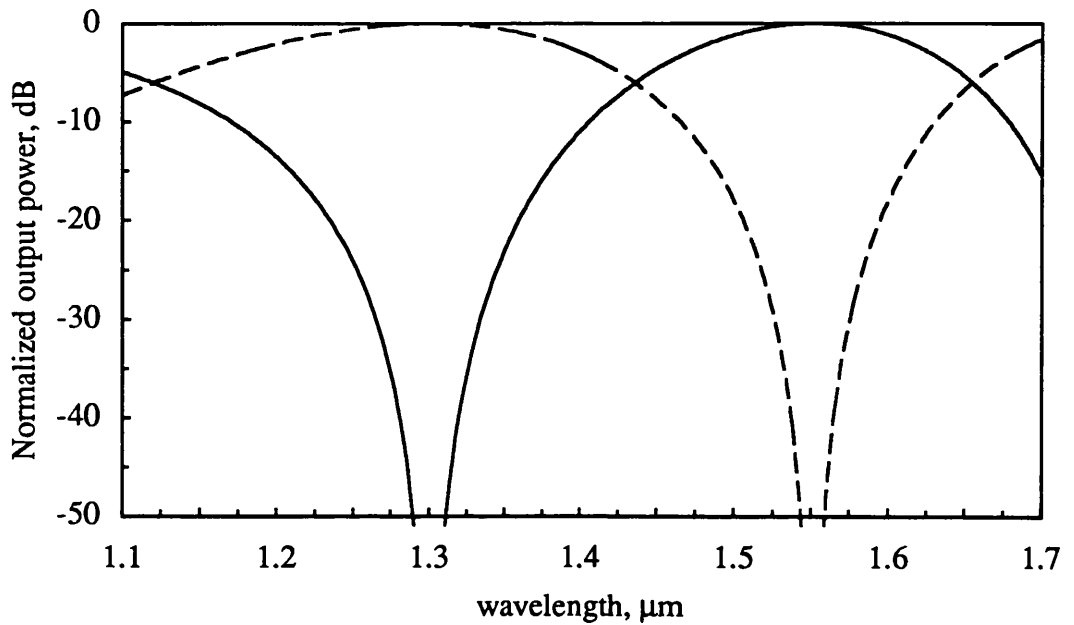


Fig. D.2 Theoretical demultiplexing characteristic of single 3WC for input to one of the outer waveguides and output from the two outer waveguides (dashed curve = 1.3 μm port, solid curve = 1.55 μm port).

For a filter with passband peaks at 0.8 and 1.3 μm , the condition above is satisfied for many different values of m_1 and m_2 . The minimum length for such a filter is achieved when the interaction length equals one coupling length at 0.8 μm and three times the coupling length at 1.3 μm , i.e. $l_C(0.8 \mu\text{m})=3l_C(1.3 \mu\text{m})$. This condition in terms of coupling coefficient becomes $K(0.8 \mu\text{m})/K(1.3 \mu\text{m})\approx 0.33$.

We consider slab coupled rib waveguides 4 μm wide and we fix the waveguide pitch separation at 6 μm . The ribs are 3.1 μm high leaving a 0.9 μm thick coupling slab. We plot now the ratio $R=K(0.8 \mu\text{m})/K(1.3 \mu\text{m})$ versus the refractive index step for the waveguides geometry chosen (Fig. D.3).

At the point of $\Delta n \approx 0.45 \%$ the value of R becomes 0.33. We can plot now the spectral response of such a 3WC versus the wavelength and verify that the output peaks for the central port correspond to $\lambda_1=0.8 \mu\text{m}$ and $\lambda_2=1.3 \mu\text{m}$ (Fig. D.4).

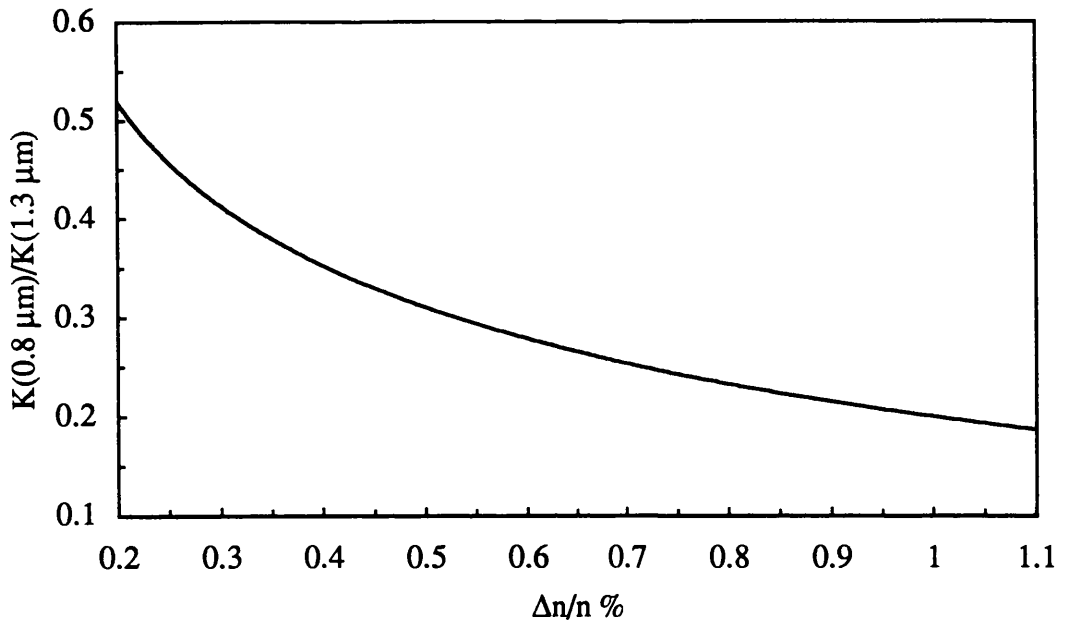


Fig. D.3 Ratio $K(0.8 \mu\text{m})/K(1.3 \mu\text{m})$ versus relative refractive index difference.

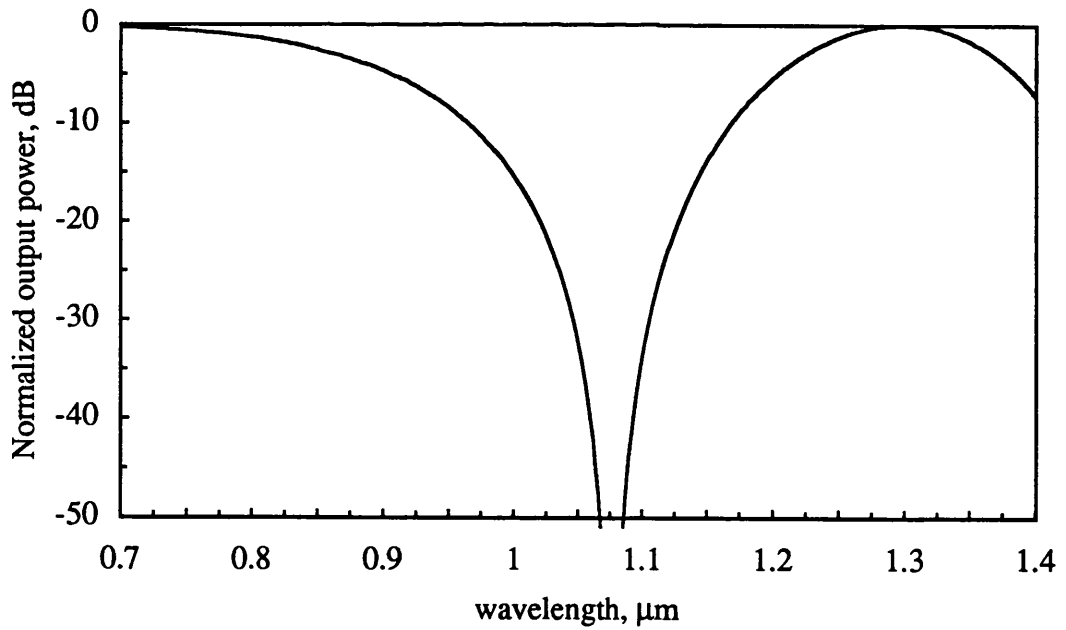


Fig. D.4 Theoretical normalised spectral response of single 3WC filter for input to one of the outer waveguides and output from the same waveguide.

General References.

The following list contains the references cited in the thesis, arranged alphabetically by principal author and year. Co-authors are listed after the principal author. Papers which have been published by the author of this thesis in the course of the research period, are marked with a *.

Ade, R.W., Bossi, D.E., Basilica, R.P. and Berak, J.M., "Vertically integrated AlGaAs waveguide and GaAs photodetector with efficient total internal reflection coupling", Technical Digest of "Integrated Photonic Research Conference", New Orleans, LA, pp. 46-47, April 1992

Ainslie, B.J., "A review of the fabrication and properties of erbium-doped fibres for optical amplifiers", *IEEE/OSA Journal of Lightwave Technology*, LT-9, (2), pp. 220-227, 1991

Albert, J., Wang, W.J. and Najafi, S.I., "Optical damage threshold of ion-exchanged glass waveguides", in "Integrated Optical Circuits", K.-K. Wong ed., *Proceedings SPIE*, 1513, pp. 27-31, 1991

Alferness, R.C. and Schmidt, R.V., "Tunable optical waveguide directional coupler filter", *Applied Physics Letters*, 33, (2), pp. 161-163, 1978

Alferness, R.C., Buhl, L.L., Koren, U., Miller, B.I., Young, M. and Koch, T.L., "Broadly tunable InGaAsP/InP buried rib waveguide vertical coupler filter", *Applied Physics Letters*, 60, (8), pp. 980-982, 1992

Allison, S.W., Gillies, G.T., Magnuson, D.W. and Pagano, T.S., "Pulsed laser damage to optical fibres", *Applied Optics*, 24, (19), pp. 3140-3145, 1985

Arai, K., Namikawa, K., Kumata, K. and Honda, T., "Aluminium or phosphorous co-doping effects on the fluorescence and the structural properties of neodymium doped silica glass", *Journal of Applied Physics*, 59, pp. 3430-3436, 1986

Barbarossa, G., "Design of an integrated optical spectrum analyzer", Laurea Thesis Dissertation (in italian), chapter 4, University of Bari, Italy, July 1988

* **Barbarossa, G. and Laybourn, P.J.R.,** "Fabrication and characterisation of SiO₂-P₂O₅ integrated optical waveguides by Flame Hydrolysis on Si substrate", in "Advance composite materials", M.D. Sacks ed., *Ceramic Transactions*, 19, pp.

313-319, 1991 a

- * **Barbarossa, G. and Laybourn, P.J.R.**, “High-silica low-loss three waveguide couplers on Si by Flame Hydrolysis Deposition”, in “Glasses for Optoelectronics II”, G.C. Righini ed., *Proceedings SPIE*, 1513, pp. 37-43, 1991 b
- * **Barbarossa, G. and Laybourn, P.J.R.**, “High-silica cascaded three-waveguide couplers for wideband filtering by Flame Hydrolysis on Si”, in “Integrated Optical Circuits”, K.K. Wong ed., *Proceedings SPIE*, 1583, pp. 122-128, 1992 a
- * **Barbarossa, G. and Laybourn, P.J.R.**, “Wide rejection band multi-demultiplexer at 1.3-1.55 μm by cascading high-silica three-waveguide couplers on Si”, *Electronics Letters*, 27, (22), pp. 2085-2086, 1992 b
- * **Barbarossa, G. and Maxwell, G.D.**, “Vertical integration of silica waveguides”, U.K. Patent Office Application 9202463.7, Priority (0), 5/2/1992 c
- * **Barbarossa, G. and Laybourn, P.J.R.**, “Vertically integrated high-silica channel waveguides on Si”, *Electronics Letters*, 28, (5), pp. 437-438, 1992 d
- * **Barbarossa, G. and Laybourn, P.J.R.**, “Vertical integration of high-silica channel waveguides on Si”, Technical Digest of “Integrated Photonic Research Conference”, New Orleans, LA, pp. 260-261, April 1992 e
- * **Barbarossa, G. and Laybourn, P.J.R.**, “Optical damage threshold of P_2O_5 and GeO_2 - P_2O_5 -doped silica waveguides”, to be published in *Proceedings SPIE*, 1794, of “OE/Fibres ‘92” held in Boston, Ma, 8-11 Sep. 1992 f
- * **Barbarossa, G. and Laybourn, P.J.R.**, “Effect of temperature gradient on sintering kinetics of high silica integrated optical waveguides by flame hydrolysis deposition”, to be published in *Proceedings SPIE*, 1794, of “OE/Fibres ‘92” held in Boston, Ma, 8-11 Sep. 1992 g
- * **Barbarossa, G., Bebbington, J.A., Aitchison, J.S. and Laybourn, P.J.R.**, “Doped silica waveguides on Si for integrated optical circuits”, submitted for publication to *Optical Engineering*, special issue “Optical Engineering in the U.K.”, 1992 h
- * **Barbier, D., Green, M. and Madden, S.J.**, “Waveguide fabrication for integrated optics by electron beam irradiation of silica”, *IEEE/OSA Journal of Lightwave Technology*, LT-9, (6), pp. 715-720, 1991
- * **Beales, K.J. and Day, C.R.**, “A review of glass fibres for optical communications”, *Physics and Chemistry of Glasses*, 21, (1), pp. 5-12, 1980
- * **Bebbington, J.A., Barbarossa, G., Aitchison, J.S.**, “Rare-earth doped silica

waveguides fabricated by flame hydrolysis deposition and aerosol doping”,
Technical Digest of OSA Annual Meeting, Albuquerque, New Mexico, 20-25
September, 1992 a

- * **Bebbington, J.A., Barbarossa, G., Bonar, J. and Aitchison, J.S.**, “Rare-earth doped silica waveguides on Si fabricated by flame hydrolysis deposition and aerosol doping”, accepted for publication in *Applied Physics Letters*, Jan. 1992 b
- Bebbington, J.A.**, “Rare earth doped silica waveguide lasers”, Ph.D. Thesis, Glasgow University, to be published, 1992 c
- Bogert, G.A.**, “Ti:LiNbO₃ three-waveguide polarisation splitter”, *Electronics Letters*, 23, (1), pp. 37-38, 1987
- Borland, W.C., Zelmon, D.E., Radens, C.J., Boyd, J.T., Jackson, H.E.**, “Properties of four-layer planar optical waveguides near cutoff”, *IEEE Journal of Quantum Electronics*, QE-23, (7), pp. 1172-1179, 1987
- Chan, W.K., von Lehmen, A., Florez, L.T., Harbison, J.P. and Nguyen, C.K.**, “Optical AND gates using vertically integrated surface emitting laser-phototransistor”, Technical Digest of Optical Fibre Communication Conference, paper PDP18-1, 1992
- Cheng, H.C. and Ramaswamy, R.V.**, “Symmetrical directional coupler as a wavelength multiplexer-demultiplexer: theory and experiment”, *IEEE Journal of Quantum Electron.*, 27, pp. 567-574, 1991
- Croteau, A.**, National Optics Institute, 369 rue Franquet, Sainte-Foy, Quebec, G1P 4N8, Canada, private communication, 1991
- Digiovanni, D.J., Morse, T.F. and Cipolla, J.W.**, “The effect of sintering on dopant incorporation in modified chemical vapour deposition”, *IEEE/OSA Journal of Lightwave Technology*, 7, (12), pp. 1967-1972, 1989
- Donnelly, J.P., De Meo, N.L. and Ferrante, G.A.**, “Three-guide optical coupler in GaAs”, *IEEE/OSA Journal of Lightwave Technology.*, LT-1, pp. 417-424, 1983
- Donnelly, J.P.**, “Limitations on power-transfer efficiency in three-guide optical couplers”, *IEEE Journal of Quantum Electronics*, QE-22, (5), pp. 610-616, 1986
- Donnelly, J.P., Haus, H.A. and Whitaker, N.**, “Symmetric three-guide optical coupler with nonidentical centre and outside guides”, *IEEE Journal of Quantum Electronics*, QE-23, (4), pp. 401-406, 1987
- Eldridge, J.M. and Balk, P.**, “Formation of phosphosilicate glass films on silicon

- dioxide”, *Transactions of the Metallurgical Society of AIME*, 242, pp. 539-545, **1968**.
- Gambling**, W.A., Payne, D.N., Hammond, C.R. and Norman, S.R., “Optical fibres based on phosphosilicate glass”, *IEE Proceedings*, 123, (6), pp. 570-576, **1976**
- Ghoshtagore**, R.N., “Phosphorous diffusion process in SiO₂ films”, *Thin Solid Films*, 25, pp. 501-513, **1975**
- Hammond**, C.R., “Fusion temperatures of SiO₂-P₂O₅ binary glasses”, *Physics and Chemistry of Glasses*, 19, (3), pp. 41-42, **1978**
- Harris**, J.H., Shubert, R. and Polky, J.N., “Beam coupling to films”, *Journal of Optical Society of America*, 60, (8), pp. 1007-1009, **1970**
- Haus**, H.A. and Fonstad, C.G., “Three-waveguide couplers for improved sampling and filtering”, *IEEE Journal of Quantum Electronics*, QE-17, (12), pp. 2321-2325, **1981**
- Henry**, C.H., Blonder, G.E. and Kazarinov, R.F., “Glass waveguides on silicon for hybrid optical packaging”, *IEEE/OSA Journal of Lightwave Technology*, LT-7, (10), pp. 1530-1539, **1989**
- Hermann**, P. and Wildmann, D., “Fabrication of planar dielectric waveguides with high optical damage threshold”, *IEEE Journal of Quantum Electronics*, QE-19, (12), pp. 1735-1738, **1983**
- Hibino**, Y., Kitagawa, T., Shimizu, M., Anawa, F.H. and Sugita, A., “Nd doped silica optical waveguide laser on silicon substrate”, *IEEE Photonics Technology Letters*, 1, (11), pp. 349-350, **1989**
- Huang**, A.S., Arie, Y., Neil, C.C. and Hammer, J.M., “Study of refractive index of SiO₂-GeO₂ mixtures using deposited-thin-film optical waveguides”, *Applied Optics*, 24, (24), pp. 4404-4407, **1985**
- Hubbard**, S.D., Ainslie, B.J., Bailey, S.A. and Maxwell, G.D., “Arsenic doped silica as a passive waveguiding material”, ECIO '89, Paris, April **1989**
- Hunsperger**, R.G., *Integrated Optics: Theory and Technology*, 2nd ed., New York, Springer-Verlag, chapter 3, **1982**
- Hyde**, J.F., “Method of making transparent articles of silica”, U.S. patent No. 2,272,342, **1934**
- Imoto**, K., Sano, H. and Miyazaki, M., “Guided-wave multi-demultiplexers with

- high stopband rejection”, *Applied Optics*, 26, (19), pp. 4214-4219, **1987**
- Imoto, K., Asai, T., Sano, H. and Maeda, M.**, “Silica glass waveguide structure and its application to a multi/demultiplexer”, Proceedings ECOC '88, Brighton, U.K., pp. 577-580, September **1988**
- Ishio, H., Minowa, J. and Nosu, K.**, “Review and status of wavelength-division multiplexing technology and its application”, *IEEE/OSA Journal of Lightwave Technology*, LT-2, pp. 448-463, **1984**
- Iwasaki, K., Kurazono, S. and Itakuna, K.**, “The coupling of modes in three dielectric slab waveguides”, *Electronics and Communications in Japan*, 58-C, (8), pp. 100-108, **1975**
- Izawa, T., Kobayashi, S., Sudo, S. and Hanawa, F.**, “Continuous fabrication of high silica fibre preform”, Technical Digest 2nd International Conference Integrated Optics and Optical Fibre Communication, Tokyo, Japan, pp. 375-379, **1977**
- Izawa, T., Mori, H., Murakami, Y. and Shimizu, N.**, “Deposited silica waveguide for integrated optical circuits”, *Applied Physics Letters*, 38, (7), pp. 483-485, **1981**
- Izawa, T. and Sudo, S.**, *Optical fibres: materials and fabrication*, Tokyo, KTK Scientific Publishers, chapter 4, **1987**
- Jackson, K.P., Flint, E.B., Cina, M.F., Lacey, D., Trehwella, J.M., Caulfield, T. and Sibley, S.**, “Compact planar processed package for multichannel, fibre-optic computer interconnects”, Technical Digest of Optical Fibre Communication Conference, pp. 121-122, **1992**
- Jackel, J.L. and Veselka, J.J.**, “Measuring losses in optical waveguides: a new method”, *Applied Optics*, 23, (2), pp. 197-199, **1984**
- Kao, K.C. and Hocklam, G.A.**, “Dielectric fibre surface waveguides for optical frequencies”, *IEE Proceedings*, 113, (7), pp. 1151-1158, **1966**
- Kashyap, R. and Blow, K.J.**, “Observation of catastrophic self-propelled self-focusing in optical fibres”, *Electronics Letters*, 24, (1), pp. 47-49, **1988**
- Kashyap, R., Ainslie, J.B. and Maxwell, G.D.**, “Second harmonic generation in GeO₂ ridge waveguides”, *Electronics Letters*, 25, (3), pp. 206-208, **1989**
- Kawachi, M., Yasu, M. and Edahiro, T.**, “Fabrication of SiO₂-TiO₂ glass planar waveguides by flame hydrolysis deposition”, *Electronics Letters*, 19, (15), pp.

583-584, 1983

Kawachi, M., "Silica waveguides on silicon and their application to integrated-optic components", *Optical and Quantum Electronics*, 22, pp. 391-416, 1990

Keck, D.B. and Schultz, P.C., "Method of forming planar optical waveguides", U.S. Patent No. 3,806,223, 1974

Keck, D.B. and Schultz, P.C., "Method of forming optical waveguide fibres", U.S. Patent No. 3,737,292, 1972

Keck, D.B., Morrow, A.J., Nolan, D.A. and Thompson, D.A., "Passive components in the subscriber loop", *IEEE/OSA Journal of Lightwave Technology*, LT-7, (11), pp. 1623-1633, 1989

Kern, W. and Rosler, R.S., "Advances in deposition processes for passivation films", *Journal of Vacuum Science Technology*, 14, (5), pp. 1082-1099, 1977

Kersten, R.T., Otto, J. and Paquet, V., "Thick coatings of doped synthetic silica glass by plasma impulse CVD", *Journal of the Ceramic Society of Japan*, 99, (10), pp. 894-902, 1991

Kirk-Othmer, "Vitreous silica" in *Encyclopaedia of chemical technology*, John Wiley & Sons, New York, vol. 20, pp. 782-817, 1972

Kishioka, K., "Improvement of the power spectral response in the three-guided coupler demultiplexer", *Applied Optics*, 29, (3), pp. 360-366, 1990

Kitagawa, T., Hattori, K., Shimizu, M., Ohmori, Y. and Kobayashi, M., "Guided-wave laser based on Erbium-doped silica planar lightwave circuit", *Electronics Letters*, 27, (4), pp. 334-335, 1991

Kitagawa, T., Hattori, K., Shuto, K., Yasu, M., Kobayashi, M. and Horiguchi, M., "Amplification in Er-doped silica-based planar lightwave circuits", Proceedings OSA Conference "Optical amplifiers and their applications", paper PD1, Sante Fe, U.S.A., June 1992

Kominato, T., Ohmori, Y., Okazaki, H. and Yasu, M., "Very low-loss GeO₂-doped silica waveguides fabricated by flame hydrolysis deposition method", *Electronics Letters*, 26, (5), pp. 327-328, 1990

Kurosawa, T. et al., "Analysis of rectangular-core dielectric waveguides: an accurate perturbation approach", *Applied Optics*, 19, (1), pp. 3124-3126, 1980

Lagasse, P.E. and Baets, R., "The beam propagation method in integrated optics", in "Hybrid formulation of wave formulation and scattering", Proceedings of

N.A.T.O. A.R.W. Castelgandolfo, Italy, 1983, pp. 112-118, Martinus Nyjhoff, L.B. Felsen Editor, Amsterdam, **1984**

Lai, Q., Gu, J.S., Smit, M.K., Schmid, J. and Melchior, H., "Simple technologies for fabrication of low-loss silica waveguides", *Electronics Letters*, 28, (11), pp. 1000-1001, **1992**

Lee, D.L., *Electromagnetic principles of Integrated Optics*, New York, John Wiley & Sons, Inc., **1986**

Lee, H.J., Henry, C.H., Orlowsky, K.J., Kazarinov, R.F. and Kometani, T.Y., "Refractive index dispersion of phosphosilicate glass, thermal oxide and silicon nitride films on silicon", *Applied Optics*, 27, (19), pp. 4104-4109, **1988**

Linnell, L.R., "A wide-band local access system using emerging-technology components", *IEEE Journal of Selected Area of Communications*, 1987, SAC-4, pp. 612-618, **1986**

Loni, A., Software for the determination of refractive index profile using the inverse WKB method, **1990**

Lorenzo, J.P. and Soref, R.A., "Electro-optical silicon devices", U.S. Patent No. 4,787,691, **1988 a**

Lorenzo, J.P. and Soref, R.A., "Method for fabricating low-loss crystalline silicon waveguides by dielectric implantation", U.S. Patent No. 4,789,642, **1988 b**

Mackenzie, J.K. and Shuttleworth, R., "A phenomenological theory of sintering", *Proceedings Physics Society London*, 62, (12-B), pp. 833-852, **1949**

Malitson, I.H., "Interspecimen comparison of the refractive index of fused silica", *Journal of Optical Society of America*, 55, (10), pp. 1205-1209, **1965**

Marcuse, D., "Directional couplers made of nonidentical asymmetric slabs. Part I: synchronous couplers", *IEEE/OSA Journal of Lightwave Technology*, 1987, LT-5, (1), pp. 113-119, **1987**

Matsumura, K. and Tomabechi, Y., "Coupling characteristics of two rectangular dielectric waveguides laid in different layers", *IEEE Journal of Quantum Electronics*, QE-22, 6, pp. 959-963, **1986**

Matsuo, S., "Selective etching of SiO₂ relative to Si by plasma reactive sputter etching", *Journal of Vacuum Science Technology*, 17, (2), pp. 587-594, **1980**

* Maxwell, G.D., Kashyap, R. and Barbarossa, G., "Second harmonic generation in GeO₂ doped silica ridge waveguides", Digest First International Ceramic

- Science and Technology Congress, Anaheim, CA, p. 87, October 1989
- Maxwell, G.D., BT Labs, Martlesham Heath, Ipswich, IP5 7RE, U.K., private communication, 1991 and 1992
- Millar, C.A., BT Labs, Martlesham Heath, Ipswich, IP5 7RE, U.K., private communication, 1990
- Miller, S.E., "Integrated Optics: an introduction", *Bell System Technical Journal*, 48, (7), pp. 2059-2069, 1969
- Miyashita, T., Sumida, S. and Sakaguchi, S., "Integrated optical devices based on silica waveguide technologies", in "Integrated optical circuit engineering VI", *Proceedings SPIE*, 993, pp. 288-294, 1988
- Morrow, A.J., Sarkar, A. and Schultz, P.C., "Outside Vapour Deposition" in *Optical Fibre Communications*, T. Li ed., Academic Press inc., London, 1985
- Morse, T.F., Kilian, A., Reinhart, L., Risen, W. and Cipolla, J.W., "Aerosol Techniques for Glass Formation", *Journal of Non-Crystalline Solids*, 129, pp. 93-100, 1991
- Naik, I.K., "Low-loss integrated optical waveguides fabricated by nitrogen ion implantation", *Applied Physics Letters*, 43, (6), pp. 519-520, 1983
- Niizeki, N., Inagaki, N. and Edhairo, T., "Vapour-Phase Axial Deposition Method" in *Optical Fibre Communications*, T. Li ed., Academic Press inc., London, 1985
- Nishihara, H., Haruna, M. and Suhara, T., *Optical Integrated Circuits*, New York, McGraw-Hill, 1989
- Nourshargh, N., Starr, E.M., Fox, N.I. and Jones, S.G., "Simple technique for measuring attenuation of integrated optical waveguides", *Electronics Letters*, 21, (18), pp. 818-820, 1985 a
- Nourshargh, N., Starr, E.M. and Mc Cormarck, J.S., "Plasma deposition of integrated optical waveguides", in "Integrated optical circuit engineering II", *Proceedings SPIE*, 578, pp. 95-99, 1985 b
- Noutsios, P.C., Yip, G.L. and Albert, J., "A novel vertical directional coupler made by graded-index ion-exchanged slab waveguides", Technical Digest of "Integrated Photonic Research Conference", New Orleans, LA, pp. 156-157, April 1992
- Ohmori, Y., Kominato, T., Okazaki, H. and Yasu, M., "Low loss GeO₂ doped

silica waveguides for large scale integrated optical devices”, Technical Digest of Optical Fibre Communication Conference, paper WE2, San Francisco, Jan. **1990**

Pedersen, J.E., Brierley, M.C., Carter, S.F. and France, P.W., “Amplification in the 1300 nm telecommunications window in a Nd-doped fluoride fibre”, *Electronics Letters*, 26, (5), pp. 329-330, **1990**

PIRI Photonic Integration Research inc., 2727 Scioto Parkway, Columbus, Ohio, 43221-4658, USA; Optical waveguide devices catalogue, **1991 and 1992**

Pliskin, W.A., “Comparison of properties of dielectric films deposited by various methods”, *Journal of Vacuum Science Technology*, 14, (5), pp. 1064-1081, **1977**

Ramaswamy, R.V., “Strip-loaded film waveguide”, *Bell System Technical Journal*, 52, (4), pp. 697-704, **1974**

Ramaswamy, R.V. and Srivastava, R., “Ion exchanged glass waveguides; a review”, *IEEE/OSA Journal of Lightwave Technology*, LT-6, (6), pp. 984-1002, **1988 a**

Ramaswamy, R.W., Chia, T., Srivastava, R., Miliou, A. and West, J., “Gel Silica waveguides”, in “Multifunctional materials”, D.R. Ulrich ed., *Proceedings SPIE*, 878, paper 11, **1988 b**

Rose, J.W., “High density optical waveguide array”, IBM Technical Disclosure Bulletin, 23, (10), pp. 4453-4454, **1981**

Safaai-Jazi, A. and Mc Keeman, J.C., “All-fibre spectral filters with nonperiodic bandpass characteristics and high extinction ratios in the wavelength range $0.8 \mu\text{m} < \lambda < 1.6 \mu\text{m}$ ”, *IEEE/OSA Journal of Lightwave Technology*, LT-9, (8), pp. 959-963, **1991**

Sanada, K., Shioda, T., Moriyama, T., Inada, K., Takahashi, S. and Kawachi, M., “PbO doped high silica fibre fabricated by modified VAD”, Proceedings of 6th ECOC, York, U.K., pp. 14-17, **1980**

Schafer, E.C. and Roy, R., *Phase diagrams for ceramists*, E. M. Levine Ed., p. 140, **1964**

Scherer, G.W., “Sintering of low-density glasses”, *Journal of the American Ceramic Society*, 60, (5-6), pp. 236-246, **1977**

Scherer, G.W. and Garino, T., “Viscous sintering on a rigid substrate”, *Journal of the American Ceramic Society*, 68, (4), pp. 216-220, **1985**

Schineller, E.R., Flam, R.P. and Wilmot, D.W., “Optical waveguides formed by

- proton irradiation of fused silica”, *Journal of Optical Society of America*, 58, (9), pp. 1171-1176, **1968**
- Schneider**, H.W., “Realisation of SiO₂-B₂O₃-TiO₂ waveguides and reflectors on Si Substrate”, MRS Meeting, Boston, USA, paper J11.2, November **1991**
- Schott**, Optical Glass Catalogue, Optics Division, P.O. Box 2480, D-6500 Mainz, Germany, **1990**
- Senior**, J.M., *Optical fibre communications: principle and practice*, Englewood Cliffs, Prentice Hall, **1992**
- Sheem**, S.K., Giallorenzi, T.G. and Koo, K., “Optical techniques to solve the signal fading problem in fibre interferometers”, *Applied Optics*, 21, (4), pp. 689-693, **1982**
- Shimizu**, N., “Fusion splicing between deposited silica waveguides and optical fibres”, *Electronics and Communications in Japan*, 67-C, (9), pp. 115-122, **1984**
- Soref**, R.A., Cortesi, E., Namavarand, F. and Friedman, L., “Vertically integrated silicon-on-insulator waveguides”, *IEEE Photonics Technology Letters*, 3, (1), pp. 22-24, **1991**
- Standley**, R.D., Gibson, W.M. and Rodgers, J.W., “Properties of ion-bombarded fused quartz for integrated optics”, *Applied Optics*, 11, (6), pp. 1313-1316, **1972**
- Stegeman**, G.I. and Seaton, C.T., “Nonlinear Integrated Optics”, *Journal of Applied Physics*, 58, (12), pp. R57-R78, **1985**
- Steinbruchel**, C., Lehmann, H.W. and Frick, K., “Mechanism of dry etching of silicon dioxide”, *Journal of Electrochemical Society*, 132, (1), pp. 180-186, **1985**
- Sudo**, S., Edahiro, T. and Kawachi, M., “Sintering process of porous preforms made by a VAD method for optical fibre fabrication”, *Transactions of the IECE Japan*, E62, pp. 731-737, **1980**
- Sudo**, S., Kawachi, M., Suda, H., Nakahara, M. and Edahiro, T., “Refractive-index profile control techniques in the vapour-phase axial deposition method”, *Transactions of the IECE of Japan*, E-64, (8), pp. 536-543, **1981**
- Sun**, C.J., Myers, W.M., Schmidt, K.M. and Sumida, S., “Silica-based circular cross-sectioned channel waveguides”, *IEEE Photonics Technology Letters*, 3, (3), pp. 238-240, **1991**
- Sze**, S.M., *VLSI Technology*, New York, McGraw-Hill, **1983**
- Takada**, K., Takato, N., Noda, J. and Uchida, N., “Interferometric optical-time-

domain reflectometer to determine backscattering characterisation of silica-based glass waveguides”, *Journal of Optical Society of America*, 7, (5), pp. 857-867, **1990**

Takahashi, H., Sanada, K., Inada, K. and Fukuda, O., “Method for producing multi-component glass fibre preform”, U.S. Patent No. 4,336,049, **1982**

Takahashi, H., Ohmori, Y., Kawachi, M., “Design and fabrication of silica-based integrated-optic 1x128 power splitter”, *Electronics Letters*, 27, (23), pp. 2131-2133, **1991**

Takato, N., Kawachi, M., Nakahara, M. and Miyashita, T., “Silica-based single-mode guided-wave devices”, *Proceedings SPIE*, 1177, pp. 92-100, **1989**

Tamir, T., *Integrated Optics: an introduction*, New York, Springer-Verlag, **1975**

Tamir, T. and Kou, F.Y., “Varieties of leaky waves and their excitation along multilayered structures”, *IEEE Journal of Quantum Electronics*, QE-22, (4), pp. 544-551, **1986**

Taylor, H.F. and Yariv, A., “Guided wave optics”, *Proceedings IEEE*, 62, (8), pp. 1044-1060, **1974**

Tien, T.Y. and Hummel, F.A., “The system SiO₂-P₂O₅”, *Journal of the American Ceramic Society*, 45 (9), pp. 422-424, **1962**

Tien, P.K., “Integrated optics and new wave phenomena in optical waveguides”, *Reviews of Modern Physics*, 49, (2), pp. 361-420, **1977**

Townsend, J.E., Poole, S.B. and Payne, D.N., “Solution-doping technique for fabrication of rare-earth-doped optical fibres”, *Electronics Letters*, 23, (7), pp. 329-331, **1987**

Tumminelli, R., Hakimi, F. and Haavisto, J., “Integrated-optic Nd:glass laser fabricated by flame hydrolysis deposition using chelates”, *Optics Letters*, 16, (14), pp. 1098-1100, **1991**

Ulrich, R. and Torge, R., “Measurement of thin film parameters with a prism coupler”, *Applied Optics*, 12, (12), pp. 2901-2908, **1973**

Ulrich, G.D., “Flame synthesis of fine particles”, *Chemistry & Engineering News*, pp. 23-29, Aug. 6, **1984**

Urquhart, P., “Compound optical-fibre-based resonators”, *Applied Optics*, 5, (6), pp. 803-812, **1988**

Valette, S., “State of the art of integrated optics technology at LETI for achieving

- passive optical components”, *Journal Modern Optics*, 35, pp. 993-1005, **1988**
- Valette**, S., Jadot, J.P., Gidon, P., Renard, S., Fournier, A., Grouillet, A.M., Denis, H., Philippe, P. and Desgranges, E., “Si-based Integrated Optics technologies”, *Solid State Technology*, pp. 69-75, February **1989**
- Verbeek**, B.H., Henry, C.H., Olsson, N.A., Orłowsky, K.J., Kazarinov, R.F. and Johnson, B.H., “Integrated four channel Mach-Zehnder multi/demultiplexer fabricated with phosphorous doped SiO₂ waveguides on Si”, *IEEE/OSA Journal Lightwave Technology*, 6, pp. 1011-1015, **1988**
- Werts**, A., “Propagation de la lumière cohérente dans les fibres optiques”, *Onde Electrique* (in french), 46, pp. 967-980, **1966**
- White**, J.M. and Heidrich, P.F., “Optical waveguide refractive index profiles determined from measurement of mode indices: a simple analysis”, *Applied Optics*, 15, (1), pp. 151-158, **1976**
- Wilkinson**, C.D.W., University of Glasgow, Department of Electronics and Electrical Engineering, G12 8QQ, Glasgow, U.K., private communication, **1992**
- Won**, Y.H., Jassaud, P.C. and Chartier, G.H., “Three-prism loss measurements of optical waveguides”, *Applied Physics Letters*, 37, (3), pp. 269-271, **1980**
- Yan**, M.F., Macchesney, J.B., Nagel, S.R. and Rhodes, W.W., “Sintering of optical waveguide glasses”, *Journal of Materials Science*, 15, pp. 1371-1378, **1980**
- Yanagawa**, H., Nakamura, S., Watanabe, K. and Miyazawa, H., “Mode field profile converting optical channel waveguide with tapered refractive index and cross-section”, *Electronics Letters*, 25, (13) pp. 849-850, **1989**
- Yariv**, A., “Coupled-mode theory for guided-wave optics”, *IEEE Journal of Quantum Electronics*, QE-9, (9), pp. 919-933, **1973**
- Yataki**, M.S., Payne, D.N. and Varnham, M.P., “All-fibre wavelength filters using concatenated fused-taper couplers”, *Electronics Letters*, 21, (6), pp. 248-249, **1985**
- Zelmon**, D.E., Jackson, H.E., Boyd, J.T., Naumaan, A. and D.B. Anderson, “A low-scattering graded-index SiO₂ planar optical waveguide thermally grown on silicon”, *Journal of Applied Physics*, 42, (7), pp. 565-566, **1983**